Investigation of Bioinspired Oxidation Mechanism by Non-Heme High-Valent Metal Intermediates

A Thesis Submitted in Partial Fulfillment of the
Requirements for the degree of

DOCTOR OF PHILOSOPHY

UMESH KUMAR BAGHA

(Roll No. 166122104)

Department of Chemistry
Indian Institute of Technology Guwahati
Guwahati-781039
Assam, India

Supervisor: Prof. Chivukula V. Sastri

January 2023

Dedicated to

My Family

CONTENTS

STATEMENT

This thesis submitted in partial fulfilment of the requirements for the doctoral degree at Indian Institute of Technology Guwahati, I hereby declare that the matter embodied in this thesis is a result of investigations carried out by me in the Department of Chemistry, Indian Institute of Technology Guwahati, India, under the supervision of Prof. Chivukula Vasudeva Sastri. In keeping with the general practice of reporting scientific observations, due acknowledgements have been made and references have been cited to the original source wherever the work is based on the findings of other investigators.

Umesh Kumar Bagha

Umesh Kumar Bagha

Date: 31/01/2023

Place: Guwahati, 781039, India

CERTIFICATE

This is to certify that Umesh Kumar Bagha (166122104), a regular full-time PhD research scholar registered to the Department of Chemistry, Indian Institute of Technology Guwahati, has been working under my supervision since Jan 2017. I am forwarding his thesis entitled "**Investigation of Bioinspired Oxidation Mechanism by Non-Heme High-Valent Metal Intermediates**" for being submitted for the PhD (Science) degree of this institute. I certify that he has fulfilled all the requirements according to the rules of this institute regarding the investigations embodied in his thesis and this work has not been submitted elsewhere for a degree.

Prof. Chivukula V. Sastri

Thesis Supervisor

Department of Chemistry

Indian Institute of Technology Guwahati

ACKNOWLEDGEMENTS

The research work that I carried out during my Ph.D. has been categorically put into order in the form of this thesis. I would like to express my gratitude and appreciation to all those who directly or indirectly helped me during my journey as a Ph.D. student at the Indian Institute of Technology Guwahati. First and foremost, I would like to express my sincere gratitude to my Ph.D. supervisor, Prof. Chivukula V. Sastri, for his excellent guidance, patience, relevant suggestions, and for providing me with a unique atmosphere for my research work. During my tough times, he was highly motivating, patient and inspirational and always tried to guide me with a unique approach to solving any kind of problem.

I would also like to thank my Doctoral Committee Chairman and Members, Prof. Gopal Das, Prof. Mohd. Qureshi, and Prof. Ashish Kumar Gupta respectively for giving their valuable time to evaluate my progress and providing me with useful suggestions for the betterment of my research work. I am thankful to the former and existing HODs of the department of Chemistry and other faculty members for their help in carrying out this research. I would like to thank all the staff of the department of Chemistry without whose support it would not have been possible to carry out the research work. I am also thankful to the Department of Chemistry and Central Instruments Facility (CIF), IIT Guwahati for providing sophisticated instruments and infrastructure; the Param Ishan server for providing Computational facilities. I would also like to thank Mr. K. K. Singh for his help in understanding the LC-MS instrument. I feel highly obliged to IIT Guwahati and MHRD (Govt. of India) for financial assistantships during the whole tenure and for providing useful resources. I am also grateful to our collaborators, Dr. Sam P. de Visser (University of Manchester, UK), Prof. Dr. Peter Comba (University of Heidelberg, Germany) and

Prof. Devesh Kumar (Siddharth University, India) for their valuable contributions to my research work.

I would like to thank my lab seniors Dr. Prasenjit Barman, Dr, Gourab Mukherjee and Dr. Sayanta Sekhar Nag for their constant support and guidance. I would be grateful to them for sharing their experiences and discussing with me innovative ideas to solve the problems. I am thankful to Jagnyesh Kumar Satpathy, Limashree Sahoo, Dr. Rolly Yadav and Payal Panwar for their valuable help and support whenever I needed it. They made the lab a beautiful working environment to thrive on productive ideas. Apart from research work, it was full of fun to spend a tea break time and also to hang out with them.

I feel blessed to be surrounded by friends who played a vital role during my stay in Guwahati. After busy research work, I have shared great memories of fun towards the weekend with my wonderful friends, viz Manoj Kumar Mohanta, Bipin Kumar Behera, Paresh Kumar Behera, Ashish Kumar Sahoo, Manmath Mishra, Sibasankar Pradhan. I feel so lucky to have elder brothers viz Dr. Manoj Kumar Pradhan, Dr. Subhasish Behera, Dr. Subas Ch. Sahoo, Dr. Biswajit Nayak and Dr. Tushar Kanta Sahu and sisters Smt. Tapaswini Mohanty and Dr. Minati Das who welcomed me to IITG and were supportive. I would like to thank Alpana Sahu and Peeyush Pandey for their support. It was a great time to have fun with them. Other friends from the department, Sulendar Kumar Mohata and Sandip Mondal, are also highly regarded and were always there for any help I needed. The Badminton court at IITG was the place where I could forget all the frustrations of research. I would like to thank my badminton partners Dr. Biswajit Nayak, Manoj Kumar Mohanta and Sourav Bhowmick for creating a sporting environment and for a wonderful memory at IITG. Apart from this, I am thankful to my brothers, Gopinath Mallick, Gopabandhu Panigrahi and Rashmi Ranjan Pattanaik for encouraging me and always backing me with all kinds of support. I would like to especially thank Santosh Kumar Sahu, my school friend who was always there for any kind of help and also for

providing me with moral support. I would also like to thank my friends viz Bhajaman Pradhan, Subal Kumar Behera, Bulu Muduli, Amir Digal, Sumit Kumar Adhikary, Laxmikanta Bhukta, Dr. Anand Kumar Sahu and Dr. Sadananda Muduli for their valuable help whenever I needed it. I am thankful to my beloved brothers Rashmiranjan Sahu, Ameer Meher and Bikash Kumar Mahapatra and sister Smt. Sarita Behera for their help and also for having great memories with them.

I would like to thank all of my teachers for believing in me and motivating me to achieve my goal. Special mention goes to my Chemistry teachers, Prasanna Kumar Basantia and Dr. Santosh Kumar Behera for inspiring and implanting in me a love for this subject. I am grateful and obliged to my all teachers viz Santosh Kumar Padhi, Pradeep Prusty, Sagarika Mahapatra, Ganesh Mishra, Santosh Kumar Mahapatra, Prafulla Kumar Sahoo, Late Laxmidhar Pattanaik, Santosh Kumar Khuntia, Pradipta Kumar Pattanaik for taking a vital role in making me the person I am today.

Last but not the least, my family and loved ones. I feel proud to have the love, support and sacrifices of my parents, Shri Surath Bagha and Smt. Laxmi Bagha, the support from my elder sisters Ms. Rita Bagha and Smt. Kabita Bagha and my younger brother Mr. Akshaya Kumar Bagha. They have always been by my side during my ups and downs. Special thanks to my brother and sisters for taking care of my home during my stay away from home. I can never imagine reaching this stage without their endless support and sacrifices. Another special person who deserves a mention and had been a constant supporter in my Ph.D. life is Ms. Rasmita Bhoi. She believed in me and kept faith in my potential to achieve my goal. It would have been difficult to reach this far without her moral support and encouragement. I feel fortunate to have so many well-wishers around that it is difficult for me to name them all. I cordially thank them all for their help.

ABSTRACT

High-valent non-heme metal intermediates have been invoked as key reactive species in various oxidative transformations. These intermediates perform crucial redox reactions which proceed *via* atom transfer or electron transfer or radical reaction pathways. The reactivity patterns of these intermediates have been studied extensively towards various organic substrates which are highly influenced by several factors such as primary and secondary coordination spheres and topology, ligand architecture, spin states of metals, solvents, pH and temperature. However, it remains a major challenge to design efficient synthetic biomimetic catalysts with high selectivity and reactivity due to the unattainability of physiological conditions. The ligand modification around the metal centre is one of the most important factors that provides stability to these metastable intermediates and hence hugely affects their reactivity. The factors that influence the reactivity profiles of these intermediates are often associated with their mechanistic pathways. Hence, to have a better understanding, it is important to investigate the mechanistic insight into various reactions performed by non-heme systems.

In the present work, the reactivity studies towards aldehyde deformylation, S-oxidation, C-H activation and oxidative dehalogenation reactions with manganese(III)-peroxo, iron(IV)-oxo and iron(IV)-imido intermediates supported by penta-dentate ligand systems have been evaluated. These reactivity studies provide remarkable insights into the mechanistic pathways of these intermediates.

The reactivities of two isomeric side-on manganese(III)-peroxo complexes with bispidine ligands have been investigated towards aldehyde deformylation reaction and was found that the reaction proceeds *via* an electrophilic hydrogen atom abstraction instead of the commonly proposed nucleophilic pathway. Comparative reactivity studies

have been performed between iron(IV)-oxo and iron(IV)-imido complexes toward S-oxidation and C-H activation reactions. In both reactions, iron(IV)-imido complexes were found to be sluggish as compared to their oxo analogue. Finally, the reactivity of iron(IV)-oxo complexes has been evaluated with a series of mono-, di- and tri-halophenols and has established a new mechanism for their oxidative dehalogenation.

LIST OF TABLES

LIST OF SCHEMES & FIGURES

Fig. 5.30. Free energy landscape (ΔG values at 298 K with zero-point energy, and thermal, solvent and entropic corrections included in kcal mol^{-1}) for the reaction of 2,4,6-TFP activation by 4b. On the sides are shown the optimized geometries of the H-atom abstraction and OH rebound barriers with bond lengths in Armstrongs and the imaginary frequency in cm^{-1}.

ABBREVIATIONS

ESI-MS	Electrospray Ionization Mass Spectrometry
UV/Vis	Ultraviolet-Visible
NMR	Nuclear Magnetic Resonance
GC	Gas Chromatography
LCMS	Liquid Chromatography Mass Spectrometry
UPLC	Ultra Performance Liquid Chromatography
EPR	Electron Paramagnetic Resonance
ROS	Reactive Oxygen Species
HRP	Horseradish Peroxidase
CYP	Cytochrome P450
NADPH	Dihydronicotinamide Adenine Dinucleotide Phosphate
SOR	Superoxide Reductase
SOD	Superoxide Dismutase
Cat	Catalase
RNR	Ribonucleotide Reductase
pdb	Protein Data Bank
His	Histidine
α-KG	α-ketoglutarate
TauD	taurine/α-KG dioxygenase
H_2O_2	Hydrogen Peroxide
KO_2	Potassium Superoxide
TEA	Triethylamine

TMC	Tetramethylcyclam
H_2bupa	bis[(N'-t-butylurealy)-N-ethyl](6-pivalamido-. 2-pyridylmethyl)-aminato
PhIO	Iodosylbenzene
TPA	Tris(2-pyridylmethyl)amine
*t*BuOOH	*tert*-butyl hydroperoxide
HAA	Hydrogen Atom Abstraction
OAT	Oxygen Atom Transfer
PPh_3	Triphenylphosphine
TBC	Tetrabenzylcyclam
TMG_3tren	1,1,1-tris{2-[N2-(1,1,3,3-tetramethylguanidino)]ethyl}amine
TQA	tris(2-quinolinylmethyl)amine
TAML	Tetraamidomacrocyclic ligand
BnTPEN	N^1-benzyl-N^1,N^2,N^2-tris(pyridine-2-ylmethyl)ethane-1,2-diamine
N4Py	N,N-bis(2-pyridylmethyl)-N-bis(2-pyridyl) methylamine
XAS	X-ray absorption spectroscopy
CH_3CN	Acetonitrile
DCM	Dichloromethane
CaH_2	Calcium Hydride
THF	Tetrahydrofuran
$PhI(OAc)_2$	(Diacetoxyiodo)benzene
CAN	Cerium (IV) ammonium nitrate
PhINTs	N-tosyliminophenyliodinane
THA	Thioanisole
2,4,6-TFP	2,4,6-trifluorophenol

2,4,6-TCP	2,4,6-trichlorophenol
2,4,6-TBP	2,4,6-tribromophenol
2,6-DFP	2,6-difluorophenol
2,6-DCP	2,6-dichlorophenol
2,6-DBP	2,6-dibromophenol
4-FP	4-fluorophenol
4-CP	4-chlorophenol
4-BP	4-bromophenol
DHA	9,10-Dihydroanthracene
2-PPA	2-phenylpropionaldehyde
CCA	cyclohexanecarboxaldehye
α-[D_1]-CCA	α-[D_1]-cyclohexanecarboxaldehye
1,2-[D2]-CCA	1,2-[D_2]-cyclohexanecarboxaldehyde
RT	Room temperature
m.p.	Melting point
CHD	1,4-Cyclohexadiene
DMAP	4-Dimethylaminopyridine
PTFE	Polytetrafluoroethylene
OTf	triflate
ppm	Parts per million
Q-TOF	Quadrupole Time of Flight
KIE	Kinetic Isotope Effect
k_{obs}	pseudo first-order rate constant
k_2	second-order rate constant

BDE	bond dissociation energy
EA	Electron affinity
LMCT	Ligand to Metal charge transfer
FTIR	Fourier transform infrared

COMPOUND ABBREVIATIONS

Chapter	Index	Description
Chapter III	L1	Bispidine ligand
	1a	$[Mn^{II}(L1)]^{2+}$
	1b	$[Mn^{III}(O_2)(L1)]^{+}$
	L2	Bispidine ligand
	2a	$[Mn^{II}(L2)]^{2+}$
	2b	$[Mn^{III}(O_2)(L2)]^{+}$
Chapter IV	L3	Bntpen ligand
	3a	$[Fe^{II}(L3)]^{2+}$
	3b	$[Fe^{IV}(O)(L3)]^{2+}$
	3c	$[Fe^{IV}(NTs)(L3)]^{2+}$
	L4	N4Py ligand
	4a	$[Fe^{II}(L4)]^{2+}$
	4b	$[Fe^{IV}(O)(L4)]^{2+}$
	4c	$[Fe^{IV}(NTs)(L4)]^{2+}$
Chapter V	L5	2PyN2Q ligand
	5a	$[Fe^{II}(L5)]^{2+}$
	5b	$[Fe^{IV}(O)(L5)]^{2+}$
	L4	N4Py ligand
	4a	$[Fe^{II}(L4)]^{2+}$
	4b	$[Fe^{IV}(O)(L4)]^{2+}$

Synopsis

The diversity of life on earth today is the result of continuous evolution and adaptation which developed some major modifications in molecular machines. Nature being the best architecture has designed specific tools and techniques for each biological function associated with life processes. Metalloenzymes play one of such vital roles and are responsible for a diverse range of specified catalytic transformations. Inspired by Nature, researchers have devoted themselves to synthesize non-heme model systems that react with several oxidants to generate high-valent reactive species and to understand their reactivity patterns with various substrates. The primary challenges associated with these processes involve the stabilization and characterization of the transient species and controlling the fast reaction kinetics. This thesis entitled "**Investigation of Bioinspired Oxidation Mechanism by Non-Heme High-Valent Metal Intermediates**" focuses on the synthesis of model systems, that could contain relevant metal ions like iron and manganese and the generation of reactive intermediates by the reaction with suitable oxidants, followed by their reaction kinetics with various organic substrates. Thus, different types of model reactions were carried out and mechanistic investigations have been established.

Mononuclear non-heme metalloenzymes containing iron and manganese play a pivotal role in a diverse range of oxidative transformations in living beings. Transition metals in the active sites of such enzymes have evolved for the activation of molecular oxygen (O_2). Depending upon the metal ion and coordination motif, a variety of high-valent reactive intermediates have generated that act as potential catalysts for such transformations. These intermediates are usually metastable in nature and various factors like ligand architecture, coordination geometry, the spin state of metal ion, solvent, pH of the medium, temperature, etc. are known to influence their stability and reactivity either

actively or passively. These non-heme Fe or Mn-containing metal intermediates are shown in Fig. S1. Among these, some of the intermediates (*viz*. manganese-peroxo, iron-oxo and iron-imido) have been studied in terms of their stability and reactivity. This thesis has been classified into five chapters. A short chapter-wise preview for each of those is given below.

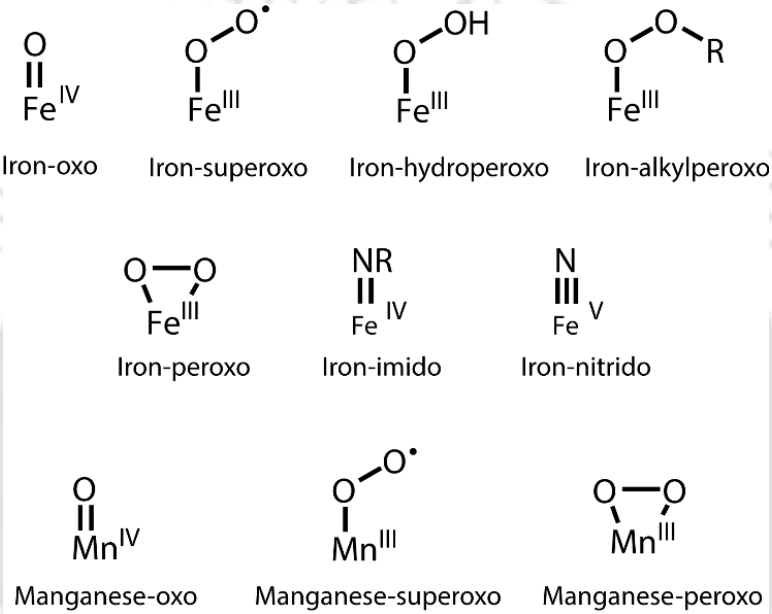

Fig. S1. Plausible high-valent iron and/or manganese containing metal intermediates.

Chapter I. A General Overview of Dioxygen Activation by Heme and Non-Heme Metalloenzymes and their Synthetic Molecular Models.

This chapter deals with the general literature survey on dioxygen activation by heme and non-heme metalloenzymes of Fe and Mn and their model systems. Also, recent advancements in the rich chemistry of manganese-peroxo, iron-imido and iron-oxo species have been discussed.

Chapter II. Synthesis and Characterization, Materials Employed and Methods Adapted.

This chapter aims to thoroughly discuss the synthetic aspects of the ligands and metal complexes, their structural characterization and other factors. The usage of solvents and thoughtful employment and synthesis of specific substrates to ascertain the reactivity profiles of various intermediates have been discussed. The synthesis of all the ligands used in this thesis have been discussed in detail along with their spectroscopic characterization. Discussions on the synthesis of the metal complexes and usage of electrospray ionization mass spectrometry (ESI-MS), Ultra Violet-Visible (UV/Vis) spectroscopy and ^{1}H-Nuclear Magnetic Resonance (NMR) spectroscopy have been done. Also, detailed procedures of the physical methods adapted and of the reaction kinetics have been depicted herewith.

Chapter III. Hydrogen by Deuterium Substitution in an Aldehyde Tunes the Regioselectivity by a Non-Heme Manganese(III)-Peroxo Complex.

Manganese metal ions are present in the active site structure of numerous enzymes that utilize molecular oxygen, and are involved in harmful superoxide detoxification, decomposition of hydrogen peroxide, and water splitting. Most of these enzymes include either a manganese–oxo, manganese-superoxo or manganese-peroxo structure as an active intermediate in their catalytic cycle. Several biomimetic manganese(III)-peroxo complexes have been synthesized and characterized with spectroscopic methods. Furthermore, for some of those, the reactivity against substrates has been tested. In general, side-on manganese(III)-peroxo reacts *via* nucleophilic pathways, for instance, through deformylation of aldehydes. Side-on manganese(III)-peroxo complexes show a versatile reactivity pattern with a variety of substrates that are poorly understood, which encouraged us to look deeper into their reactivity with substrates.

In this work, we describe the synthesis and characterization of two side-on manganese(III)-peroxo complexes (Fig. S2) with pentadentate N5 bispidine ligand backbones, namely $[Mn^{III}(O_2)(L1)]^+$ (**1b**) and $[Mn^{III}(O_2)(L2)]^+$ (**2b**) with L1= dimethyl-2,4-di(2-pyridyl)3-(pyridin-2-ylmethyl)-7-benzyl-3,7-diazabicyclo[3.3.1]nonan-9-one-1,5-dicarboxylate and L2=dimethyl 2,4-di(2-pyridyl)-3-benzyl-7-(pyridin-2-ylmethyl)-3,7-diazabicyclo[3.3.1]nonan-9-one-1,5-dicarboxylate.

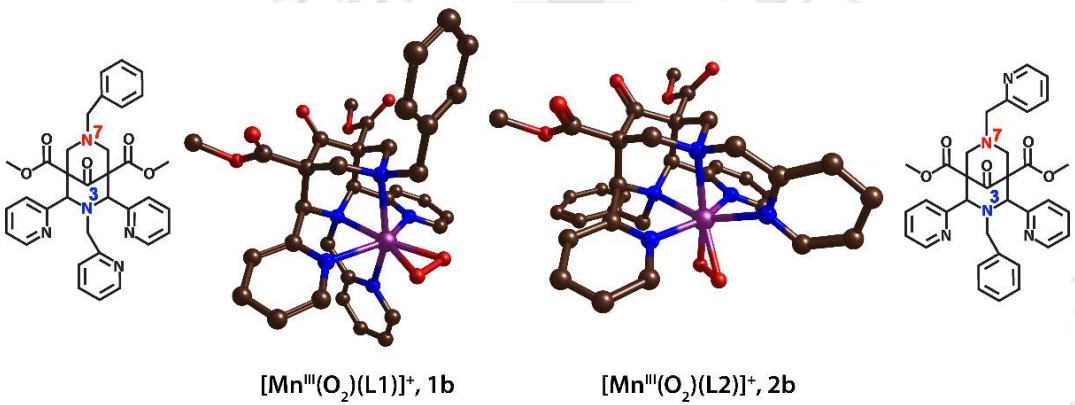

Fig. S2. Ligand frameworks and Manganese(III)-peroxo complexes investigated in this work.

Treatment of a colour-less solution of the manganese(II) precursor with 10 equivalents of H_2O_2 and triethylamine (TEA; 2.5 equivalents) in CH_3CN at 15 °C results in the formation of a blue and brown intermediate for **1b** and **2b**, respectively. The identity of complexes **1b** and **2b** was confirmed by ultraviolet-visible absorption spectroscopy at wavelengths 605 nm and 450 nm, respectively (Fig. S3) and also characterized by electrospray ionization-mass spectrometry.

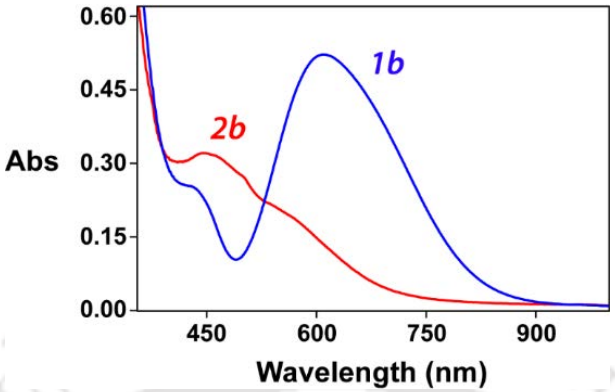

Fig. S3. UV/Vis spectra of the formation of $[Mn^{III}(O_2)(L1)]^+$ (**1b**) and $[Mn^{III}(O_2)(L2)]^+$ (**2b**) (2 mM) upon addition of $[Mn(L)]^{2+}$ in the presence of TEA (5 mM) and H_2O_2 (20 mM) in CH_3CN at 15 °C.

Metal-peroxo oxidants have been reported that react *via* hydrogen-atom abstraction reactions, therefore, we decided to extend our work to other substrates to evaluate the factors responsible for such unique reaction pathways. As such we investigated the reactivity of complexes **1b** and **2b** with cyclohexane carboxaldehyde (CCA) as it is a classical substrate used in several reactivity studies by manganese(III)-peroxo complexes and generally gives cyclohexanone as product. Upon the addition of 40 equivalents of CCA to **1b** in CH_3CN at 15 °C, the intermediate decayed immediately and led to cyclohexanone as a product (Fig. S4).

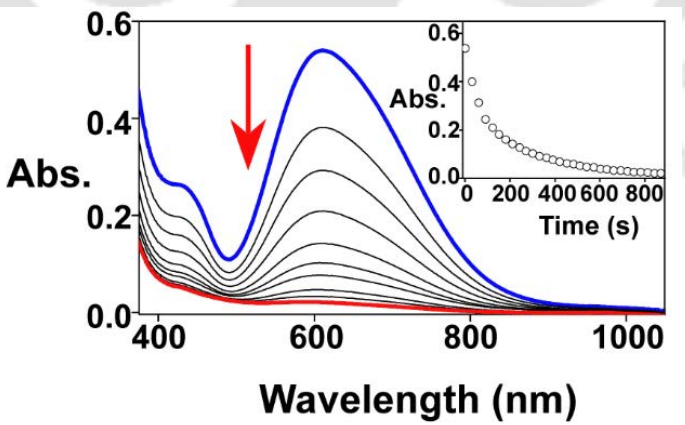

Fig. S4. UV-Vis spectral changes of **1b** (2 mM) upon addition of CCA (120 mM) in the presence of TEA (5 mM) and H_2O_2 (20 mM) in CH_3CN at 15 °C. Inset shows the decay profile at 605 nm.

The pseudo-first-order rate constant of the decay of **1b** increased linearly with increasing CCA concentration, thus enabling us to determine the second-order rate constant of the reaction: k_2= 0.064 M^{-1} s^{-1} (Fig. S5). In contrast, the second-order rate constant for the oxidation of CCA by **2b** gave a rate constant k_2 of 0.291 M^{-1} s^{-1} (Fig. S5).

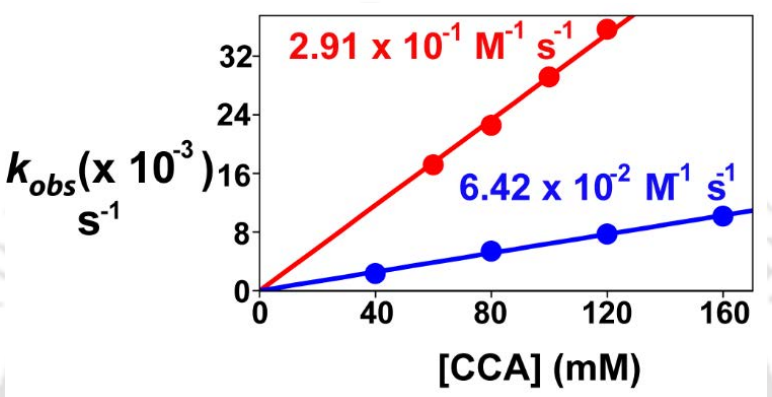

Fig. S5. Plot of k_{obs} against the concentration of CCA: second-order rate constant for the reaction of 2 mM **1b** (blue •) and **2b** (red •) with various substrate concentrations in CH_3CN at 15 °C.

The second-order rate constant for the reactivity of α-[D_1]-CCA with **1b** was 50 times faster when compared with parent CCA and implicated an effective kinetic isotope effect (KIE) of 0.02. The product analysis by NMR spectroscopy revealed that the product for the reaction of α-[D_1]-CCA with **1b** was cyclohexane carboxylic acid (Scheme S1.), rather than the expected cyclohexanone.

Scheme S1. Products obtained for the reaction of 1b and 2b with substrates.

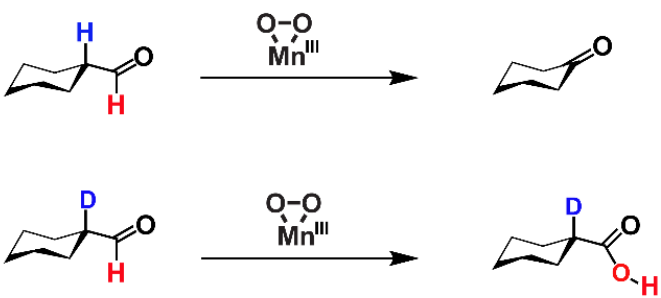

Thus, we have synthesized a couple of Mn^{III}-peroxo complexes bearing pentadentate bispidine backbone and were characterized. Herein, we demonstrate for the first time that the Mn^{III}-peroxo complex can perform electrophilic oxidation of substrates through the hydrogen-atom abstraction from the C-H bond of an aldehyde to give the corresponding acid as the product.

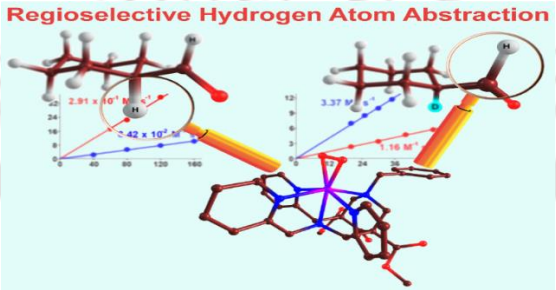

Chapter IV. Sluggish Reactivity by a Non-Heme Iron(IV)-tosylimido Complex as Compared to its Oxo Analogue.

High-valent metal-oxo and metal-nitrido species are common intermediates in enzymes and are found in the catalytic cycles of several oxidases as well as in nitrogenases. Thus, in many of these oxygenases, the enzymes utilize molecular oxygen to create a high-valent non-heme iron(IV)-oxo or iron(IV)-oxo heme cation radical species as active oxidant. On the other hand, few enzymes use nitrogen to generate a high-valent iron(IV)-nitrido or -imido active species. Nevertheless, the latter has been proposed as an intermediate in nitrogenase.

There are still many gaps in the understanding of iron-imido, iron-nitrido and iron-oxo oxidants. To gain insight into the properties and reactivities of these biomimetic species, we synthesized $[Fe^{IV}(NTs)(Bntpen)]^{2+}$, $[Fe^{IV}(O)(Bntpen)]^{2+}$, $[Fe^{IV}(NTs)(N4Py)]^{2+}$ and $[Fe^{IV}(O)(N4Py)]^{2+}$. The studies show differences in spectroscopic and electronic properties based on the pentadentate ligand, but also the differences between iron(IV)-oxo and iron(IV)-imido are explored. In order to find out

how the ligand framework affects the reactivity patterns of iron(IV)-tosylimido oxidants, we decided to do a comparative study between the $[Fe^{IV}(O)(Bntpen)]^{2+}$ (**3b**) and $[Fe^{IV}(NTs)(Bntpen)]^{2+}$ (**3c**) $[Fe^{IV}(O)(N4Py)]^{2+}$ (**4b**), $[Fe^{IV}(NTs)(N4Py)]^{2+}$ (**4c**). The work shows that the ligand framework affects the substrate approach as well as the redox properties of the oxidant.

Complex **3c** was synthesized using the nitrene transfer reagent PhINTs under an argon atmosphere. Similar to complex **4c**, the formation of **3c** was identified by an intense LMCT band at 460 nm (ε = 4100 M^{-1} cm^{-1}) and a weaker band at 650 nm (ε = 330 M^{-1} cm^{-1}) due to ligand field transitions characteristic for S = 1 iron(IV) complexes, see Fig. S6a. Further characterization of the $[Fe^{IV}(NTs)(Bntpen)]^{2+}$, (**3c**) was done by electrospray ionization (ESI)-mass spectrometry (MS) (Fig. S6b), proton NMR spectroscopy and Fourier transform infrared (FTIR) spectroscopy.

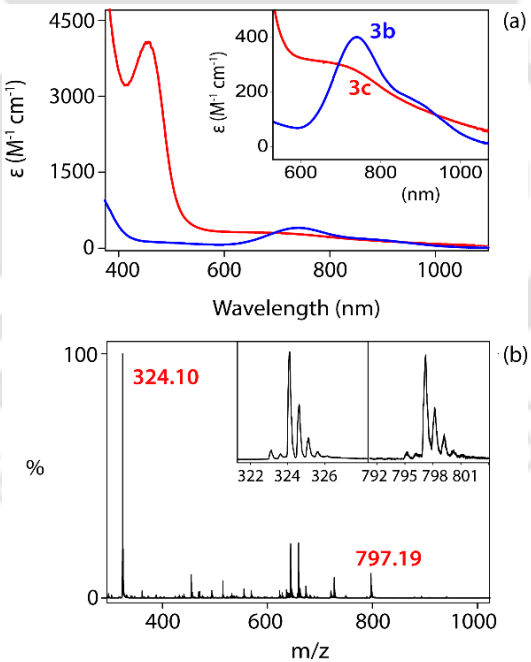

Fig. S6. (a) UV/Vis spectra of 1 mM solutions of $[Fe^{IV}(O)(Bntpen)]^{2+}$ (**3b**, blue line) and $[Fe^{IV}(NTs)(Bntpen)]^{2+}$ (**3c**, red line) in CH_3CN at 298 K. (b) ESI-MS spectra of **3c** in CH_3CN. Insets show the isotopic distribution patterns for the peaks at *m/z* 324.10 and 797.19.

To understand the oxidative properties of complex **3c**, we decided to investigate its heteroatom transfer reactivity to thioanisole as the model substrate. Unlike N4Py, the NTs complex **3c** reacts sluggishly with thioanisole with considerably lower rate constants than those seen for the corresponding oxo complex **3b**.[9] The second-order rate constant for the reaction of **3c** with thioanisole was 5.4 x 10^{-2} M^{-1} s^{-1} at 298 K, whereas for the same reaction with **4c**, a value of 26 x 10^{-2} M^{-1} s^{-1} was reported at 273 K.[9] Thus the rate of the reaction for **3c** is expected to be even slower at 273 K. The slower reaction rate of **3c** with thioanisole is, therefore, speculated to originate from a group transfer reaction instead of an electron transfer mechanism. In order to establish the mechanism with conviction, we repeated the reaction using various *para*-substituted thioanisole substrates at 298 K to obtain second-order rate constants (Fig. S7).

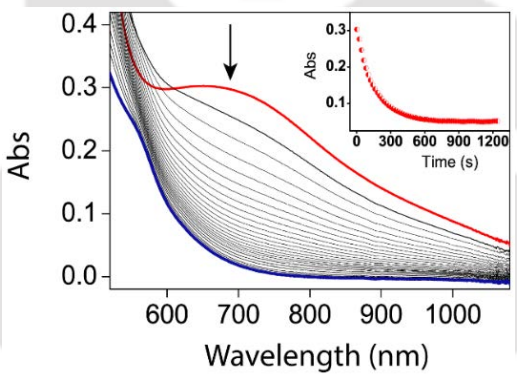

Fig. S7. Decay profile for the 750 nm band due to addition of 150 equiv. of thioanisole to **3c** in CH_3CN at 298 K.

Then these second-order rate constants were plotted against the *para*-substituent constant (σ_p^+) for each substrate to obtain a Hammett plot (Fig S8). Thus, a ρ value of –2.55 was obtained with a better-fitting correlation to the experimental data. Complex **4c**, in comparison, produced a negative slope of –1.92 when the rates were plotted against σ_p^+. Nevertheless, these values from the Hammett plots for **3c** are substantial evidence of an operating electron transfer mechanism in spite of slower reaction rates than the fellow tosylimido complex **4c.**

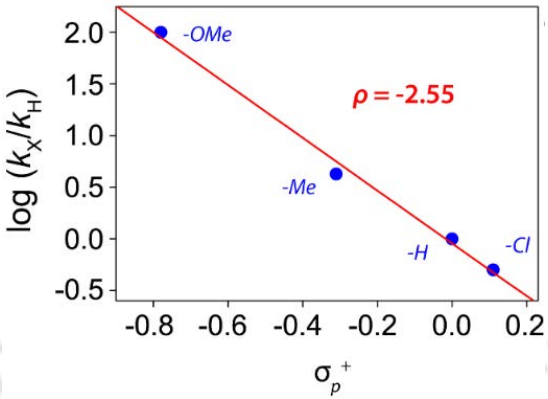

Fig. S8. Hammett plot obtained by plotting the log (k_X/k_H) values against the σ_p^+ Hammett values of *para*-X-thioanisole (X = OMe, Me, H and Cl) substrates in their reaction with **3c** in CH_3CN at 298 K.

We also tested the alcohol oxidation reactivity of **3c** using benzyl alcohol as the model substrate and compared the results with the other oxidants. The second-order rate constants for the complexes **3b**, **3c**, **4b** and **4c** were found to be 115.61 x 10^{-2} $M^{-1}s^{-1}$, 0.39 x 10^{-2} $M^{-1}s^{-1}$, 8.20 x 10^{-2} $M^{-1}s^{-1}$ and 1.48 x 10^{-2} $M^{-1}s^{-1}$, respectively. Thus, it clearly indicates the iron(IV)-tosylimido complex of Bntpen reacts slower with substrates than the other complexes.

In this work, we present the synthesis and characterization of an iron(IV)-tosylimido complex and compared its reactivities with iron(IV)-oxo complexes. Experimental studies revealed that the iron(IV)-tosylimido forms strong N–H bonds after hydrogen atom abstraction but has a larger redox potential and therefore reacts slower with substrates.

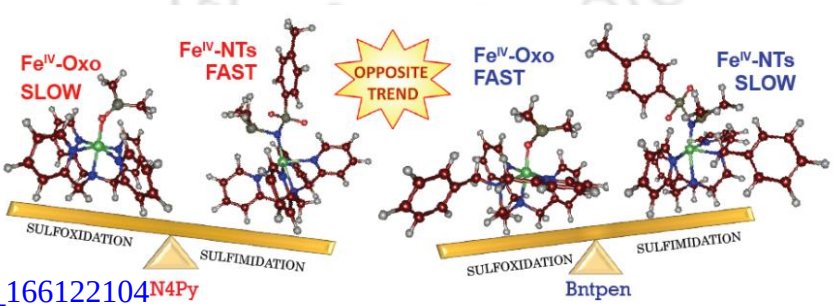

Chapter V. Mechanistic Insights into Dehalogenation Reaction by High-Valent Non-Heme Iron(IV)-oxo Intermediates.

High-valent iron(IV)-oxo complexes have been invoked as the key reactive intermediate in the catalytic cycle of non-heme iron enzymes and their model systems. The non-heme iron(IV)-oxo species is reportedly the active oxidant involved in enzymatic and biomimetic reactions. These iron(IV)-oxo intermediates have been shown to catalyze a wide variety of biological oxidative transformations. These are versatile intermediates towards hydrogen atom transfer (HAT) and oxygen atom transfer (OAT) reactions. In addition, mononuclear high-valent iron(IV)-oxo complexes have been considered reactive intermediates for the degradation of toxic organic pollutants. Among these organic pollutants, halophenols are a major class of toxic organic pollutants that enter into the human body through the food chain causing serious health concerns as they are potentially carcinogenic. Therefore, it is necessary to implement different techniques that can help in the detoxification of these pollutants and convert them to non-hazardous chemicals.

A variety of techniques have been developed for the degradation of halophenols that include physical, chemical and biological processes. All of those are costly and energy-intensive. Moreover, many of these processes produce by-products or more toxic intermediates. On the other hand, bacterial degradation is one of the most efficient methods to detoxify halophenols. The dehalogenation mechanism of dehaloperoxidase (DHP) has been investigated by several groups but as yet remains unresolved. Enzymes such as DHP, *Caldariomyces fumago* chloroperoxidase (CCPO), horseradish peroxidase (HRP) and lignin peroxidases degrade halophenols. The proposed mechanism for the conversion of halophenols to quinones by these enzymes involves two successive one-electron transfer steps mediated by iron(IV)-oxo intermediates and it is seen that the oxygen atom in the quinone product is derived from a solvent water molecule.

In this work, we have employed iron(IV)-oxo species (Fig. S9) supported by pentadentate ligands 2PyN2Q (1,1-di(pyridin-2yl)-N, N-bis(quinolin-2-ylmethyl)methanamine) and N4Py (N, N-bis(2-pyridylmethyl)-N-bis(2-pyridyl)methylamine) in an acetonitrile solvent, which degrade halophenols by an oxidative pathway. The proposed mechanism of oxidative dehalogenation of halophenols by these iron(IV)-oxo intermediates proceeds *via* an initial hydrogen atom abstraction from the phenolic O-H resulting in the formation of a new intermediate which leads to the formation of corresponding quinone products.

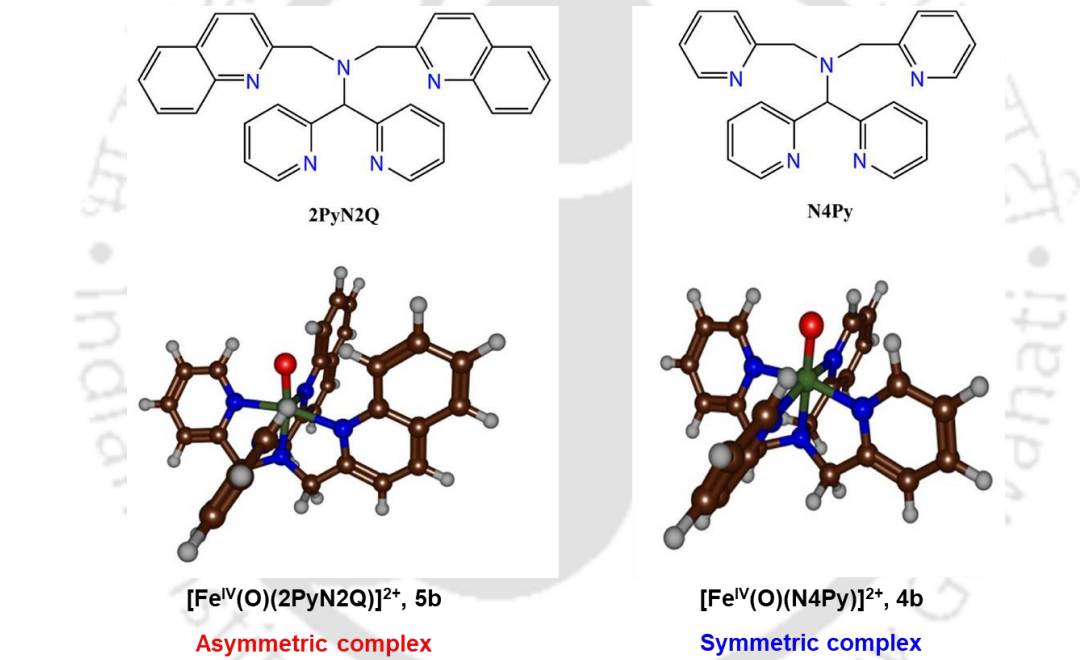

Fig. S9. Ligand frameworks and iron(IV)-oxo complexes investigated in this work.

We started our work by synthesizing [Fe^{II}(2PyN2Q)(OTf)$_2$], **5a** complex and generated [Fe^{IV}(O)(2PyN2Q)]$^{2+}$, **5b** by the addition of 1.5 equivalents of PhI(OAc)$_2$ to **5a** in CH_3CN under ambient conditions, a pale green iron(IV)-oxo complex with distinctive absorption features in UV-Vis absorption (λ_{max} = 770 nm, ε = 340 L M^{-1} cm^{-1}, $t_{1/2}$ = 50 min at RT) and was also characterized by ESI-MS.

The electrophilic nature of $[Fe^{IV}(O)(2PyN2Q)]^{2+}$, **5b** was investigated by reacting it with a series of tri-, di- and mono-halophenols with various steric demands and different electronic impulses. At -40 ºC, the addition of tri-halophenols to **5b** led to the gradual pseudo-first-order decay of the iron(IV)-oxo characteristic band at 770 nm in the UV-vis spectrum with concomitant formation of the corresponding iron(II) precursor with an isosbestic point at 620 nm as shown in Fig. S10a. The pseudo-first-order rate constants increased linearly with an increase in the concentration of the substrates enabling us to procure the second-order rate constants (k_2). The second-order constants (k_2) for **5b** with different tri-halophenols were evaluated, as shown in Fig. S10b and the reactivity order was found to be 2,4,6-TBP > 2,4,6-TCP > 2,4,6-TFP.

The reactivity of di- and mono-halophenols with **5b** was studied and second-order rate constants were evaluated (Table S1.). The product analysis of the reaction mixture confirms the formation of quinones with *p*-quinone as the major product. When the reaction of *p*-halophenols with **5b** was carried out at 0 ºC, a new intermediate was observed, however, the formation was slow. Thus, the reaction at room temperature resulted in a new absorption band at 614 nm, typical of the characteristic LMCT band usually seen for oxygen adducts of iron such as iron(III)-OOH and/or iron(III)-OOR.

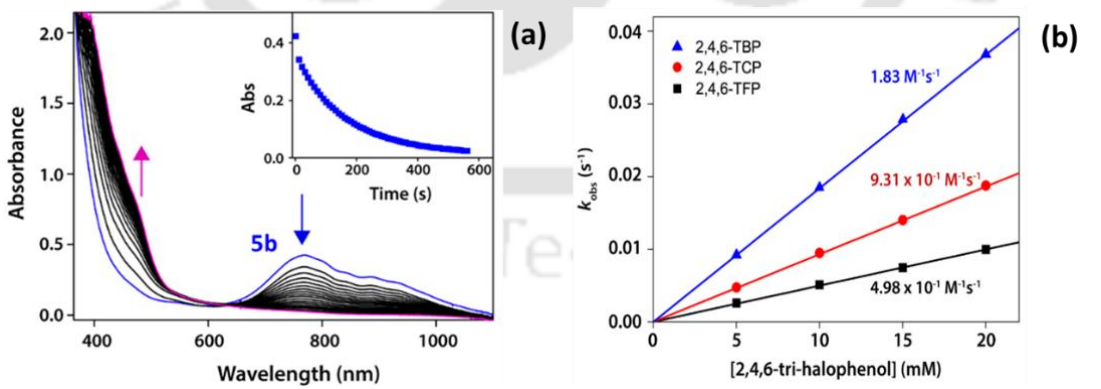

Fig. S10. (a) UV-vis spectral changes of **5b** upon addition of 10 equiv. 2,4,6-TCP in CH_3CN at -40 ºC. Inset shows the decay profile of the 770 nm band. (b) Second order rate constants determined for **5b** (1mM) with (a) 2,4,6-TFP (■), 2,4,6-TCP (●) and 2,4,6-TBP (▲) at -40 ºC.

Table S1. Second-order rate constant (k_2) and product distribution for 5b (1 mM in CH_3CN solution) with mono-, di- and tri-halophenols.

Substrate	10^{-1} x k_2 (in $M^{-1}s^{-1}$)	Temperature	Product distribution % (*ortho* : *para*) quinone
2,4,6-TFP	4.98	-40° C	35 : 21
2,4,6-TCP	9.3	-40° C	30 : 15
2,4,6-TBP	18.3	-40° C	50 : 10
2,6-DFP	3.55	-40° C	30 : 0
2,6-DCP	8.54	-40° C	33 : 0
2,6-DBP	14.6	-40° C	21 : 0
4-FP	20.8	0° C	30 : 25
4-CP	19.8	0° C	40 : 31
4-BP	16	0° C	38 : 10

The formation of these intermediates was observed only in 2,4,6-TFP, 2,6-DFP and in all *p*-halophenols due to the steric hinderance between bulkier halogens and quinoline groups of **5b**. This motivated us to choose a symmetric metal complex to observe the new intermediate formation with all the halophenols. We have employed an $[Fe^{IV}(O)(N4Py)]^{2+}$, **4b** complex supported by a symmetric N4Py ligand which detoxifies all these halophenols into their non-hazardous forms. Upon addition of 10 equiv. of tri-halophenols to the complex **4b** at ambient conditions in CH_3CN solvent resulted in the immediate decay of the iron(iv)-oxo characteristics d-d- transition band at 695 nm and concomitant formation of the purple-coloured intermediates at a wavelength range of 558-595 nm depending on the phenolic substrates used (Fig. S11). These new intermediates are the substrate-bound adducts coordinated to the ferrous species as evidenced by the shift in wavelengths in UV-Vis absorption.

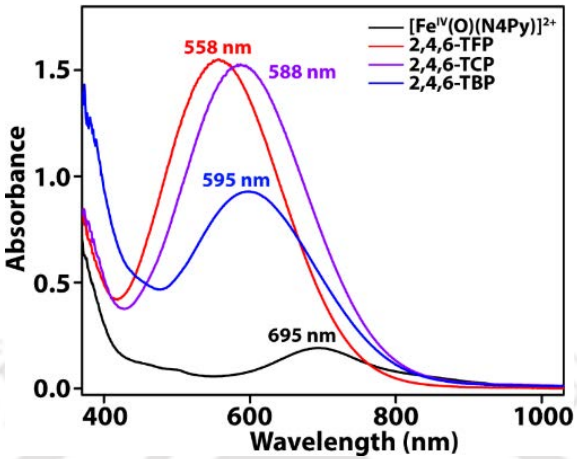

Fig. S11. UV/Vis spectra for the formation of substrate-bound adducts by the addition of 10 equiv. of 2,4,6-TFP (red line), 2,4,6-TCP (violet line) and 2,4,6-TBP (blue line) to $[Fe^{IV}(O)(N4Py)]^{2+}$ (**4b**) (black line) in CH_3CN at 25 °C.

In this work, we have employed iron(IV)-oxo complexes supported by both asymmetric 2PyN2Q and symmetric N4Py ligands which detoxify a series of halophenols into quinones. A combined experimental and theoretical studies revealed a unique reaction mechanism for the oxidative dehalogenation of these halophenols which proceeds *via* a Fe(II)-phenolate adduct formation.

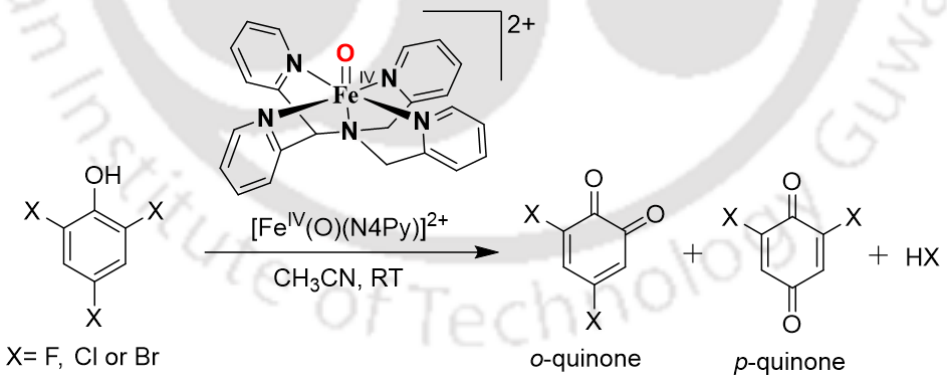

GRAPHICAL ABSTRACT

Chapter 3

Angew. Chem. Int. Ed. **2019**, *58*, 10639-10643

Chapter 5

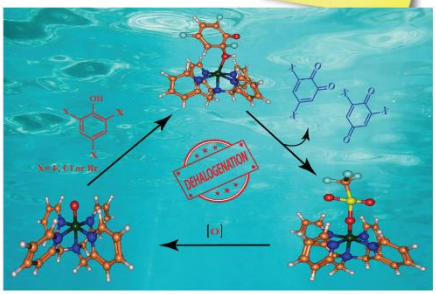

Faraday Discuss. **2022**, *234*, 58-69.

THESIS OVERVIEW

Chapter 4

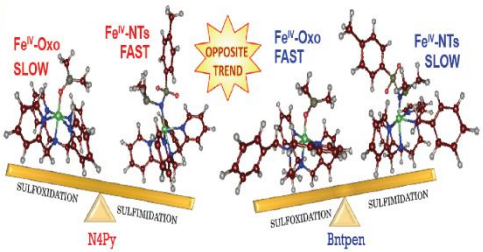

Dalton Trans. **2020**, *49*, 5921-5931.

CHAPTER – I

A General Overview of Dioxygen Activation by Heme and Non-Heme Metalloenzymes and their Synthetic Molecular Models

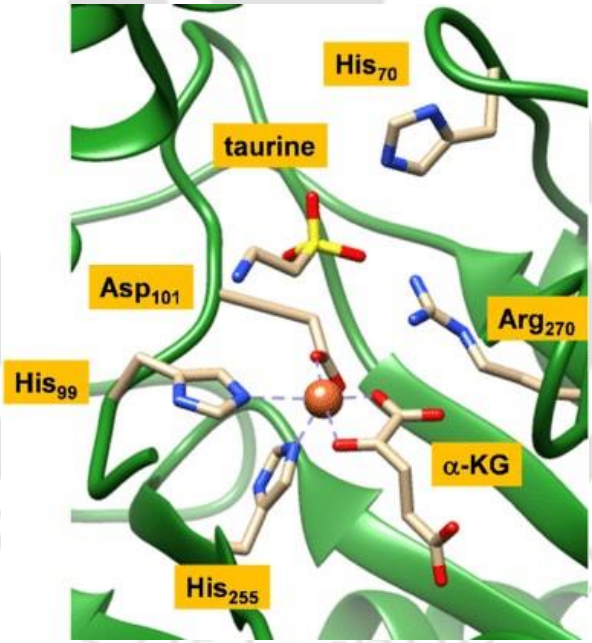

1.1. Introduction

The diversity of life on earth today is the result of continuous evolution and adaptation which developed some major modifications in molecular machines. Nature being the best architect has designed unique tools and techniques for all of the biological processes involved in life. One of those crucial roles is played by metalloenzymes, which carry out a variety of specific catalytic reactions. The majority of enzymes are metalloproteins that Nature has employed to its full advantage to minimize the issues brought on by various oxidation and reduction processes in mild and normal physiological conditions. These enzymes act as biocatalysts that use metal ions as cofactors to carry out numerous biochemical reactions. Metalloenzymes mainly use transition metals like Mn, Fe, Co, Ni, Cu and Zn due to their tendency to exhibit variable oxidation states and hence are involved in various redox processes. Enzymomimetics can be contemplated as a subclass of Biomimetics which deals with the synthesis of model systems and the generation of reactive intermediates that efficiently mimic the potential active sites of various metalloenzymes. This thesis mainly focuses on mechanistic insights into the reactivity patterns of synthetic enzymomimetic model systems toward the oxidation of various proficient organic substrates.

1.2. Dioxygen Activation

Nature has provided us with an atmosphere for living organisms to succeed with an abundant and renewable chemical oxidant; i.e. molecular oxygen. The evolution of humans and all other living things depend on the presence of molecular oxygen in the atmosphere.[1,2] Dioxygen acts as an efficient oxidant and exists as a radical species because of its unique electronic configuration having two unpaired electrons. Thus, it undergoes a thermodynamically feasible reaction that requires an additional four electrons to create water, which is used as a universal solvent by all living organisms.[1,2]

Metalloenzymes play an important role in activating this molecular oxygen to perform an array of oxidative transformations. In the metal-binding mode, the reduction of dioxygen leads to the formation of different species like superoxide (O_2^-), peroxide (O_2^{2-}), oxide (O^{2-}) or hydroxyl radical ($OH^{\bullet}$).[3] These species are more reactive than the corresponding non-radical species and are considered reactive oxygen species (ROS).[4] The production and removal of ROS species must be carefully controlled as these are toxic substances. An organism may suffer from oxidative damage such as Parkinson's disease, DNA damage, mutagenesis, etc. when the levels of ROS outweigh its defence mechanisms.[5,6] For instance, superoxides target certain substrates and are detrimental to an organism's health.[5-7] Nature precisely utilizes various metalloenzymes to control the toxicity of these ROS species and consequently, it is imperative to investigate ROS. The non-heme iron enzymes in particular can function as a potential defensive mechanism to degrade these ROS.[8]

Despite making up less than 1% of the total protein weight in metalloenzymes, metal ions play a critical role in the catalytic activity to promote a diverse range of selective biochemical and biological reactions like oxygen activation.[9] These metal ions are usually coordinated to heteroatoms such as N, O or S of various amino acids in the polypeptide linkages of the proteins. These donor groups are often provided with some side chains and can provide stability to numerous reactive species, which are essential in many metalloenzyme catalytic cycles. In actuality, the properties of the metal ions and their coordination units have a great influence on regulating the enzyme's activities. The shape and structure of the active site of the metalloenzymes are determined by the coordination of the metal centre with the donor groups and their spatial orientation in three dimensions, which in turn regulates the approachability and trajectory of the substrates. The many processes that metalloenzymes carry out inside a live body are very synchronised with their surroundings, but it is challenging to model these systems while

maintaining the physical and chemical features of the enzymes. The majority of these reactions are multistep processes that occur consecutively within milliseconds while producing reactive intermediates. Thus, it becomes a fundamental obstacle for many researchers to characterize these intermediates. The characterization of these intermediates is achieved by freezing the reactions at lower temperatures, which confirms each step involved to mimic their reaction pathway. The selection of an appropriate non-aqueous solvent system is required, as water is not a suitable solvent at lower temperatures. Also, the usage of organic solvents affects the native structure of proteins by disrupting the hydrogen bonds among the non-polar side chains thereby causing denaturation of the protein. Therefore, it has been a major challenge for researchers to overcome these limitations during the kinetics study of enzymatic reactions. Small synthetic molecules that accurately imitate the active site and the primary coordination sphere of the metalloenzymes were introduced as a partial solution to these restrictions.[10] Scientists have successfully imitated and simulated the reactions of the key metalloenzymes using these molecular models by using the appropriate solvents and regulating a range of temperatures.[11]

1.3. Iron and Manganese-containing Heme and Non-Heme Metalloenzymes

The fourth most common element in the crust of the earth is iron, which is one of the most crucial elements for life activities due to its propensity to exhibit a variety of oxidation states, such as Fe(I), Fe(II), Fe(III), Fe(IV), and Fe(V).[11] Therefore, it acts as an active site in different types of enzymes like oxidases, horseradish peroxidase (HRP), hydrogenases, reductases, oxygenases and dehydrogenases and performs a wide range of biological transformations.[12] Iron-sulfur proteins, heme and non-heme enzymes containing mononuclear and dinuclear metal centres utilize iron due to its redox efficiency. Heme and non-heme proteins are the two categories into which these enzymes are structurally divided. Again, these enzymes can be classified into two groups:

monooxygenase and dioxygenase. Enzymes are referred to as dioxygenases if they incorporate both oxygen atoms from dioxygen into the substrates, whereas monooxygenases only incorporate one oxygen atom. As seen in Fig. 1.1, the proto-heme IX prosthetic group makes up the majority of heme iron oxygenase.

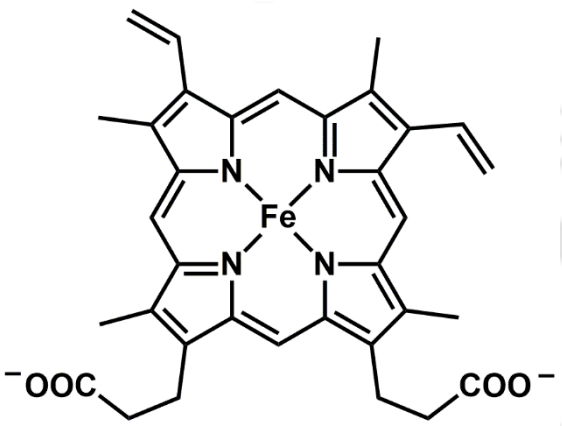

Fig. 1.1. Basic Proto-heme IX structure.

The pivotal involvement of dioxygen in the operation of numerous metalloenzymes makes its activation essential. Numerous functionally and mechanistically varied enzymes use mononuclear non-heme metal centres that are crucial to biology to activate molecular oxygen and carry out a variety of challenging reactions, such as the highly selective oxidation of various substrates.[13-16] The cytochrome P450 (CYP) family of oxygen-activating metalloenzymes is one of the most well-known varied families.[17] These superfamily of heme enzymes are versatile in nature that perform a variety of biological oxidation reactions such as alkane hydroxylation, olefin epoxidation, heteroatom oxidation, N-dealkylation, etc. The P450 superfamily's universally accepted mechanism of dioxygen activation has been shown in Fig. 1.2.[18,19] In the resting state, the Fe(III) is coordinated to tetra-nitrogen donors present on the equatorial plane of the porphyrin ring, the fifth coordination site is linked to the protein residue *via* a thiolate linkage of cysteine and the sixth coordinated site is occupied with an H_2O molecule *trans*

to the sulfur situated at the axial position. The labile coordination of water molecule to the iron(III) centre is disrupted during the substrate approach, resulting in the formation of the species [A]. After receiving an electron from NADPH, this Fe(III) species undergoes reduction to create the Fe(II) species [B], which activates molecular oxygen to create [C]. The species [C] is an end-on Fe(III)-superoxide intermediate that accepts another electron along with a proton to form an Fe(III)-hydroperoxo intermediate [D], which is considered as an active oxidant in numerous epoxidation reactions.[20,21] An iron(IV)-oxo cation radical species [E] is produced as a result of the heterolytic cleavage of the O-O bond due to both the *push effect* from cysteine and the *pull effect* from the distal protein.[22-24] This intermediate [E] is an active oxidant and is considered as compound I, which potentially abstracts an H-atom from various substrates leading to the formation of a radical in the substrate along with an Fe(IV)-OH intermediate [F], which is comparable to compound II in the catalytic activities of chloroperoxidase.[25] Finally, rebounding of the hydroxyl group from the species [F] takes place to the substrate radical which results in substrate hydroxylation.[13,26-30] Hence, compound I is found to be the active oxidant in the catalytic cycles of the dioxygen activation by Cytochrome P450. This species has been isolated and characterized by M. T. Green and co-workers,[31] and several iron(IV)-oxo intermediates related to cytochrome C peroxidase have been characterized.[32,33] These Cytochrome P450 enzymes utilize Fenton reagents and with an additional sophistication carry out highly regio- and chemo-selective reactions. However, enzymatic oxidation catalysis is different from the Fenton oxidation process. The striking difference between these two processes is: reduced forms of enzymes are involved in Fenton oxidation, whereas enzymatic oxidation catalysis utilizes molecular oxygen.[34,35]

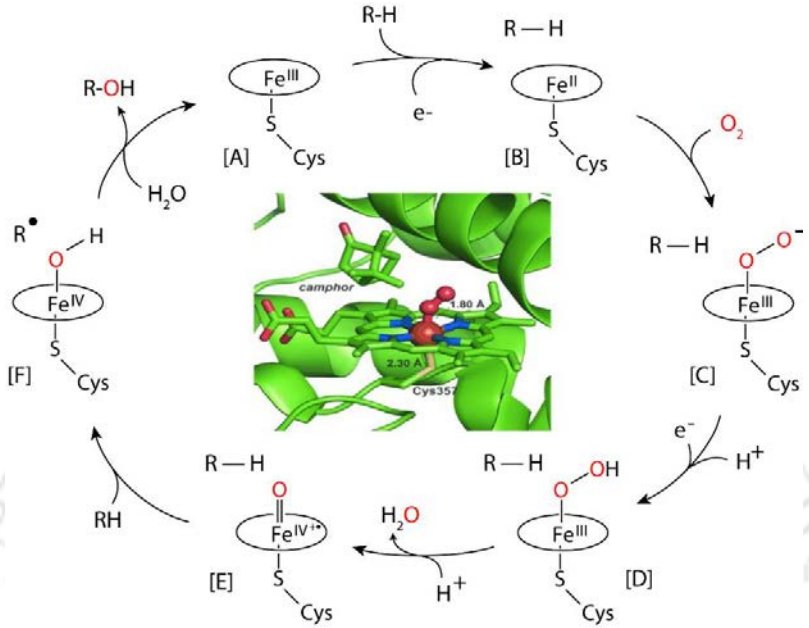

Fig. 1.2. General dioxygen activation mechanism by cytochrome P450. The inset shows the molecular oxygen bound in the active site of Cyt. P450cam (pdb code 1DZ9) and cysteine linkage with the protein residue and the camphor substrate.

Apart from iron, manganese metal also acts as an active site in various enzymes because like iron, manganese also exhibits multiple oxidation states and similar coordination geometries. Manganese-oxygen adducts like Mn(III)-superoxo and Mn(III)-peroxo that are crucial in biological and synthetic model systems. The relevance of these species to synthetic models and a number of Mn-containing enzymes, including photosystem II, Mn-superoxide dismutase (Mn-SOD), Mn-catalase (Mn-Cat), Mn-ribonucleotide reductase (Mn-RNR), and Mn-dependent catechol oxygenases (MndD). These adducts play a vital role in various functions such as detoxification of reactive oxygen species (ROS)[36,37]aromatic hydroxylation,[38] transformation of ribo- to deoxyribonucleotides,[39,40] and formation of oxygen from water.[41]

Exquisite mononuclear transition metals (Fe, Mn, Ni, Co, etc.) in the active sites of various metalloenzymes have evolved for the activation of molecular oxygen (O_2) to

generate metal-oxygen intermediates such as metal(III)–peroxo, metal(III)–hydroperoxo, metal(III)–superoxo and metal(IV)–oxo and are considered as reactive species in the oxidation of numerous organic substrates as well as in many biological processes.[42-58] Many non-heme enzymes containing Fe/Mn metal perform metabolically important functions by catalyzing the activation of dioxygen (O_2).[59-64] The speculated intermediates involved in all those iron and manganese-catalyzed biotransformations are shown below (Fig. 1.3). [64,65]

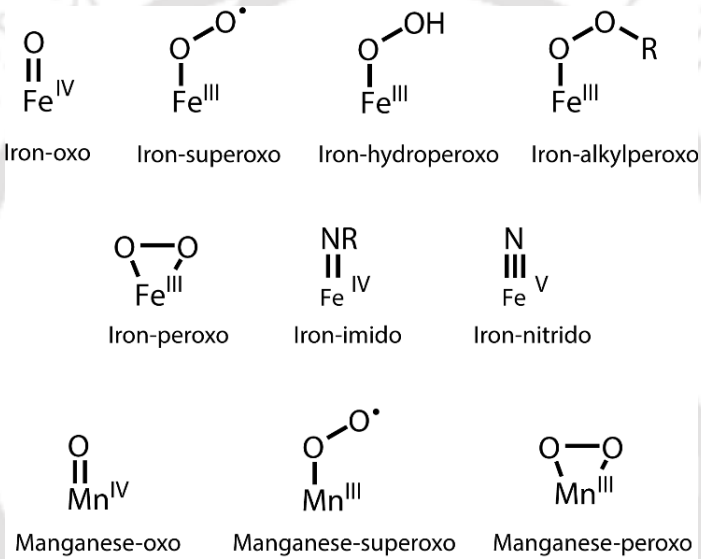

Fig. 1.3. Proposed intermediates of high-valent Iron and Manganese with Oxygen and Nitrogen.

Mechanistic developments in enzymatic oxidation reactions help in the understanding of the activation of dioxygen and especially nature of the active oxidizing species involved in various catalytic cycles of enzymes and their model systems like oxygen atom transfer reaction by α-KG-dependent oxygenases (TauD).[66,67] For decades, numerous biological oxidation processes have been attributed to high-valent mononuclear non-heme iron(IV)-oxo intermediates as the important reactive species. Studies of numerous α-ketoglutarate-dependent (α-KG) oxygenases (TauD) that catalyze either the

hydroxylation or halogenation of organic substrates have led to the first direct characterisation of such reactive intermediates (see Fig. 1.4).[68] A general mechanism of dioxygen activation by α-KG-dependent enzymes using TauD as the active site is depicted in the catalytic cycle as in Fig. 1.4.[66]

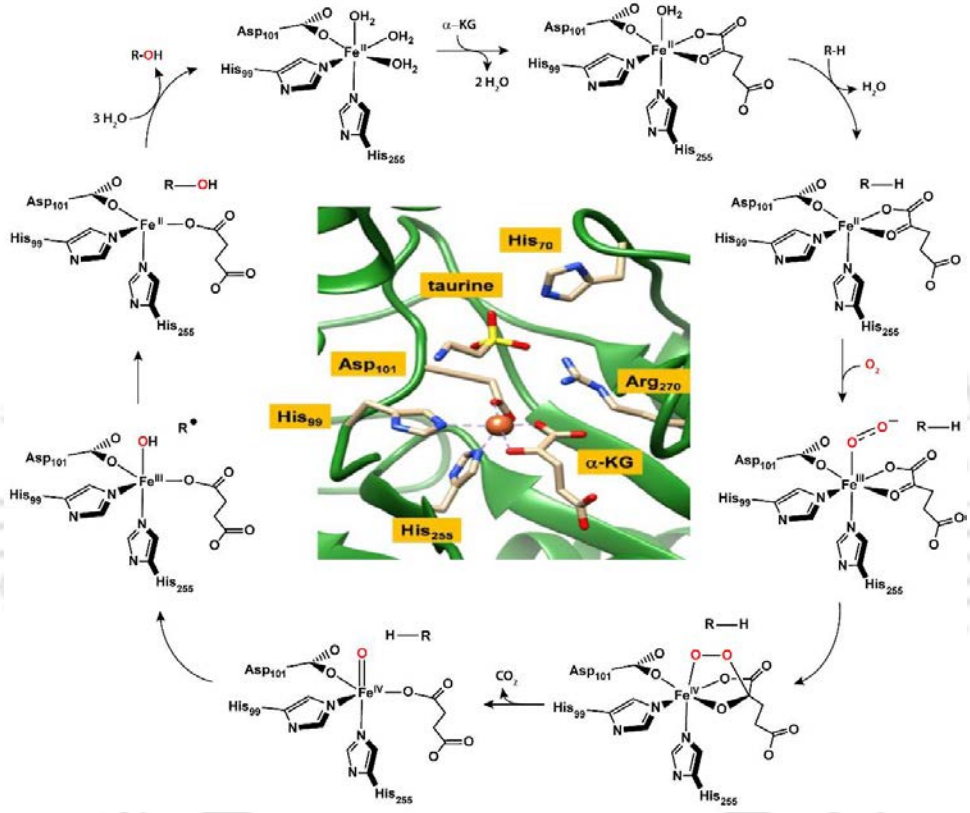

Fig. 1.4. General mechanism of dioxygen activation by TauD enzyme. Inset shows the active-site of TauD enzyme as taken from the 1OS7 pdb file.[68]

Upon the approach of α-KG to the Fe(II) centre, two H_2O molecules are released out of the primary coordination sphere, and then α-KG coordinates with the iron centre in a bidentate manner. It also follows the removal of another H_2O molecule during the substrate approach and creates space for the dioxygen which then binds to the iron centre to create the iron(III)-superoxide species in an end-on manner. Then the oxygen atom at

distal position binds the carbon atom of α-KG, which then undergoes decarboxylation. Subsequently, the homolysis of the O-O linkage leads to the formation of the proposed high-valent iron(IV)-oxo intermediate,[69-72] which mostly causes the hydroxylation of the C-H bonds. Rapid freeze-quench procedures can be used to capture the reactive intermediates in non-heme systems, unlike heme metalloenzymes.[67] Prof. Que and colleagues reported the first crystal structure of non-heme iron(II) coupled to a α-keto acid using benzoyl formate.[69]

A '*rebound mechanism*' is used to carry out the hydroxylation of the substrates in heme (cytochrome P450) as well as non-heme systems (TauD). A hydrogen atom is abstracted from the substrate by the iron(IV)-oxo species, which is then reduced by one electron, thus forming an Fe(III)-hydroxo intermediate and a substrate radical. The hydroxylated product and reducing iron centre are formed when the -OH group from the iron(III)-hydroxo species bounces back to the substrate radical (see Scheme 1.1).[73,74]

Scheme 1.1. Oxygen rebound mechanism of iron(IV)-oxo complex in substrate hydroxylation.

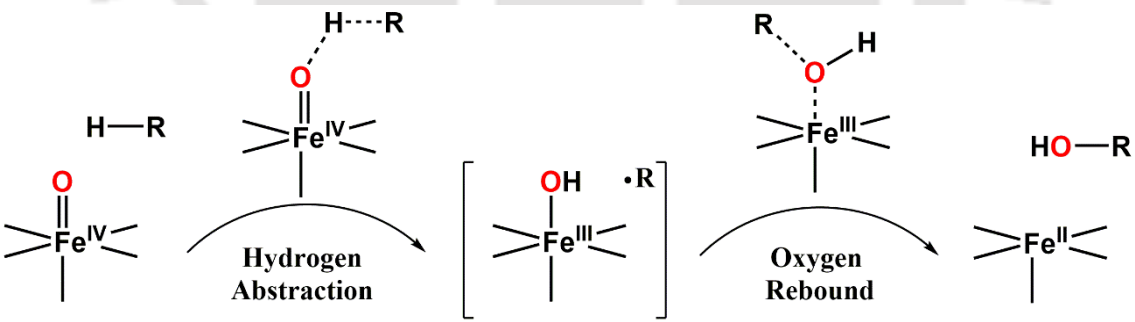

1.4. Enzymomimetic Models and Reactivity

Numerous non-heme metalloenzymes containing Fe and Mn metals that are significant in performing various functions in biological systems. From the literature survey, many such systems need synthetic models which can effectively imitate the active

site of enzymes and also biological reactions. Inspired by Nature, researchers have put their efforts to synthesize such model systems that are reacting with many oxidants to produce high-valent transient intermediates. These intermediates were reacted with various substrates to understand their reaction mechanisms.[75,76] The difficulties encountered in these processes are: stabilization and characterization of these transient species and controlling the fast reaction kinetics. This thesis focuses on the synthesis of synthetic models, which may contain transition metal ions, such as iron and manganese, as well as the generation of reactive intermediates through reactions with appropriate oxidants and the kinetics of those reactions with diverse organic substrates. As a result, many model reactions were performed, and mechanistic studies were established.

Various reactive intermediates such as iron(IV)-oxo, iron(IV)-tosylimido, and Mn(III)-peroxo were effectively produced and characterized while working on the aforementioned processes. Depending on the stability of these intermediates and their reaction kinetics, the mechanistic details for different reactions have been investigated at suitable temperatures.

1.4.1. Non-Heme Manganese(III)-Peroxo Mimics

Manganese-containing enzymes react with an oxygen molecule in its different reduced forms and are particularly essential in biology for specific functions like detoxification superoxide and H_2O_2 and the biodegradation of pollutants.[36, 77-79] There are numerous synthetic Mn(III)-peroxo intermediates that have been synthesized by oxidizing Mn(II)-Precursors with either hydrogen peroxide (H_2O_2) in basic condition or potassium superoxide (KO_2).[80-86] However, the utilization of dioxygen as an oxidant has been reported to generate a high-spin (S = 2) Mn(III)-peroxo intermediate.[87] These intermediates are thermally unstable and are highly reactive, often requiring low temperatures for their kinetic studies. These are found to react with aldehydes.[87] X-ray

crystal structure of such complexes reveals an O-O bond lengths of 1.40-1.43 Å, confirming the Mn(III)-peroxo moieties.[81, 83, 85] Nam and co-workers have used a tetradentate N4 macrocyclic ligand (TMC) and have generated a mononuclear Mn(III)-peroxo species, $[Mn^{III}(TMC)(O_2)]^+$, (TMC = 1,4,8,11-tetramethyl-1,4,8,11-tetraazacyclotetradecane) by reacting hydrogen peroxide (5 equiv.) with a $[Mn(TMC)(CF_3SO_3)_2]$ solution in the presence of base triethylamine (2.5 equiv.) in acetonitrile at ambient conditions.[83] Unlike the other peroxo complexes, this complex has a high degree of stability and is presumably caused by steric bulk around the peroxo unit from N-methyl substituents in the TMC macrocyclic ligand. Borovik group have reported the formation of peroxomanaganese(III) complexs with $[Mn^{II}H_2bupa]^-$ ($[H_2bupa]^{3-}$, bis[(N'-t-butylurealy)-N-ethyl](6-pivalamido-. 2-pyridylmethyl)-aminato) ligand system and O_2 at ambient conditions.[87] A number of manganese(III)-peroxo complexes bearing aminopyridyl ligand systems has been generated either with hydrogen peroxide in the presence of triethylamine or with KO_2 in CH_3CN at -40 °C.[86] Jackson and co-workers have demonstrated the electrochemical synthesis of such manganese(III)-peroxo complexes with pentadentate amino pyridine and imidazole ligands.[88] These manganese(III)-peroxo intermediates perform aldehyde deformylation reactions and it has been found that the reaction mechanism for the same proceeds *via* a nucleophilic pathway for most of these complexes.[89-94] The rate of aldehyde deformylation reaction has been monitored by tuning the axial ligands by introducing a variety of ligands (X) such as CN^-, NCS^-, $CF_3CO_2^-$, and N_3^- in $[Mn^{III}(O_2)(13\text{-}TMC)(X)]^+$.[95] Aldehyde deformylation reaction is a characteristic reaction of aldehydes to ketone, as observed in $[Mn^{III}(O_2)(TMC)]^+$ and $[Mn^{III}(O_2)(H_3bupa)]^-$ intermediates.[83, 87]

1.4.2. Non-Heme Iron(IV)-Oxo Mimics

Several non-heme iron enzymatic catalytic cycles have been hypothesised to include high-valent iron(IV)-oxo species as an active oxidant. The α-keto acid-dependent

TauD enzyme is the only mononuclear non-heme enzyme to include such species.[68,96] As a consequence, many iron(IV)-oxo species involved in model systems were characterized.[97-101] The synthesis of such iron(IV)-oxo intermediates was carried out by treating the iron(II)-precursors with suitable oxidants such as PhIO, peracetic acid or H_2O_2.[102] These intermediates are potential oxidants in performing various oxidative transformations.[103] In 1979, for the first time, Groves and group reported the catalytic hydroxylation of alkanes by a mononuclear iron(III) species bearing a 5,10,15,20-tetrakis(phenyl)porphyrin system using PhIO as oxidant.[104] It has been found that the stability of the catalysts is enhanced under oxidizing conditions due to the incorporation of bulkier arenes with different substituents at the *meso* positions along with the electron-withdrawing groups at β-position of the pyrrole rings.[105] Thus, it clearly indicates that the catalytic performance depends on the kind of ligands as well as oxidants. In 1990, Que and colleagues demonstrated the synthesis of iron intermediates such as $[Fe^{III}(TPA)Cl_2](ClO_4)$ and $[Fe^{III}(TPA)Br_2](ClO_4)$ and studied their catalytic activity with cyclohexane.[106,107] Thereafter, a series of μ-oxo bridged diiron complexes with TPA derivatives were studied, that showed significant turnovers in the catalytic process using cyclohexane as a substrate and by the addition of *tert*-butyl hydroperoxide (*t*BuOOH).[108,109] Upon introduction of three electron-withdrawing nitro groups in the TPA ligand system, the catalytic activity was found to be decreased with lower yield and also selective oxidation of cyclohexane as observed by Hitomi and co-workers.[110,111] Not only the ligand system but also the solvent has a significant role in the catalytic cycles as evident from TPA and N3Py-based intermediates, where there was greater selective oxidation of cyclohexane as well as *cis*-1,2-dimethylcyclohexane in acetonitrile solvent rather than in acetone.[112,113] In 2000, Weighardt and group synthesized the first non-heme iron(IV)-oxo complex bearing a cyclam-acetate ligand framework.[114] This complex was synthesized by the ozonolysis of $[Fe^{III}(\text{cyclam-acetate})(CF_3SO_3)]^+$ at a lower temperature (-40°C or -80°C) in a mixture solvent of water and acetone, and a green-coloured species

was generated and characterized by Ultaviolet-visible spectroscopy (λ_{max} = 676 nm) having a stability of less than an hour. The formation of this iron(IV)-oxo complex was confirmed from the Mössbauer data with (δ = 0.01 mm/s and ΔE_Q = 1.37 mm/s) that were relatable with heme iron(IV)-oxo complexes. Que and Nam demonstrated a non-heme iron(IV)-oxo species, $[Fe^{IV}(O)(TMC)(CH_3CN)]^{2+}$ supported by a macrocyclic TMC ligand by reacting the corresponding iron(II) complex with any one of the oxidants such as PhIO or H_2O_2 in acetonitrile at a lower temperature (-40 °C), hence resulting in the formation of a green-coloured solution with an absorption band at λ_{max} 820 nm (ε = 400 M^{-1} cm^{-1}). Mössbauer data with δ = 0.17 mm/s and ΔE_Q = 1.24 mm/s are in great agreement with the generation of this iron(IV)-oxo species.[98] The tuning of axial ligand effect in the same TMC framework has been studied by Sastri and co-workers with the introduction of axial groups like CH_3CN, CF_3COO^-, and N_3^- and electron-donating ability of these groups led to interesting results in the hydrogen atom abstraction (HAA) from hydrocarbons and phenolic substrates and also in oxygen atom transfer (OAT) to the substrate PPh_3.[115] Further, the ring strain in the ligand framework also has a huge role in the reactivity of iron(IV)-oxo complexes as observed by the Nam group. The TBC ligand was synthesized by introducing four benzyl groups in place of the methyl groups in TMC, which resulted in a greater strain in the cyclam ring and steric hindrance among the groups.[116] A comparative reactivity of the iron(IV)-oxo complexes generated using TBC and TMC ligands showed that despite the ring strain, $[Fe^{IV}(O)(TBC)(CH_3CN)]^{2+}$ shows $>10^2$ folds greater reactivity than $[Fe^{IV}(O)(TMC)(CH_3CN)]^{2+}$ in HAA as well as OAT reactions.[116] Que and co-workers employed a tetradentate ligand TPA and generated its iron(IV)-oxo complex, $[Fe^{IV}(O)(TPA)(CH_3CN)]^{2+}$ at -40 °C in CH_3CN. The synthesis of this complex was evident from a low-intensity near-IR band at 724 nm (ε = 300 M^{-1} cm^{-1}), that also confirmed by Mössbauer and ESI-MS analysis.[117]

There are many non-heme mononuclear iron(IV)-oxo complexes that have been generated and studied using a variety of spectroscopic techniques, although the majority of them are produced in non-aqueous solvents and include low-spin S = 1 iron centre.[100,101,118-121] An exceptional iron(IV)-oxo intermediate $[Fe^{IV}(O)(OH_2)_5]^{2+}$ with high-spin S=2 was synthesized in an aqueous solvent by Bakac and group.[122-124] In addition, one more example of a high-spin iron(IV)-oxo intermediate, $[Fe^{IV}(O)(TMG_3tren)](CF_3SO_3)_2$ was synthesized by Que et al. using TMG_3tren system, which is quite stable with a $t_{1/2}$ of 4.3 h at -30 °C and about 30 sec at room temperature.[125] Thereafter, Nam and group employed an iron(IV)-oxo intermediate that has shown greater reactivity as compared to the cytochrome P450 model compound I. By substituting three N-methylbenzimidazole groups for the pyridine rings, the reactivity patterns of this iron(IV)-oxo complex was increased towards oxidative reactions.[126] However, greater reactivity of an iron(IV)-oxo intermediate does not necessarily depend on its high-spin character.[127] In addition, another high-spin iron(IV)-oxo intermediate, $[Fe^{IV}(O)(TQA)]^{2+}$ was generated by Que and group by the substitution of bulky quinolines in place of pyridine groups in TPA. The steric crowding in the ligand framework prevented the development of shorter Fe-N bonds that are needed for the formation of a low-spin complex and hence led to the formation of an iron-oxo complex with high-spin S= 2.[128] There are a few iron(IV)-oxo intermediates with a high-spin character have been synthesized and they all have a trigonal bipyramidal geometry that forces the oxo moiety to be properly buried in a sterically inhibited cavity.[129-131] Iron exists in +4 oxidation state in all the above-discussed iron-oxo complexes, but Collins and co-workers have successfully generated an iron(V)-oxo complex by using the TAML framework (TAML = tetra-amido macrocyclic ligand).[132,133] The electron-rich TAML ligand acquires almost a square planer geometry that stabilizes the oxo complex with S = ½. The reactivity of all these iron(IV)-oxo complexes is influenced by various factors like ligand topology,[100,126,134] axial ligations,[115,135] metal spin state[127] and coordination of

various metals and protons[136-139] to the iron-oxo group that have been thoroughly investigated for last few decades.

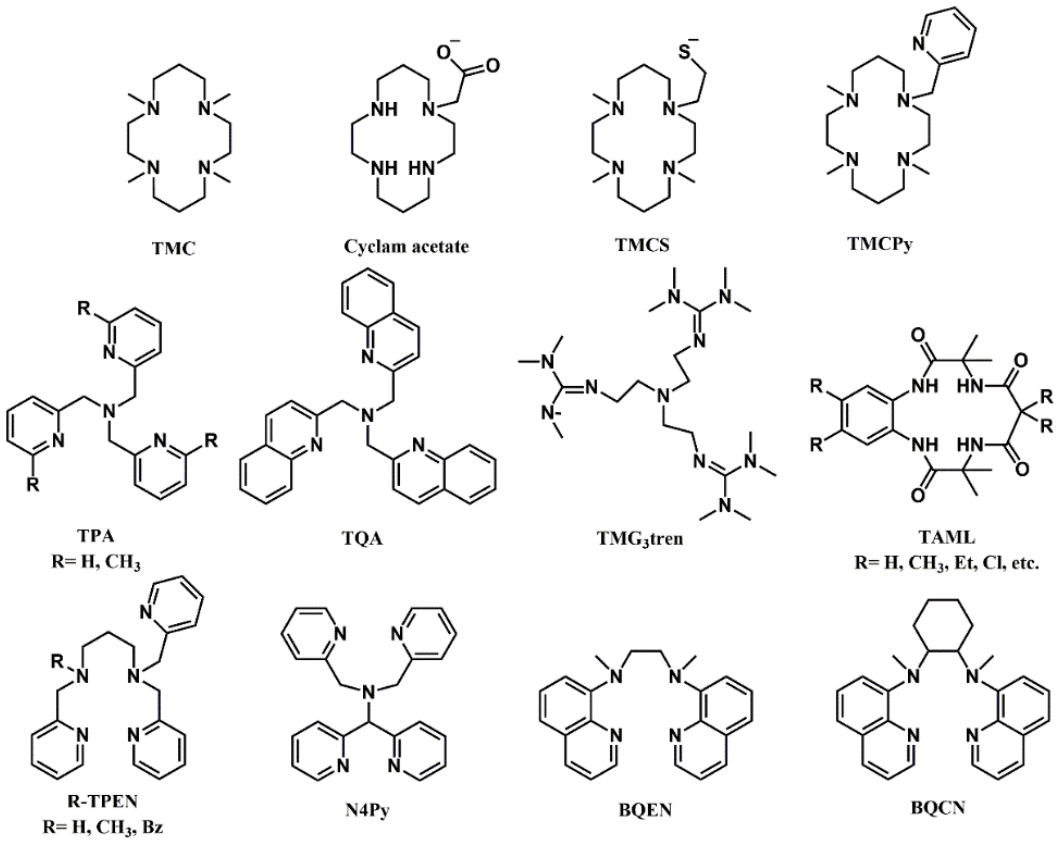

Fig. 1.5. Ligand systems discussed that can stabilize various high-valent iron-oxo complexes.

Synthetic mononuclear non-heme iron(IV)-oxo complexes are potential oxidants that perform a diverse family of reactivities like sulfoxidation, phosphorous oxidation, alcohol oxidation, epoxidation, hydroxylation, halide oxidation, N-dealkylation, C-H activation, electron transfer, hydride transfer, ligand and water exchange reactions, etc. (see Fig. 1.6).

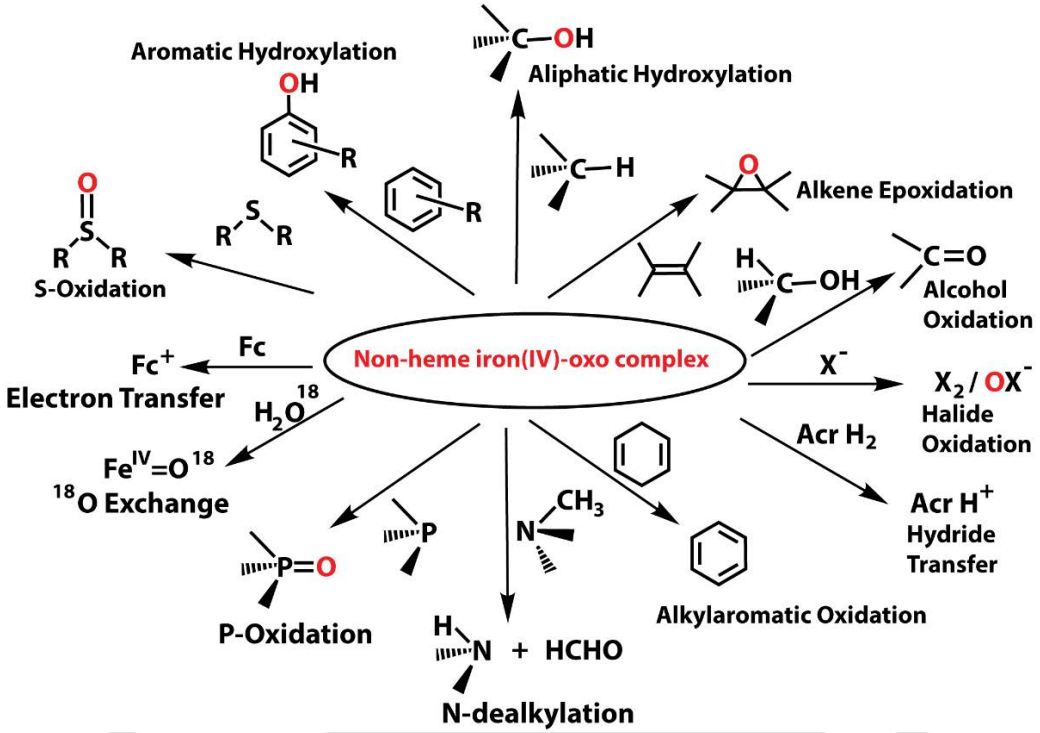

Fig. 1.6. Diversity of oxidative transformations by non-heme iron(IV)-oxo complexes.

1.4.3. Non-Heme iron isolobal intermediates

Though there is an extensive study on high-valent iron-oxygen intermediates, limited reports are there on their ioslobal analogues. Iron complexes with terminal nitrido or imido are a few such systems that are well-studied. The iron metal in these complexes exists in higher oxidation states like +4, +5 and +6.[140-142] In 2000, Weighart and co-workers demonstrated the first high-valent iron(V)-nitrido intermediate in a non-heme system by the photolysis of a ferric-azide cyclam-acetate complex.[114,141] Characterization of this complex confirmed that the spin state of the iron is $S = 1/2$ in its ground state with a shorter Fe-N bond length of 1.61 Å. Furthermore, the same group has also reported an iron(VI)-nitrido species supported by a trimethyl cyclam-acetate ligand framework by treating laser radiation to the electrochemical generation of an iron(IV)-azide complex

followed by its photo-oxidation.[142] In non-heme iron(IV) category, isolobal iron(IV)-nitrido complexes were synthesized using tris-(phosphino)borate ligand systems.[140,143] These complexes were generated in two steps. The first step involves the treatment of an iron(I) complex using a nitrene transfer oxidant Li(dbabh) to produce iron(III)-imide species, then in the next step, a high-valent iron(IV)-nitrido intermediate was generated by slowing heating the pre-synthesized iron-imide with a release of anthracene molecule.[140,143] The iron metal in these complexes was found to be in low spin $S = 0$ in the ground state. XAS studies of these complexes revealed a shorter Fe-N bond length of 1.51-1.55 Å, which is in great agreement with the formation of a triple bond between Fe and N atoms as observed in earlier reported iron-nitrides.[143]

In 2000, the first iron(IV)-imido species, $[Fe_4(\mu_3\text{-}N^tBu)_4]$ was reported by Lee and co-workers.[144] Its structure is similar to a cubane, with the iron(IV) centre located in one of its corners. The complex was formed by a self-assembly process with a poor yield of just 2% or less, in which three bridging Fe centres were bonded to a terminal Cl^- anion and then another Fe centre was coordinated to a terminal t-butylimide. The iron oxidation state in this iron(IV)-imido complex was confirmed by Mössbauer analysis whereas the single crystal X-ray data are consistent with the iron-nitrogen bond distances of 1.635(4) Å and a linear Fe-N-C bond angle of about 178.6(3)°.[144] Later, iron(IV)-imido complexes were reported in high yield using different ligand frameworks.[145-155] These high-valent iron-nitrides and imides complexes are excellent oxidants and are vital in catalyzing amination reactions like other isolobal analogues. Over the last few years, several groups have been studied on the reactivity of these metal nitrides and amides towards the aziridination of different alkenes and aminidation of alkanes by iminoiodane.[145-154] However, a thorough investigation of their ability to act as a nitrogen atom transfer oxidant is yet lacking as well as a little is known about their reactivity as compared to the isolobal iron(IV)-oxo complexes.[155]

1.5. Scope and Aim of the Thesis

Over the last decade, the reactivity of high-valent metal complexes towards a diverse array of oxidation reactions and the investigation of their mechanistic pathways have gained immense importance in biomimetic chemistry. From the comprehensive literature survey as discussed above, it is evident that the research area on non-heme enzymomimetic reactions looks encouraging. Nature has designed various metalloenzymes that perform a diversity of oxidative transformations through successfully tuned and established catalytic cycles. Inspired by Nature, researchers synthesize synthetic model systems to mimic various flawless molecular machines and imitate their performance. Although a comprehensive study has been conducted on non-heme systems over the decades, the performance of these enzymes is very little as compared to natural metalloenzymes. This poor performance of non-heme metalloenzymes is mainly due to many challenging factors faced by the researchers such as stability factor, characterization of the reactive intermediate species, phase issues, selectivity problems, turnover numbers, etc. Designing the ligand architecture is crucial because that provides stability to the intermediates and also has a role in determining the spin states of the metal centre that ultimately influences the reactivity of these synthetic complexes. This thesis contributes a little to the large research works on mononuclear non-heme enzymomimetic models as well as their reactivity. Initially, a set of nitrogen-based pentadentate ligands have been synthesized, which then followed the synthesis of complexes of Fe and Mn metals. These metal complexes have been used as precursors to generate various high-valent transient species. These species are reactive intermediates that play a pivotal role in the catalytic reactions of various metalloenzymes toward the oxidation of organic substrates. The reactivity of these intermediates with various substrates has been monitored kinetically and the mechanistic details for these reactions have been investigated. Chapter-II describes the synthesis of a set of ligands and their

metal complexes along with their characterization by different spectroscopic techniques and also the usage of different reagents, solvents, oxidants, etc. Chapter-III depicts an electrophilic deformylation of aldehydes by two isomeric side-on Mn(III)-peroxo intermediates and also the effect of isotopic substitution in aldehydes on tuning the regioselective switch in the H-atom abstraction from α-position to the aldehyde group. Chapter IV describes the sluggish reactivity of an iron(IV)-tosylimido complex as compared to its oxo-analogoue towards the hetero atom transfer and HAA reactions. Finally, Chapter-V analyses the oxidative dehalogenation of two iron(IV)-oxo complexes with a series of halophenols and a unique mechanism for the same has been elucidated that proceeds *via* a substrate-bound adduct formation.

1.6. References

1. J. M. McCord, *Am. J. Med.* **2000**, *108*, 652-659.
2. J. M. McCord, *J. Nutr.* **2004**, *134*, 3171S-3172S.
3. R. Y. N. Ho, J. F. Liebman, J. S. Valentine, In *Active Oxygen in Biochemistry*, J. S. Valentine, C. S. Foote, A. Greenberg, J. F. Liebman, Ed.; Chapman & Hall, New York, **1995**, Vol. 3, pp. 1-36.
4. J. M. McCord, *Semin Hematol* **1998**, *35*, 5-12.
5. H. Otani, M. Umemoto, K. Kagawa, Y. Nakamura, K. Omoto, K. Tanaka, T. Sato, A. Nonoyama, T. Kagawa, *J. Surg. Res.* **1986**, *41*, 126-133.
6. I. Fridovich, *Annu. Rev. Pharmacol. Toxicol.* **1983**, *23*, 239-257.
7. I. Fridovich, *J. Exp. Biol.* **1998**, *201*, 1203-1209.
8. F. Auchère, F. Rusnak, *J. Biol. Inorg. Chem.* **2002**, 7, 664-667.
9. I. Bertini, H. B. Gray, E. I. Stiefel, S. J. Valentine, *Biological Inorganic Chemistry: Structure and Reactivity*. University Science Books, Sausalito, California, **2007**.
10. L. Que, Jr., *Acc. Chem. Res.* **2007**, *40*, 493-500.
11. H. B. Kraatz, N. Metzler-Nolte, *Concepts and Models in Bioinorganic Chemistry*. Wiley-VCH, Weinheim, **2006**.
12. F. A. Cotton, G. Wilkinson, C. A. Murillo, M. Bochmann, Copper: Group 11. In *Advanced Inorganic Chemistry*, 6th Ed. John Wiley and Sons, New York, **1999**.
13. I. G. Denisov, T. M. Makris, S. G. Siligar, I.Schlichting, *Chem. Rev.* **2005,** *105*, 2253–2277.
14. B. Meunier, S. P. de Visser, S. Shaik, *Chem. Rev.* **2004,** *104*, 3947–3980.
15. M. M. Abu–Omar, A. Loaiza, N. Hontzeas, *Chem. Rev.* **2005***, 105*, 2227–2252.
16. M. Costas, M. P. Mehn, M. P. Jensen, L. Que Jr., *Chem. Rev.* **2004,** *104,* 939–986.

17. *Cytochrome P450: Structure, Mechanism, and Biochemistry*, 3rd ed. (Ed.: P. R. Ortiz de Montellano), Kluwer Academic/Plenum Publishers, New York, **2005**.
18. J. T. Groves, *J. Chem. Ed.* **1985**, *62*, 928-931.
19. J. T. Groves, Y.-Z. Han, In *Cytochrome P-450: Structure, Mechanism and Biochemistry*, P. R. Oritz de Montellano, Ed. Plenum Press, New York, **1995**, pp. 3-48.
20. S. Jin, T. M. Makris, T. A. Bryson, S. G. Sligar, J. H. Dawson, *J. Am. Chem. Soc.* **2003**, *125*, 3406-3407.
21. I. G. Denisov, T. M. Makris, S. G. Sligar, I. Schlichting, *Chem. Rev.* **2005**, *105*, 2253-2277.
22. F. Ogliaro, S. P. de Visser, S. Shaik, *J. Inorg. Biochem*. **2002**, *91*, 554-567.
23. D. L. Harris, G. H. Loew, *J. Am. Chem. Soc.* **1998**, *120*, 8941-8948.
24. D. L. Harris, G. H. Loew, *J. Am. Chem. Soc.* **1996**, *118*, 6377-6387.
25. M. T. Green, J. H. Dawson, H. B. Gray, *Science* **2004**, *304*, 1653-1656.
26. J. T. Groves, In *Cytochrome P450: Structure, Mechanism, and Biochemistry*; 3rd ed.; P. R. Ortiz de Montellano, Ed.; Plenum Publishers: New York, **2005**, pp. 1-43.
27. M. Newcomb, M.-H. Le Tadic, D. A. Putt, P. F. Hollenberg, *J. Am. Chem. Soc.* **1995**, *777*, 3312-3313.
28. V. W. Dowry, K. U. Ingold, *J. Am. Chem. Soc.* **1991**, *113*, 5699-5707.
29. M. Filatov, N. Harris, S. Shaik, *Angew. Chem. Int. Ed. Engl.* **1999**, *38*, 3510-3512.
30. F. Ogliaro, N. Harris, S. Cohen, M. Filatov, S. P. deVisser, S. Shaik, *J. Am. Chem. Soc.* **2000**, *122*, 8977-8989.
31. J. Rittle and M. T. Green, *Science* **2010**, *330*, 933–937.
32. C. A. Bonagura, B. Bhaskar, H. Shimizu, H. Li, M. Sundaramoorthy, D. E. McRee, D. B. Goodin, T. L. Poulos, *Biochemistry* **2003**, *42*, 5600-5608.

33. S. L. Edwards, X. Nguyen-Huu, R. C. Hamlin, J. Kraut, *Biochemistry* **1987**, *26*, 1503-1511.
34. S. Jin, T. M. Makris, T. A. Bryson, S. G. Sligar, J. H. Dawson, *J. Am. Chem. Soc.* **2003**, *125*, 3406-3407.
35. I. G. Denisov, T. M. Makris, S. G. Sligar, I. Schlichting, *Chem. Rev.* **2005**, *105*, 2253-2277.
36. A. J. Wu, J. E. Penner-Hahn, V. L. Pecoraro, *Chem. Rev.* **2004**, *104*, 903-938.
37. A. F. Miller, *Superoxide processing, In Comprehensive Coordination Chemistry II*; Elsevier Ltd: Oxford, UK., **2004**.
38. J. P. Emerson, E. G. Kovaleva, E. R. Farquhar, J. D. Lipscomb, L. Que, Jr., *Proc. Natl. Acad. Sci.* **2008**, *105*, 7347-7352.
39. J. A. Cotruvo, J. Stubbe, *Biochemistry* **2010**, *49*, 1297-1309.
40. A. Willing, H. Follmann, G. Auling, *Eur. J. Biochem.* **1988**, *170*, 603-611.
41. V. L. Pecoraro, W. Y. Hsieh, *Inorg. Chem*. **2008**, *47*, 1765-1778.
42. E. I. Solomon, *Chem. Rev*. **2000**, *100*, 235–350.
43. E. G. Kovaleva, J. D. Lipscomb, *Nature Chem. Biol.* **2008**, *4*, 186–193.
44. L. C. Blasiak, F. H. Vaillancourt, C. T. Walsh, C. L. Drennan, *Nature* **2006**, *440*,368–371.
45. J. Rittle, M. T. Green, *Science* **2010**, *330*, 933–937.
46. E. G. Kovaleva, J. D. Lipscomb, *Science* **2007**, *316*, 453–457.
47. A. Karlsson, *Science* **2003**, *299*, 1039–1042.
48. R. M.Cicchillo, *Nature* **2009**, *459*, 871–874.
49. M. J. Park, J. Lee, Y. Suh, J. Kim, W. Nam, *J. Am. Chem. Soc.* **2006**, *128*, 2630–2634.
50. Y. M. Kim, K.−B. Cho, J. Cho, B. Wang, C. Li, S. Shaik, W. Nam, *J. Am. Chem. Soc.* **2013**, *135,* 8838−8841.

51. L. V. Liu, S. Hong, J. Cho, W. Nam, E. I. Solomon, *J. Am. Chem. Soc.* **2013,** *135*, 3286−3299.

52. H. So, Y. J. Park, K.−B. Cho, Y.−M. Lee, M. S. Seo, J. Cho, R. Sarangi, W. Nam, *J. Am. Chem. Soc.* **2014**, *136*, 12229−12232.

53. J. Annaraj, Y. Suh, M. S. Seo, S. O. Kim, W. Nam, *Chem. Commun*. **2005**, 4529–4531.

54. J. Annaraj, J. Cho, Y.–M. Lee, S. Y. Kim, R. Latifi, S. P. de Visser, W. Nam, *Angew. Chem. Int. Ed*. **2009**, *48*, 4150–4153.

55. M. S. Seo, J. Y. Kim, J. Annaraj, Y. Kim, Y.–M. Lee, S.–J. Kim, J. Kim, W. Nam, *Angew. Chem. Int. Ed.* **2007**, *46*, 377–380.

56. R. A. Geiger, S. Chattopadhyay, V. W. Day, T. A. Jackson, *Dalton Trans.* **2011**, *40*, 1707–1715.

57. Y. Goto, S. Wada, I. Morishima, Y. Watanabe, *J. Inorg. Biochem.* **1998**, *69*, 241–247.

58. J. Cho, R. Sarangi, J. Annaraj, S. Y. Kim, M. Kubo, T. Ogura, E. I. Solomon, W. Nam, *Nat. Chem*. **2009**, *1*, 568–572.

59. E. I. Solomon, T. C. Brunold, M. I. Davis, J. N. Kemsley, S.–K. Lee, N. Lehnert, F. Neese, A. J. Skulan, Y.–S. Yang, J. Zhou, *Chem. Rev.* **2000**, *100*, 235–349.

60. M. Costas, M. P. Mehn, M. P.Jensen, L. Que Jr., *Chem. Rev.* **2004,** *104,* 939–986.

61. R. P. Hausinger, *Crit. Rev. Biochem. Mol. Biol*. **2004**, *39*, 21–68.

62. E. G. Kovaleva, J. D. Lipscomb, *Nat. Chem. Biol*. **2008**, *4*, 186–193.

63. C. Loenarz, C. J. Schofield, *Nat. Chem. Biol*. **2008**, *4*, 152–156.

64. W. Nam, *Acc. Chem. Res*. **2007**, *40*, 522–531, and review articles in the special issue.

65. M. J. Park, J. Lee, Y. Suh, J. Kim and W. Nam, *J. Am. Chem. Soc.* **2006,** *128,* 2630–2634.

66. J. M. Bollinger Jr., J. C. Price, L. M. Hoffart, E. W. Barr, C. Krebs, *Eur. J. Inorg. Chem.* **2005**, 4245–4254.

67. C. Krebs, J. C. Price, J. Baldwin, L. Saleh, M. T. Green, J. M. Bollinger Jr., *Inorg. Chem.* **2005**, *44*, 742–757.

68. J. C. Price, E. W. Barr, B. Tirupati, J. M. Bollinger Jr., C. Krebs, *Biochemistry* **2003**, *42*, 7497–7508.

69. Y.-M. Chiou, L. Que, Jr., *J. Am. Chem. Soc.* **1995**, *117*, 3999−4013.

70. E. H. Ha, R. Y. N. Ho, J. F. Kisiel, J. S. Valentine, *Inorg. Chem.* **1995**, *34*, 2265−2266.

71. E. L. Hegg, R. Y. N. Ho, L. Que, Jr., *J. Am. Chem. Soc.* **1999**, *121*, 1972−1973.

72. H. M. Hanauske-Abel, V. Günzler, *Theor. Biol.* **1982**, *94*, 421−455.

73. R. J. Balahura, A. Sorokin, J. Bernadou, B. Meunier, *Inorg. Chem.* **1997**, *36*, 3488-3492.

74. M. Costas, *Coord. Chem. Rev.* **2011**, *255*, 2912−2932.

75. J.-J. Girerd, F. Banse, A. J. Simaan, *Struct. Bonding* **2000**, *97*, 145−177.

76. J.-U. Rohde, M. R. Bukowski, L. Que, Jr., *Curr. Op. Chem. Biol.* **2003**.

77. J. P. Emerson, E. G. Kovaleva, E. R. Farquhar, J. D. Lipscomb, L. Que, Jr., *Proc. Natl. Acad. Sci. U.S.A.* **2008**, *105*, 7347−7352.

78. L. E. Grove, T. C. Brunold, *Comments Inorg. Chem.* **2008**, *29*, 134-168.

79. A.-F. Miller, *Curr. Opin. Chem. Biol.* **2004**, *8*, 162−168.

80. S. Groni, G. Blain, R. Guillot, C. Policar, E. Anxolabéhére-Mallart, *Inorg. Chem*. **2007**, *46*, 1951−1953.

81. N. Kitajima, H. Komatsuzaki, S. Hikichi, M. Osawa, Y. Moro-oka, *J. Am. Chem. Soc*. **1994**, *116*, 11596−11597.

82. R. L. Shook, W. A. Gunderson, J. Greaves, J. W. Ziller, M. P. Hendrich, A. S. Borovik, *J. Am. Chem. Soc*. **2008**, *130*, 8888–8889.
83. M. S. Seo, J. Y. Kim, J. Annaraj, Y. Kim, Y.–M. Lee, S.–J. Kim, J. Kim, W. Nam, *Angew. Chem. Int. Ed.* **2007**, *46*, 377–380.
84. R. A. Geiger, S. Chattopadhyay, V. W. Day, T. A. Jackson, *Dalton Trans.* **2011**, *40*, 1707–1715.
85. R. B. VanAtta, C. E. Strouse, L. K. Hanson, J. S. Valentine, *J. Am. Chem. Soc*. **1987**, *109*, 1425–1434.
86. R. A. Geiger, S. Chattopadhyay, V. W. Day, T. A. Jackson, *J. Am. Chem. Soc.* **2010**, *132*, 2821–2831.
87. R. L. Shook, W. A. Gunderson, J. Greaves, J. W. Ziller, M. P. Hendrich, A. S. Borovik, *J. Am. Chem. Soc*. **2008**, *130*, 8888–8889.
88. S. E. Ghachtouli, H. Y. V. Ching, B. Lassalle-Kaiser, R. Guillot, D. F. Leto, S. Chattopadhyay, T. A. Jackson, P. Dorlet, E. Anxolabéhére–Mallart, *Chem. Commun.* **2013**, *49*, 5696–5698.
89. W. Nam, *Acc. Chem. Res*. **2007**, *40*, 522 – 531.
90. M. K. Coggins, J. A. Kovacs, *J. Am. Chem. Soc.* **2011**, *133*, 12470 – 12473.
91. M. K. Coggins, V. Martin-Diaconescu, S. DeBeer, J. A. Kovacs, *J. Am. Chem. Soc.* **2013**, *135*, 4260 – 4272.
92. H. E. Colmer, A. W. Howcroft, T. A. Jackson, *Inorg. Chem.* **2016**, *55*, 2055−2069.
93. J. Cho, R. Sarangi, W. Nam, *Acc. Chem. Res.* **2012**, *45*, 1321− 1330.
94. Q. Zhang, A. Bell-Taylor, F. M. Bronston, J. D. Gorden, C. R. Goldsmith, *Inorg. Chem.* **2017**, *56*, 773−782.
95. J. Annaraj, J. Cho, Y.-M. Lee, S. Y. Kim, R. Latifi, S. P. de Visser, W. Nam, *Angew. Chem. Int. Ed.* **2009**, *48*, 4150−4153.
96. D. A. Proshlyakov, T. F. Henshaw, G. R. Monterosso, M. J. Ryle, R. P. Hausinger, *J. Am. Chem. Soc.* **2004**, *126*, 1022−1023.

97. C. A. Grapperhaus, B. Mienert, E. Bill, T. Weyhermtiller, K. Wieghardt, *Inorg. Chem*. **2000**, *39*, 5306−5317.

98. J.-U. Rohde, J.-H. In, M. H. Lim, W. W. Brennessel, M. R. Bukowski, A. Stubna, E. Münck, W. Nam, L. Que, Jr., *Science* **2003**, *299*, 1037−1039.

99. M. H. Lim, J.-U. Rohde, A. Stubna, M. R. Bukowski, M. Costas, R. Y. N. Ho, E. Münck, W. Nam, L. Que, Jr., *Proc. Natl. Acad. Sci. USA.* **2003**, *100*, 3665−3670.

100. J. Kaizer, E. J. Klinker, N. Y. Oh, J.-U. Rohde, W. J. Song, A. Stubna, J. Kim, W. Nam, E. Münck, L. Que, Jr., *J. Am. Chem. Soc.* **2004**, *126*, 472-473.

101. V. Balland, M.-F. Chariot, F. Banse, J.-J. Girerd, T. A. Mattioli, E. Bill, J.-F. Bartoli, P. Battioni, D. Mansuy, *Eur. J. Inorg. Chem.* **2004**, 301-308.

102. J.-U. Rohde, L. Que, Jr., *Angew. Chem. Int. Ed.* **2005**, *44*, 2255-2258.

103. J. T. Groves, J. T. In *Cytochrome P450: Structure, Mechanism, and Biochemistry*; 3rd ed.; Ortiz de Montellano, P. R., Ed.; Plenum Publishers: New York, **2005**, p 1-43.

104. J. T. Groves, T. E. Nemo, R. S. Myers, *J. Am. Chem. Soc.* **1979**, *101*, 1032–1033.

105. B. Meunier, *Chem. Rev.* **1992**, *92*, 1411–1456.

106. R. A. Leising, R. E. Norman, L. Que, Jr., *Inorg. Chem.* **1990**, *29*, 2553–2555.

107. R. A. Leising, B. A. Brennan, L. Que, Jr., B. G. Fox, E. Münck, *J. Am. Chem. Soc.* **1991**, *113*, 3988–3990.

108. T. Kojima, R. A. Leising, S. Yan, L. Que, Jr., *J. Am. Chem. Soc.* **1993**, *115*, 11328–11335.

109. R. A. Leising, J. Kim, M. A. Pérez, L. Que, Jr., *J. Am. Chem. Soc.* **1993**, *115*, 9524–9530.

110. Y. Hitomi, S. Furukawa, M. Higuchi, T. Shishido, T. Tanaka, *J. Mol. Catal. A: Chem.* **2008**, *288*, 83–86.

111. H. Jaafar, B. Vileno, A. Thibon, D. Mandon, *Dalton Trans.* **2011**, *40*, 92–106.

112. A. Mairata i Payeras, R. Y. N. Ho, M. Fujita, L. Que, Jr., *Chem. –Eur. J.* **2004**, *10*, 4944–4953.

113. M. Klopstra, G. Roelfes, R. Hage, R. M. Kellogg, B. L. Feringa, *Eur. J. Inorg. Chem*. **2004**, 846–856.

114. C. A. Grapperhaus, B. Mienert, E. Bill, T. Weyhermüller, K. Wieghardt, *Inorg. Chem.* **2000**, *39*, 5306-5317.

115. C. V. Sastri, J. Lee, K. Oh, Y. J. Lee, J. Lee, T. A. Jackson, K. Ray, H. Hirao, W. Shin, J. A. Halfen, J. Kim, L. Que, Jr., S. Shaik, W. Nam, *Proc. Natl. Acad. Sci.* **2007**, *104*, 19181-19186.

116. S. A. Wilson, J. Chen, S. Hong, Y.-M. Lee, M. Clémancey, R. Garcia-Serres, T. Nomura, T. Ogura, J.-M. Latour, B. Hedman, K. O. Hodgson, W. Nam, E. I. Solomon, *J. Am. Chem. Soc.* **2012**, *134*, 11791−11806.

117. M. H. Lim, J.–U. Rohde, A. Stubna, M. R. Bukowski, M. Costas, R. Y. N. Ho, E. Münck, W. Nam, L. Que, Jr., *Proc. Natl. Acad. Sci. USA.* **2003**, *100*, 3665–3670.

118. M. R. Bukowski, K. D. Koehntop, A. Stubna, E. L. Bominaar, J. A. Halfen, E. Münck, W. Nam, L. Que, Jr., *Science* **2005**, *310*, 1000–1002.

119. J. Kaizer, M. Costas and L. Que, Jr., *Angew. Chem. Int. Ed.* **2003**, *42*, 3671–3673.

120. M. Martinho, F. Banse, J.–F. Bartoli, T. A. Mattioli, P. Battioni, O. Horner, S. Bourcier, J.–J. Girerd, *Inorg. Chem*. **2005**, *44*, 9592–9596.

121. T. K. Paine, M. Costas, J. Kaizer, L. Que, Jr., *J. Biol. Inorg. Chem.* **2006**, *11*, 272–276.

122. O. Pestovsky, S. Stoian, E. Bominaar, X. Shan, E. Münck, L. Que, Jr., A. Bakac, *Angew. Chem. Int. Ed.* **2005**, *44*, 6871–6874.

123. C. V. Sastri, M. S. Seo, M. J. Park, K. M. Kim, W. Nam, *Chem. Commun.* **2005**, 1405–1407.

124. J. Bautz, M. R. Bukowski, M. Kerscher, A. Stubna, P. Comba, A. Lienke, E. Münck, L. Que, Jr., *Angew. Chem. Int. Ed*. **2006**, *45*, 5681–5684.
125. J. England, Y. Guo, E. R. Farquhar, V. G. Young Jr., E. Münck, L. Que, Jr., *J. Am. Chem. Soc.* **2010**, *132*, 8635–8644.
126. M. S. Seo, N. H. Kim, K.-B. Cho, J. E. So, S. K. Park, M. Clémancey, R. G. Serres, J.-M. Latour, S. Shaik, W. Nam, *Chem. Sci.* **2011**, *2*, 1039–1045.
127. D. Janardanan, Y. Wang, P. Schyman, L. Que, Jr., S. Shaik, *Angew. Chem. Int. Ed.* **2010**, *49*, 3342 –3345.
128. A. N. Biswas, M. Puri, K. K. Meier, W. N. Oloo, G. T. Rohde, E. L. Bominaar, E. Münck, L. Que, Jr., *J. Am. Chem. Soc.* **2015**, *137*, 2428–2431.
129. C. E. Macbeth, A. P. Golombek, V. G. Young Jr, C. Yang, K. Kuczera, M. P. Hendrich, A. S. Borovik, *Science*, **2000**, *289*, 938–941.
130. J. England, M. Martinho, E. R. Farquhar, J. R. Frisch, E. L. Bominaar, E. Münck, L. Que, Jr., *Angew. Chem. Int. Ed.* **2009**, *48*, 3622–3626.
131. J. P. Bigi, W. H. Harman, B. Lassalle-Kaiser, D. M. Robles, T. A. Stich, J. Yano, R. D. Britt, C. J. Chang, *J. Am. Chem. Soc.* **2012**, *134*, 1536–1542.
132. F. Tiago de Oliveira, A. Chanda, D. Banerjee, X. Shan, S. Mondal, L. Que, Jr., E. Bominaar, E. Münck, T. J. Collins, *Science*, **2007**, *315*, 835–838.
133. T. J. Collins, A. D. Ryabov, *Chem. Rev.* **2017**, *117*, 9140-9162.
134. S. Hong, Y.-M. Lee, K.-B. Cho, K. Sundaravel, J. Cho, M. J. Kim, W. Shin, W. Nam, *J. Am. Chem. Soc.* **2011**, *133*, 11876−11879.
135. H. Hirao, L. Que, Jr., W. Nam, S. Shaik, *Chem. - Eur. J.* **2008**, *14*, 1740−1756.
136. S. Fukuzumi, Y. Morimoto, Y. Kotani, P. Naumov, Y.-M. Lee, W. Nam, *Nat. Chem.* **2010**, *2*, 756−759.
137. J. Park, Y. Morimoto, Y.-M. Lee, W. Nam, S. Fukuzumi, *J. Am. Chem. Soc.* **2011**, *133*, 5236−5239.

138. J. Park, Y. Morimoto, Y.-M. Lee, Y. You, W. Nam, S. Fukuzumi, *Inorg. Chem.* **2011**, *50*, 11612−11622.

139. J. Park, Y. Morimoto, Y.-M. Lee, W. Nam, S. Fukuzumi, *J. Am. Chem. Soc*. **2012**, *134*, 3903−3911.

140. T. A. Betley, J. C. Peters. *J. Am. Chem. Soc.* **2004**, *126*, 6252–6254.

141. N. Aliaga-Alcalde, S. D. George, B. Mienert, E. Bill, K. Wieghardt, F. Neese. *Angew. Chem. Int. Ed.* **2005**, *44*, 2908–2912.

142. J. F. Berry, E. Bill, E. Bothe, S. D. George, B. Mienert, F. Neese, K. Wieghardt, *Science* **2006**, *312*, 1937-1941.

143. J. –U. Rohde, T. A. Betley, T. A. Jackson, C. T. Saouma, J. C. Peters L. Que Jr., *Inorg. Chem.* **1999**, *38*, 1929–1936.

144. A. K. Verma, T. N. Nazif, C. Achim, S. C. Lee, *J. Am. Chem. Soc.* **2000**, *122*, 11013–11014.

145. C. M. Thomas, N. P. Mankad, J. C. Peters, *J. Am. Chem. Soc.* **2006**, *128*, 4956–4957.

146. J. F. Berry, E. Bill, E. Bothe, S. D. George, B. Mienert, F. Neese, K. Wieghardt, *Science* **2006**, *312*, 1937–1941.

147. P. Comba, C. Lang, C. Lopez de Laorden, A. Muruganatham, G. Rajaraman, H. Wadepohl, M. Zajaczkowski, *Chem. Eur. J*. **2008**, *14,* 5313–5328.

148. K. L. Klotz, L. M. Slominski, M. E. Riemer, J. A. Phillips, J. A. Halfen, *Inorg. Chem.* **2009**, *48*, 801–803.

149. J. J. Scepaniak, J. A. Young, R. P. Bontchev, J. M. Smith, *Angew. Chem. Int. Ed*. **2009**, *48*, 3158–3160.

150. P. Leeladee, G. N. L. Jameson, M. A. Siegler, D. Kumar, S. P. de Visser, D. P. Goldberg, *Inorg. Chem*. **2013**, *52,* 4668–4682.

151. M. J. Zdilla, M. M. Abu-Omar, *J. Am. Chem. Soc*. **2006**, *128,* 16971-16979.

152. S. Kundu, E. Miceli, E. Farquhar, F. F. Pfaff, U. Kuhlmann, P. Hildebrandt, B. Braun, C. Greco, K. Ray, *J. Am. Chem. Soc.* **2012**, *134*, 14710−14713.
153. J. W. W. Chang, P. W. H. Chan, *Angew. Chem. Int. Ed.* **2008**, *47,* 1138–1140.
154. E. T. Hennessy, T. A. Betley, *Science* **2013**, *340,* 591–595.
155. A. K. Vardhaman, P. Barman, S. Kumar, C. V. Sastri, D. Kumar and S. P. de visser, *Angew. Chem. Int. Ed.* **2013**, *52,* 12288–12292.

CHAPTER – II

Synthesis and Characterization,

Materials Employed and Methods Adapted

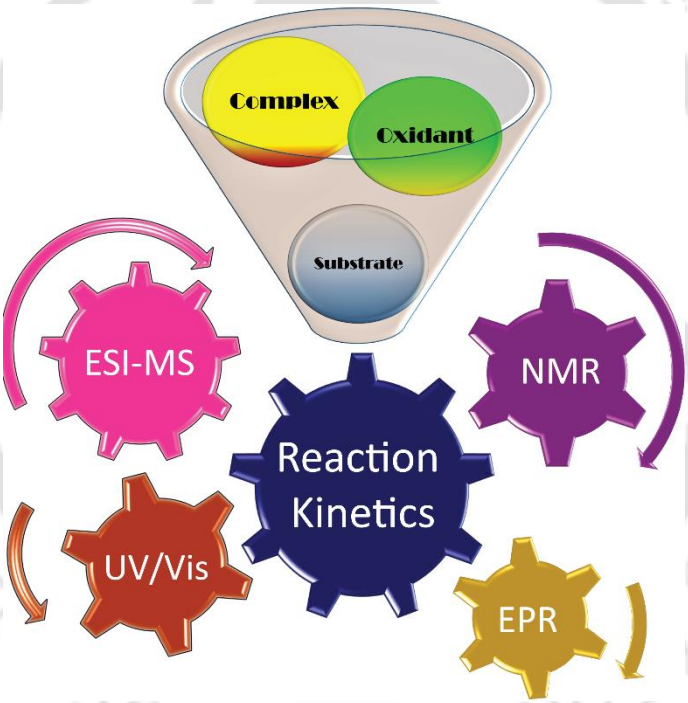

2.1. Introduction

This chapter represents a list of materials introduced at different stages of their investigation. The synthesis of these materials requires some well-designed experimental procedures and vigilant observations. A thorough analysis of each work results in a set of tasks like the synthesis of the ligands, synthesis of the oxidants and commercially unavailable substrates, synthesis of the metal complexes, generation and stabilization of the metal intermediates, optimization of the reaction conditions, kinetic study, product analysis and finally interpretation and evaluation of the obtained results.

Precautions and safety measures were followed before every experiment. Also, accurate experimental results require careful analysis of the purity of the chemicals. Procedures followed for the purification, synthesis, spectroscopic characterization and instrumentation are discussed in detail below.

2.2. Experimental Section

2.2.1. Solvents

Solvents were dried following published procedures[1] and distilled under argon before use. Acetonitrile (CH_3CN) was dried over Calcium hydride powder (CaH_2) for 48 hours in a solvent still-head distillation apparatus fitted with a condenser on a heating mantle. Other solvents like Tetrahydrofuran (THF) and diethyl ether were dried using a similar setup and were dried over sodium using benzophenone as an indicator. Solvents were collected from the solvent still-head distillation apparatus into dry glassware through a cannula using vacuum pumps. Glassware were extensively dried using either flame or kept inside a hot oven for a prolonged period before use.

2.2.2. Oxidants

Generation of the different types of reaction intermediates requires different types of oxidants such as iodosylbenzene (PhIO), (Diacetoxyiodo)benzene ($PhI(OAc)_2$), peracetic acid, oxone, CAN, hydrogen peroxide, sodium chlorite, *N*-tosyliminophenyliodinane (PhINTs), *tert*-butyl hydroperoxide, potassium superoxide, etc. that react with the metal complexes. Some of the oxidants were purchased commercially whereas some of them were synthesized by following previously reported procedures. The commercially available oxidants were $PhI(OAc)_2$ (Aldrich Chemical Company) and hydrogen peroxide (H_2O_2) (Merck). The synthesized oxidants were PhIO and PhINTs.

- *Synthesis of Iodosylbenzene (PhIO)*:

Iodosylbenzene was prepared by following a literature procedure.[2] 32.2 g (100 mM) of finely grounded (iodosobenzene)diacetate was taken in a 250 mL beaker, then 150 mL of NaOH solution (3 N) was added slowly over 5 minutes with vigorous stirring. Then the lumps formed were ground thoroughly for 15 minutes with a glass rod and spatula, and the reaction mixture was allowed to stir for another 45 minutes for the completion of the reaction. Then 100 mL of water was added to the reaction mixture, stirred vigorously and filtered through a Büchner funnel. The crude solid iodosylbenzene was collected and returned to the beaker and triturated in 200 mL water. The solid was again collected by Büchner funnel, washed with 200 mL of water and dried over the vacuum. Finally, it was triturated with 75 mL of chloroform in a beaker to remove any unreacted starting material, filtered, dried over a vacuum and stored in a cold and dark place.

- *Synthesis of N-tosyliminophenyliodinane (PhINTs)*:

PhINTs was prepared by following a literature method.[3] 3.20 g (10 mmol) (Diacetoxyiodo)benzene was added to the mixture of *para*-toluenesulonamide and potassium hydroxide in methanol at below 10 ºC under stirring condition. The resulting yellow-colored solution was allowed to stir for 3 hours at room temperature. Then the reaction mixture was poured into water to get yellow colored solid, which was recrystallized from methanol to afford crystalline *N*-tosyliminophenyliodinane.

50 % H_2O_2 was purchased from Merck-India.

2.2.3. Substrates

Almost all the chemicals were purchased from Sigma-Aldrich Chemical Co., were in the best available purity and were used without further purification unless otherwise indicated . Thioanisole (THA) and its *para*-X-derivatives (X = -OMe, -Me, -Cl), benzyl alcohol and its *para*-X-derivatives (X = -OMe, -Me, -Cl), xanthene, fluorene, 2,4,6-trifluorophenol (2,4,6-TFP), 2,4,6-trichlorophenol (2,4,6-TCP), 2,4,6-tribromophenol (2,4,6-TBP), 2,6-difluorophenol (2,6-DFP), 2,6-dichlorophenol (2,6-DCP), 2,6-dibromophenol (2,6-DBP), 4-fluorophenol (4-FP), 4-chlorophenol (4-CP) and 4-bromophenol (4-BP) were purchased from Aldrich Chemical company. Triphenylmethane was purchased from Avra Synthesis Pvt. Ltd. and 9,10-Dihydroanthracene (DHA), was obtained from TCI Chemicals Pvt. Ltd. Cyclohexanecarboxaldehye (CCA) was purchased from Alfa Aesar by Thermo Fisher Scientific Pvt. Ltd. α-[D_1]-cyclohexanecarboxaldehye (~ 90 %, D enriched) was purchased from RVL Scientific & Engineering Pvt. Ltd. (Lucknow, India). Benzyl alcohol-D7 was purchased from Cambridge Isotope Laboratories, Inc. Other deuterated

solvents like $CDCl_3$, CD_3CN, D_2O, DMSO-D6 and CD_3OD were bought from Aldrich Chemical Company.

The deuterated substrate of halophenols were prepared by using reported procedure.[4] Halophenol substarte (100 mg) was dissolved in DMSO-d_6 (3 mL) solvent along with NaH (1.1 equiv.) under an inert atmosphere. The colourless solution was stirred at room temperature for overnight, and the reaction mixture was quenched with D_2O (5 mL). The product was extracted with CH_2Cl_2 and dried in vacuum. ^{1}H-NMR confirmed >99% deuteration. All other substrates used in this thesis were prepared by following reported procedures in good yields.

Scheme 2.1. Synthesis of 1,2-D_2-cyclohexanecarboxaldehyde (1,2-[D_2]-CCA).

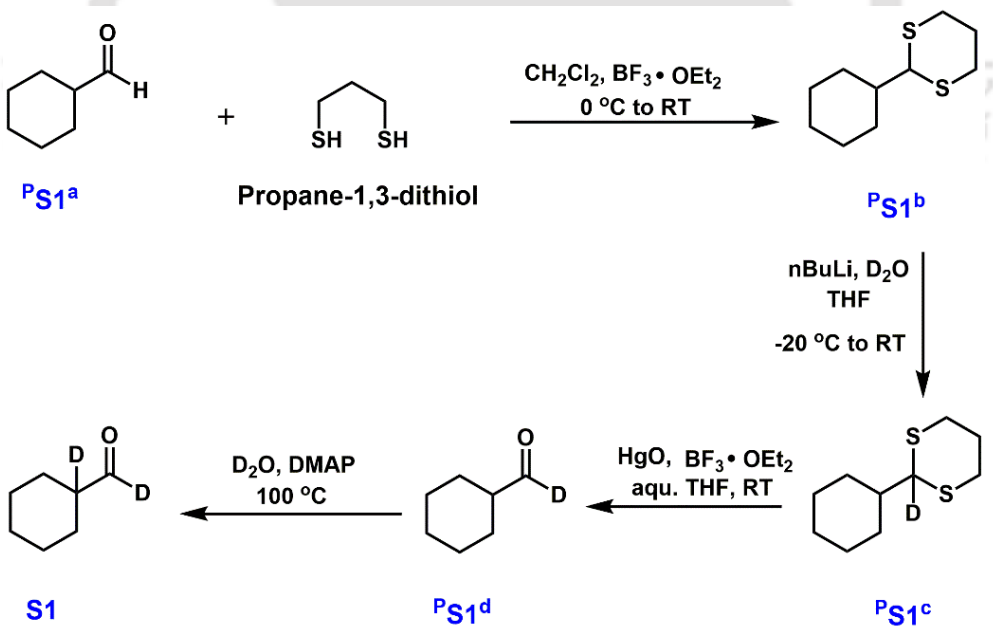

- *Synthesis of 1,2-D_2-cyclohexanecarboxaldehyde (1,2-D_2-CCA)* :

The synthesis of 1,2-[D_2]-cyclohexanecarboxaldehyde was synthesized following a reported procedure.[5]

Synthesis of $^{P}S1^{b}$: To a solution of cyclohexanecarboxaldehyde ($^{P}S1^{a}$) (30 mmol) and propane-1,3-dithiol (30 mmol) in dichloromethane, BF_3•OEt_2 (15 mmol) was added dropwise at 0 °C. Then the reaction was allowed to stir for 30 minutes at the same temperature and was warmed to room temperature for another 30 minutes with continuous stirring. After the completion of the reaction, the reaction mixture was washed with brine (50 mL), 5% $NaHCO_3$ (50 mL), and brine (50 mL) successively. The organic layer was dried over Na_2SO_4 and the solvent was removed under reduced pressure using a rotary evaporator to give the crude product. It was then recrystallized from cold hexane to get pure product 2-Cyclohexyl-1,3-dithiane as a white solid (5.5 g, 27.2 mmol, 90% yield).

Synthesis of $^{P}S1^{c}$: To a solution of 2-cyclohexyl-1,3-dithiane (20 mmol) in dry THF (100 mL), nBuLi (26 mmol) was added dropwise at –20 °C. The reaction mixture was then warmed slowly to room temperature for 4 h. Then it was again cooled to –20 °C, D_2O (8 mL) was added slowly and the mixture was slowly warmed to room temperature. The reaction mixture was then concentrated under reduced pressure using a rotary evaporator, and the residue was diluted with CH_2Cl_2 (50 mL). It was then washed with brine (80 mL) and dried over Na_2SO_4. The removal of the solvent under reduced pressure gave the crude product. It was then recrystallized from cold hexane to afford the pure product 2-Cyclohexyl-2-deuteryl-1,3-dithiane as a white solid (3.6 g, 17.88 mmol, 91% yield).

Synthesis of $^{P}S1^{d}$: To a suspension of mercury (II) oxide (33.2 mmol) and BF_3•OEt_2 (33.2 mmol) in 15% aq. THF (40 mL), a solution of 2-cyclohexyl-2-deuteryl-1,3-dithiane (16.6 mmol) was added dropwise in a minimum amount of THF *via* a

dropping funnel within 15 minutes. The red mercury (II) oxide gradually dissolved during this period and a white precipitate appeared. After 2 hours, 100 mL of ether was added to the reaction mixture and the precipitated salts were filtered. Then the ether layer was washed with saturated $NaHCO_3$ solution (80 mL) and brine (80 mL). After drying over anhydrous Na_2SO_4, ether was evaporated under a vacuum to give crude aldehyde. The crude product was then purified by vacuum distillation to obtain 1-Deuterio-cyclohexanecarbaldehyde (α-[D_1]-CCA) as a clear colorless oil (620 mg, 5.4 mmol, 33% yield).

Synthesis of S1 : To a solution of 1-Deuterio-cyclohexanecarbaldehyde (4 mmol) in D_2O (0.25 mL), DMAP (0.4 mmol) was added and the reaction mixture was heated to reflux for 4 h. The reaction mixture was allowed to cool to room temperature and was diluted with CH_2Cl_2 (20 mL). The organic layer was then washed with 1M HCl (20 mL), saturated $NaHCO_3$ (20 mL) and brine (20 mL) successively. After drying over anhydrous Na_2SO_4, the solvent was removed under reduced pressure to give a crude product. Then the crude product was purified by vacuum distillation using Kugelrohr Distillation apparatus to yield 1,2-Di-deuterio-cyclohexanecarbaldehyde (1,2-[D_2]-CCA) as a clear colorless oil (340 mg, 2.98 mmol, 75% yield). The purity was confirmed using ^{1}H-NMR spectroscopy to ensure 97% D-incorporation at the aldehyde-H. A comparative ^{1}H-NMR spectra of CCA, α-[D_1]-CCA and 1,2-[D_2]-CCA is shown below (see Fig. 2.1, 2.2, 2.3).

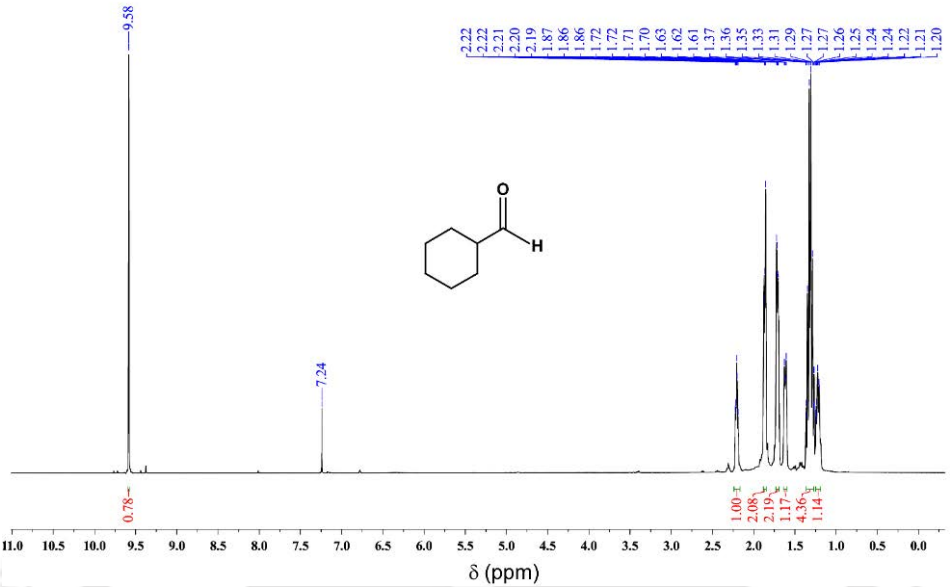

Fig. 2.1. ^{1}H NMR (600 MHz) spectrum of CCA in $CDCl_3$ at 298 K.

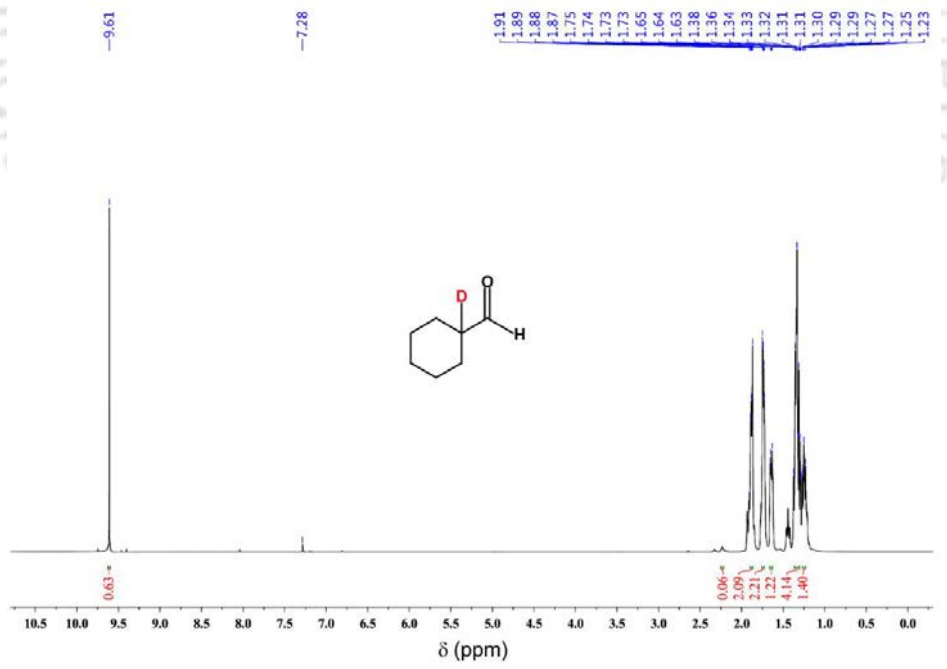

Fig. 2.2. ^{1}H NMR (600 MHz) spectrum of α-[D_1]-CCA in $CDCl_3$ at 298 K.

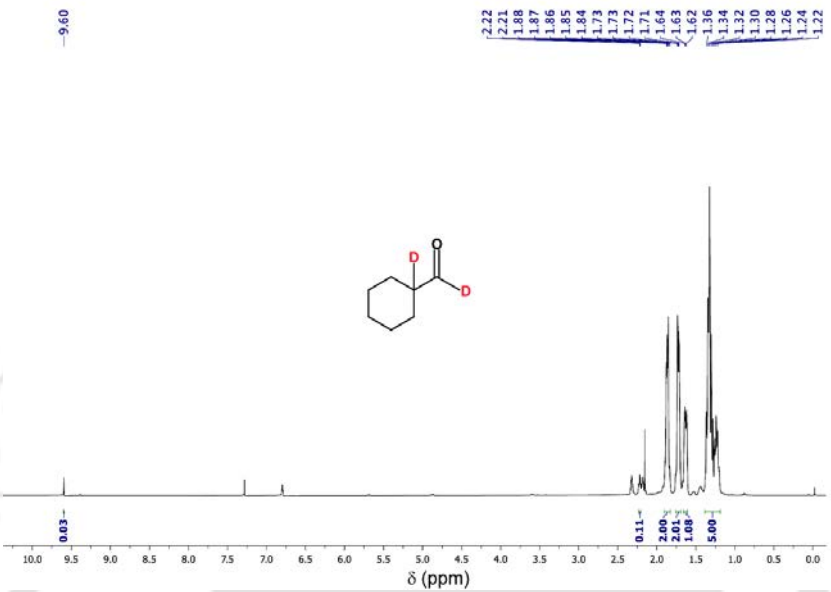

Fig. 2.3. ^{1}H NMR (600 MHz) spectrum of 1,2-[D_2]-CCA in $CDCl_3$ at 298 K.

2.2.4. Ligands

Scheme 2.2. Ligand systems used and discussed throughout.

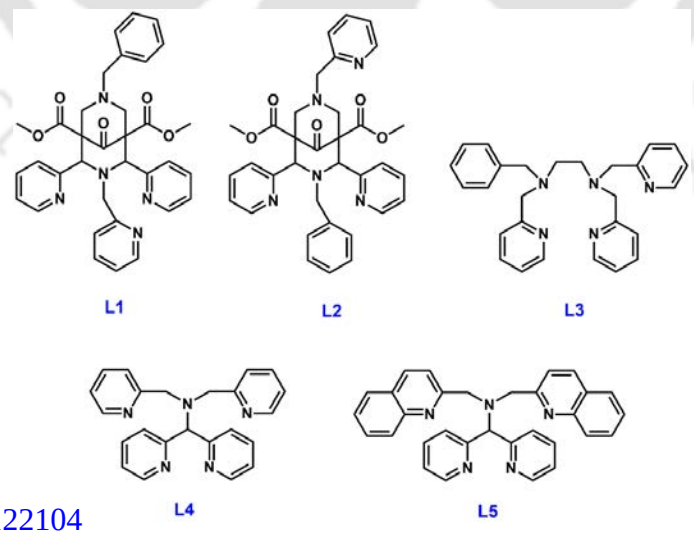

- *Synthesis of the ligand L1 and L2* :

The bispidine ligands L1 and L2 were synthesized by following the reported procedures.[6-9]

General Procedure for the Synthesis of $^{P}L1$ and $^{P}L2$: Dimethylacetone dicarboxylate (7.35 mL, 50 mM) was taken in a round-bottomed flask containing 20 mL CH_3OH and was pre-cooled to 0 °C in an ice bath. Subsequently pyridine-2-carboxaldehyde (9.51 mL, 100 mM) and 50 mM of picolyl amine (for $^{P}L1$) / benzyl amine (for $^{P}L2$) were slowly added to the cold solution. After adding amine, the resulting solution was allowed to come to room temperature slowly and left to stir for overnight. An off-white thick precipitate formed was filtered and washed with cold ethanol several times and dried in vacuum. The product was then recrystallized from warm ethanol to afford colourless crystals in stoichiometric yields (84% for $^{P}L1$ and 80% for $^{P}L2$).

Scheme 2.3. Synthesis of ligand L1.

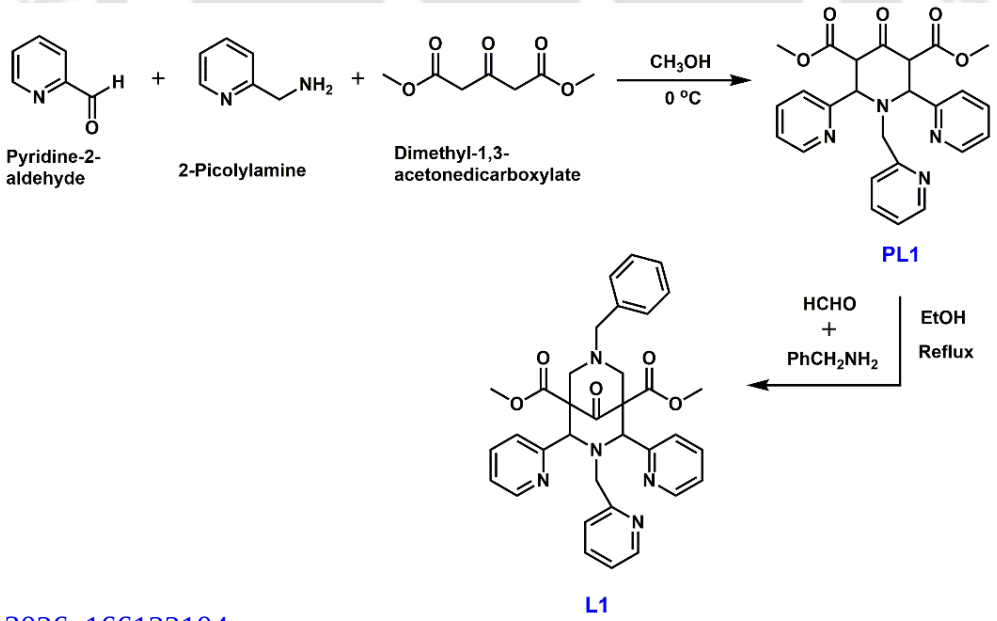

Scheme 2.4. Synthesis of ligand L2.

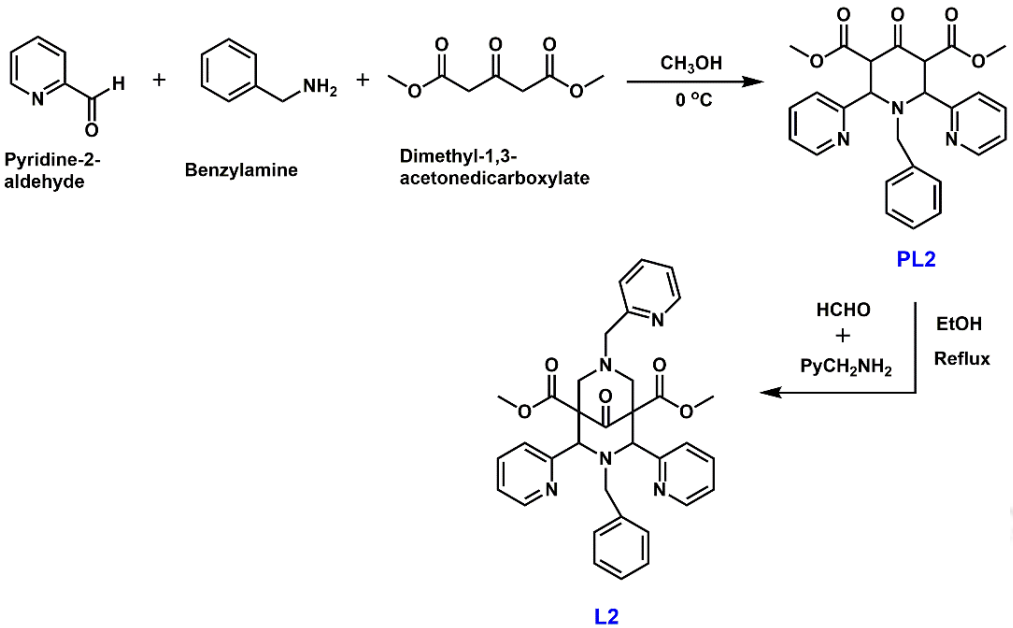

General Procedure for the Synthesis of L1, and L2: To the suspension of the piperidone (^{P}L1, or ^{P}L2) (36 mM) in 200 mL ethanol, formaldehyde (37%, 7.3 mL, 90 mM) and 40 mM of benzyl amine (for L1) / picolyl amine (for L2) were added in a dropwise manner. The reaction mixture was refluxed for 4 hours. The resulting brown/yellow solution obtained after completion of the reaction was then concentrated under vacuum and layered with diethyl ether and kept in fridge at -20 °C for slow diffusion. White crystalline products were obtained after a few days (see Scheme 2.3 and 2.4).

- *Synthesis of the ligand Bn-tpen (L3)* :

The ligand L3, N-benzyl-N, N', N'-tris(2-pyridylmethyl)ethane-1,2-diamine (Bn-Tpen) was synthesized by following a reported proceure.[10]

To a solution of 2-(chloromethyl) pyridine hydrochloride (6.55 g, 40 mmol) in water (20 mL), was added a solution of N-benzylethylenediamine (2.0 g, 13.3 mmol) in CH_2Cl_2 (20 mL). NaOH (3.2 g, 80 mmol) in water (10 mL) was added in small portions over a period of 5 days, keeping the reaction under an argon atmosphere. The reaction mixture was extracted with methylene chloride (3 × 25 mL). The combined organic phases were dried over MgSO4 and concentrated in vacuum to afford a white solid. It was purified by extraction in a Soxhlet apparatus using low boiling petroleum (see Scheme 2.5).

Scheme 2.5. Synthesis of ligand L3.

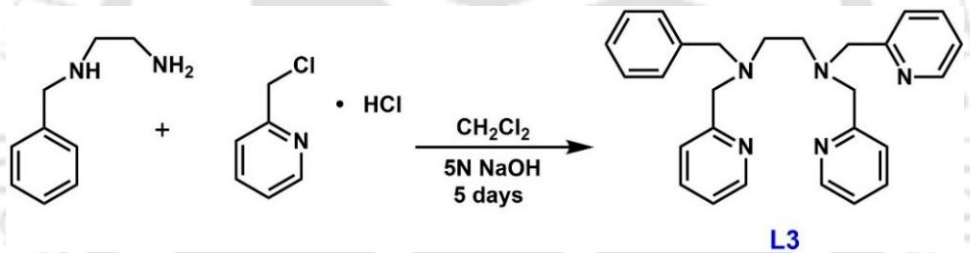

- *Synthesis of the ligand N4Py (L4)* :

N,N-bis(2-pyridylmethyl)-N-bis(2-pyridyl)methylamine (L4) was synthesized following a reported procedure.[11]

Synthesis of $^{P}L1^{b}$: Di(2-pyridyl) ketone ($^{P}L1^{a}$) (27 mM, 5 g), hydroxylamine hydrochloride (60 mM, 4.17 g) and ethanol (10 mL) were taken in a 100 mL round-bottomed flask which contained NaOH (4 g) and 20 mL of water. The reaction mixture was refluxed for 3 - 4 hours. The excess ethanol was evaporated in vacuum and the solution was diluted by pouring it to 1 L of water. Then the resulting solution was neutralized (pH = 7) with dilute HCl properly. A pinkish-white precipitate of Di-2-pyridyl ketone oxime was appeared, and the precipitate was filtered off and dried for a day.

Synthesis of $^{P}L1^{c}$: The Di-2-pyridyl ketone oxime formed was taken in a three-necked round-bottomed flask (500 mL) in ethanol (90 mL) and was fitted with a reflux condenser. Hydrazine hydrate (60 mL) and Zn powder were added to this solution in conjugative steps over 6 hours. Then the solution was allowed to reflux for overnight. The reduced product obtained was dissolved in 5N NaOH solution (40 mL). The resulting alkaline solution was extracted with ethyl acetate (3 x 200 mL) to obtain di(pyridin-2-yl)methanamine as sticky solid.

Synthesis of L4 : Di(pyridin-2-yl)methanamine obtained was taken in a 250 mL round-bottomed flask containing an alkaline NaOH solution (5N, 50 mL). To this solution, 2-(Chloromethyl)pyridine hydrochloride (2.2 equivalents) was added and the solution was refluxed for two days. A brown solution obtained was neutralized by $HClO_4$ to afford the desired solid compound (yield: 3.1 g) (see Scheme 2.6).

- *Synthesis of the ligand 2PyN2Q / L5* :

Synthesis of 1,1-di(pyridin-2-yl)-*N*,*N*-bis(quinolin-2-ylmethyl)methanamine (L5) was done by a slight modification from the reported procedure.[12]

$^{P}L5^{b}$ and $^{P}L5^{c}$ are the same compounds as $^{P}L4^{b}$ and $^{P}L4^{c}$.

Synthesis of L5 : 2.2 equivalents of 2-(Chloromethyl)quinoline hydrochloride was added to $^{P}L5^{c}$ taken in 50 mL alkaline solution. The reaction mixture was allowed to stir for 10 days at room temperature. Upon continuous stirring a brown solid was appeared and was extracted with ethyl acetate (3 x 200 mL). Then the organic phase was washed with brine and evaporated under vacuum to afford the desired ligand in good yield (yield 6.6 g) (see Scheme 2.6).

Scheme 2.6. Synthesis of ligands L4 and L5.

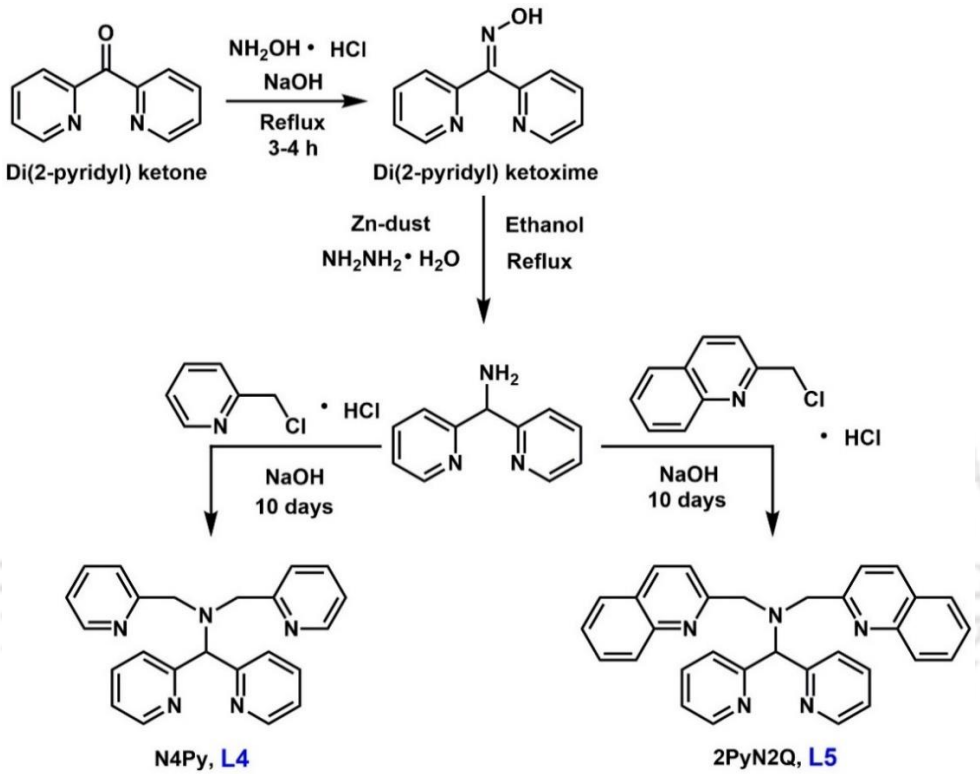

^{1}H NMR (600 MHz, $CDCl_3$): δ 4.20 (s, 4H, CH_2), 5.43 (s, 1H, CH), 7.14-8.04 (m, 18H), 8.58 (dd, 2H). ^{13}C NMR (150 MHz, $CDCl_3$): δ 58.25, 72.37, 121.30, 122.20, 124.33, 126.01, 127.22, 127.39, 128.99, 129.25, 136.14, 136.36, 147.51, 149.32, 159.88, 160.47. (see Fig. 2.4, 2.5; solvent peaks are denoted by *).

NMR Characterization of L5.

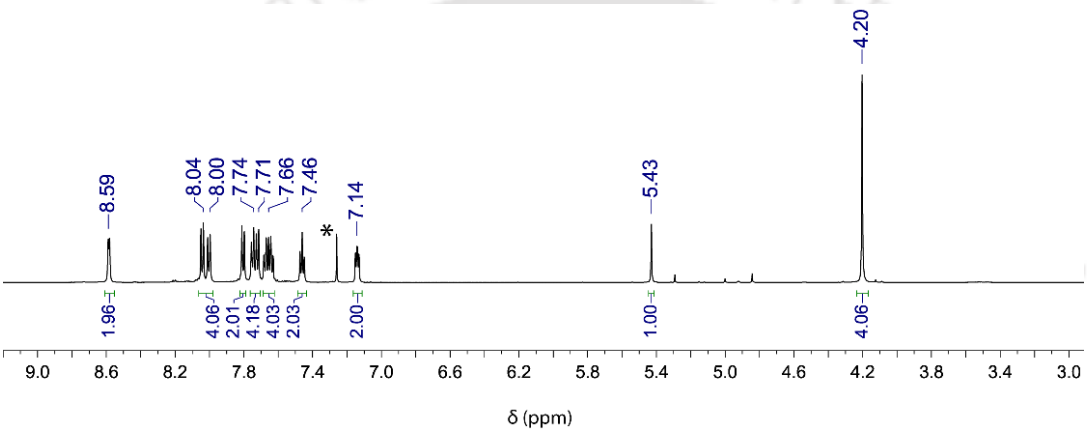

Fig. 2.4. ^{1}H NMR (600 MHz) spectrum of ligand L5 in $CDCl_3$.

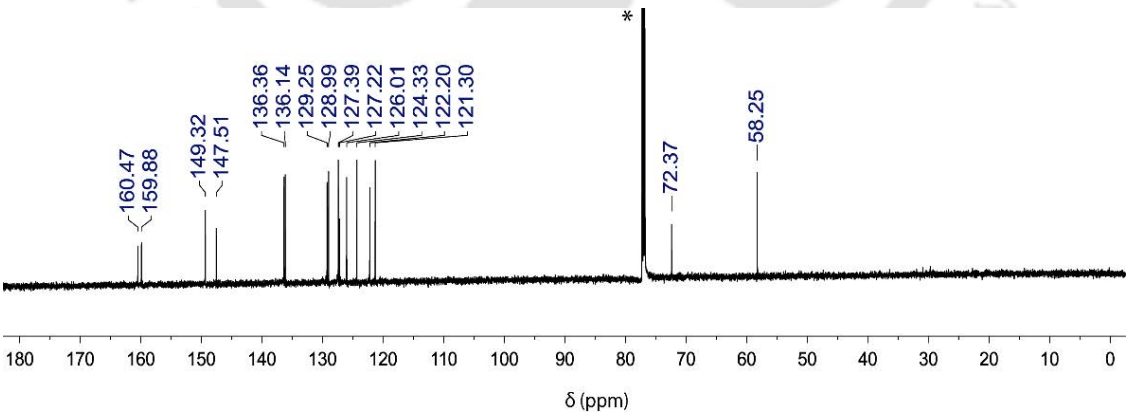

Fig. 2.5. ^{13}C NMR (150 MHz) spectrum of ligand L5 in $CDCl_3$.

2.2.5. Metal Complexes

- *General Procedure for the synthesis of the Mn(II)-complexes.*

Bispidine ligands L1 and L2 (100 mg) were dissolved in CH_3CN and $Mn^{II}(ClO_4)_2$ salt (1.2 equivalents) in CH_3CN was added dropwise under inert conditions. The pale yellow solution was allowed to reflux overnight. After the completion of the reaction, the solution was filtered using 0.2 μm PTFE syringe filters and layered with diethyl ether to obtain colourless crystalline products (See Table 2.1).

- *General Procedure for the synthesis of the Fe(II)-complexes.*

The ferrous complexes were synthesized using the following general procedure. 100 mg ligand was taken in a glass vial and dissolved in CH_3CN / CH_2Cl_2 (3 mL) inside a glove box filled with Argon. To this solution was added 1.2 equivalents of Fe(II)-salts (triflates, perchlorates or tetrafluoroborates) in CH_3CN / CH_2Cl_2 (2 mL) and stirred overnight to ensure complete metalation. The resulting solution was filtered using 0.2 μm PTFE syringe filters and crystallized by slow vapour diffusion of diethyl ether into a CH_3CN solution and stored at -40 ˚C. The complexes obtained were washed with diethyl ether and dried under vacuum to obtain the desired metal complexes (See Table 2.1).

Table 2.1. Synthetic parameters and characteristics of metal complexes.

Complex	Ligand	Metal Salt	Solvent	Colour	Texture	Yield
$Mn^{II}(L1)(ClO_4)_2$ (**1a**)	L1	$Mn^{II}(CH_3CN)_2(ClO_4)_2$	CH_3CN	Colourless	Crystalline	91%
$Mn^{II}(L2)(ClO_4)_2$ (**2a**)	L2	$Mn^{II}(CH_3CN)_2(ClO_4)_2$	CH_3CN	Colourless	Crystalline	85%
$Fe^{II}(L3)(OTf)_2$ (**3a**)	L3	$Fe^{II}(CH_3CN)_2(OTf)_2$	CH_3CN/ CH_2Cl_2	Yellow red	Crystalline	92%
$Fe^{II}(L4)(OTf)_2$ (**4a**)	L4	$Fe^{II}(CH_3CN)_2(OTf)_2$	CH_3CN	Dark red	Crystalline	91%
$Fe^{II}(L5)(OTf)_2$ (**5a**)	L5	$Fe^{II}(CH_3CN)_2(OTf)_2$	CH_3CN	Dark yellow	Powder	90%

Caution! Although no accident while dealing with the perchlorate salts was experienced, but they are potential explosives upon heating and should be handled with care.

2.3. Characterization of the Fe(II) and Mn(II)-Complexes

2.3.1. ESI-MS

The electrospray ionization mass spectra of all the Fe(II) and Mn(II)-complexes were recorded in acetonitrile solvent, at room temperature. The concentration of the metal complexes to record ESI-MS was generally kept consistent at 1 mM. The samples were filtered through syringe filters before injecting into the mass spectrometer.

- *ESI-MS spectrum of* $[Mn^{II}(L1)(ClO_4)]^+$ *and* $[Mn^{II}(L2)(ClO_4)]^+$:

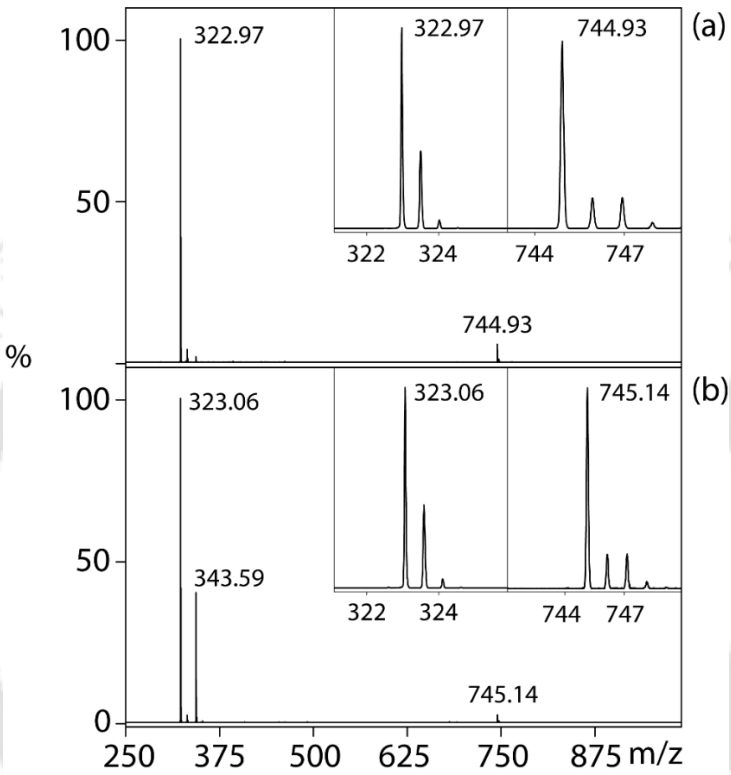

Fig. 2.6. ESI-MS spectrum of (a) $[Mn^{II}(L1)(ClO_4)]^+$; *m/z* 322.97 and 744.93 corresponds to $[Mn(L1)]^{2+}$ and $[Mn(L1)(ClO_4)]^+$, respectively. Inset shows their isotopic distribution pattern. (b) $[Mn^{II}(L2)(ClO_4)]^+$; *m/z* 323.06, 343.59 and 745.14 corresponds to $[Mn(L2)]^{2+}$, $[Mn(L2)(CH_3CN)]^{2+}$ and $[Mn(L2)(ClO_4)]^+$, respectively. Inset shows their isotopic distribution pattern.

- *ESI-MS spectrum of* $[Fe^{II}(L3)(OTf)]^+$:

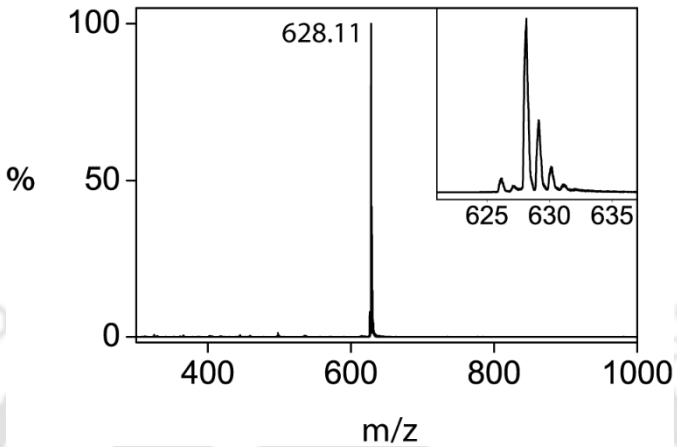

Fig. 2.7. ESI-MS spectrum of $[Fe^{II}(L3)(OTf)]^+$; *m/z* 628.11 corresponds to $[Fe^{II}(L3)(OTf)]^+$ respectively. Inset shows the isotopic distribution pattern for the *m/z* 628.11.

- *ESI-MS spectrum of* $[Fe^{II}(L4)(OTf)]^+$:

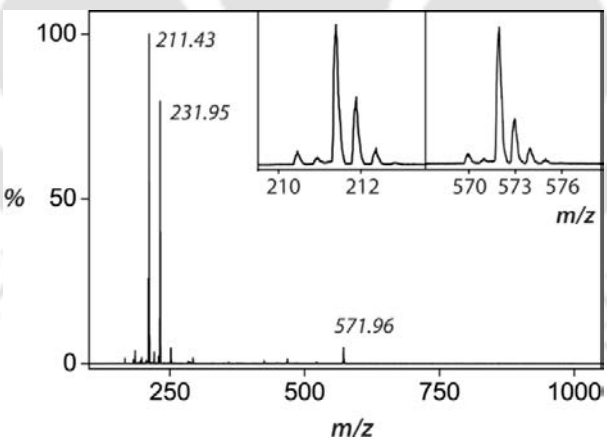

Fig. 2.8. ESI-MS spectrum of $[Fe^{II}(L4)(OTf)]^+$; *m/z* 211.43, 231.95 and 571.96 corresponds to $[Fe^{II}(L4)]^{2+}$, $[Fe^{II}(L4)(CH_3CN)]^{2+}$ and $[Fe^{II}(L4)(OTf)]^+$ respectively. Inset shows the isotopic distribution pattern for the *m/z* values of 211.43 and 571.96.

- *ESI-MS spectrum of* $[Fe^{II}(L5)(OTf)]^+$:

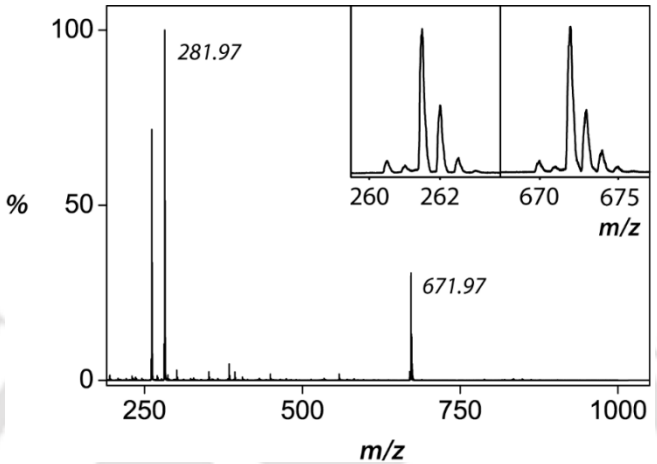

Fig. 2.9. ESI-MS spectrum of $[Fe^{II}(L5)(OTf)]^+$; *m/z* 261.49, 281.97 and 671.97 corresponds to $[Fe^{II}(L5)]^{2+}$, $[Fe^{II}(L5)(CH_3CN)]^{2+}$ and $[Fe^{II}(L5)(OTf)]^+$ respectively. Inset shows the isotopic distribution pattern for the *m/z* values of 261.49 and 671.97.

2.4. Generation of the Reactive Metal Intermediates

Two isomeric side on manganese(III)-peroxo complexes $[Mn^{III}(L1)(O_2)]^+$ and $[Mn^{III}(L2)(O_2)]^+$ were generated by reacting their corresponding cocourless Mn^{II} complexes with 10 equivalents of H_2O_2 and 2.5 equivalents of triethylamine (TEA) in CH_3CN at 15 ºC. The formation of the $[Fe^{IV}(O)(L3)]^{2+}$ and $[Fe^{IV}(NTs)(L3)]^{2+}$ intermediates were achieved by vigorous stirring of the Fe(II) complex with excess solid PhIO and PhINTs, respectively in acetonitrile solvent and filtering off the unreacted excess oxidant using 0.2 μm PTFE syringe filters. The resulting clean filtrates were stored in cold and used for further studies. The Fe(IV)-oxo complex $[Fe^{IV}(O)(L4)]^{2+}$ was synthesized by vigorous stirring of the Fe(II) complex with excess solid PhIO oxidant at room temperature in acetonitrile. The complex $[Fe^{IV}(O)(L5)]^{2+}$ was synthesized *in situ*

from the corresponding Fe(II) precursor complex at room temperature by the addition of 1.5 equivalents of $PhI(OAc)_2$ in acetonitrile. However, the rate of formation, stability and rate of self-decay of these intermediates were highly influenced by the temperature parameter. The stability of these intermediates was crucial in order to successfully characterize them using various spectroscopic tools like ESI-MS, UV/Vis, EPR, etc. The formation, stability, characterization and reactivity of these high valent reactive intermediates are discussed latter in their respective chapters.

2.5. Physical Methods

UV/Vis spectra were recorded on a Hewlett Packard 8453 spectrophotometer equipped with either constant temperature circulating water bath or a liquid nitrogen cryostat (Unisoku) with a temperature controller. High-resolution electrospray ionization-mass spectra (ESI-MS) were recorded on a Waters (Micromass MS Technologies) Q-TOF Premier mass spectrometer by infusing analyte samples directly into the source at 15 μL min^{-1} using a syringe pump. The spray voltage was set at 2 kV and the capillary temperature at 80 °C unless otherwise stated. Also, few mass spectra were recorded with the help of Agilent-Q-TOF 6520 instrument in positive mode equipped with a Mass hunter workstation; the spray voltage was set at 3 kV and the drying gas flow and temperature were maintained as 5.0 L min^{-1} and 200 °C respectively. NMR spectra were recorded on Bruker Avance III HD 600 MHz and 400 MHz spectrometers and a Jeol Advanced Solution State 400 MHz spectrometer (JNMECZ400S) using TMS as internal standard under ambient conditions unless otherwise mentioned. The reported chemical shifts (in ppm) are in reference to the residual solvent peaks.

2.6. Reaction Kinetics

All the kinetic reactions were run in a 10 mm path length UV/Vis cuvette by monitoring UV/Vis spectral changes of reaction solutions. The kinetics studies were performed under pseudo first-order conditions with excess substrate concentration. The reactions were monitored by following the decrease of the characteristic absorption bands of various intermediates as a function of time. The rate constants were determined by fitting the changes in absorbance of the intermediates under study. Reactions were run at least in triplicate and the data reported represent the average of those. Standard deviation was less than 10 % of the given values.

2 mM solutions of $[Mn^{III}(L1)(O_2)]^+$ (1b) and/or $[Mn^{III}(L2)(O_2)]^+$ (2b) were prepared from 2 mM solutions of $[Mn^{II}(L1)(ClO_4)_2]$ (1a) and/or $[Mn^{II}(L2)(ClO_4)_2]$ (2a) by reacting with 10 equivalents of H_2O_2 in the presence of 2.5 equivalents of triethylamine (TEA, 5 mM) in CH_3CN at 15 ºC. Each time 2.5 mL of Mn(II) complex solution was prepared in a 4 mL glass vial and 2 mL of it was transferred into a cuvette and deoxygenated with argon gas sealed with rubber septum and kept in UV/Vis spectrophotometer cuvette holder which was attached to a low temperature cryostat and waited till equilibrated at 15 ºC, then slowly 50 µL of 10 equivalents of H_2O_2 was added in the presence of 2.5 equivalents triethylamine through a 250 µL hamiltonian syringe, immediately mixed with another 1 ml syringe until characteristic peaks of the intermediates were obtained in the visible region. After it reaches the maximum formation of Mn(III)-peroxo intermediate a few minutes were given to equilibrate the solution temperature. Then substrates were slowly added through a 250 µL Hamiltonian syringe to the solutions, mixed with another 1 mL syringe and the time course of the decay of the Mn(III)-peroxo chromophore was monitored.

Iron(IV)-oxo complexes, $[Fe^{IV}(O)(L3)]^{2+}$ (3b) and $[Fe^{IV}(O)(L4)]^{2+}$ (4b), and iron(IV)-tosylimido complex, $[Fe^{IV}(NTs)(L3)]^{2+}$ (3c) were prepared at 25 ºC, from 1 mM solution of its ferrous complexes in CH_3CN. Each time, a 2.5 mL portion of the iron(II) solution in a 4 mL glass vial was taken and excess solid PhIO was added and thoroughly mixed by vortex for a couple of minutes affording the corresponding oxo complexes 3b and 4b. However, the complex 3c was prepared using the similar procedure by the addition of excess PhINTs oxidant. Then the solution was filtered through 0.2 µM syringe filters into another clean and dry 4 mL glass vial and deoxygenated with argon gas. 2 mL of it was transferred into a cuvette and sealed with rubber septum and kept in UV/Vis spectrophotometer cuvette holder. The substrates were then slowly added using a 250 µL Hamiltonian syringe to the reaction mixture and mixed with another 1 mL syringe. The time course of the decay of the iron(IV)-oxo and iron(IV)-tosylimido chromophores were monitored. The concentration of the iron(IV)-oxo complex 4b was taken either 0.5 mM or 1 mM depending upon its kinetic investigations.

The iron(IV)-oxo complex, $[Fe^{IV}(O)(L5)]^{2+}$ (5b) with 1 mM concentration was prepared from 1 mM solutions of its ferrous precursor complex 5a by reacting with 1.5 equivalents of $PhI(OAc)_2$ in acetonitrile at room temperature. Each time 2.5 mL portion of the Fe(II) solution was taken in a 4 mL glass vial and 2 mL was transferred into the quartz cuvette and deoxygenated with argon gas sealed with rubber septum and kept in UV/Vis spectrophotometer cuvette holder. For fast reactions, low temperature setup was employed using the low temperature cryostat when the oxidants were added through a 250 µL Hamiltonian syringe, immediately mixed with another 1 mL syringe until the characteristic absorption band of intermediate was monitored in the UV/Vis spectrophotometer. Upon the maximum formation of Fe(IV)-oxo chromophore, few minutes were given to equilibrate the solution temperature. The substrates were then

slowly added through a 250 µL Hamiltonian syringe into the quartz cuvette and mixed with another 1 mL syringe. The time course of the decay of the Fe(IV)-oxo chromophore was monitored. Concentrations of the substrates used in each case varied and were adjusted to achieve convenient reaction time and control.

In general, reactions were monitored through a kinetic rate over 5 half-lives ($t_{1/2}$) and the pseudo first-order rate constants (k_{obs}) were determined by fitting the decay profile of the UV/Vis bands for the respective intermediates to the equation:

$[A] = [A_0] + b*(e^{-kt})$

Second-order rate constants (k_2) were determined from the linear fit of the k_{obs} values against substrate concentrations for each system. The reaction mixtures were removed from the cuvette, oxidation products and metal salts were separated and passed through the silica gel and washed subsequently with CH_3CN. Product yields were determined by peak area ratios relative to the standard samples by different (like NMR and ESI-MS) spectroscopic techniques.

2.7. Product Analysis

Product analyses of the reaction mixtures were carried out by ESI-MS, NMR (^1H and ^{13}C) with a Varian 600/150 or 500/125 MHz spectrometer and LCMS with WATERS ACQUITY UPLC equipped with a variable wavelength UV-200 detector. The products were separated on Waters Symmetry C18 reverse phase column (4.6 x 250 mm), and detection was observed at 215 and 254 nm and product yields were calculated by comparison with standard curves of known authentic samples. Also, for few samples, the reaction mixtures were allowed to pass through a silica column and the products were

collected either in ethyl acetate or in axetonitrile. The collected solutions were concentrated under reduced pressure using a rotary evaporator. The crude product was dissolved in $CDCl_3$ solvent and recorded ^1H NMR spectra taking an internal standard. The percentage ratio of different products were quantified by comparing the NMR signals to those of authentic compounds.

2.8. References

1. W. L. F. Armarego in *Purification of Laboratory Chemicals*, (Ed: D. D. Perrin), Pergamon Press, Oxford, **1997**.
2. H. Saltzman, in *Organic Syntheses*, Vol. V (Ed: J. G. Sharefkin), Wiley, New York, **1973**, pp. 658.
3. S. Taylor , J. Gullick , P. McMorn , D. Bethell , P. C. Bulman Page , F. E. Hancock, F. King, G. J. Hutchings, *J. Chem. Soc. Perkin Trans*. **2001**, *2*, 1714–1723.
4. C. R. Goldsmith, R. T. Jonas, T. D. P. Stack, *J. Am. Chem. Soc.* **2002**, *124*, 83–96.
5. S. A. Moteki, A. Usui, S. Selvakumar, T. Zhang, K. Maruoka, *Angew. Chem. Int. Ed.* **2014**, *53*, 11060–11064.
6. H. B rzel, P. Comba, K. S. Hagen, Y. D. Lampeka, A. Lienke, G. Linti, M. Merz, H. Pritzkow, L. V. Tsymbal, *Inorg. Chim. Acta* **2002**, *337*, 407−419.
7. P. Comba, S. Kuwata, G. Linti, H. Pritzkow, M. Tarnai, H. Wadepohl, *Chem. Commun.* **2006**, 2074− 2076.
8. P. Comba, B. Kanellakopulos, C. Katsichtis, A. Lienke, H. Pritzkow, F. J. Rominger, *Chem. Soc. Dalton Trans.* **1998**, 3997− 4001.

9. P. Barman, A. K. Vardhaman, B. Martin, S. J. W rner, C. V. Sastri, P. Comba, *Angew. Chem., Int. Ed.* **2015**, *54*, 2095−2099.

10. L. Duelund, R. Hazell, C. J. McKenzie, L. P. Nielsen, H. J. Toftlund, *J. Chem. Soc. Dalton Trans.* **2001**, 152-156.

11. M. Lubben, A. Meetsma, E. C. Wilkinson, B. Feringa, L. Que, Jr., *Angew. Chem. Int. Ed.* **1995**, *34*, 1512-1514.

12. W. K. C. Lo, C. J. McAdam, A. G. Blackman, J. D. Crowley, D. A. McMorran, *Inorg. Chim. Acta* **2015**, *426*, 183-194.

CHAPTER – III

Hydrogen by Deuterium Substitution in an Aldehyde Tunes the Regioselectivity by a Non-Heme Manganese(III)-Peroxo Complex

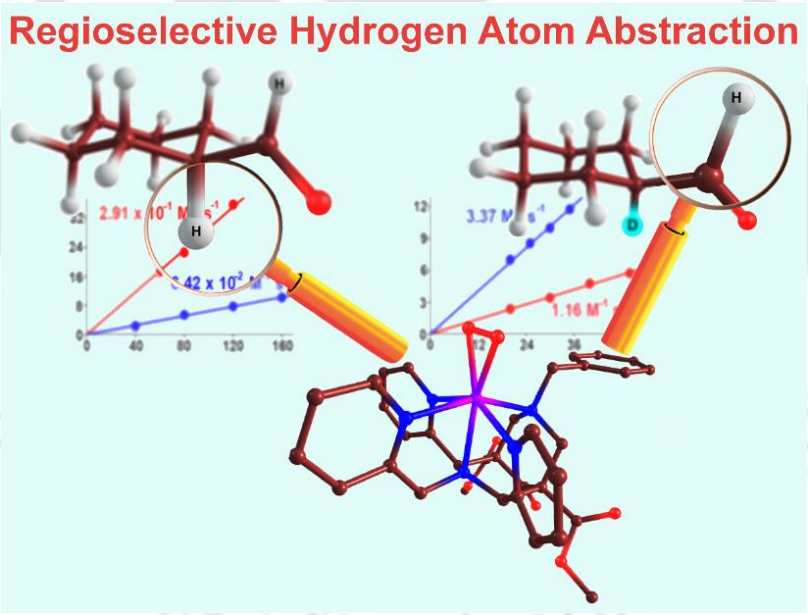

■ Adapted from *Angew. Chem. Int. Ed.* **2019**, *58*, 10639 –10643 with permission from John Wiley & Sons, Inc. ■

3.1. Introduction

In general, dioxygen in nature is mostly inert and will not react with substrates directly. To activate oxygen to its more reactive form, enzymes bind dioxygen on a transition metal centre and through the use of either protons/electrons or a co-substrate convert it into a high-valent metal-oxo, metal-peroxo, metal-hydroperoxo, or metal-superoxo species.[1,2] These intermediates are responsible for the biological transformations of substrates in enzymes.[3-5] As the active oxygen species in enzymes are short-lived and highly reactive they are difficult to study experimentally. Manganese ions are present in the active site structure of numerous enzymes that utilize molecular oxygen, and are involved in harmful superoxide detoxification, decomposition of hydrogen peroxide, and water splitting.[6-8] Most of these enzymes include either a manganese–oxo, manganese-superoxo or manganese-peroxo structure as active intermediate in their catalytic cycle; however, these structures are short-lived and few have been characterized experimentally. As a consequence, biomimetic models have been created of manganese(III)-peroxo complexes that have ligand features of the enzymatic structures but lack the protein surrounding.[9-16]

A number of biomimetic manganese(III)-peroxo complexes have been synthesized and characterized with spectroscopic methods.[17-23] Furthermore, for some of those the reactivity against substrates has been tested.[24-28] In general, side-on manganese(III)-peroxo reacts via nucleophilic pathways, for instance, through deformylation of aldehydes.[29-32] Several of these metal-peroxo complexes have shown unusual reactivity patterns, whereby, for instance, aldehydes are converted into alkanes in the presence of a switchable H-atom donor.[33] Recent work of our groups implicated aldehyde deformylation of 2-phenylpropionaldehyde (2-PPA) to start with an initial and rate-determining hydrogen-atom abstraction, followed by keto-enol tautomerization and a deformylation reaction, and confirmed the electrophilic nature of these oxidants.[34,35]

Clearly, side-on manganese(III)-peroxo complexes show a versatile reactivity pattern with a variety of substrates that is poorly understood, which encouraged us to look deeper into their reactivity with substrates.

3.2. Results and Discussion

3.2.1. Synthesis and Characterization

In this work, we describe the synthesis and characterization of two side-on manganese(III)-peroxo complexes (see Fig. 3.1) with pentadentate N5 bispidine ligand backbones, namely $[Mn^{III}(O_2)(L1)]^+$ (**1b**) and $[Mn^{III}(O_2)(L2)]^+$ (**2b**) with L1= dimethyl-2,4-di(2-pyridyl)3-(pyridin-2-ylmethyl)-7-benzyl-3,7-diazabicyclo[3.3.1]nonan-9-one-1,5-dicarboxylate and L2=dimethyl 2,4-di(2-pyridyl)-3-benzyl-7-(pyridin-2-ylmethyl)-3,7-diazabicyclo[3.3.1]nonan-9-one-1,5-dicarboxylate.[34-37]

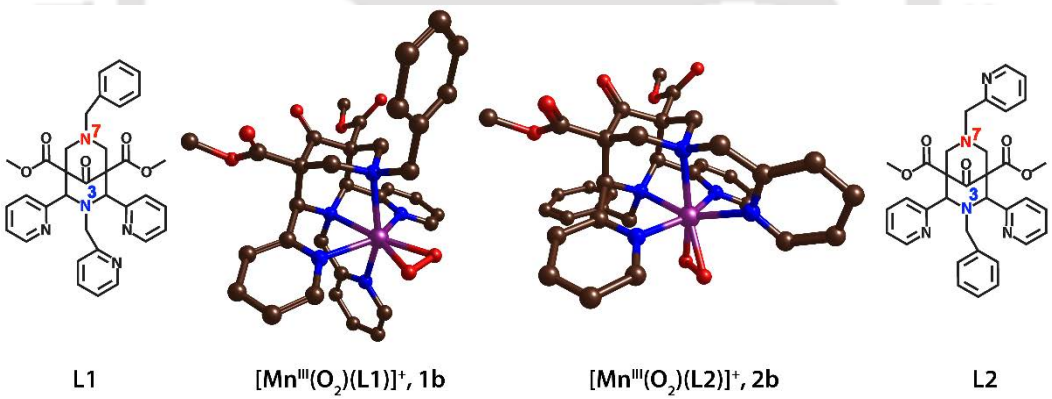

Fig. 3.1. Ligand frameworks and Manganese(III)-peroxo complexes investigated in this work.

The piperidone backbone of the ligands L1 and L2 were prepared according to a previously reported literature method[38-41] and used to generate the $[Mn^{II}(L1)](ClO_4)_2$ (**1a**)

and $[Mn^{II}(L2)](ClO_4)_2$ (**2a**) complexes. These Mn(II) complexes were synthesized using previously reported procedures[41] and characterized by ESI-MS (see Fig. 2.6, Chapter-II).

Treatment of a colour-less solution of the manganese(II) precursor with 10 equivalents of H_2O_2 and triethylamine (TEA; 2.5 equivalents) in CH_3CN at 15 °C results in the formation of a blue and brown intermediate for **1b** and **2b**, respectively.[36] The identity of complexes **1b** and **2b** was confirmed by ultraviolet-visible absorption spectroscopy at wavelengths 605 nm and 450 nm, respectively (see Fig. 3.2) and electrospray ionization-mass spectrometry (ESI-MS) studies (see Fig. 3.3 and Fig. 3.4).[34-36]

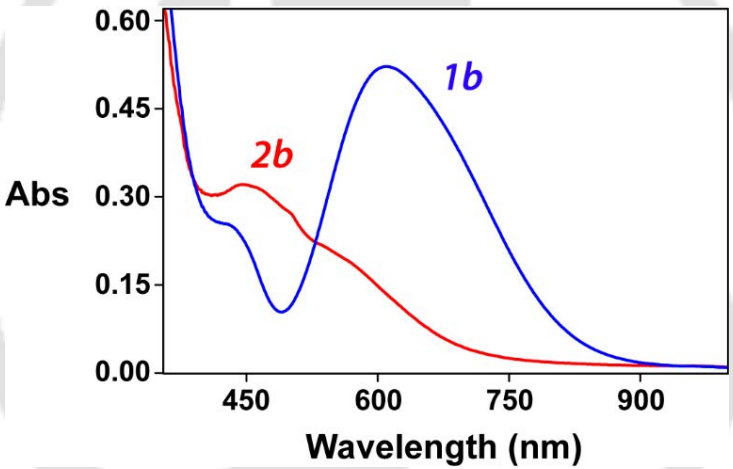

Fig. 3.2. UV/Vis spectra of the formation of $[Mn^{III}(O_2)(L1)]^+$ (**1b**) and $[Mn^{III}(O_2)(L2)]^+$ (**2b**) (2 mM) upon addition of H_2O_2 (20 mM) to $[Mn(L)]^{2+}$ in the presence of TEA (5 mM) in CH_3CN at 15 °C.

The ESI mass spectra of **1b** and **2b** were recorded by infusing pre-cooled samples directly into the source at 15 μL min^{-1} using a syringe pump.[42] The spray voltage was set at 2 kV and the capillary temperature at 80 °C. Prominent peak at *m/z* 678.31 and 678.28 were obtained and an isotope distribution pattern indicates the formation of $[Mn^{III}(O_2)(L1)]^+$ (**1b**) (see Fig. 3.3) and $[Mn^{III}(O_2)(L2)]^+$ (**2b**) (see Fig. 3.4), respectively.

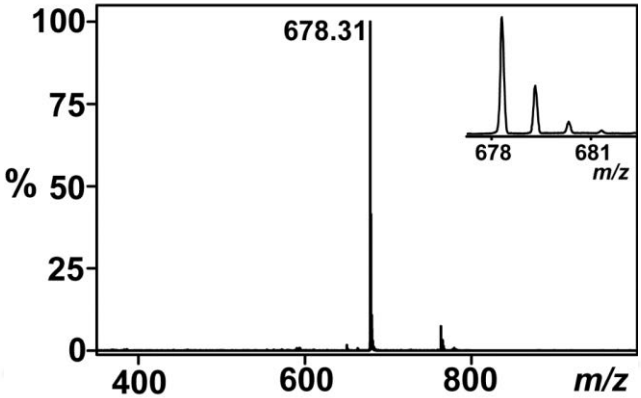

Fig. 3.3. ESI-MS spectrum of **1b** in CH_3CN at 15 °C. Mass peak at *m/z* = 678.31 is assigned for $[Mn^{III}(O_2)(L1)]^+$. Inset shows the observed isotope distribution patterns for $[Mn^{III}(O_2)(L1)]^+$.

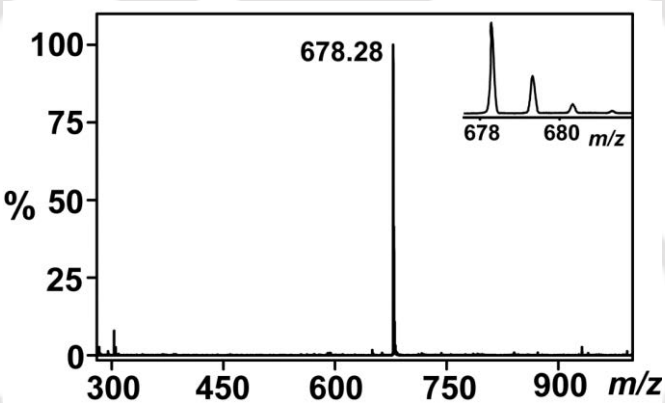

Fig. 3.4. ESI-MS spectrum of **2b** in CH_3CN at 15 °C. Mass peak at *m/z* = 678.28 is assigned for $[Mn^{III}(O_2)(L2)]^+$. Inset shows the observed isotope distribution patterns for $[Mn^{III}(O_2)(L2)]^+$.

3.2.2. Reaction Kinetics

Metal-peroxo oxidants have been reported that react via hydrogen-atom abstraction reactions, therefore, we decided to extend our work to other substrates to evaluate the factors responsible for such unique reaction pathways. As such we investigated the reactivity of complexes **1b** and **2b** with cyclohexanecarboxaldehyde (CCA) as it is a classical substrate used in several reactivity studies by manganese(III)-

peroxo complexes and generally gives cyclohexanone as product.[32, 43] Upon addition of 40 equivalents of CCA to **1b** in CH_3CN at 15 °C, the intermediate decayed immediately and led to cyclohexanone as product (see Fig. 3.5a). The pseudo-first-order rate constant of the decay of **1b** increased linearly with increasing CCA concentration, thus enabling us to determine the second-order rate constant of the reaction: k_2= 0.064 M^{-1} s^{-1} (see Fig. 3.5b). In contrast, the second-order rate constant for the oxidation of CCA by **2b** gave a rate constant k_2 of 0.291 M^{-1} s^{-1} (Table 3.1.). The rate changes between **1b** and **2b** are similar to those reported previously for the oxidation of 2-PPA.[34, 35]

Table 3.1. Second-order rate constants (k_2) determined for the reaction of 1b and 2b (2 mM solution in CH_3CN) with CCA, α-[D_1]-CCA and 1,2-[D_2]-CCA at 15 °C in CH_3CN.[a]

Substrates	k_2 for $[Mn^{III}(O_2)(L1)]^+$ (1b)	k_2 for $[Mn^{III}(O_2)(L2)]^+$ (2b)
CCA	0.064 $M^{-1}s^{-1}$	0.029 $M^{-1}s^{-1}$
α-[D_1]-CCA	3.37 $M^{-1}s^{-1}$	1.16 $M^{-1}s^{-1}$
1,2-[D_2]-CCA	4.80 x 10^{-2} $M^{-1}s^{-1}$	Not determined

[a] All the reactions were followed by monitoring the UV/Vis spectral changes of the reaction solution.

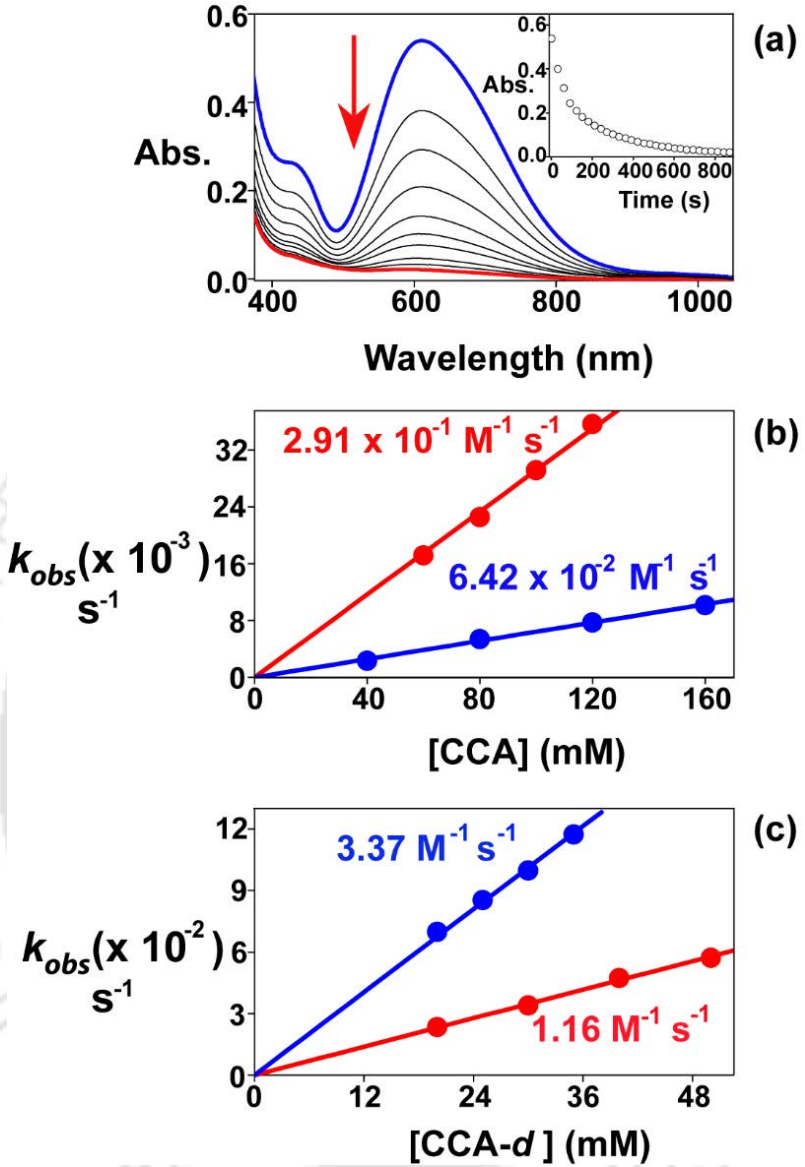

Fig. 3.5. Kinetic studies for the reaction of **1b** and **2b** with CCA: (a) UV-Vis spectral changes of **1b** (2 mM) upon addition of CCA (120 mM) in the presence of TEA (5 mM) and hydrogen peroxide (20 mM) in CH_3CN at 15 °C. Inset shows the time course of the absorbance at 605 nm. (b) Plot of k_{obs} against the concentration of CCA: second-order rate constant for the reaction of 2 mM **1b** (blue •) and **2b** (red •) with various substrate concentrations in CH_3CN at 15 °C. (c) Plot of k_{obs} against the concentration of α-[D_1]-CCA (~90%, D enriched) with 2 mM **1b** (blue •) and **2b** (red •) in CH_3CN at 15 °C.

As previous work reported a rate-determining hydrogen atom abstraction reaction, we decided to synthesize α-[D_1]-CCA and repeat the kinetics experiments with **1b** and **2b** (Fig. 3.5c). Surprisingly, upon addition of 40 equivalents of α-[D_1]-CCA to **1b** at 15 °C, an enhanced reaction rate compared to CCA was observed. The second-order rate constant for the reactivity of α-[D_1]-CCA with **1b** was 50 times faster when compared with parent CCA and implicated an effective inverse kinetic isotope effect (KIE) of 0.02. The product analysis by NMR spectroscopy revealed that the product for the reaction of α-[D_1]-CCA with **1b** was cyclohexanecarboxylic acid (Scheme 3.1. and Fig. 3.13), rather than the expected cyclohexanone.

Scheme 3.1. Products obtained for the reaction of 1b and 2b with substrates.

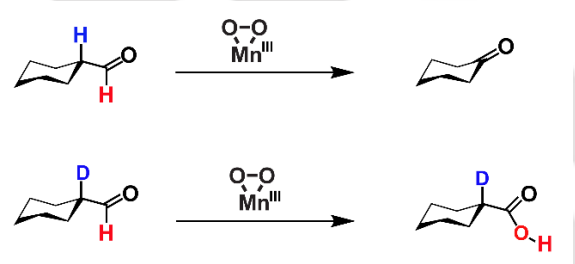

This clearly indicates a regioselectivity switch for hydrogen atom abstraction from the α-position of substrate to the aldehyde hydrogen atom. The observed second-order rate constants for the reaction of α-[D_1]-CCA with **1b** and **2b** were 3.37 M^{-1} s^{-1} and 1.16 M^{-1} s^{-1}, respectively. These observed trends are in contrast to those obtained for the reaction of **1b** and **2b** with 2-PPA. As far as we know, our observation of the oxidation of α-[D_1]-CCA to its corresponding acid is the first experimental evidence of a Mn^{III}-peroxo intermediate that reacts via an electrophilic oxidation reaction. The observed oxidation rates of **1b** and **2b** follow a similar trend as shown previously for $[Mn^{IV}(O)(L1)]^{2+}$ versus $[Mn^{IV}(O)(L2)]^{2+}$.[36] This unique regioselectivity switch observed here may be the result of two competing pathways that are close in energy and deuteration reverses the ordering of the transition states and hence the product distributions, as seen,

for instance, in the hydroxylation of ethylbenzene versus ethylbenzene-[D_{10}] with iron(IV)-oxo complexes.[44, 45]

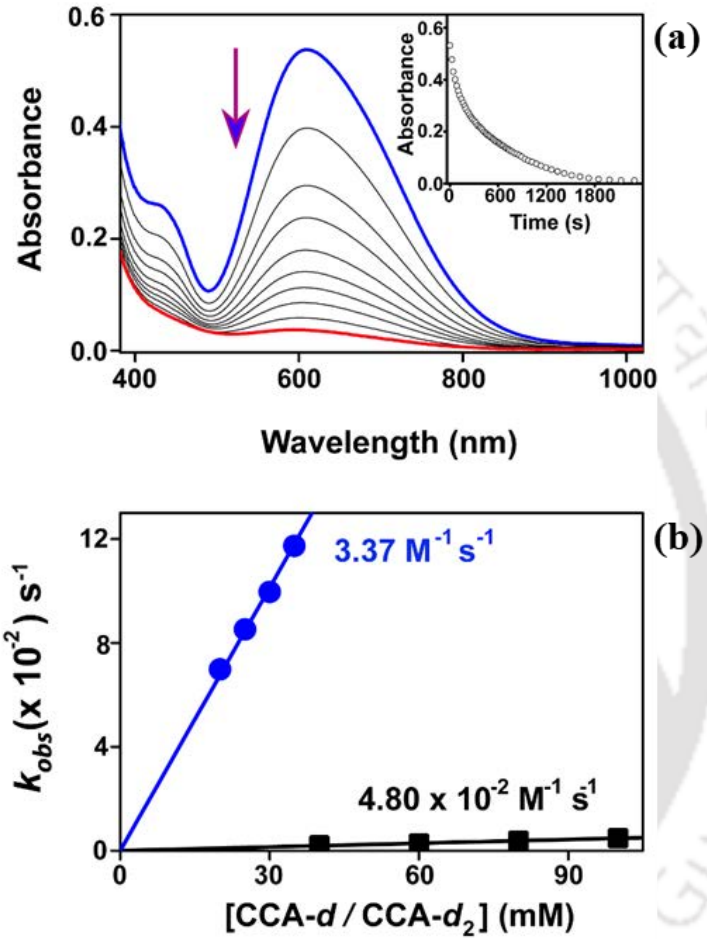

Fig. 3.6. (a) UV/Vis spectral changes of **1b** (2 mM) upon addition of 1,2-di-deuterio-cyclohexanecarboxaldehyde (60 mM) in the presence of TEA (5 mM) and hydrogen peroxide (20 mM) in CH_3CN at 15 ºC. Inset shows the time trace during the course of the reaction. (b) Plot of k_{obs} against α-[D_1]-CCA concentration and 1,2-di-deuterio-cyclohexanecarboxaldehyde (1,2-[D_2]-CCA) to determine a second-order rate constant in the reaction of **1b** (2 mM) against various concentration of α-[D_1]-CCA (blue •) and 1,2-[D_2]-CCA (black •) in CH_3CN at 15 ºC.

To substantiate our hypothesis further, we synthesized 1,2-di-deuterio-cyclohexanecarboxaldehyde (approximately 90%, D enriched, 1,2-[D_2]-CCA). Upon addition of 40 equivalents of 1,2-[D_2]-CCA to **1b** in CH_3CN at 15 °C, the corresponding intermediate readily decayed, enabling us to follow the reaction spectroscopically (see Fig. 3.6a). A second-order rate constant of 4.8 X 10^{-2} M^{-1} s^{-1} with an effective KIE of 70 was determined (see Fig. 3.6b).

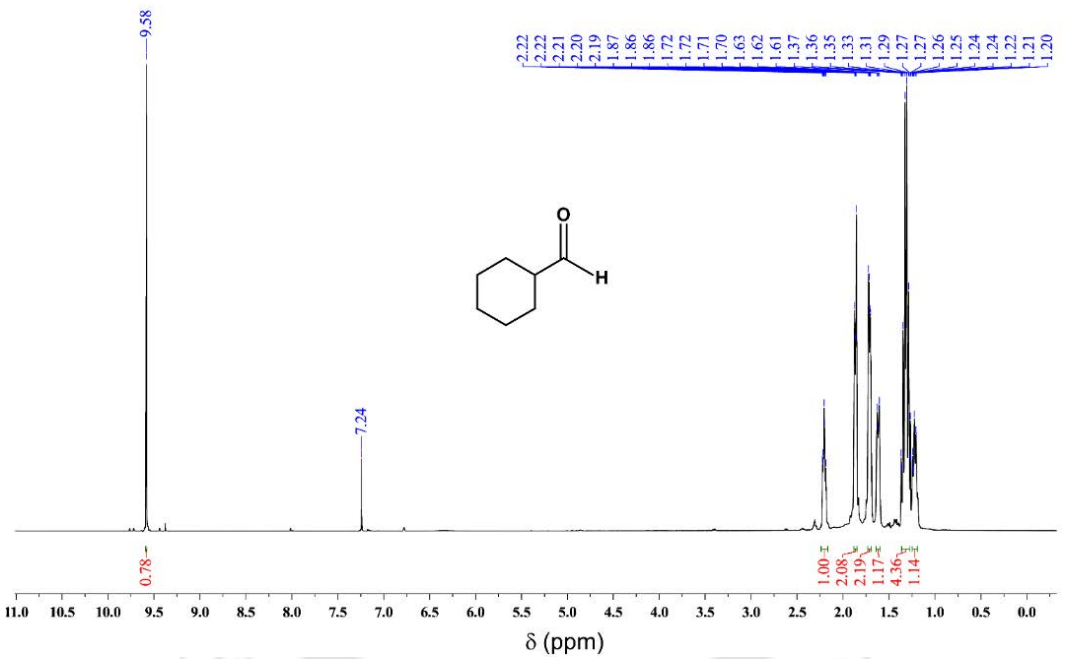

Fig. 3.7. ^{1}H NMR (600 MHz) spectrum of cyclohexanecarboxaldehyde (CCA) in $CDCl_3$.

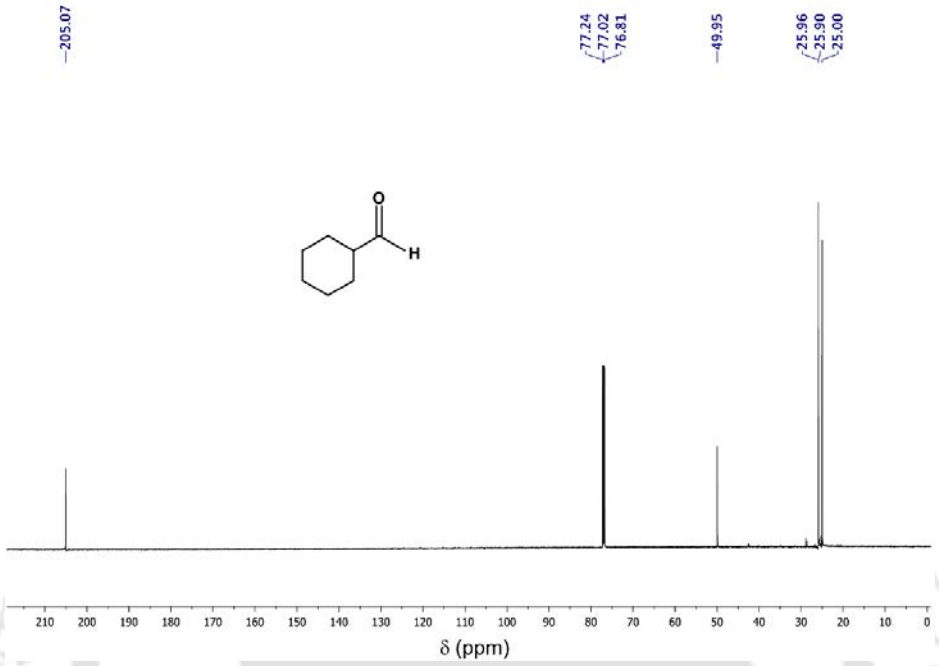

Fig. 3.8. ^{13}C NMR (150 MHz) spectrum of cyclohexanecarboxaldehyde (CCA) in $CDCl_3$.

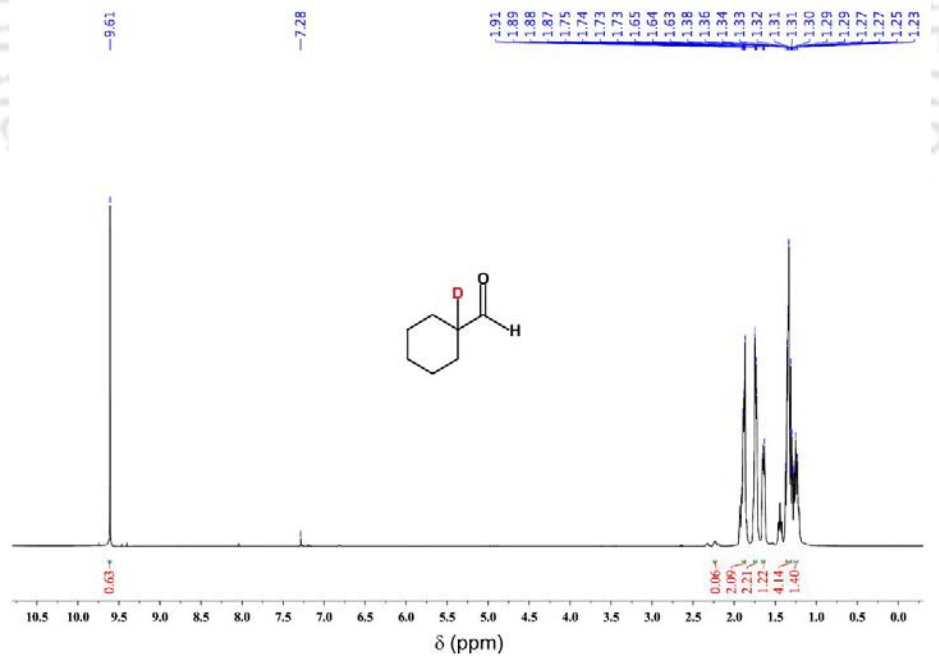

Fig. 3.9. ^1H NMR (600 MHz) spectrum of α-[D_1]-CCA in $CDCl_3$.

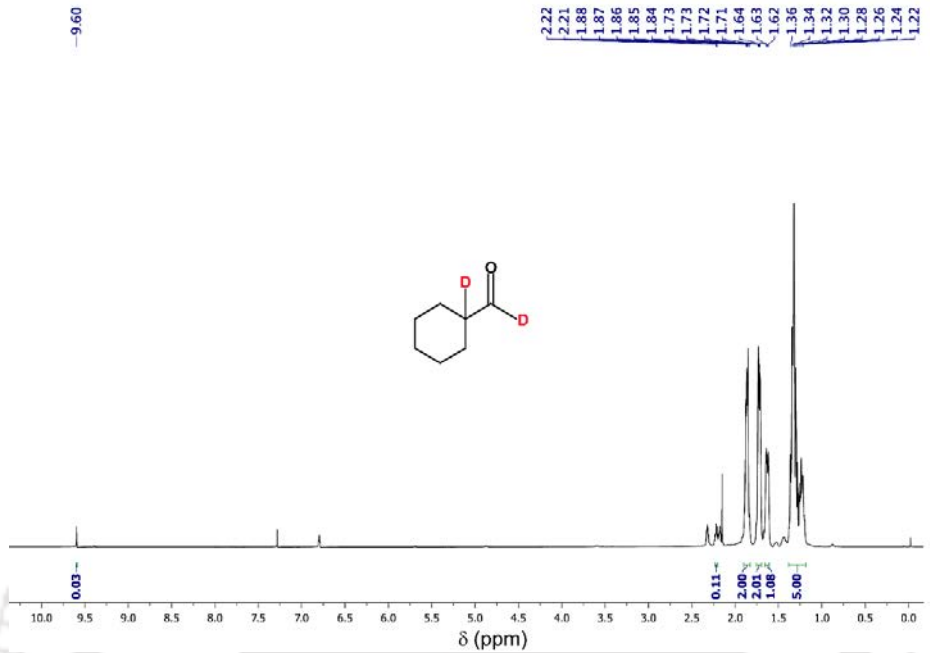

Fig. 3.10. ^{1}H NMR (600 MHz) spectrum of 1,2-[D_2]-CCA in $CDCl_3$.

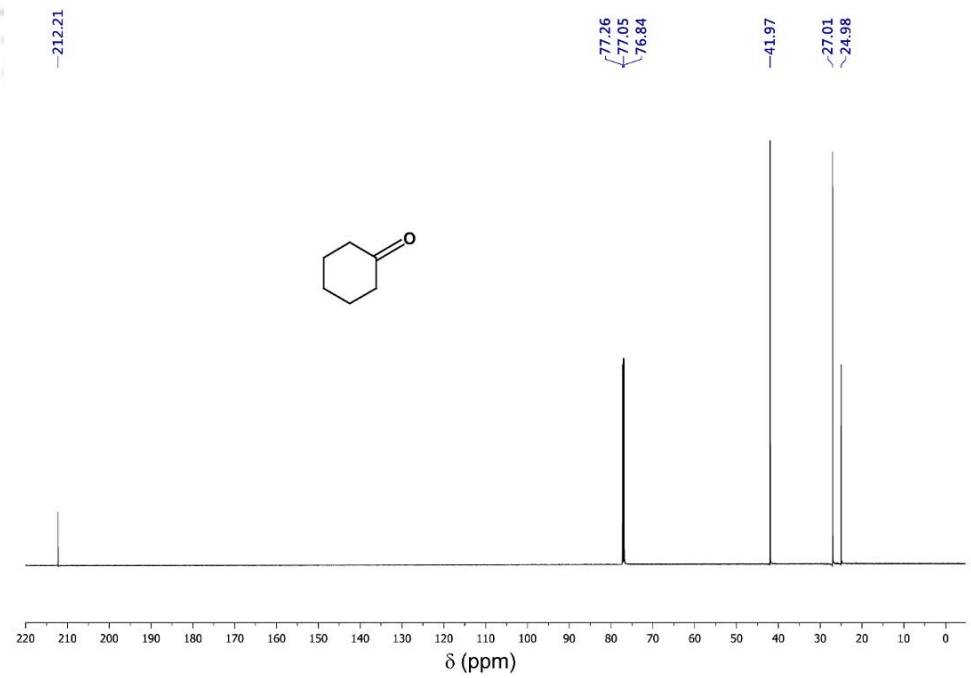

Fig. 3.11. ^{13}C NMR (150 MHz) spectrum of cyclohexanone in $CDCl_3$.

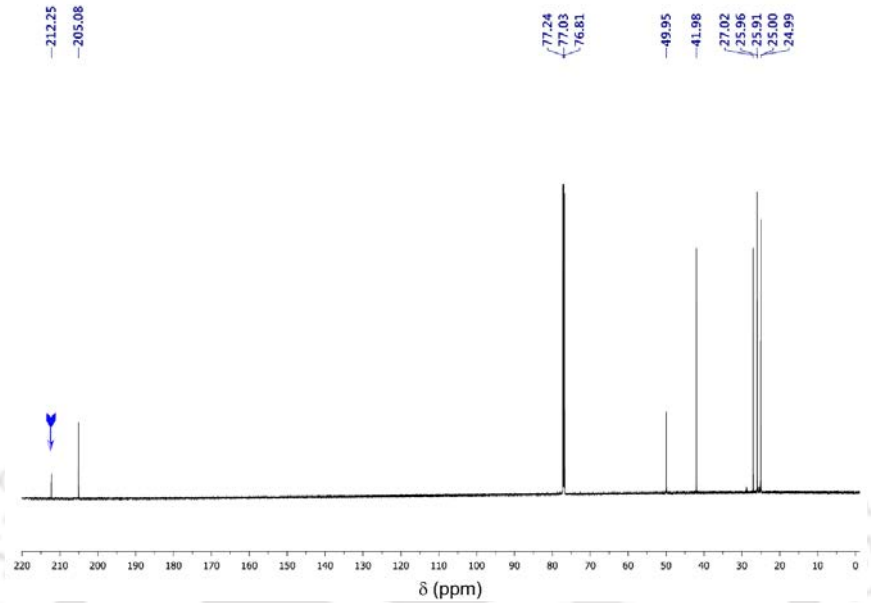

Fig. 3.12. ^{13}C NMR (150 MHz) spectrum of the products formed by the reaction of CCA and intermediate **1b** in CH_3CN at 15 ºC.

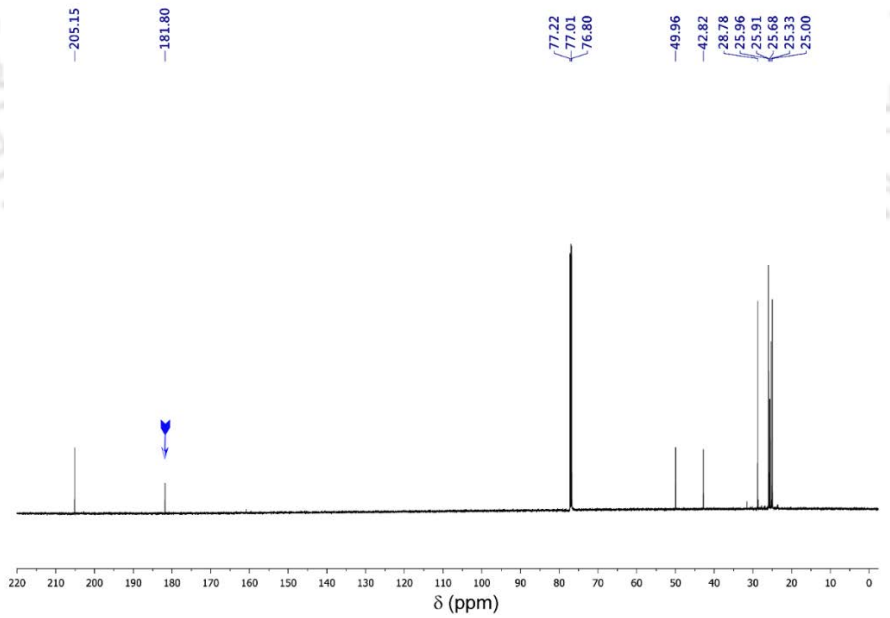

Fig. 3.13. ^{13}C NMR (150 MHz) spectrum of the products formed by the reaction of α-[D_1]-CCA and intermediate **1b** in CH_3CN at 15 ºC.

3.2.3. Computational Backup

To gain insight into the regioselectivity switch and the nature of the oxidant and reactivity patterns, we decided to complement our work with a density functional theory (DFT) study. In general, all methods predict the same trends and give analogous optimized structures. We calculated a reactant complex (**Re**) of CCA with using B3LYP and B3LYP-D3 methods. The geometry and electronic configuration of the manganese(III)-peroxo complex changed little upon complexation with CCA. Thereafter, two hydrogen atom abstraction pathways were investigated, namely *via* transition state $^{5}\mathbf{TS}_{HA,ald}$ for hydrogen atom abstraction from the aldehyde C–H bond and via transition state $^{5}\mathbf{TS}_{HA,\alpha}$ for hydrogen atom abstraction from the C^{α}-H bond of CCA (see Fig. 3.14).

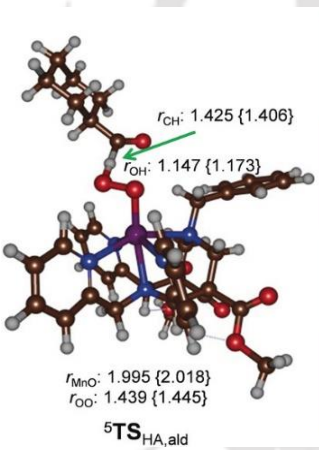

	$\Delta G^{\ddagger}_{ald}$	$\Delta G^{\ddagger}_{\alpha}$
	ΔG_{Wertz} / ΔG_{vibr}	ΔG_{Wertz} / ΔG_{vibr}
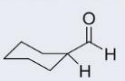	17.8 / 18.6	18.9 / 18.1
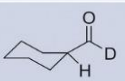	19.6 / 19.5	18.6 / 18.0
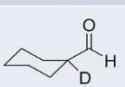	17.5 / 18.0	19.7 / 18.5

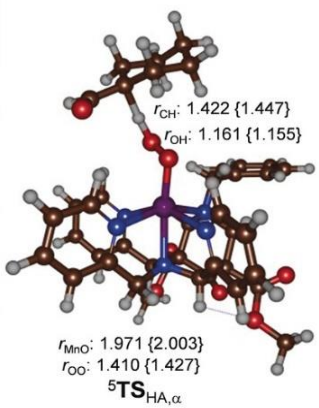

Fig. 3.14. Hydrogen atom abstraction transition states optimized at UB3LYP/BS1 {UB3LYP-D3/BS2} from aldehyde group (left) and C^{α}–H bond (right) with bond lengths in angstroms. The Table gives corrected (Wertz/vibrational) free energies of activation calculated at UB3LYP/BS2//UB3LYP/BS1 level of theory for the two pathways for hydrogen atom subtraction by **1b** from CCA, 1-[D_1]-CCA and 2-[D_1]-CCA with values in kcal mol^{-1}.

In both cases, an end-on manganese-hydroperoxo with a substrate radical is formed ($\mathbf{I}_{HA,ald}$ and $\mathbf{I}_{HA,\alpha}$) after hydrogen atom abstraction. The two hydrogen atom abstraction transition states are shown in Fig. 3.14 and give the typical features seen

before.[34,35] Thus, ^{5}**TS**$_{HA,Ald}$ is late with a long C–H distance of 1.425 {1.406} Å and a short O–H distance of 1.147 {1.173} Å and with the hydroperoxo group in end-on configuration as calculated at the B3LYP/BS1 {B3LYP-D3/BS2} level of theory. Upon approach of substrate to oxidant it reorients from side-on to end-on Mn(III)-peroxo without an isomerization barrier. The aliphatic hydrogen atom abstraction barrier (^{5}**TS**$_{HA,\alpha}$) also is late with similar C–H and O–H distances with respect to ^{5}**TS**$_{HA,ald}$ with distances of 1.422 {1.447} and 1.161 {1.155} Å as calculated at the B3LYP/BS1 {B3LYP-D3/BS2} level of theory, respectively. In general, late hydrogen atom abstraction transition states correspond to energetically high barriers,[46] which indeed is seen for this process and matches the experimental reaction rates well.

Free energies of activation for the two reaction pathways were calculated from the Gaussian frequencies using thermal, solvent and entropic corrections to the enthalpy. As gas-phase calculated entropies tend to be overestimated with respect to experiment,[47] we applied two entropic correction models. Firstly, we used the Wertz correction in model 1 that scales the molecular entropy of each compound ($\Delta G_{Wertz}^{\ddagger}$). Secondly, the lowest entropy contributions for low vibrational frequencies (<50 cm^{-1}) were ignored from the free energies in model 2 ($\Delta G_{vibr}^{\ddagger}$). These two different free energies of activation for hydrogen atom abstraction from the α- and aldehyde C–H positions are given in the Table in Fig. 3.14. As can be seen from Fig. 3.14, the two barriers (^{5}**TS**$_{HA,ald}$ and ^{5}**TS**$_{HA,\alpha}$) are within 1 kcal mol^{-1} from each other and dependent on the model and calculation procedure either ^{5}**TS**$_{HA,\alpha}$ or ^{5}**TS**$_{HA,ald}$ is lower in energy. Within transition state theory, the experimental rate constant of 6.4×10^{-2} M^{-1}s^{-1} would correspond to a free energy of activation of 18.4 kcal mol^{-1}. Therefore, our computed barriers with vibrational corrections included are in excellent agreement with the experimental values and also predict the correct regioselectivity.

With vibrational corrections applied, the lowest free energy of activation is via ^{5}**TS**$_{HA,\alpha}$ with a $\Delta G^{\ddagger}_{\alpha,vibr}$ = 18.1 kcal mol^{-1}, while the aldehyde hydrogen atom abstraction is $\Delta G^{\ddagger}_{ald,vibr}$ = 18.6 kcal mol^{-1}. As such, the calculations reproduce the experimental product distributions and predict regioselective hydrogen atom abstraction of the C$^{\alpha}$–H bond. Although the Wertz-corrected free energies point to a reversed regioselectivity, actually upon deuteration of the C$^{\alpha}$–H group both models predict a rise of ^{5}**TS**$_{HA,\alpha}$ by about 1 kcal mol^{-1}, while the ^{5}**TS**$_{HA,ald}$ barrier drops slightly. As a consequence, singly deuteration of the C$^{\alpha}$–H group results in a regioselectivity switch from C$^{\alpha}$–H hydrogen atom abstraction to aldehyde hydrogen atom abstraction. On the other hand, deuteration of the aldehyde position of the substrate raises the ^{5}**TS**$_{HA,ald}$ barriers, but keeps the ^{5}**TS**$_{HA,\alpha}$ barriers more or less the same. The computational trends, therefore, are in great agreement with experimental observation and implicate a regioselectivity switch upon deuteration of the α-position of the CCA substrate. As reasoned before,[47] a HAT reaction has a large zero-point energy due to the loss of one C–H vibration in the complex. In general, HAT barriers increase in energy by a few kcal mol^{-1} upon deuteration of the transferring hydrogen atom.[45] Thus, with two competing barriers very close in energy, substrate deuteration raises the lowest barrier in energy and leads to a regioselectivity switch.

As shown before, hydrogen atom abstraction reactions often have barriers that correlate with the strength of the C–H bond that is broken in the process.[48] Therefore, we calculated the C–H bond dissociation energy (BDE) of the C$^{\alpha}$–H and C$_{aldehyde}$–H bonds from the energy of the substrate with respect to an isolated hydrogen atom and the substrate radical and find values of ΔG = 72.1 and 79.5 kcal mol^{-1}. Based on these values, the reaction should give dominant hydrogen atom abstraction from the C$^{\alpha}$–H bond as seen for the natural substrate. The reason the ^{5}**TS**$_{HA,\alpha}$ and ^{5}**TS**$_{HA,ald}$ barriers are within 1 kcal mol^{-1} probably is due to electrostatic repulsions between the L1 ligand protons and those

from the approaching substrate that are stronger in $^{5}\mathbf{TS}_{HA,\alpha}$ than in $^{5}\mathbf{TS}_{HA,ald}$, where the cyclohexane ring is further away from the ligand structure.

3.2.4. Reaction Mechanism

From a combined experimental and computational studies, we have proposed a mechanism for the aldehyde deformyation reaction of **1b** and **2b** with CCA which proceeds *via* an electrophilic pathway instead of a commonly proposed nucleophilic pathway. There are two possible mechanisms for the aldehyde deformylation which is initiated either by α-hydrogen atom abstraction (HA_{α}) or by aldehyde hydrogen atom abstraction (HA_{ald}) form CCA. When the Mn(III)-peroxo intermediate abstracts aldehyde hydrogen, it proceeds *via* $TS_{HA,ald}$ as shown in scheme 3.2 and results in the formation of a radical at carbonyl carbon of CCA and a Mn(II)-hydroperoxo species. Then the hydroxyl radical ($OH^{\bullet}$) generated from the homolytic cleavage of O-O bond in the hydroperoxo species attacks the radical at carbonyl carbon to form cyclohexanecarboxylic acid as a product. However, α-hydrogen atom abstraction by peroxo intermediate proceeds *via* $TS_{HA,\alpha}$ and forms a substrate radical at α-position of CCA and a hydroperoxo species (see Scheme 3.2). Finally, the rebound of the hydroxyl radical ($OH^{\bullet}$) from hydroperoxo species to the substrate radical takes place and subsequently results in the formation of a cyclohexanone product. The formation of cyclohexanecarboxylic acid from CCA by the Mn(III)-peroxo species **1b** and **2b** is the first report for the aldehyde deformylation which proceeds with an electrophilic aldehyde hydrogen atom abstraction form the CCA substrate.

Scheme 3.2. Plausible mechanism for the aldehyde deformylation of CCA by Mn(III)-peroxo complexes (1b and 2b).

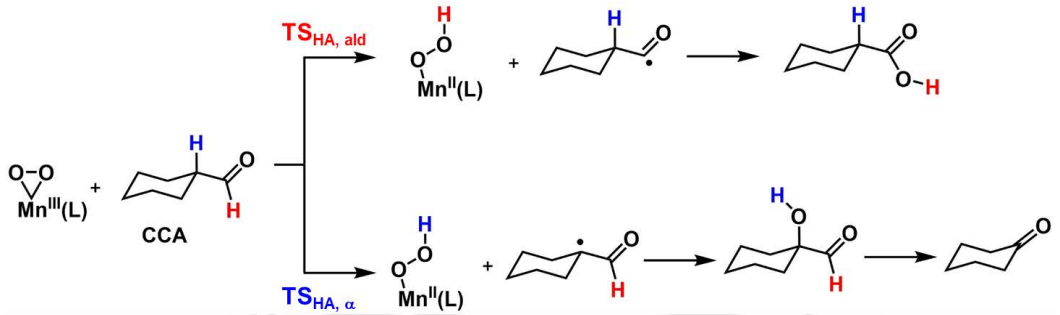

3.3. Conclusion

A couple of Mn^{III}-peroxo complexes bearing pentadentate bispidine backbone were synthesized and characterized with various spectroscopic techniques and studied with DFT. We demonstrate here for the first time that the Mn^{III}-peroxo complex can perform electrophilic oxidation of substrates through the hydrogen-atom abstraction from the C-H bond of an aldehyde to give the corresponding acid as the product.

3.4. References

1. Cytochrome P450: Structure, Mechanism, and Biochemistry, 3rd ed. (Ed.: P. R. Ortiz de Montellano), Kluwer Academic/Plenum Publishers, New York, **2005**.
2. Biomimetic Oxidations Catalyzed by Transition Metal Complexes (Ed.: B. Meunier), Imperial College Press, London, **2000**.
3. M. Costas, M. P. Mehn, M. P. Jensen, L. Que Jr., *Chem. Rev.* **2004**, *104*, 939–986.
4. C. Krebs, D. G. Fujimori, C. T. Walsh, J. M. Bollinger Jr., *Acc. Chem. Res.* **2007**, *40*, 484–492.
5. E. I. Solomon, K. M. Light, L. V. Liu, M. Srnec, S. D. Wong, *Acc. Chem. Res.* **2013**, *46*, 2725–2739.
6. A. F. Miller, *Acc. Chem. Res.* **2008**, *41*, 501–510.
7. R. Eisenberg, H. B. Gray, *Inorg. Chem.* **2008**, *47*, 1697–1699.
8. A. J. Wu, J. E. Penner-Hahn, V. L. Pecoraro, *Chem. Rev.* **2004**, *104*, 903–938.
9. S. V. Kryatov, E. V. Rybak-Akimova, S. Schindler, *Chem. Rev.* **2005**, *105*, 2175–2226.
10. M. M. Abu-Omar, A. Loaiza, N. Hontzeas, *Chem. Rev.* **2005**, *105*, 2227–2252.
11. W. Nam, Acc. *Chem. Res.* **2007**, *40*, 522–531.
12. P. C. A. Bruijnincx, G. van Koten, R. J. M. Klein Gebbink, *Chem. Soc. Rev.* **2008**, *37*, 2716–2744.
13. M. Atanasov, P. Comba, S. Hausberg, B. Martin, *Coord. Chem. Rev.* **2009**, *253*, 2306–2314.
14. M. Costas, *Coord. Chem. Rev*. **2011**, *255*, 2912–2932.
15. A. R. McDonald, L. Que Jr., *Coord. Chem. Rev.* **2013**, *257*, 414–428.
16. P. Saisaha, J. W. de Boer, W. R. Browne, *Chem. Soc. Rev.* **2013**, *42*, 2059–2074.

17. G. Roelfes, V. Vrajmasu, K. Chen, R. Y. N. Ho, J.-U. Rohde, C. Zondervan, R. M. la Crois, E. P. Schudde, M. Lutz, A. L. Spek, R. Hage, B. L. Feringa, E. Münck, L. Que Jr., *Inorg. Chem.* **2003**, *42*, 2639–2653.
18. J. Annaraj, Y. Suh, M. S. Seo, S. O. Kim, W. Nam, *Chem. Commun.* **2005**, 4529–4531.
19. A. Thibon, J.-F. Bartoli, S. Bourcier, F. Banse, *Dalton Trans.* **2009**, 9587–9584.
20. A. Mukherjee, M. A. Cranswick, M. Chakrabarti, T. K. Paine, K. Fujisawa, E. Münck, L. Que Jr., *Inorg. Chem.* **2010**, *49*, 3618–3628.
21. J. Cho, S. Jeon, S. A. Wilson, L. V. Liu, E. A. Kang, J. J. Braymer, M. H. Lim, B. Hedman, K. O. Hodgson, J. S. Valentine, E. I. Solomon, W. Nam, *Nature* **2011**, *478*, 502–505.
22. D. F. Leto, S. Chattopadhyaay, V. W. Day, T. A. Jackson, *Dalton Trans.* **2013**, *42*, 13014–13025.
23. D. Brazzolotto, F. G. Cantú Reinhard, J. Smith-Jones, M. Retegan, L. Amidani, A. S. Faponle, K. Ray, C. Philouze, S. P. de Visser, M. Gennari, C. Duboc, *Angew. Chem. Int. Ed.* **2017**, *56*, 8211–8215; *Angew. Chem.* **2017**, *129*, 8323–8327.
24. M. K. Coggins, J. A. Kovacs, *J. Am. Chem. Soc.* **2011**, *133*, 12470–12473.
25. J. Cho, R. Sarangi, W. Nam, *Acc. Chem. Res.* **2012**, *45*, 1321–1330.
26. M. K. Coggins, V. Martin-Diaconescu, S. DeBeer, J. *A. Kovacs, J. Am. Chem. Soc.* **2013**, *135*, 4260–4272.
27. H. E. Colmer, A. W. Howcroft, T. A. Jackson, *Inorg. Chem.* **2016**, *55*, 2055–2069.
28. Q. Zhang, A. Bell-Taylor, F. M. Bronston, J. D. Gorden, C. R. Goldsmith, *Inorg. Chem.* **2017**, *56*, 773–782.
29. R. B. VanAtta, C. E. Strouse, L. K. Hanson, J. S. Valentine, *J. Am. Chem. Soc.* **1987**, *109*, 1425–1434.
30. N. Kitajima, H. Komatsuzaki, S. Hikichi, M. Osawa, Y. Moro-Oka, *J. Am. Chem. Soc.* **1994**, *116*, 11596–11597.

31. M. S. Seo, J. Y. Kim, J. Annaraj, Y. Kim, Y.–M. Lee, S.–J. Kim, J. Kim, W. Nam, *Angew. Chem. Int. Ed.* **2007**, *46*, 377–380.
32. R. A. Geiger, S. Chattopadhyay, V. W. Day, T. A. Jackson, *Dalton Trans.* **2011**, *40*, 1707–1715.
33. A. Shokri, L. Que, Jr., *J. Am. Chem. Soc.* **2015**, *137*, 7686–7691.
34. P. Barman, P. Upadhyay, A. S. Faponle, J. Kumar, S. S. Nag, D. Kumar, C. V. Sastri, S. P. de Visser, *Angew. Chem. Int. Ed.* **2016**, *55*, 11091–11095; *Angew. Chem.* **2016**, *128*, 11257–11261.
35. F. G. Cantú Reinhard, P. Barman, G. Mukherjee, J. Kumar, D. Kumar, D. Kumar, C. V. Sastri, S. P. de Visser, *J. Am. Chem. Soc.* **2017**, *139*, 18328–18338.
36. P. Barman, A. K. Vardhaman, B. Martin, S. J. Wörner, C. V. Sastri, P. Comba, *Angew. Chem. Int. Ed.* **2015**, *54*, 2095–2099.
37. L1 = dimethyl-2,4-di(2-pyridyl)3-(pyridin-2-ylmethyl)-7-benzyl-3,7-diaza-bicyclo[3.3.1] nonan-9-one-1,5-dicarboxylate and L2 = dimethyl 2,4-di(2-pyridyl)-3-benzyl-7-(pyridin-2-ylmethyl)-3,7-diazabicyclo[3.3.1] nonan-9-one-1,5-dicarboxylate).
38. H. B rzel, P. Comba, K. S. Hagen, Y. D. Lampeka, A. Lienke, G. Linti, M. Merz, H. Pritzkow, L. V. Tsymbal, *Inorg. Chim. Acta* **2002**, *337*, 407−419.
39. P. Comba, S. Kuwata, G. Linti, H. Pritzkow, M. Tarnai, H. Wadepohl, *Chem. Commun.* **2006**, 2074− 2076.
40. P. Comba, B. Kanellakopulos, C. Katsichtis, A. Lienke, H. Pritzkow, F. J. Rominger, *Chem. Soc. Dalton Trans.* **1998**, 3997− 4001.
41. P. Barman, A. K. Vardhaman, B. Martin, S. J. W rner, C. V. Sastri, P. Comba, *Angew. Chem. Int. Ed.* **2015**, *54*, 2095−2099.
42. P. Barman, P. Upadhyay, A. S. Faponle, J. Kumar, S. S. Nag, D. Kumar, C. V. Sastri, S. P. de Visser, *Angew. Chem. Int. Ed.* **2016**, *55*, 11091−11095.

43. R. L. Shook, W. A. Gunderson, J. Greaves, J. W. Ziller, M. P. Hendrich, A. S. Borovik, *J. Am. Chem. Soc.* **2008**, *130*, 8888–8889.
44. W. J. Song, Y. O. Ryu, R. Song, W. Nam, *J. Biol. Inorg. Chem.* **2005**, *10*, 294–304.
45. S. P. de Visser, *Chem. Eur. J.* **2006**, *12*, 8168–8177.
46. S. Shaik, D. Kumar, S. P. de Visser, *J. Am. Chem. Soc.* **2008**, *130*, 10128–10140.
47. S. P. de Visser, F. Ogliaro, P. K. Sharma, S. Shaik, *Angew. Chem. Int. Ed.* **2002**, *41*, 1947–1951; *Angew. Chem.* **2002**, *114*, 2027–2031.
48. F. G. Cantú Reinhard, A. S. Faponle, S. P. de Visser, J. Phys. Chem. A 2016, 120, 9805–9814.

CHAPTER – IV

Sluggish Reactivity by a Non-Heme Iron(IV)-tosylimido Complex as Compared to its Oxo Analogue

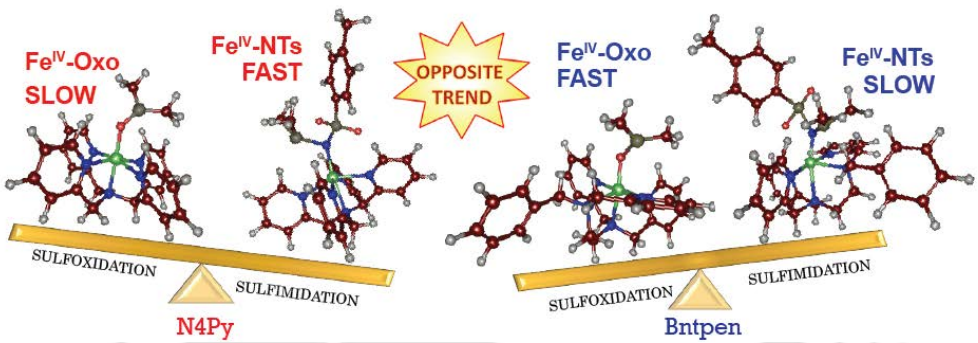

■ Adapted from *Dalton Trans*. **2020**, *49*, 5921-5931 with permission from the Royal Society of Chemistry ■

4.1. Introduction

High-valent metal-oxo and metal-nitrido species are common intermediates in enzymes and are found in the catalytic cycles of several oxidases as well as in nitrogenases.[1-10] Thus, in many of these oxygenases, the enzymes utilize molecular oxygen to create a high-valent non-heme iron(IV)-oxo or iron(IV)-oxo heme cation radical species as active oxidant. On the other hand, few enzymes use nitrogen to generate a high-valent iron(IV)-nitrido or -imido active species. Nevertheless, the latter has been proposed as an intermediate in nitrogenase: the enzyme that binds molecular nitrogen on a FeMo cluster containing seven iron and a molybdenum atom bridged by sulphides.[8-10] The FeMo co-factor in nitrogenases reduces nitrogen to ammonia. The only other enzyme that is known to form a high-valent iron(IV)-imido intermediate is the heme enzyme cytochrome P450 possibly as part of a substrate aziridation and imidation reaction of substrates.[11-14]

As these high-valent intermediates are short-lived they are difficult to trap and characterize and consequently few reports on enzymatic non-heme iron(IV)-oxo intermediates are known,[15-17] and even fewer on iron(IV)-nitrido.[11-14] To gain insight into these short-lived enzymatic intermediates, many biomimetic models have been synthesized that have the active site features of the metal but lack the protein environment.[18-25] Especially, a significant number of reports on biomimetic non-heme iron model systems containing a central iron(IV)-oxo species are known.[26-29] On the other hand, on the analogous iron(IV)-tosylimido or iron(IV)-nitrido species very few investigations have been reported.[30-46] The iron(IV)-tosylimido systems are interesting to study as their bulkier tail, as compared to iron(IV)-oxo or iron(IV)-nitrido, makes the approach of crowded substrates difficult. However, the spectroscopic characterization of these iron(IV)-tosylimido species is also challenging.

Using the pentadentate N4Py ligand, i.e. N,N-bis(2-pyridylmethyl)-N-bis(2-pyridyl) methyl amine (Scheme 4.1.), the corresponding iron(IV)-oxo and iron(IV)-tosylimido oxidants were synthesized, trapped and characterized with a range of spectroscopic methods.[42,47,48] Over the past few years, effective perturbations in the equatorial ligand field of the N4Py ligand were induced to explore the second-coordination sphere effects on the reactivity of the iron(IV)-oxo species with substrates and its spectroscopic parameters.[49-59] These N4Py derivatives (2nd generation N4Py ligands) were shown not only to stabilize the iron(IV)-oxo species better, but also to drastically improve their catalytic efficiency. Unfortunately, for many of these N4Py derivatives the iron(IV)-imido moiety has been tested but due to additional bulk on the equatorial ligand field, such exercises remained futile. Recently, Nam and co-workers have showcased the stabilization and reactivity of iron(V)-tosylimido species with the anionic TAML (tetraamidomacrocyclic ligand) ligand, [Fe^{IV}(NTs)(TAML)], which also offers a planar structure for the tosylimido group to sit upon.[60,61] It was also pointed out that in the coordination sphere of the iron(IV)-NTs active species, apart from the relative positioning of the donor atoms, the nature and number of donor groups is also responsible for their relative stability.[62] It was shown that the ligand architecture of N4Py affects the oxidant positioning as well as the substrate approach. Other fundamental properties like one-electron reduction potential and the reorganization energies in electron transfer (ET) along with a substantial change in reaction mechanism between iron(IV)-oxo and iron(IV)-imido complexes has been demonstrated by Vardhaman et al.[63]

Clearly, there are still many gaps in the understanding of iron-imido, iron-nitrido and iron-oxo oxidants. To gain insight into the properties and reactivities of these biomimetic species, we synthesized [Fe^{IV}(NTs)(Bntpen)]$^{2+}$, [Fe^{IV}(O)(Bntpen)]$^{2+}$, [Fe^{IV}(NTs)(N4Py)]$^{2+}$ and [Fe^{IV}(O)(N4Py)]$^{2+}$. The studies show differences in spectroscopic and electronic properties based on the pentadentate ligand, but also the differences between iron(IV)-oxo and iron(IV)-imido are explored.

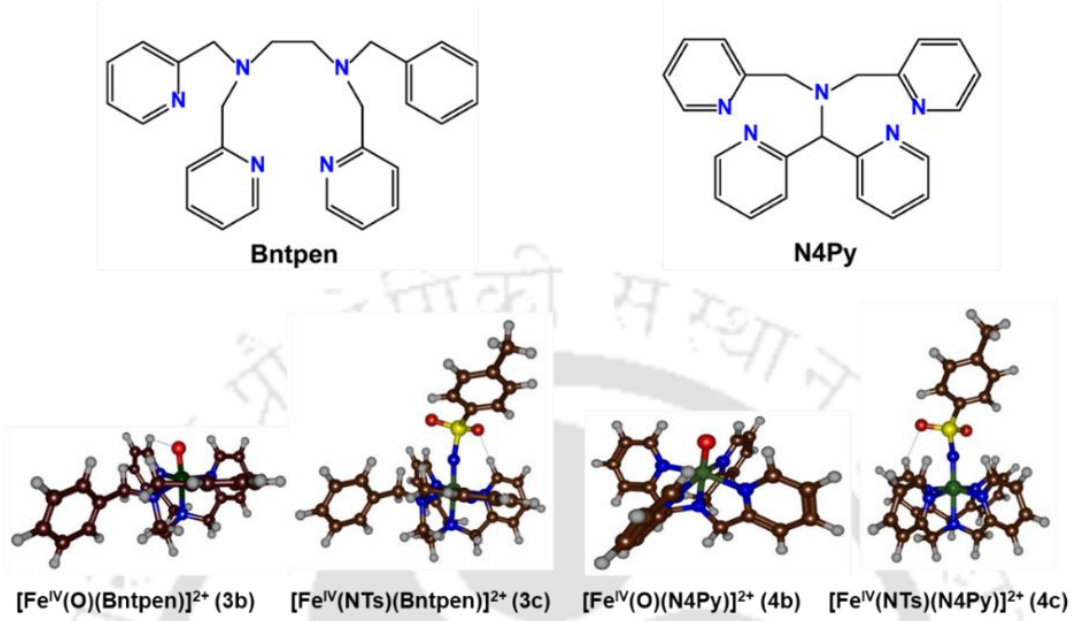

Fig. 4.1. Basic ligand frameworks and structures of oxidants discussed in this work.

4.2. Results and Discussion

4.2.1. Synthesis and Characterization

We started our study with synthesizing the basic ligand framework of N^1-benzyl-N^1,N^2,N^2-tris(pyridine-2-ylmethyl) ethane-1,2-diamine (Bntpen),[64] which is a less symmetrical framework as compared to the N4Py ligand (see Fig. 4.1). The ferrous complex $[Fe^{II}(Bntpen)(CH_3CN)](OTf)_2$ (**3a**) was synthesized with Bntpen ligand system by following a reported procedure[64-67] and was characterized by ESI-mass spectrometry (see Fig. 2.7, Chapter-II). Then its oxo derivative. i.e. $[Fe^{IV}(O)(Bntpen)]^{2+}$ (**3b**), was synthesized inside a glove-box filled with argon as described previously.[68-70] Similar procedures as for $[Fe^{IV}(NTs)(N4Py)]^{2+}$ (**4c**) have been followed in this work to generate the iron(IV)-imido complex $[Fe^{IV}(NTs)(Bntpen)]^{2+}$ (**3c**).[47,48] A comparative reactivity study between $[Fe^{IV}(O)(N4Py)]^{2+}$ (**4b**) and $[Fe^{IV}(O)(Bntpen)]^{2+}$ (**3b**)complexes with various hydrocarbons was reported by Que and co-workers, where, the latter was known

to be a better oxidant in terms of kinetic reaction rates.[64] In particular, the iron(IV)-oxo complex, $[Fe^{IV}(O)(Bntpen)]^{2+}$, was found to react faster with every organic substrate tested than $[Fe^{IV}(O)(N4Py)]^{2+}$. When a detailed kinetic study was done between $[Fe^{IV}(NTs)(N4Py)]^{2+}$ and $[Fe^{IV}(O)(N4Py)]^{2+}$, the former showed faster reactivity in the sulfimidation reaction of thioanisole. However, the trend was found to be reversed for C–H abstraction reactions instead.[47,48] In order to find out how the ligand framework affects the reactivity patterns of iron(IV)-tosylimido oxidants, we decided to do a comparative study between the $[Fe^{IV}(O)(Bntpen)]^{2+}$ (**3b**), $[Fe^{IV}(NTs)(Bntpen)]^{2+}$ (**3c**), $[Fe^{IV}(O)(N4Py)]^{2+}$ (**4b**) and $[Fe^{IV}(NTs)(N4Py)]^{2+}$ (**4c**). The work shows that the ligand framework affects substrate approach as well as the redox properties of the oxidant.

Complex **3c** was synthesized using the nitrene transfer reagent PhINTs under an argon atmosphere. Similar to complex **4c**, the formation of **3c** was identified by an intense LMCT band at 460 nm (ε = 4100 M^{-1} cm^{-1}) and a weaker band at 650 nm (ε = 330 M^{-1} cm^{-1}) due to ligand field transitions characteristic for S = 1 iron(IV) complexes (see Fig. 4.2). Further characterization of the $[Fe^{IV}(NTs)(Bntpen)]^{2+}$, (**3c**), was done by electrospray ionization (ESI)-mass spectrometry (MS) (see Fig. 4.3), proton NMR spectroscopy and Fourier transform infrared (FTIR) spectroscopy.

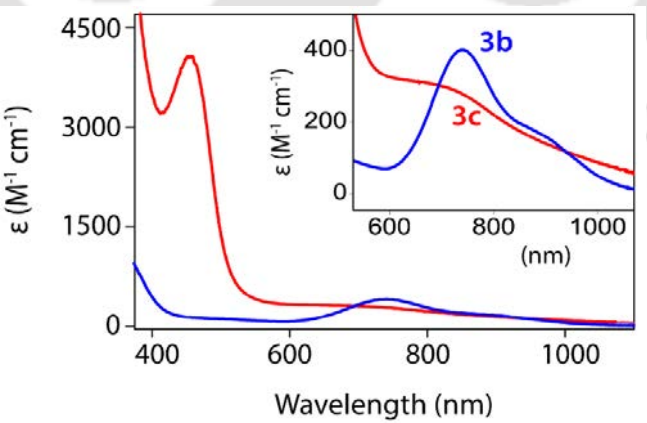

Fig. 4.2 UV/Vis spectra of 1 mM solutions of $[Fe^{IV}(O)(Bntpen)]^{2+}$ (**3b**, blue line) and $[Fe^{IV}(NTs)(Bntpen)]^{2+}$ (**3c**, red line) in CH_3CN at 298 K.

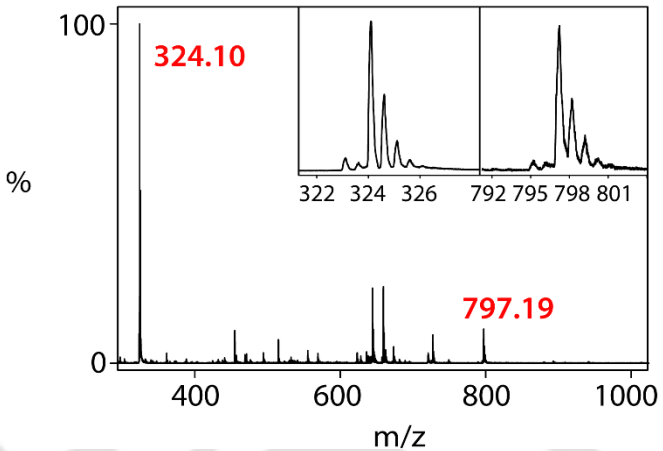

Fig. 4.3. ESI-MS spectrum of **3c** in CH_3CN. Insets shows the isotopic distribution patterns for the peaks at *m/z* 324.10 and 797.19.

Unfortunately, under normal mass separation-conditions, unlike the case of $[Fe^{IV}(O)(Bntpen)(OTf)]^+$, we did not manage to obtain a clear spectrum most probably due to thermal degradation of the intermediate under routine mass spectrometry conditions. This indicates weaker Fe=N bonding in **3c** than the Fe=O bonding in **3b** and **4b**, which is also evident from the corresponding stretch vibrations discussed later. Their thermal stability values at 298 K also reflect the same trend of bond strengths ($t_{1/2}$ of **3b** = ~6 h while t1/2 of **3c** = ~3 h).

However, the mass spectrum was obtained by infusing cold samples directly into the source (Fig. 4.3). The spectrum shows a major peak at *m/z* 324.10 that can be attributed to the ion cluster $[Fe^{IV}(Bntpen)(NTs)]^{2+}$ (calculated *m/z* 324.0979) and a smaller peak at *m/z* 797.19 corresponding to $[Fe^{IV}(Bntpen)(NTs)(OTf)]^+$ (calculated *m/z* 797.1490). Another peak at *m/z* 644.16 most likely can be assigned to traces of $[Fe^{IV}(O)(Bntpen)(OTf)]^+$ in the sample which thereby implicates the hydrolysis of the oxidant, PhINTs into PhIO (most probably this is due to the trace amount of water present in the solvent that enables oxidant exchange under ESI-MS conditions). Under normal conditions though, addition of water does not hydrolyse **3c** into **3b**.

In the ^{1}H-NMR spectrum, the Fe(II) complex, $[Fe^{II}(Bntpen)(CH_3CN)]^{2+}$ (**3a**) in $CDCl_3$ shows a paramagnetic shift of peaks to higher δ values which is typical for an S = 2 spin state on iron (see Fig. 4.4).[57,71]

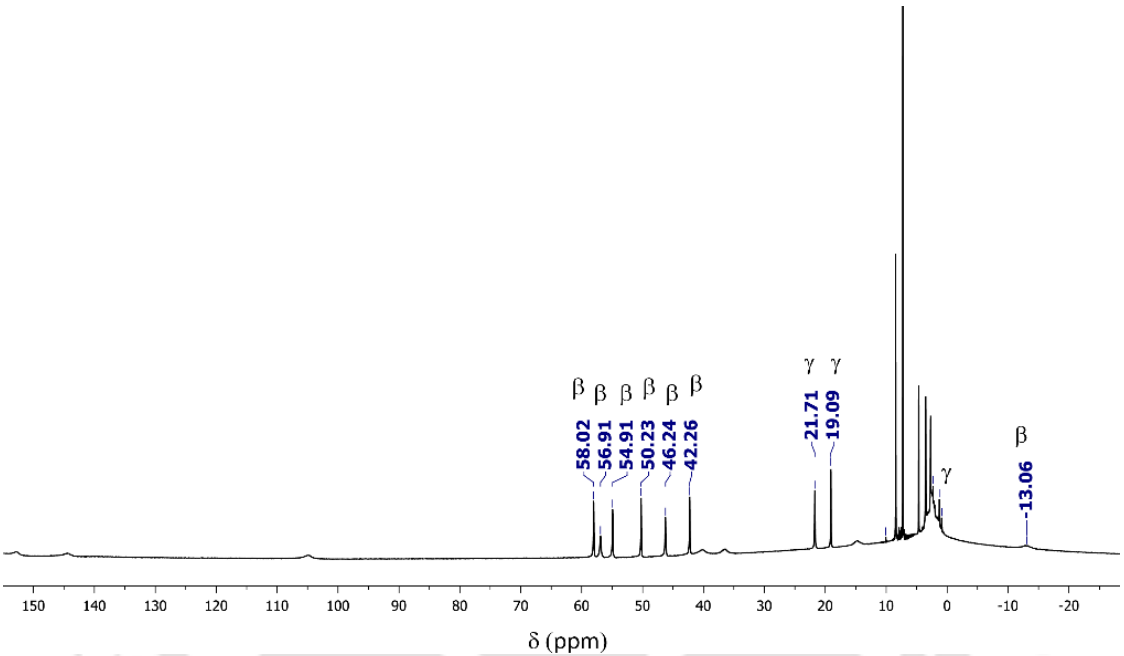

Fig. 4.4. ^{1}H-NMR (400 MHz) spectrum of the complex, $[Fe^{II}(Bntpen)(CH_3CN)]^{2+}$ (**3a**) in $CDCl_3$ at 295 K with a spectral width of ~200 ppm (scans: 128). The peaks have been assigned based of previously reported literature.[72-74]

By contrast, both the ferryl complexes, $[Fe^{IV}(O)(Bntpen)]^{2+}$ (**3b**) and $[Fe^{IV}(NTs)(Bntpen)]^{2+}$ (**3c**), give characteristic shifts in the NMR spectra of the S = 1 Fe centres in CD_3CN (Fig. 4.5 and 4.6).[36,42,71] The overall NMR spectra for **3b** and **3c** are more complicated than those of **4b** and **4c** due to lack of symmetry in the Bntpen ligand framework as compared to the N4Py.[57, 64, 71] In **3b** and **3c**, there are pyridine rings both perpendicular and parallel to the Fe=X axis (X = O, N) rendering an uneven shift pattern due to unequal interactions of the pyridine rings with the Fe=X core.[64] The unique shift pattern of the pyridine β-protons to positive (downfield) and negative (upfield) δ values

infers that the Fe centre is oxidized to the $^{+4}$ oxidation state, which is linked to the terminal oxidant being oxo or NTs (see Fig. 4.5 and 4.6).

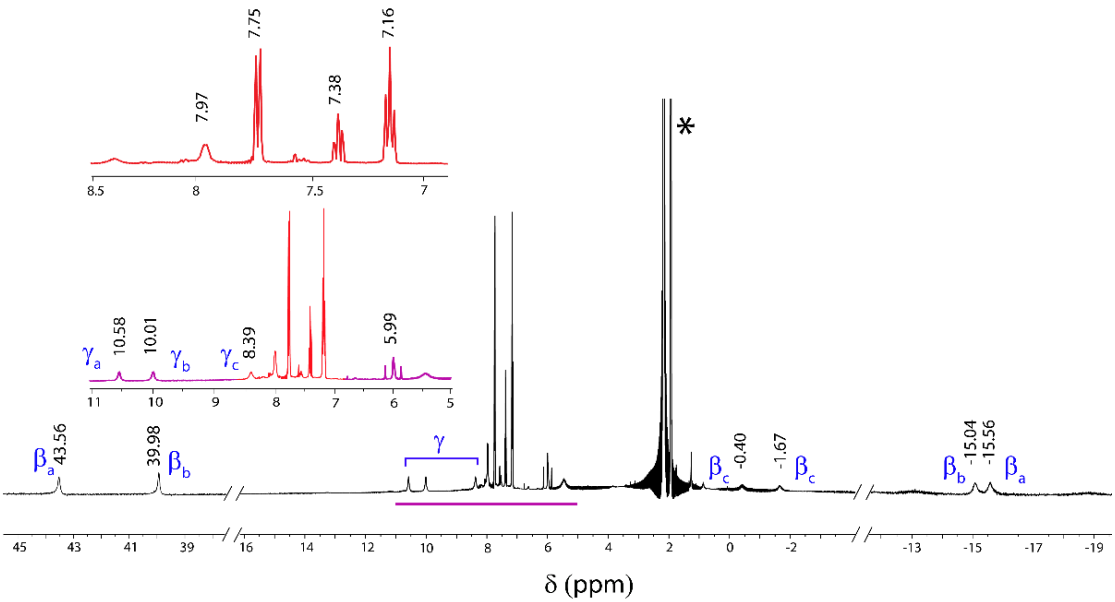

Fig. 4.5. ^{1}H-NMR (400 MHz) spectrum of the complex, $[Fe^{IV}(O)(Bntpen)]^{2+}$ (**3b**) in CD_3CN at 295 K with a spectral width of ~200 ppm (scans: 256). The peaks have been assigned based on previously reported literature.[36,57,67,71] Residual solvent peaks are denoted by *.

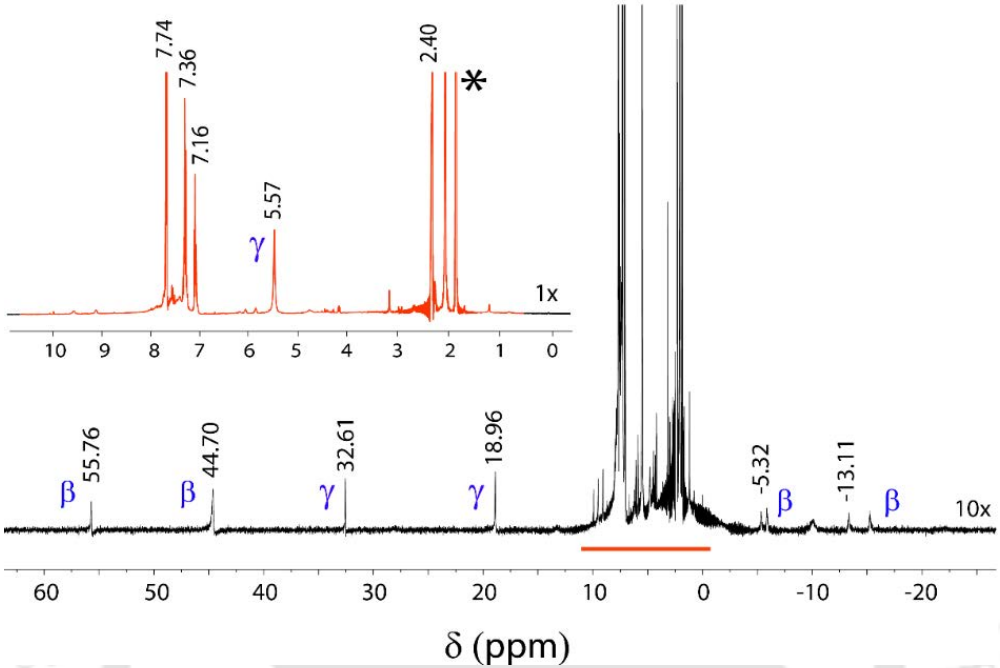

Fig. 4.6. ^{1}H-NMR (400 MHz) spectrum of the complex, $[Fe^{IV}(NTs)(Bntpen)]^{2+}$ (**3c**) in CD_3CN at 295 K with a spectral width of ~200 ppm (scans: 256). The peaks have been assigned based on previously reported literature.[36,42] Peaks at δ 7.74 and δ 7.36 ppm correspond to tosyl resonances belonging to the tosylimide ligated to the iron centre as reported for similar Fe(IV)=NTs complex, **4c**.[42] The ^{1}H-NMR spectrum of the oxidant, PhINTs, is reported to signal at δ 2.30 ppm (CH_3) and δ 7.00-7.80 ppm (aromatic protons)[75]. Residual solvent peaks are denoted by *.

FTIR spectra were recorded on a Perkin Elmer FTIR spectrometer at 298 K. The Fe(IV)=O stretching vibrations are usually around 830-850 cm^{-1}. However, the resonance RAMAN studies on **4c** indicates signals at around 998 cm^{-1} corresponding to the Fe=N stretching vibration.[36] Similar Fe(IV)=NTs complexes like $[Fe^{IV}(NTs)(MePy_2tacn)](OTf)_2$ and $[Fe^{IV}(NTs)(Me_2(CHPy_2)tacn)](OTf)_2$ with pentadentate ligand frameworks have shown stretching vibrations around 984 cm^{-1}.[36] The FTIR spectrum shown in Fig. 4.7 for **3c** shows a transmittance at 997 cm^{-1} which corresponds to the Fe=N vibration.

TH-3026_166122104

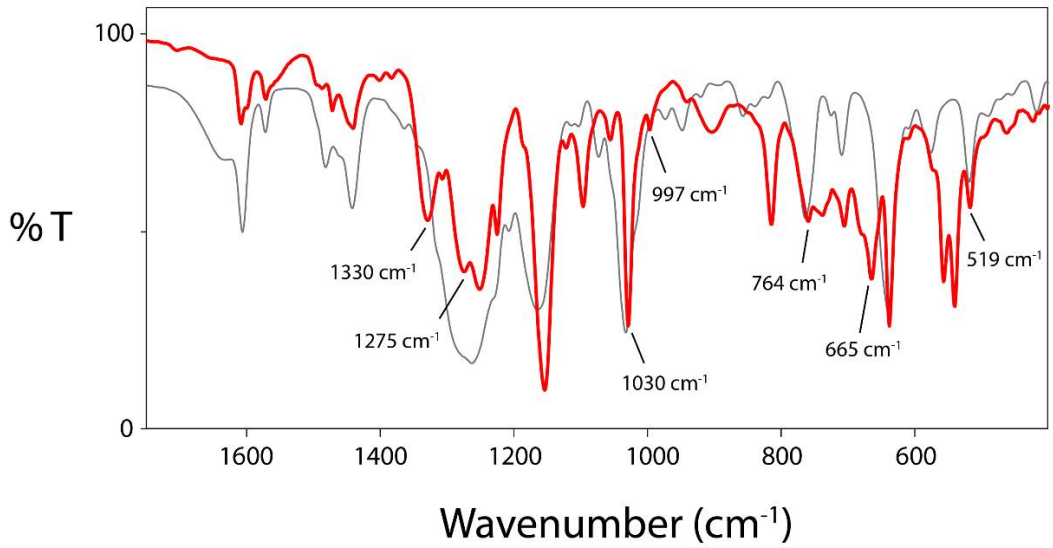

Fig. 4.7. FTIR spectra of complex $[Fe^{IV}(NTs)(Bntpen)]^{2+}$, **3c** (red line) in CH_3CN at 298 K. Black line shows the same for the Fe(II)-complex, $[Fe^{II}(Bntpen)(OTf)]^{+}$. The peak at 997 cm^{-1} is assigned to the Fe=N stretching frequency in **3c**.

4.2.2. Reaction Kinetics

To understand the oxidative properties of complex **3c**, we decided to investigate its heteroatom transfer reactivity to thioanisole as the model substrate. As reported previously, complex **4c**, $[Fe^{IV}(NTs)(N4Py)]^{2+}$ is five times more reactive than its oxo counterpart **4b**.[47,48] Surprisingly, in the case of Bntpen, an opposite trend was observed to that found for N4Py. Unlike N4Py, the NTs complex **3c** reacts sluggishly with thioanisole with considerably lower rate constants than those seen for the corresponding oxo complex **3b**.[47,48] The second-order rate constant for the reaction of **3c** with thioanisole was 5.4 x 10^{-2} M^{-1} s^{-1} at 298 K, whereas for the same reaction with **4c**, a value of 26 x 10^{-2} M^{-1} s^{-1} was reported at 273 K.[47,48] Thus the rate of the reaction for **3c** is expected to be even slower at 273 K, although we were not able to record it at that temperature due to solubility issues. The slower reaction rate of **3c** with thioanisole is, therefore, speculated to originate from a group transfer reaction instead of an electron transfer mechanism.

Table 4.1. Hammett parameters and second-order rate constants (k_2) determined in the reaction of 3c (1 mM solution in CH_3CN) with various *para*-substituted thioanisole substrates in CH_3CN at 298 K.[a]

p-X	σ_p [b]	σ_p+ [b]	k_2 (M^{-1} s^{-1})	k_X/k_H [c]	log (k_X/k_H)
-OMe	–0.27	–0.78	541.4×10^{-2}	100.3	2.00
-Me	–0.17	–0.31	22.9×10^{-2}	4.2	0.63
-H	0.00	0.00	5.4×10^{-2}	1.0	0.00
-Cl	0.23	0.11	2.7×10^{-2}	0.5	–0.30

[a]All the reactions were followed by monitoring the UV/Vis spectral changes of the reaction solution. [b]Data taken from the reported literature.[68] [c]Relative rate constant obtained by dividing the k_2 of *p*-X-thioanisole by k_2 of *p*-H-thioanisole.

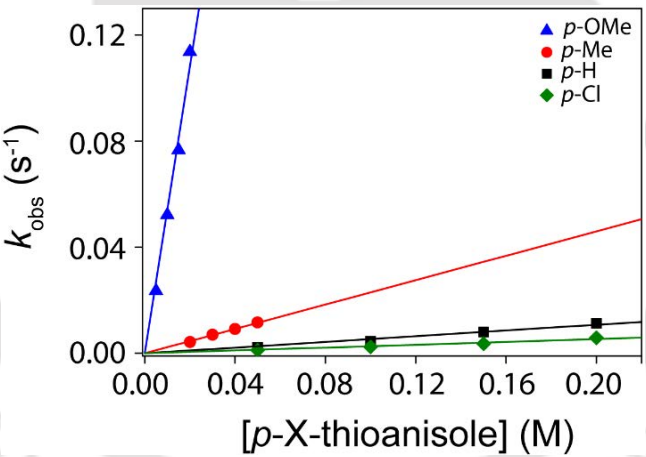

Fig. 4.8. Plot of k_{obs} against substrate concentration to determine second order rate constants for the reactions of **3c** (1 mM) with *para*-X-thioanisole (X = -OMe ▲, -Me ●, -H ■, -Cl ◆) in CH_3CN at 298 K.

In order to establish the mechanism with conviction, we repeated the reaction using various *para*-substituted thioanisole substrates at 298 K to obtain second order rate constants (Fig. 4.8). Then these second order rate constants were plotted against the *para*-substituent constant (σ_p) for each substrate to obtain a Hammett plot (Table 4.1).[68-70] A

large negative slope ρ = - 4.13 is found, which is indicative of an electron transfer reaction (Fig. 4.9). This value is larger than the one for N4Py where a negative slope of –3.36 has been reported corresponding to electron transfer reaction.[47] Thus the *para*-substituents on the thioanisole substrates contribute with quite a substantial effect on the rates of the reactions for **3c**.

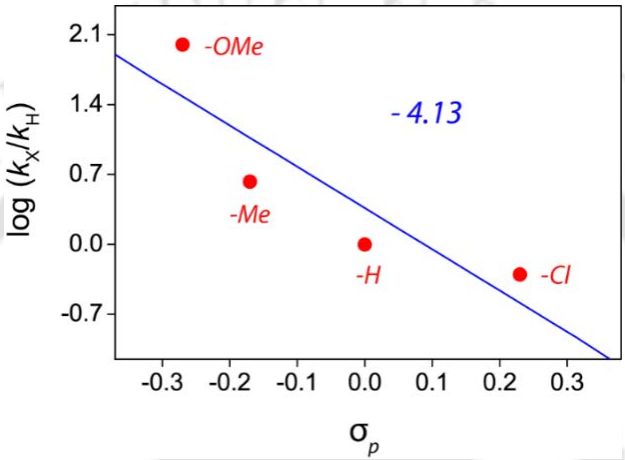

Fig. 4.9. Hammett plot obtained by plotting the log(k_X/k_H) values against σ_p values[75] of *para*-X-thioanisole (X = OMe, Me, H and Cl) substrates for their reaction with **3c** in CH_3CN at 298 K.

The huge slope in the Hammett plot implicates an additional stabilization of positive charge in the transition state by electron-donating groups in the *para*-position of thioanisole and thus enhances the overall rate of the reaction when methoxy or methyl groups are employed. Therefore, the σ_p values for the barrier heights for the reaction of *para*-substituted thioanisole with $[Fe^{IV}(NTs)(Bntpen)]^{2+}$ are insufficiently negative for electron-rich *para*-substituents. In order to accommodate this effect, the Hammett plot was replotted using σ_p^+ on the x-axis instead, where the scale is shifted to further negative values of the substituent constants and thereby produces a better fitting. Thus, a ρ value of –2.55 was obtained (Fig. 4.10b) with a better fitting correlation to the experimental data. Complex **4c**, in comparison, produced a negative slope of –1.92 when the rates were plotted against σ_p^+.[47] Nevertheless, these values from the Hammett plots for **3c** are

DOI: 10.26678/ABCD.CHEM.2026.166122104

substantial evidence of an operating electron transfer mechanism in spite of slower reaction rates than the fellow tosylimido complex **4c**.

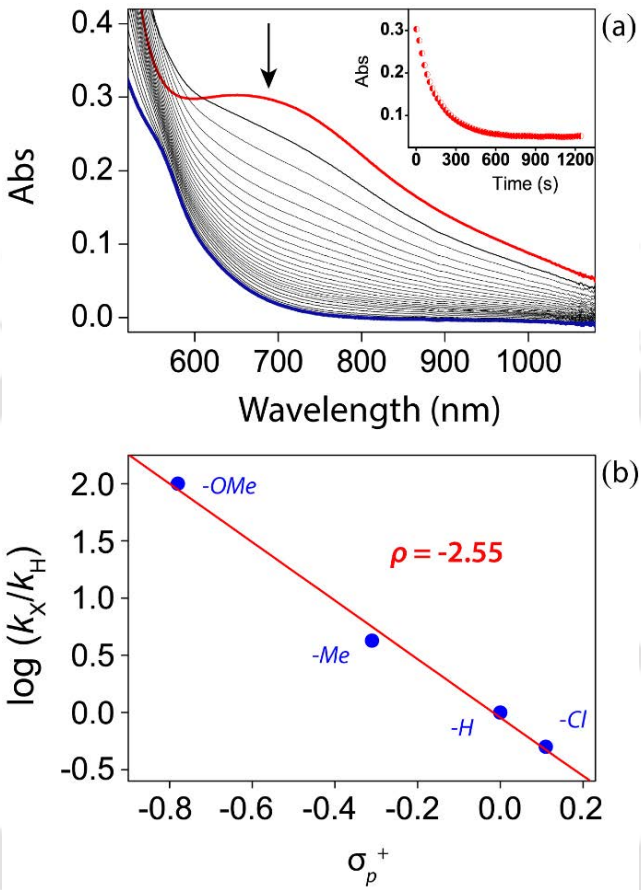

Fig. 4.10. (a) Decay profile for the 750 nm band due to addition of 150 equiv. of thioanisole to **3c** in CH_3CN at 298 K; inset shows the time trace corresponding to the same decay. (b) Hammett plot obtained by plotting the log (k_X/k_H) values against the σ_p^+ Hammett values of *para*-X-thioanisole (X = OMe, Me, H and Cl) substrates in their reaction with **3c** in CH_3CN at 298 K.

The iron(IV)-tosylimido complexes are usually weaker oxidants then their corresponding iron(IV)-oxo counterparts towards C–H abstraction reactions and often cannot react with substrates with sacrificial C–H bond dissociation energies (BDE) larger than ~80 kcal mol^{-1}. By contrast, the iron(IV)-oxo species of both Bntpen and N4Py are known to react with cyclohexane (BDE = 99 kcal mol^{-1})[64,76-79] by hydrogen atom

abstraction. We tested the alcohol oxidation reactivity of **3c** using benzyl alcohol as the model substrate, (Fig. 4.11) and compared the results with the other oxidants. However, In the case of benzyl alcohol, the activation of the methylene C–H bond by **3c** was investigated at 298 K and led to the formation of benzaldehyde although at a slower rate compared to the analogous $[Fe^{IV}(NTs)(N4Py)]^{2+}$ complex. While the second-order rate constant for benzyl alcohol oxidation by **4c** was reported to be 1.48 x 10^{-2} M^{-1} s^{-1}, the same reaction with **3c** as oxidant revealed a second-order rate constant of 0.39 x 10^{-2} M^{-1} s^{-1} at 298 K (Fig. 4.11).[48] Thus the iron(IV)-tosylimido complex of Bntpen reacts even slower with substrates than the one with N4Py ligand.

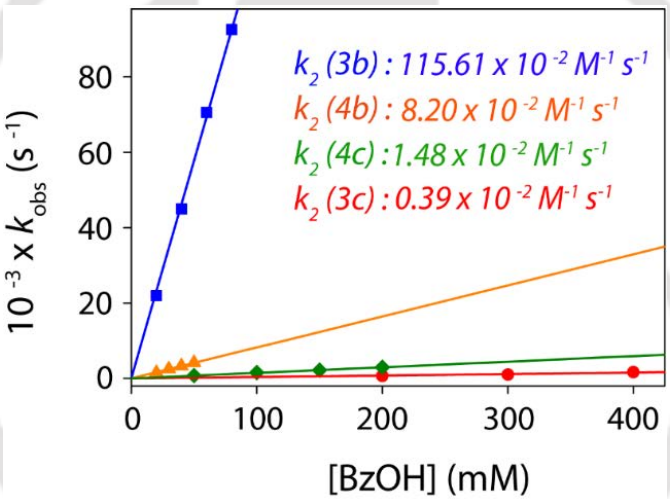

Fig. 4.11. Second order rate constants determined for the reaction of benzyl alcohol (BzOH) with **3b** (■), **3c** (●), **4b** (▲) and **4c** (◆), in CH_3CN at 298 K.

A comparison of the $[Fe^{IV}(O)(Bntpen)]^{2+}$ (**3b**) and $[Fe^{IV}(NTs)(Bntpen)]^{2+}$ (**3c**) complexes shows that **3c** reacts 300 times slower than complex **3b** under comparable reaction conditions. Thus, as compiled in Fig. 4.11, the $[Fe^{IV}(O)(Bntpen)]^{2+}$ complex (**3b**) is 14 times more reactive than the $[Fe^{IV}(O)(N4Py)]^{2+}$ complex (**4b**), whereas, the $[Fe^{IV}(NTs)(Bntpen)]^{2+}$ complex (**3c**) is four times slower than the $[Fe^{IV}(NTs)(N4Py)]^{2+}$ complex (**4c**) towards an alcohol oxidation reaction.[26-29]

Kinetic isotope effect (KIE) studies were performed on **3c** using benzyl alcohol-[D_7] as a substrate and a KIE value of 4 was obtained (Fig. 4.12 and Table 4.2). Hence, the KIE experiment reveals hydrogen atom abstraction as the rate determining step in the reaction mechanism. A similar KIE value of 7 was obtained for complex **4c**, which suggests an analogous reaction mechanism.[48] Unlike the iron(IV)-tosylimido group, the corresponding iron(IV)-oxo complexes produce higher KIE values, probably due to tunnelling like mechanism.[47,48]

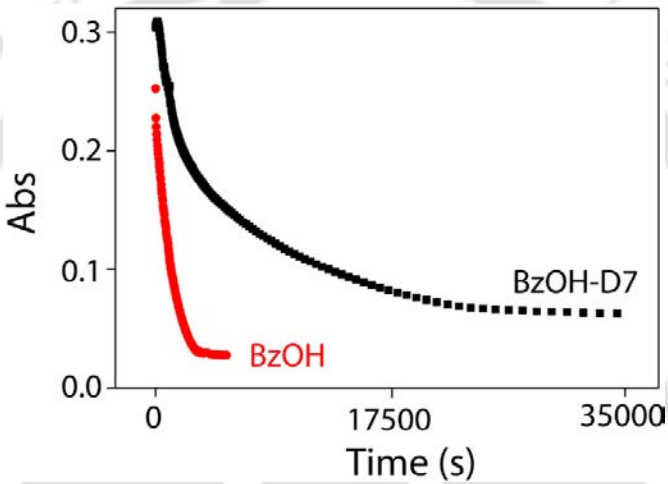

Fig. 4.12. Decay profile for the reaction of $[Fe^{IV}(NTs)(Bntpen)]^{2+}$ (**3c**) (1 mM) with 300 equivalents of benzyl alcohol (BzOH, ●) and benzyl alcohol-D_7 (BzOH-D7, ■) in CH_3CN at 298 K.

To ascertain the effect of intrinsic parameters including electron donating or withdrawing groups on the reacting substrate, we repeated the reactions using 200 equivalents of *para*-OMe, –Me, –H and –Cl substituents of benzyl alcohol. The reaction of **3c** with each of these substrates follows pseudo first-order kinetics, as excess amounts (200 equiv.) of substrate concentrations were employed to obtain the pseudo first-order rate constant (k_{obs}) values (Table 4.3).

Table 4.2. Pseudo first-order rate constant (k_{obs}) for the reaction of 1 mM of 3c with excess benzyl alcohol and benzyl alcohol-D_7 at 298 K.

Complex	Substrate concentration [300 mM]		KIE
	Benzyl alcohol	Benzyl alcohol – D_7	
3c	1.064×10^{-3}	2.814×10^{-4}	4

Table 4.3. Hammett parameters and pseudo first-order rate constants (k_{obs}) determined in the reaction of 3c (1 mM) with various *para*-substituted benzyl alcohols (200 mM) in CH_3CN at 298 K.[a]

p-X	σ_p [b]	σ_p^+ [b]	k_{obs} (s^{-1}) x 10^{-4}	k_x/k_H [c]	log (k_x/k_H)
-OMe	–0.27	–0.78	57.40	7.90	0.89
-Me	–0.17	–0.31	9.94	1.37	0.14
-H	0.00	0.00	7.26	1.00	0.00
-Cl	0.23	0.11	4.76	0.65	–0.18

[a]All the reactions were followed by monitoring the UV/Vis spectral changes of the reaction solution. [b]Data taken from the reported literature.[68]. [c]Relative rate constant obtained by dividing the k_{obs} of *p*-X-benzyl alcohol by k_{obs} of *p*-H- benzyl alcohol.

Table 4.4. Hammett parameters and second-order rate constants (k_2) determined for the reaction of 3b (1 mM) with various *para*-substituted benzyl alcohols in CH_3CN at 298 K.[a]

p-X-benzyl alcohol	σ_p [b]	σ_p^+ [b]	k_2 (M^{-1} s^{-1})	k_X/k_H [c]	log (k_X/k_H)
-OMe	–0.27	–0.78	0.865	1.469	0.167
-Me	–0.17	–0.31	0.623	1.058	0.024
-H	0.00	0.00	0.589	1.000	0.000
-Cl	0.23	0.11	0.371	0.628	–0.202

[a] All the reactions were followed by monitoring the UV/Vis spectral changes of the reaction solution. [b] Data taken from ref.[68] [c] Relative rate constant obtained by dividing the k_2 of *p*-X-benzyl alcohol by k_2 of *p*-H-benzyl alcohol.

A Hammett plot of the natural logarithm of the rate constant ratio of *para*-X-benzyl alcohol activation versus benzyl alcohol against σ_p^+ Hammett parameter gives a ρ value of –1.16 for **3c** which is close to the value reported above for complex **4c** (Table 4.4 and Fig. 4.13).[48] This Hammett value is indicative of substantial positive charge build-up in the transition state. Therefore, the reaction rates are strongly affected by tuning the electronic charge content in the reacting substrates during the transition state.

Other hydrocarbon substrates *viz*. xanthene, 9,10-dihydroanthracene (DHA) and fluorene, were tested for C–H abstraction reactions using **3c** as the catalyst in order to envisage a comparative trend with complex **4c**. However, those reaction results were not pertinent due to solubility issues in CH_3CN. Therefore, unlike the $[Fe^{IV}(NTs)(N4Py)]^{2+}$ (**4c**) complex, the $[Fe^{IV}(NTs)(Bntpen)]^{2+}$ (**3c**) is a less effective oxidant than its corresponding iron(IV)-oxo analogue in both the heteroatom amination and C–H abstraction reactions.

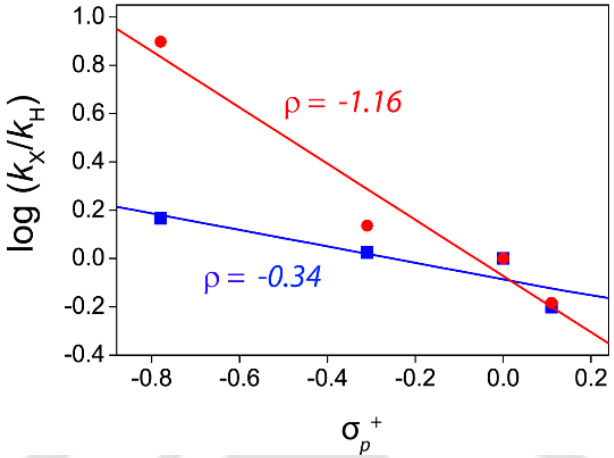

Fig. 4.13. Hammett plot obtained by plotting the log (k_X/k_H) against σ_p^+ values of *para*-X-benzyl alcohol (X = OMe, Me, H and Cl) substrates (200 equiv.) in their reaction with **3b** (●) and **3c** (■) in CH_3CN at 298 K.

4.2.3. Computational Backup

To complement our understanding on the reactivity differences of $[Fe^{IV}(X)(Bntpen)]^{2+}$ vs $[Fe^{IV}(X)(N4Py)]^{2+}$ with X = NTs/O, we performed a density functional theory study with 1,3-cyclohexadiene (CHD) and dimethylsulfide (DMS) as model substrates. CHD dehydrogenation is a stepwise process with two sequential hydrogen atom abstraction steps (via transition states $TS1_{CHD}$ and $TS2_{CHD}$) that passes a radical intermediate ($IR1_{CHD}$) to ultimately form the benzene product (Prd_{CHD}). Heteroatom transfer (NTs or O) to sulphide is a concerted reaction with a single transition state (TS_{DMS}) leading to products (Prd_{DMS}).

Before going into detail of the reaction mechanisms with substrates, let us first look into the electronic properties of the iron(IV)-oxo and iron(IV)-imido reactants with Bntpen ligand system. Thus, the high-lying occupied and low-lying virtual orbitals of $[Fe^{IV}(NTs)(Bntpen)]^{2+}$ and $[Fe^{IV}(O)(Bntpen)]^{2+}$ and the optimized geometries are given in Fig. 4.14. In both $[Fe^{IV}(NTs)(Bntpen)]^{2+}$ and $[Fe^{IV}(O)(Bntpen)]^{2+}$ the triplet spin state is

the ground state, which matches experimental studies as well as previous DFT calculations.[42,78-82] The five metal 3d-orbitals are occupied with four electrons and the lowest energy conformation is the triplet spin state with $\delta_{xy}^2\ \pi^*_{xz}{}^1\ \pi^*_{yz}{}^1$ occupation (Fig. 4.14) This is commonly seen in hexacoordinated iron(IV)-oxo species and matches previous computational studies on non-heme iron complexes.[83-90] The alternative quintet spin state has orbital occupation $\delta_{xy}{}^1\ \pi^*_{xz}{}^1\ \pi^*_{yz}{}^1\ \sigma^*_{x2-y2}{}^1$. This state is ΔE + ZPE = 2.0 kcal mol^{-1} higher in energy than the triplet spin state for the iron(IV)-tosylimido complex, whereas in the iron(IV)-oxo species it is higher by 1.5 kcal mol^{-1}. As such, the change from oxo to tosylimido in the iron(IV)-Bntpen complex has little effect on the spin state ordering and relative energies.

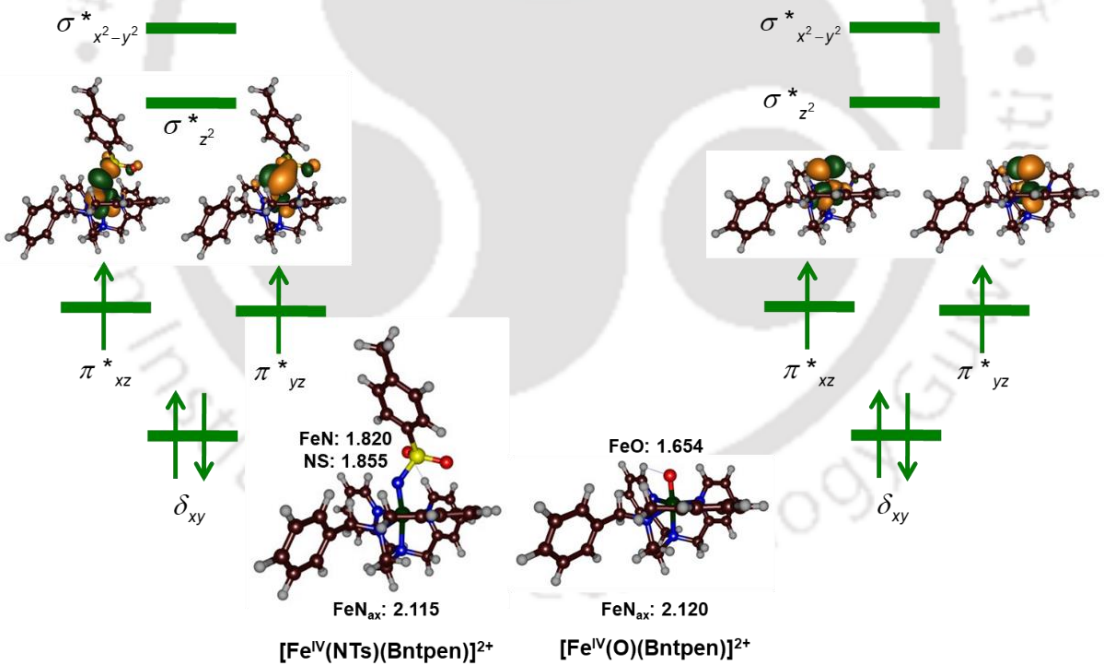

Fig. 4.14. Optimized geometries and molecular orbital occupation of $[Fe^{IV}(NTs)(Bntpen)]^{2+}$ (**3c**) and $[Fe^{IV}(O)(Bntpen)]^{2+}$ (**3b**)as obtained with DFT. Bond lengths are in angstroms.

Next, we explored the dehydrogenation of cyclohexadiene (CHD) by both complexes and the results are given in Fig. 4.15. We located transition state structures for the triplet spin surface; however, on the quintet spin state the transition from reactants to intermediates is facile and no barrier could be located. In the triplet spin state reaching the radical intermediate is an exergonic process by –17.0 / –16.2 kcal mol^{-1} for $[Fe^{IV}(NTs)(Bntpen)]^{2+}$ versus $[Fe^{IV}(O)(Bntpen)]^{2+}$. In the next step a second hydrogen atom abstraction takes place, which is facile and leads to products with large exothermicity. As such on the triplet spin state surface the initial hydrogen atom abstraction is rate-determining. The transition state is shown in Fig. 4.15 and displays an early structure with short C–H distance of 1.271Å and a much longer N–H distance of 1.544Å. Interestingly, the transition state for the iron(IV)-oxo species in the triplet spin

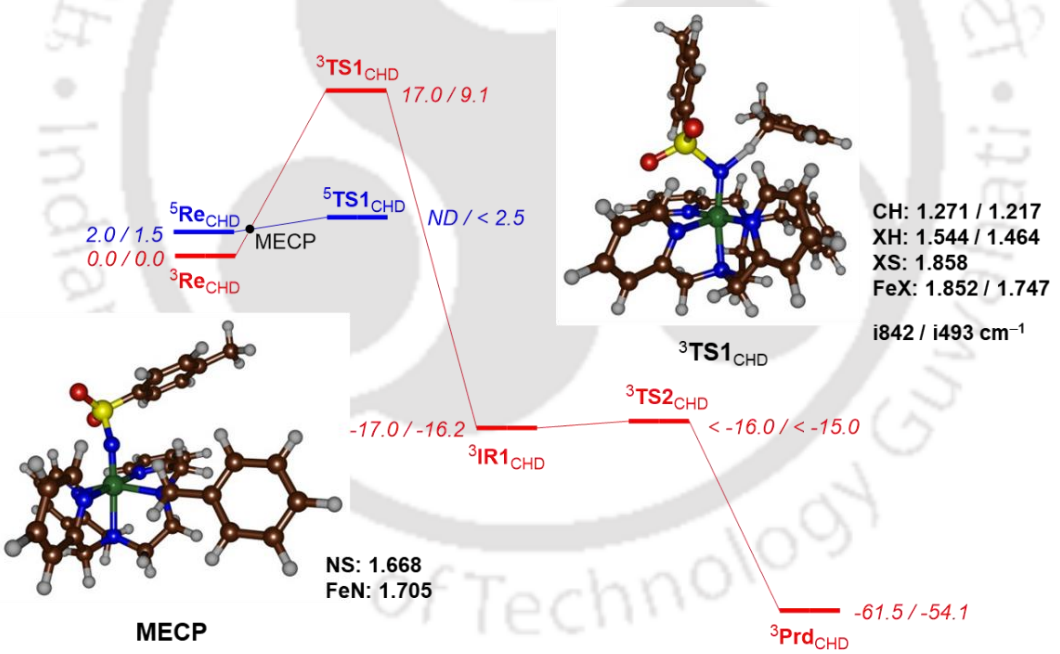

Fig. 4.15. UB3LYP/BS2//UB3LYP/BS1 calculated reaction mechanism for CHD activation by $[Fe^{IV}(NTs)(Bntpen)]^{2+}$ (**3c**)/ $[Fe^{IV}(O)(Bntpen)]^{2+}$ (**3b**). Energies obtained at UB3LYP/BS2//UB3LYP/BS1 and contain zero-point and solvent corrections (in kcal mol^{-1}). Optimized geometries of the transition states and MECP give distances in angstroms and the imaginary frequencies are in cm^{-1}.

state is very similar with a C–H distance of 1.217Å and an O–H distance of 1.464Å. Energetically; however, they are very different and ^{3}**TS1**$_{CHD,NTs}$ is 17.0 kcal mol^{-1} above reactants, while the corresponding iron-oxo transition state only has a barrier of 9.1 kcal mol^{-1}. Subsequently, we evaluated substrate sulfoxidation by using DMS as a model substrate. As before, the reaction is concerted via a single intermediate to give sulfoxide products.[91,92] Similarly to the hydrogen atom abstraction process in Fig 4.15, also sulfoxidation has a high energy barrier on the triplet spin state (25.6 kcal mol^{-1})on the triplet spin state (25.6 kcal mol^{-1}) for the [Fe^{IV}(NTs)(Bntpen)]$^{2+}$ oxidant, while it is much lower for the [Fe^{IV}(O)(Bntpen)]$^{2+}$ system at 10.1 kcal mol^{-1}. The transition state structures shown in Fig 4.16 display a long N–S distance between tosylimido and substrate of 2.344 Å, while the iron-oxo system has the transition state at a distance of 2.083 Å. In addition,

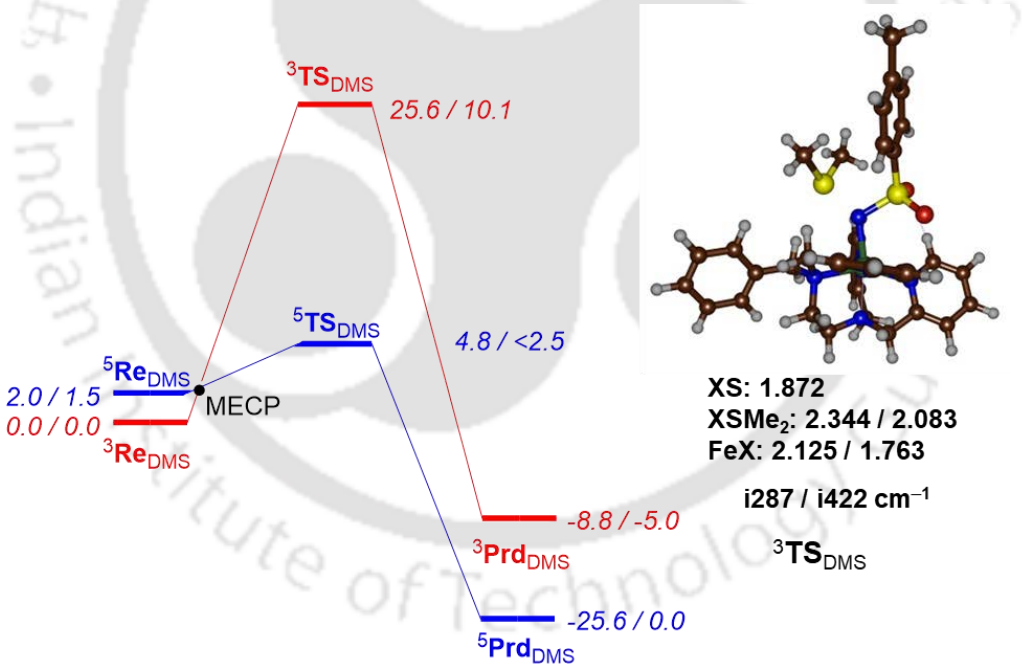

Fig. 4.16. UB3LYP/BS2//UB3LYP/BS1 calculated reaction mechanism for DMS activation by [Fe^{IV}(NTs)(Bntpen)]$^{2+}$ (**3c**)/ [Fe^{IV}(O)(Bntpen)]$^{2+}$ (**3b**). Energies obtained at UB3LYP/BS2//UB3LYP/BS1 and contain zero-point and solvent corrections (in kcal mol^{-1}). Optimized geometries of the transition states give distances in angstroms and the imaginary frequencies are in cm^{-1}.

the imaginary frequency in the transition state is large for the oxo-transfer (i422 cm^{-1}), while tosylimido transfer gives an imaginary frequency of only i287 cm^{-1}. These relative barriers contrast those found for the analogous N4Py system,[48] that found faster reactivity with sulfides for the iron(IV)-tosylimido complex.

To understand the differences in properties and reactivity of the four set of oxidants investigated here, i.e. $[Fe^{IV}(NTs)(Bntpen)]^{2+}$, $[Fe^{IV}(O)(Bntpen)]^{2+}$, $[Fe^{IV}(NTs)(N4Py)]^{2+}$ and $[Fe^{IV}(O)(N4Py)]^{2+}$, we calculated the thermochemical properties of each of these reactant species. Firstly, we calculated the X–H (X = NTs/O) bond dissociation energy (BDE_{XH}) as the difference in energy between the iron(IV)-oxo/iron(IV)-tosylimido species, a hydrogen atom and the corresponding iron(III)-hydroxo/iron(III)-hydrotosylimido species. We also calculated the one-electron reduction potential or electron affinity (EA) as the adiabatic energy difference of the iron(IV)-tosylimido/iron(IV)-oxo and the one-electron reduced species. As before,[93-95] we calculated the gas-phase acidity (ΔG_{acid}) from the difference in BDE_{XH}, EA and the ionization energy of a hydrogen atom (I_{EH}) using the experimentally reported value of I_{EH} = 313.9 kcal mol^{-1}.[96] The calculated values for BDE_{XH}, EA and ΔG_{acid} of the four iron(IV) oxidants are 82.0, 88.8, 83.1 and 90.7 kcal mol^{-1} for $[Fe^{IV}(O)(Bntpen)]^{2+}$ (**3b**), $[Fe^{IV}(NTs)(Bntpen)]^{2+}$ (**3c**), $[Fe^{IV}(O)(N4Py)]^{2+}$ (**4b**) and $[Fe^{IV}(NTs)(N4Py)]^{2+}$ (**4c**), respectively. As can be seen the four BDE_{XH} values range within a narrow window from 82.0 kcal mol^{-1} for the $[Fe^{IV}(O)(Bntpen)]^{2+}$ species to 90.7 kcal mol^{-1} for the $[Fe^{IV}(NTs)(N4Py)]^{2+}$ system. Nevertheless, the two iron(IV)-oxo species have similar BDE_{XH} values and so do the pair of iron(IV)-tosylimido complexes. Based on this, similar hydrogen atom abstraction barriers from substrates for the pair of iron(IV)-oxo and iron(IV)-tosylimido complexes are expected.

4.3. Conclusion

In this work we present a combined experimental and computational study on the properties and reactivities of iron(IV)-oxo and iron(IV)-tosylimido complexes. In particular, we synthesize and spectroscopically characterize the iron(IV)-tosylimido and iron(IV)-oxo complexes with the pentacoordinate ligand system, Bntpen, and compared with those of the existing N4Py framework. Its spectroscopic fingerprint shows similar features as the analogous N4Py ligated system, particularly in the UV/Vis spectrum. Subsequently, a series of reactivity studies with iron(IV)-oxo and iron(IV)-tosylimido was done with respect to *para*-X-thioanisole and *para*-X-benzyl alcohol as substrate. Overall, the iron(IV)-tosylimido complexes with Bntpen ligand are weaker oxidants for hydrogen atom abstraction and group transfer reactions than their corresponding iron(IV)-oxo species. We then did a computational study to support the experiments and find that generally the iron(IV)-tosylimido forms strong N–H bonds after hydrogen atom abstraction but has a larger redox potential and therefore reacts slower with substrates.

4.4. References

1. E. I. Solomon, T. C. Brunold, M. I. Davis, J. N. Kemsley, S.-K. Lee, N. Lehnert, F. Neese, A. J. Skulan, Y.-S. Yang, J. Zhou, *Chem. Rev.* **2000**, *100*, 235-350.
2. T. D. H. Bugg, *Curr. Opin. Chem. Biol.* **2001**, *5*, 550-555.
3. M. J. Ryle, R. P. Hausinger, *Curr. Opin. Chem. Biol.* **2002**, *6*, 193-201.
4. M. Costas, M. P. Mehn, M. P. Jensen, L. Que Jr, *Chem. Rev*. **2004**, *104*, 939-986.
5. B. Meunier, S. P. de Visser, S. Shaik, *Chem. Rev.* **2004**, *104*, 3947-3980.
6. K. M. Kadish, K. M. Smith, R. Guilard (Eds.), Handbook Of Porphyrin Science, World Scientific Publishing Co., New Jersey, 2010.
7. X. Huang, J. T. Groves, *Chem. Rev*. **2018**, *118*, 2491-2553.
8. B. K. Burgess, D. J. Lowe, *Chem. Rev*. **1996**, *96*, 2983-3012.
9. B. M. Hoffman, D. Lukoyanov, D. R. Dean, L. C. Seefeldt, *Acc. Chem. Res.* **2013**, *46*, 587-595.
10. R. R. Eady, S. V. Antonyuk, S. S. Hasnain, *Curr. Opin. Chem. Biol.* **2016**, *31*, 103-112.
11. R. E. White, M. B. McCarthy, *J. Am. Chem. Soc.* **1984**, *106*, 4922-4926.
12. E. W. Svastits, J. H. Dawson, R. Breslow, S. H. Gellman, *J. Am. Chem. Soc*. **1985**, *107*, 6427-6428.
13. J.-P. Mahy, G. Bedi, P. Battioni, D. Mansuy, J. Chem. Soc. *Perkin Trans. II* **1988**, 1517-1524.
14. G. Sabenya, L. L zaro, I. Gamba, V. Martin-Diaconescu, E. Andris, T. Weyherm ller, F. Neese, J. Roithova, E. Bill, J. Lloret-Fillol, M. Costas, *J. Am. Chem. Soc*. **2017**, *139*, 9168-9177.
15. J. C. Price, E. W. Barr, B. Tirupati, J. M. Bollinger Jr, C. Krebs, *Biochemistry* **2003**, *42*, 7497-7508.
16. D. A. Proshlyakov, T. F. Henshaw, G. R. Monterosso, M. J. Ryle, R. P. Hausinger, *J. Am. Chem. Soc.* **2004**, *126*, 1022-1023.

17. J. M. Bollinger Jr., J. C. Price, L. M. Hoffart, E. W. Barr, C. Krebs, Eur. J. *Inorg. Chem.* **2005**, 4245-4254.
18. M. Atanasov, P. Comba, S. Hausberg, B. Martin, *Coord. Chem. Rev*. **2009**, *253*, 2306-2314.
19. M. Costas, *Coord. Chem. Rev*. **2011**, *255*, 2912-2932.
20. C. V. Sastri, J. Lee, K. Oh, Y. J. Lee, J. Lee, T. A. Jackson, K. Ray, H. Hirao, W. Shin, J. A. Halfen, J. Kim, L. Que Jr., S. Shaik, W. Nam, *Proc. Natl. Acad. Sci. U. S. A.* **2007**, *104*, 19181-19186.
21. C. Buron, K. Sénéchal-David, R. Ricoux, J.-P. Le Caër, V. Guérineau, P. Méjanelle, R. Guillot, C. Herrero, J.-P. Mahy, F. Banse, *Chem. Eur. J*. **2015**, *21*, 12188-12193.
22. X. Engelmann, I. Monte-Pérez, K. Ray, *Angew. Chem. Int. Ed.* **2016**, *55*, 7632-7649.
23. K. Ray, F. F. Pfaff, B. Wang, W. Nam, *J. Am. Chem. Soc*. **2014**, *136*, 13942-13958.
24. A. R. McDonald, L. Que Jr, *Coord. Chem. Rev*. **2013**, *257*, 414-428.
25. W. Nam, Y.-M. Lee, S. Fukuzumi, *Acc. Chem. Res*. **2014**, *47*, 1146-1154.
26. M. R. Bukowski, K. D. Koehntop, A. Stubna, E. L. Bominaar, J. A. Halfen, E. Münck, W. Nam, L. Que Jr, *Science* **2005**, *310*, 1000-1002.
27. J.-U. Rohde, J.-H. In, M. H. Lim, W. W. Brennessel, M. R. Bukowski, A. Stubna, E. Münck, W. Nam, L. Que Jr, *Science* **2003**, *299*, 1037-1039.
28. M. Martinho, F. Banse, J.-F. Bartoli, T. A. Mattioli, P. Battioni, O. Horner, S. Bourcier, J.-J. Girerd, *Inorg. Chem*. **2005**, *44*, 9592-9596.
29. C. V. Sastri, M. S. Seo, M. J. Park, K. M. Kim, W. Nam, *Chem. Commun*. **2005**, 1405-1407.
30. C.-M. Che, V. K.-Y. Lo, C.-Y. Zhou, J.-S. Huang, *Chem. Soc. Rev*. **2011**, *40*, 1950-1975.

31. H. Lu, X. P. Zhang, *Chem. Soc. Rev*. **2011**, *40*, 1899-1909.
32. Z. Long, D. Liang, Chin. *Science Bull*. **2012**, *57*, 2352-2360.
33. M. J. Zdilla, J. L. Dexheimer, M. M. Abu-Omar, *J. Am. Chem. Soc*. **2007**, *129*, 11505-11511.
34. J. J. Scepaniak, C. G. Margarit, J. N. Harvey, J. M. Smith, *Inorg. Chem*. **2011**, *50*, 9508-9517.
35. Y. Liu, X. Guan, E. Lai-Ming Wong, P. Liu, J.-Sheng Huang, C.-Ming Che, *J. Am. Chem. Soc*. **2013**, *135*, 7194-7204.
36. G. Sabenya, I. Gamba, L. Gómez, M. Clémancey, J. R. Frisch, E. J. Klinker, G. Blondin, S. Torelli, L. Que Jr, V. Martin-Diaconescu, J.-M. Latour, J. Lloret-Fillol, M. Costas, *Chem. Sci*. **2019**, *10*, 9513-9517.
37. M. Jaccob, G. Rajaraman, *Dalton Trans*. **2012**, *41*, 10430-10439.
38. E. Gouré, D. Senthilnathan, G. Coin, F. Albrieux, F. Avenier, P. Dubourdeaux, C. Lebrun, P. Maldivi, J.-M. Latour, *Angew. Chem. Int. Ed.* **2017**, *56*, 4305-4309.
39. W.-Tsung Lee, R. A. Juarez, J. J. Scepaniak, S. B. Muñoz, D. A. Dickie, H. Wang, J. M. Smith, *Inorg. Chem*. **2014**, *53*, 8425-8430.
40. J. J. Scepaniak, J. A. Young, R. P. Bontchev, J. M. Smith, *Angew. Chem. Int. Ed.* **2009**, *48*, 3158-3160.
41. J. Hohenberger, K. Ray, K. Meyer, *Nature Communications* **2012**, *3*, 720.
42. E. J. Klinker, T. A. Jackson, M. P. Jensen, A. Stubna, G. Juhász, E. L. Bominaar, E. Münck, L. Que Jr, *Angew. Chem. Int. Ed*. **2006**, *45*, 7394-7397.
43. C.-M. Che, V. K.-Y. Lo, C.-Y.; Zhou, J.-S. Huang, *Chem. Soc. Rev*. **2011**, *40*, 1950-1975.
44. H. Lu, X. P. Zhang, *Chem. Soc. Rev*. **2011**, *40*, 1899-1909.
45. M. J. Zdilla, J. L. Dexheimer, M. M. Abu-Omar, *J. Am. Chem. Soc*. **2007**, *129*, 11505-11511.

46. E. Gouré, F. Avenier, P. Dubourdeaux, O. Sénèque, F. Albrieux, C. Lebrun, M. Clémancey, P. Maldivi, J.-M. Latour, *Angew. Chem. Int. Ed*. **2014**, *53*, 1580-1584.
47. A. K. Vardhaman, P. Barman, S. Kumar, C. V. Sastri, D. Kumar, S. P. de Visser, *Angew. Chem. Int. Ed.* **2013**, *52*, 12288-12292.
48. S. Kumar, A. S. Faponle, P. Barman, A. K. Vardhaman, C. V. Sastri, D. Kumar, S. P. de Visser, *J. Am. Chem. Soc.* **2014**, *136*, 17102-17105.
49. A. C. McQuilken, Y. Jiang, M. A. Siegler, D. P. Goldberg, *J. Am. Chem. Soc*. **2012**, *134*, 8758-8761.
50. S. Sahu, L. R. Widger, M. G. Quesne, S. P. de Visser, H. Matsumura, P. Moënne-Loccoz, M. A. Siegler, D. P. Goldberg, *J. Am. Chem. Soc*. **2013**, *135*, 10590-10593.
51. L. R. Widger, C. G. Davies, T. Yang, M. A. Siegler, O. Troeppner, G. N. L. Jameson, I. Ivanović-Burmazović, D. P. Goldberg, *J. Am. Chem. Soc*. **2014**, *136*, 2699-2702.
52. S. Sahu, M. G. Quesne, C. G. Davies, M. Derr, I. Ivanović-Burmazović, M. A. Siegler, G. N. L. Jameson, S. P. de Visser, D. P. Goldberg, *J. Am. Chem. Soc*. **2014**, *136*, 13542-13543.
53. S. Sahu, B. Zhang, C. J. Pollock, M. Derr, C. G. Davies, A. M. Confer, I. Ivanović-Burmazović, M. A. Siegler, G. N. L. Jameson, C. Krebs, D. P. Goldberg, *J. Am. Chem. Soc*. **2016**, *138*, 12791-12802.
54. M. Mitra, H. Nimir, S. Demeshko, S. S. Bhat, S. O. Malinkin, M. Haukka, J. Lloret-Fillol, G. C. Lisensky, F. Meyer, A. A. Shteinman, W. R. Browne, D. A. Hrovat, M. G. Richmond, M. Costas, E. Nordlander, *Inorg. Chem*. **2015**, *54*, 7152-7164.
55. S. Rana, A. Dey, D. Maiti, *Chem. Commun*. **2015**, *51*, 14469-14472.

56. W. Rasheed, A. Draksharapu, S. Banerjee, V. G. Young Jr, R. Fan, Y. Guo, M. Ozerov, J. Nehrkorn, J. Krzystek, J. Telser, L. Que Jr, *Angew. Chem. Int. Ed*. **2018**, *57*, 9387-9391; *Angew. Chem.* **2018**, *130*, 9531-9535.
57. G. Mukherjee, C. W. Z. Lee, S. S. Nag, A. Alili, F. G. Cantú Reinhard, D. Kumar, C. V. Sastri, S. P. de Visser, *Dalton Trans*. **2018**, *47*, 14945-14957.
58. S. Rana, J. P. Biswas, A. Sen, M. Clémancey, G. Blondin, J.-M. Latour, G. Rajaraman, D. Maiti, *Chem. Sci*. **2018**, *9*, 7843-7858.
59. G. Mukherjee, A. Alili, P. Barman, D. Kumar, C. V. Sastri, S. P. de Visser, *Chem. Eur. J*. **2019**, *25*, 5086-5098.
60. S. Hong, K. D. Sutherlin, A. K. Vardhaman, J. J. Yan, S. Park, Y.-M. Lee, S. Jang, X. Lu, T. Ohta, T. Ogura, E. I. Solomon, W. Nam, *J. Am. Chem. Soc*. **2017**, *139*, 8800-8803.
61. S. Hong, X. Lu, Y.-M. Lee, M. S. Seo, T. Ohta, T. Ogura, M. Clémancey, P. Maldivi, J.-M. Latour, R. Sarangi, W. Nam, *J. Am. Chem. Soc*. **2017**, *139*, 14372-14375.
62. R. Patra and P. Maldivi, *J. Mol. Model*. **2016**, *22*, 278.
63. A. K. Vardhaman, Y.-M. Lee, J. Jung, K. Ohkubo, W. Nam and S. Fukuzumi, *Angew. Chem. Int. Ed*. **2016**, *55*, 3709-3713.
64. J. Kaizer, E. J. Klinker, N. Y. Oh, J.-U. Rohde, W. J. Song, A. Stubna, J. Kim, E. Münck, W. Nam, L. Que, Jr. *J. Am. Chem. Soc*. **2004**, *126*, 472-473.
65. L. Duelund, R. Hazell, C. J. McKenzie, L. Preuss Nielsen, H. Toftlund, *J. Chem. Soc., Dalton Trans*. **2001**, 152-156.
66. J.-U. Rohde, S. Torelli, X. Shan, M. H. Lim, E. J. Klinker, J. Kaizer, K. Chen, W. Nam, L. Que, Jr, *J. Am. Chem. Soc*. **2004**, *126*, 16750-16761.
67. E. J. Klinker, J. Kaizer, W. W. Brennessel, N. L. Woodrum, C. J. Cramer, L. Que Jr, *Angew. Chem. Int. Ed*. **2005**, *44*, 3690-3694.
68. H. C. Brown, Y. Okamoto, *J. Am. Chem. Soc*. **1958**, *80*, 4979-4987.

69. C. Hansch, A. Leo, R. W. Taft, *Chem. Rev*. **1991**, *91*, 165-195.
70. Y. Goto, T. Matsui, S. I. Ozaki, Y. Watanabe, S. Fukuzumi, *J. Am. Chem. Soc*. **1999**, *121*, 9497-9502.
71. S. Banerjee, W. Rasheed, R. Fan, A. Draksharapu, W. N. Oloo, Y. Guo, L. Que Jr., *Chem. Eur. J*. **2019**, *25*, 9608-9613.
72. Y. Zang, L. Que Jr, *Inorg. Chem*. **1995**, *34*, 1030-1035.
73. Y. Zang, J. Kim, Y. Dong, E. C. Wilkinson, E. H. Appelman, L. Que Jr, *J. Am. Chem. Soc*. **1997**, *119*, 4197-4205.
74. S. Hong, Y.-Min Lee, W. Shin, S. Fukuzumi, W. Nam, *J. Am. Chem. Soc*. **2009**, *131*, 13910-13911.
75. Y. Yamada, T. Yamamoto and M. Okawara, *Chem. Lett*. **1975**, *4*, 361-362.
76. L. E. Friedrich, *J. Org. Chem*. **1983**, *48*, 3851-3852.
77. J. M. Mayer, *Acc. Chem. Res*. **1998**, *31*, 441-450.
78. M. Lubben, A. Meetsma, E. C. Wilkinson, B. Feringa, L. Que Jr., *Angew. Chem. Int. Ed*. **1995**, *34*, 1512-1513.
79. D. Wang, K. Ray, M. J. Collins, E. R. Farquhar, J. R. Frisch, L. Gómez, T. A. Jackson, M. Kerscher, A. Waleska, P. Comba, M. Costas, L. Que Jr., *Chem. Sci*. **2013**, *4*, 282-291.
80. D. Kumar, H. Hirao, L. Que Jr, S. Shaik, *J. Am. Chem. Soc*. **2005**, *127*, 8026-8027.
81. F. G. Cantú Reinhard, A. S. Faponle, S. P. de Visser, *J. Phys. Chem. A* **2016**, *120*, 9805-9814.
82. T. Z. H. Gani and H. J. Kulik, *ACS Catal*. **2018**, *8*, 975-986.
83. H. Hirao, D. Kumar, L. Que Jr, S. Shaik, *J. Am. Chem. Soc*. **2006**, *128*, 8590-8606.
84. S. P. de Visser, *J. Am. Chem. Soc*. **2006**, *128*, 9813-9824.
85. L. Bernasconi, E.-J. Baerends, *Eur. J. Inorg. Chem*. **2008**, 1672-1681.

86. S. D. Wong, C. B. Bell III, L. V. Liu, Y. Kwak, J. England, E. E. Alp, J. Zhao, L. Que Jr, E. I. Solomon, *Angew. Chem. Int. Ed.* **2011**, *50*, 3215-3218.
87. S. F. Ye, F. Neese, *Proc. Natl. Acad. Sci. USA* **2011**, *108*, 1228-1233.
88. R. Latifi, M. A. Sainna, E. V. Rybak-Akimova, S. P. de Visser, *Chem. Eur. J.* **2013**, *19*, 4058-4068.
89. A. Ansari, A. Kaushik, G. Rajaraman, *J. Am. Chem. Soc.* **2013**, *135*, 4235-4249.
90. F. G. Cantú Reinhard, S. P. de Visser, *Chem. Eur. J.* **2017**, *23*, 2935-2944.
91. D. Kumar, S. P. de Visser, P. K. Sharma, H. Hirao, S. Shaik, *Biochemistry* **2005**, *44*, 8148-8158.
92. D. Kumar, G. N. Sastry, S. P. de Visser, *Chem. Eur. J.* **2011**, *17*, 6196-6205.
93. S. P. de Visser, D. Kumar, S. Cohen, R. Shacham, S. Shaik, *J. Am. Chem. Soc.* **2004**, *126*, 8362-8363.
94. S. P. de Visser, *J. Am. Chem. Soc.* **2010**, *132*, 1087-1097.
95. S. Ghafoor, A. Mansha, S. P. de Visser, *J. Am. Chem. Soc.* **2019**, *141*, 20278-20292.
96. E. P. Hunter and S. G. Lias, NIST Chemistry Webbook, NIST Standard Reference Database, Number 69; Eds.: P. J. Linstrom and W. G. Mallard, National Institute of Standards and Technology: Gaithersburg MD, **2018**, 20899, (retrieved 29 October 2019), http://webbook.nist.gov.

CHAPTER – V

Mechanistic Insight into Dehalogenation Reaction by High-Valent Non-Heme Iron(IV)-oxo Intermediates

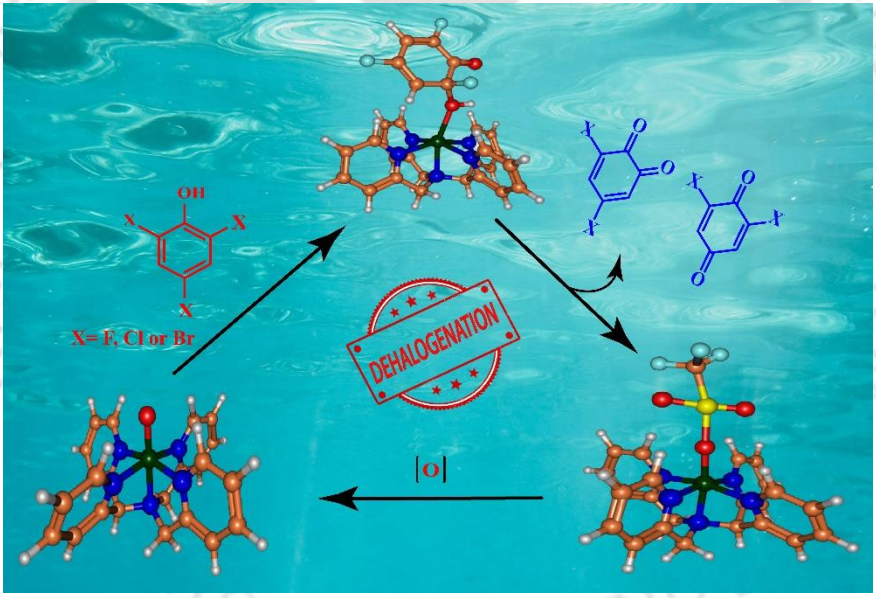

■ Adapted from *Faraday Discuss*. **2022**, *234*, 58-69 with permission from the Royal Society of Chemistry ■

5.1. Introduction

High-valent iron(IV)-oxo complexes have been invoked as the key reactive intermediate in the catalytic cycle of non-heme iron enzymes and their model systems.[1,2] The non-heme iron(IV)-oxo species is reportedly the active oxidant involved in enzymatic and biomimetic reactions.[3,4] These iron(IV)-oxo intermediates have shown to catalyze a wide variety of biological oxidation processes such as alkane hydroxylation, olefin epoxidation, alcohol oxidation, sulfoxidation, N-dealkylation, etc.[5] Mononuclear non-heme iron enzymes perform oxidative transformations of various organic substrates in biological systems.[6-11] High valent iron(IV)-oxo intermediates have been identified as the important species in such oxidative transformations[12-17] and several non-heme dioxygenases have been isolated and characterized.[18,19] These are versatile intermediates towards hydrogen atom transfer (HAT) and oxygen atom transfer (OAT) reactions.[20-25] In addition, mononuclear high-valent iron(IV)-oxo complexes have been considered as reactive intermediates for the degradation of toxic organic pollutants[26], which are potential threats to the continuous increase of environmental pollution. Among these organic pollutants, halophenols are a major class of toxic organic pollutants which include 4-fluorophenols, 4-chlorophenols, 4-bromophenols, 2,6-difluorophenols, 2,6-dichorophenols, 2,6-dibromophenols, 2,4,6-trifluorophenols, 2,4,6-trichlorophenols, 2,4,6-tribromophenols. The main sources of these compounds are industrial waste, pesticides, herbicides, disinfectants and dyes.[27,28] The extensive usage and resistance to biodegradation cause their accumulation in the soil and groundwater.[29-31] As a consequence, these pollutants enter the human body through the food chain causing serious health concerns as they are potentially carcinogenic.[27,32,33] In addition, many chlorophenols such as 2,4,6-trichlorophenols are included in the US Environmental Protection Agency's priority list of dangerous pollutants because of their high persistence in the environment.[34] Therefore, it is necessary to implement different techniques that can

help in the detoxification of these pollutants and convert them to non-hazardous chemicals.

A variety of techniques have been developed for the degradation of halophenols that include physical, chemical and biological processes.[35-38] Despite the fact that a variety of physical and chemical processes are available for the degradation of halophenols, such as adsorption, ion exchange, liquid-liquid extraction, chemical oxidation, and advanced oxidation processes, all of those are costly and energy-intensive. Moreover, many of these processes produce by-products or more toxic intermediates. For example, the incineration of chlorophenol wastes produces even more toxic compounds such as polychlorinated dibenzofurans or dibenzo-p-dioxins.[37] On the other hand, bacterial degradation is one of the most efficient methods to detoxify halophenols. Chlorophenols and their derivatives are removed from the environment by several bacteria such as *Pseudoomonas knackmussii* B-13, *Rhodococcus opacus* 1G, *Ralstonia picketti* etc.[27] These are considered as cost-effective and eco-friendly methods to remove chlorophenols.

The dehalogenation mechanism of dehaloperoxidase (DHP) has been investigated by several groups but as yet remains unresolved.[39-43] Enzymatic assays suggest that the mechanism is similar to that for the same reaction catalysed by *Caldariomyces fumago* chloroperoxidase (CCPO),[44] horseradish peroxidase (HRP)[45] and lignin peroxidases.[46,47] The proposed mechanism for the conversion of halophenols to quinones by these enzymes involves two successive one-electron transfer steps mediated by iron(IV)-oxo intermediates and it is seen that the oxygen atom in the quinone product is derived from a solvent water molecule.[44] Interestingly, a different dehalogenation mechanism has been proposed for dehaloperoxidase-hemoglobin A (DHP A), which involves substrate binding in the internal active site of an enzyme where the substrate gets oxidized to quinone in

two sequential one-electron steps followed by the addition of a water molecule as shown in Scheme 5.1.[48]

Scheme 5.1. Schematic representation of the mechanisms for oxidation of substrate by DHP A.[48]

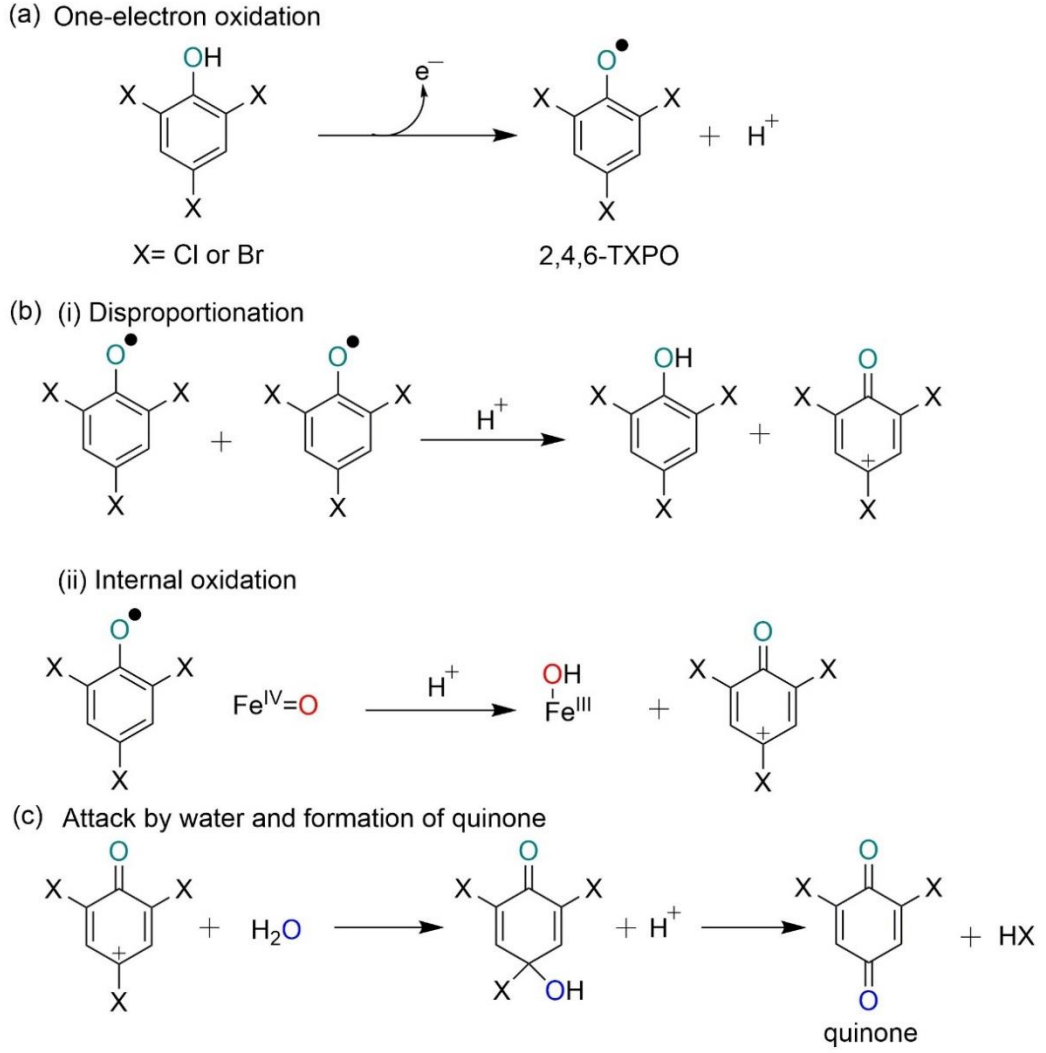

The first step is initiated with the oxidative electron transfer from the substrate and loss of a proton resulting in the formation of a phenoxy radical, 2,4,6-TXPO (X = Cl or Br) (Scheme 5.1a). In the second step, oxidation of the 2,4,6-TXPO radical takes place by two probable alternative mechanisms: disproportionation or internal oxidation. In the disproportionation mechanism which occurs in solution, one equivalent of each of the reactant and phenoxy cation is formed from two equivalents of phenoxy radicals, whereas in internal oxidation, the substrate remains immobilized inside the enzyme for a second electron transfer to produce a phenoxy cation (Scheme 5.1b). Further, the phenoxy cation is attacked by a water molecule in the *para*-position to form the 2,6-dihaloquinone product with the loss of HX (Scheme 5.1c).

However, limited literature is available on the detoxification of organic pollutants by the non-heme iron(IV)-oxo species. Recently, Paine and co-workers have synthesized a series of iron(IV)-oxo complexes supported by polydentate nitrogen donor ligands which perform oxidative degradation of halophenols in an aqueous medium.[49] It was observed that water plays a vital role in most of the processes used for the degradation of halophenols. However, all the intermediates might not be stable in a water medium. We; therefore, envisaged that the solvent system has a huge role to play in the catalytic dehalogenation of the phenolic systems, and, in particular, in stabilizing the much-elusive substrate-bound species involved in the mechanism. In this work, we employed an iron(IV)-oxo species supported by a pentadentate ligand 2PyN2Q (1,1-di(pyridin-2yl)-N, N-bis(quinolin-2-ylmethyl)methanamine),[50] in an acetonitrile solvent, which degrades halophenols by an oxidative pathway. The proposed mechanism of oxidative dehalogenation of halophenols by this iron(IV)-oxo intermediate proceeds via an initial hydrogen atom abstraction from the phenolic O-H resulting in the formation of a new intermediate, a phenolate adduct of the ferric species which leads to the formation of corresponding quinone product.

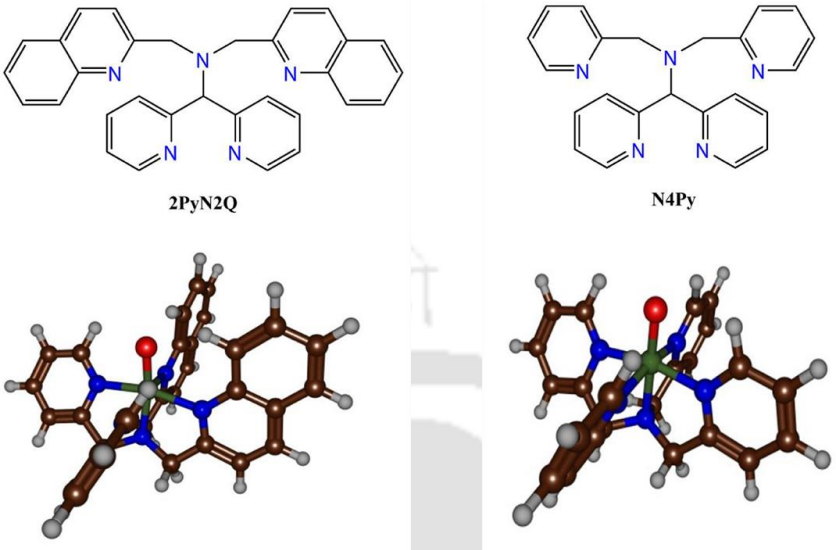

Fig. 5.1. Ligand frameworks studied and DFT-optimised structures of the corresponding iron(IV)-oxo complexes.

5.2. Results and Discussion

5.2.1. Synthesis and Characterization

We started our work by synthesizing the ferrous complex $[Fe^{II}(2PyN2Q)(OTf)_2]$, **5a**, supported by a pentadentate ligand 2PyN2Q.[50] The asymmetric geometry of the ligand framework has been taken into account to study the substrate approach parameters. The dark yellow compound **5a** was synthesized following reported procedures,[51-53] by the dropwise addition of an acetonitrile solution of $Fe^{II}(OTf)_2{\cdot}2CH_3CN$ to the ligand. UV-vis spectroscopy and electrospray ionization-mass spectrometry (ESI-MS) confirms the ligation of the iron(II) species in the complex. Upon addition of 1.5 equivalents of $PhI(OAc)_2$ to **5a** in CH_3CN under ambient conditions, a pale green iron(IV)-oxo complex $[Fe^{IV}(O)(2PyN2Q)]^{2+}$, **5b**, was generated with distinctive absorption features (λ_{max} = 770

nm, ε = 340 L M^{-1} cm^{-1}, $t_{1/2}$ = 50 min at RT) (Fig. 5.2) as reported previously.[50] This absorption band corresponds to the d-d transition features of the iron(IV)-oxo species generated in situ. Further, the formation of the oxo-species, **5b** was confirmed by ESI-MS, that shows a major peak at *m/z* 269.57 and a minor peak at *m/z* 688.08 corresponding to $[Fe^{IV}(O)(2PyN2Q)]^{2+}$ and $[Fe^{IV}(O)(2PyN2Q)(OTf)]^{+}$, respectively, (see Fig. 5.3).

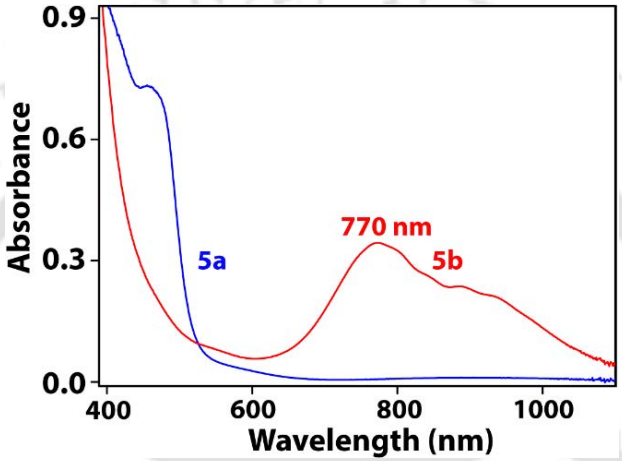

Fig. 5.2. UV-vis spectrum of $[Fe^{II}(2PyN2Q)(OTf)_2]$, **5a** (blue line) and $[Fe^{IV}(O)(2PyN2Q)]^{2+}$, **5b** (red line) in CH_3CN at 25 °C.

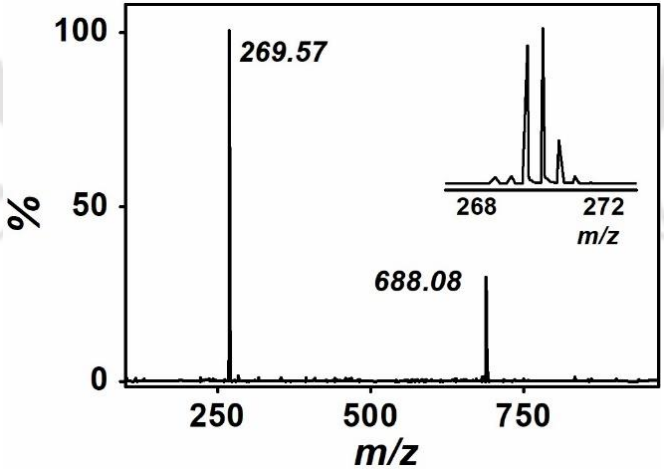

Fig. 5.3. ESI-MS spectrum of **5b** in CH_3CN at 25 ºC. The peaks at *m/z* 269.57 and 688.08 are assigned to $[Fe^{IV}(O)(2PyN2Q)]^{2+}$ and $[Fe^{IV}(O)(2PyN2Q)(OTf)]^{+}$, respectively. Inset shows the observed isotopic distribution pattern of *m/z* 269.57.

5.2.2. Reaction Kinetics

The complex $[Fe^{IV}(O)(2PyN2Q)]^{2+}$, **5b** as shown in Fig. 5.1, has an asymmetric skeleton with two quinolines on one side of it - guarding the iron-oxo core, and directing the approach of the substrates from the other side of the complex. We, therefore, decided to investigate several halophenols with various steric demands and different electronic impulses toward the iron-oxo active site and see how the backbone affects the substrate binding and approach. As exhibited in Fig. 5.4, several mono-di- and tri-halophenols were employed as substrates to study the oxidative dehalogenation reactions of complex **5b**. However, the use of iodophenols was precluded due to solubility issues in our generalized conditions. The reactions were monitored by following the changes in the UV-vis absorption spectra as a function of time upon the addition of the substrates. Initially, tri-halophenols such as2,4,6-trifluorophenol (2,4,6-TFP), 2,4,6-trichlorophenol (2,4,6-TCP) and 2,4,6-tribromophenol (2,4,6-TBP) were reacted with **5b**. Complex **5b** is known to be a better catalyst for sulfoxidation and C-H abstraction reactions.[50] Similar trends were observed in the reactivity with halo-phenols.

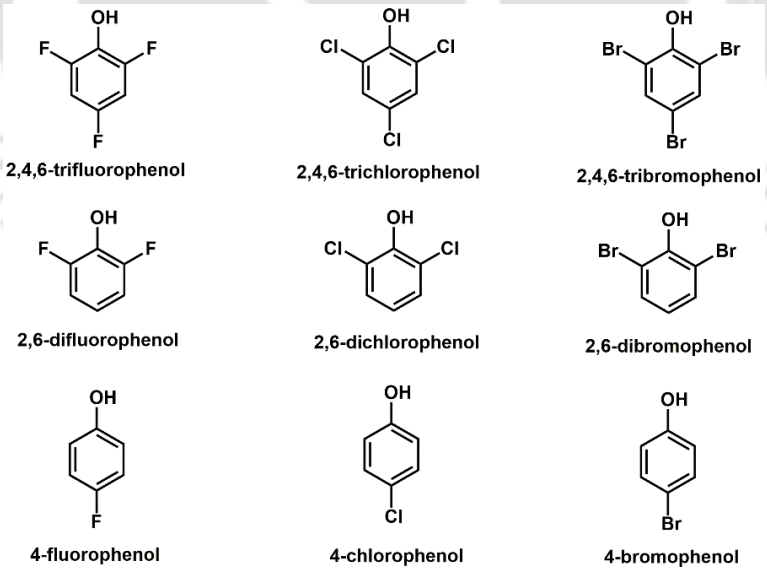

Fig 5.4 Halo-phenolic substrates used in this work.

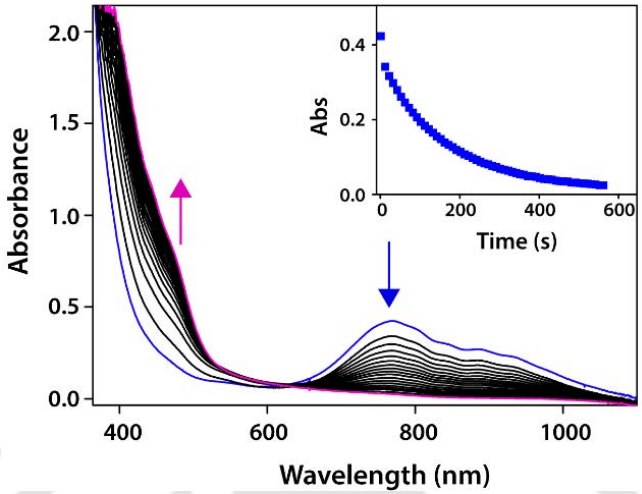

Fig. 5.5. UV-vis spectral changes of **5b** upon addition of 10 equiv. 2,4,6-TCP in CH_3CN at -40 ºC. Inset shows the decay profile of the 770 nm band.

At -40 ºC, the addition of tri-halophenols to **5b** led to the gradual pseudo-first-order decay of the iron(IV)-oxo characteristic band at 770 nm in the UV-vis spectrum with concomitant formation of the corresponding iron(II) precursor with an isosbestic point at 620 nm as shown in Fig. 5.5. The pseudo-first-order rate constants increased linearly with an increase in the concentration of the substrates enabling us to procure the second-order rate constants (k_2). The second-order constants (k_2) for **5b** with different tri-halophenols were evaluated, as shown in Fig. 5.6a and the reactivity order was found to be 2,4,6-TBP > 2,4,6-TCP > 2,4,6-TFP. This trend in the reactivity establishes the electrophilicity of the iron(IV)-oxo species involved in the reactions. A similar reactivity order was also observed for the reactivity of heme metalloenzymes with tri-halophenols.[54]

When we substituted the phenolic hydrogen with deuterium and repeated the experiments with 2,4,6-TCP-d_1 (2,4,6-trichlorophenol-d_1), a second-order rate constant of 3.54 x 10^{-2} $M^{-1}s^{-1}$ was obtained at -40 ºC. This gives a non-classical kinetic isotope effect (KIE) value of 26 that confirms the abstraction of the phenolic hydrogen and the corresponding formation of the phenolate radical in the mechanism of the dehalogenation

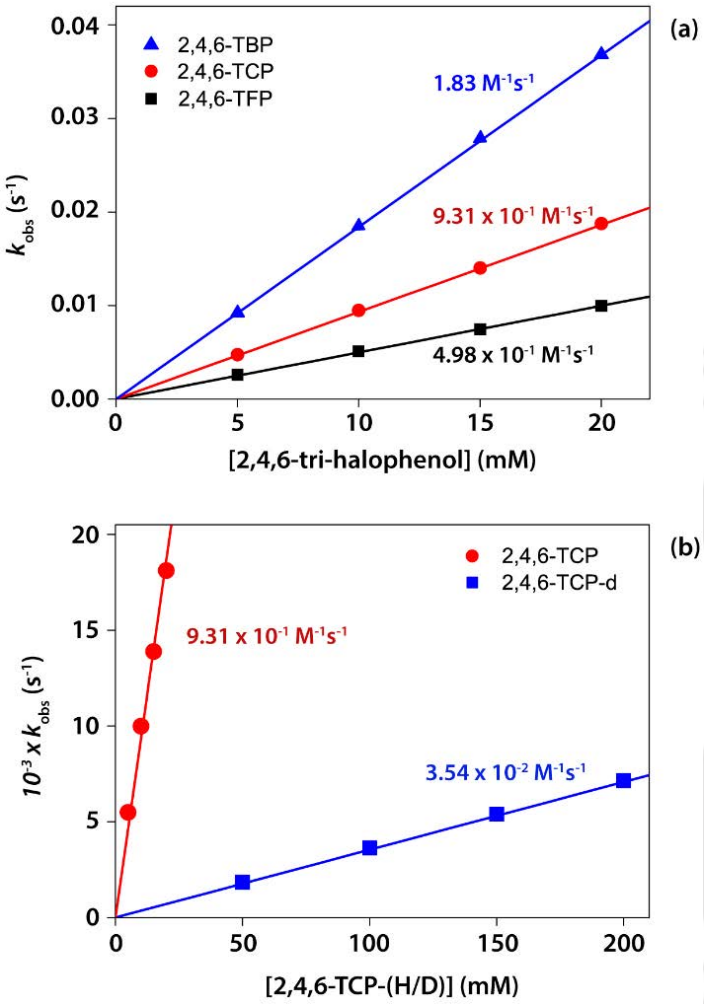

Fig. 5.6. Second-order rate constants determined for **5b** (1mM) with (a) 2,4,6-TFP (■), 2,4,6-TCP (●) and 2,4,6-TBP (▲) at -40 ºC; (b) Plot of k_{obs} against the concentration of 2,4,6-TCP (●) and 2,4,6-TCP-d (■) with **5b** in CH_3CN at -40 ºC.

process, see Fig. 5.6b.[21,55] Having that established, it is also understood that the size of the substrate, however, has no role to play in the H-abstraction step, since 2,4,6-tribromophenol was found to be the most reactive among the three. This size vs nucleophilicity balance among the substrates investigated led us to further check the dehalogenation of **5b** with di-and mono-halophenols. The addition of di-halophenols to

intermediate **5b** in CH_3CN under the same conditions resulted in the decay of the absorption band at 770 nm in a pseudo first-order manner as a function of time. A similar pattern was obtained for the di-halophenols as well i.e. 2,6-DBP > 2,6-DCP > 2,6-DFP. The second-order constants (k_2) for **5b** with different di-halophenols were evaluated, as shown in Table 5.1.

By contrast, for *para*-halophenols, the reactions were sluggish at -40 °C. Clearly, the phenolate radicals resulting from the H-atom abstraction were less stabilized for the mono-halo substrates compared to the di- and tri-halophenols. Interestingly, the addition of the *p*-halophenols to the intermediate **5b** at 0 °C resulted in the decay of the d-d band of **5b**. However, the decay profile was not clean at 770 nm. A new feature was observed at about 600 nm. Thus, second-order rate constants for the oxidation of *p*-halophenols were evaluated as a function of the change in absorption band at 885 nm with time (see Table 5.1). These rates were found to be comparable for all three *p*-halophenols,

Table 5.1. Second-order rate constant (k_2) and product distribution for 5b (1 mM in CH_3CN solution) with mono-, di- and tri-halophenols.

Substrate	10^{-1} x k_2 (in $M^{-1}s^{-1}$)	Temperature	Product distribution % (*ortho* : *para*) quinone
2,4,6-TFP	4.98	-40 °C	35 : 21
2,4,6-TCP	9.3	-40 °C	30 : 15
2,4,6-TBP	18.3	-40 °C	50 : 10
2,6-DFP	3.55	-40 °C	30 : 0
2,6-DCP	8.54	-40 °C	33 : 0
2,6-DBP	14.6	-40 °C	21 : 0
4-FP	20.8	0 °C	30 : 25
4-CP	19.8	0 °C	40 : 31
4-BP	16	0 °C	38 : 10

indicating that the formation of this new species is independent of the nucleophilicity of the employed substrate. However, it has a definite implication towards the size of the substrate utilized for dehalogenation, as this feature was not observed in the cases of di- and tri-halophenols under identical conditions. When the reaction of 4-FP with **5b** was carried at room temperature a new absorption band at 614 nm as shown in Fig. 5.7, is typical of the characteristic LMCT band usually seen for oxygen adducts of iron such as iron(III)-OOH and/or iron(III)-OOR.[56-61] Although, unlike such intermediates, this new species is sufficiently stable having a half-life time of about 10 h at room temperature. To further characterize this species, high-resolution mass spectrometry (HRMS) was conducted, but unfortunately, it resulted into excessive fragmentation, thereby precluding the correct assessment of the molecular ion fragment. The X-band EPR spectrum of the adduct was recorded at 77 K (see Fig. 5.8) that shows a broad signal at g = 5.04 along with additional high-end g values at 6.55, 8.39 and 13.74. This indicates the presence of a Fe(III)-species with dominant high-spin characteristics.[59,62]

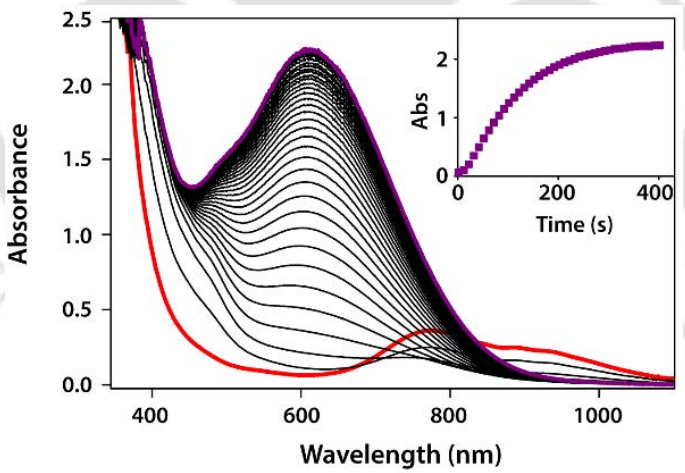

Fig. 5.7. UV-vis spectral changes of **5b** upon addition of 10 equiv. 4-FP in CH_3CN at room temperature. Inset shows the formation profile of the absorption band at 614 nm.

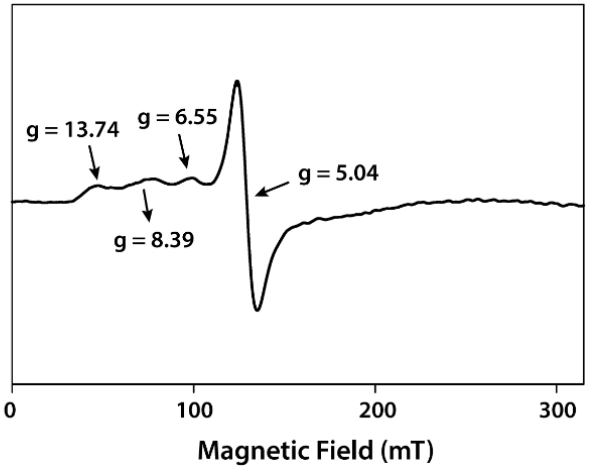

Fig. 5.8. X-band EPR spectrum of the adduct $[(2PyN2Q)(OH)Fe^{III}(O\text{-}FP)]^{+}$ at 77 K in CH_3CN. EPR parameters: microwave power: 0.995 mW, modulation frequency: 100 kHz, modulation amplitude: 1 mT, microwave frequency: 9136 MHz.

We speculate the new species to be a substrate-bound intermediate, where the phenolate radical, deprived of its hydrogen, binds with the iron(III)-OH species, thereby forming a hepta-coordinated adduct of iron. Arguably, the active site structure is crowded at this point of time. The steric demand of the ligand framework is hereby brought into effect as the new substrate-bound adduct should be mostly stable for *p*-halophenols, and less stable for di- and tri-halophenols that have bulky halogen atoms in the *ortho*-position. This was indeed observed in the UV-vis spectrum, where the formation of the LMCT band was not observed for phenols having chloro and/or bromo at the *ortho*-positions of the phenol. The bulky size of the bromo component in the *ortho*-position restricts the ease of approach of the phenolate radical to bind with the iron(III)-species. On the other hand, fluorine having a comparatively much smaller atomic size was tolerated by the hepta-coordinated iron(III)-adduct and the formation of the new bands were observed at 558 nm and 583 nm for 2,4,6-TFP and 2,6-DFP, respectively (see Fig. 5.9). Also, a shift of the λ_{max} from 614 nm to 558 nm for 4-FP and 2,4,6-TFP respectively, further reinforces the argument of the substrate-bound iron(III)-species.

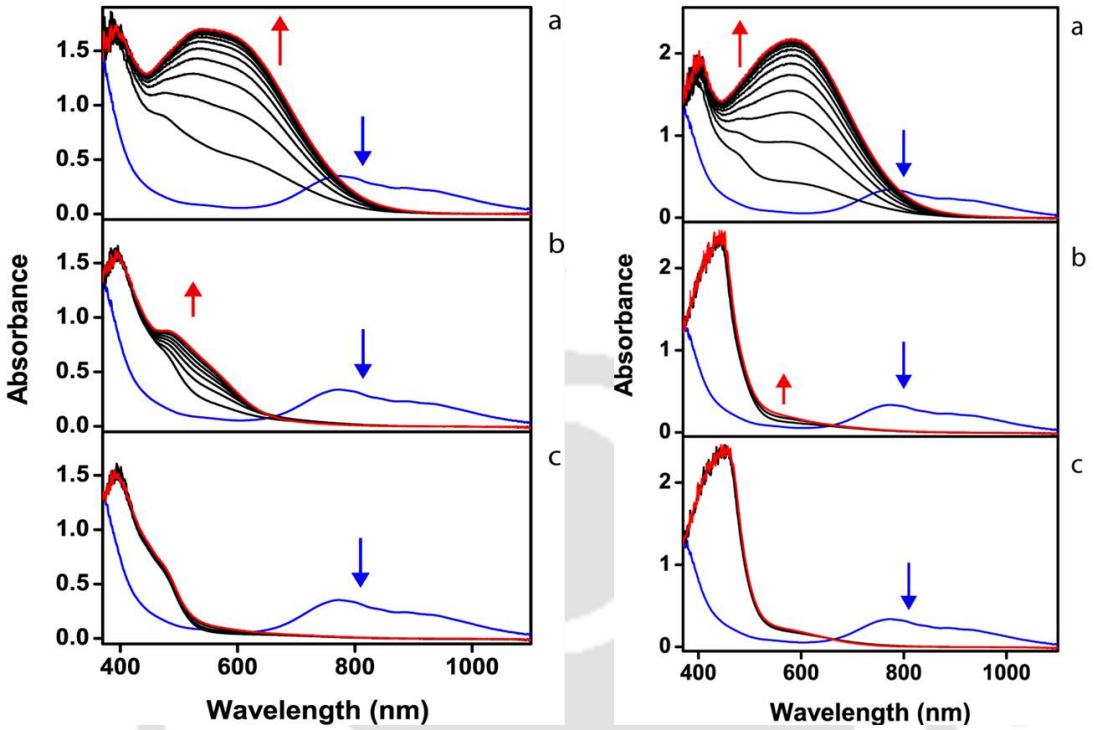

Fig. 5.9. UV-vis spectral changes of **5b** upon addition of (left) (a) 10 equiv. 2,4,6-TFP (b) 10 equiv. 2,4,6-TCP and (c) 10 equiv. 2,4,6-TBP in CH_3CN at room temperature, (right) (a) 10 equiv. 2,6-DFP (b) 10 equiv. 2,6-DCP and (c) 10 equiv. 2,6-DBP in CH_3CN at room temperature. The formation of the adducts was observed for 400 s.

To understand the details of the reaction mechanism, analyses of the oxidized products were carried out. In the reaction of **5b** with 2,4,6-TCP, we found mixtures of 2,4-dichloro-*ortho*-benzoquinone (*o*-quinone) and 2,6-dichloro-*para*-benzoquinone (*p*-quinone), the former being the major product. To gain further insights, the *ortho*-: *para*-quinone ratios for all the halophenols were evaluated (see Fig. 5.10 – Fig. 5.18) and are listed in Table 5.1. Interestingly, *o*-quinone was found to be the major product in every case. In fact, for all the three 2,6-dihalophenols discussed here, *o*-quinone was found to be the sole product.

The product distribution hereby obtained guided us to propose a plausible mechanism for the dehalogenation reaction. The reaction mechanism involves two

consecutive one-electron reduction of the iron(IV)-oxo species.[44-48] The reaction commences with the abstraction of the phenolic hydrogen atom thereby forming iron(III)-OH and a phenolate radial species. Thereafter, the phenolate radical overcomes the steric fencing around the iron centre to coordinate to the ferric species as a substrate-bound adduct (A). In the adduct (A), the hydroxyl group (-OH) being in the vicinity of the *ortho*-position of the phenolate cyclize to form the adduct (B). Finally, the adduct (B) undergoes a second electron transfer step to produce the *o*-quinone in a concerted fashion as shown in Scheme 5.2. The formation of *p*-quinone could be attributed to the presence of a trace amount of water in the solvent.

Scheme 5.2. A plausible mechanism for the oxidative dehalogenation of *p*-halophenols by the intermediate 5b.

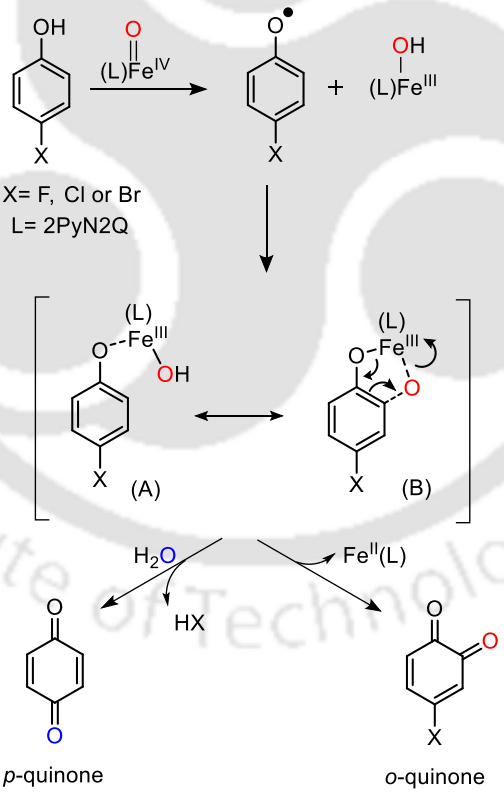

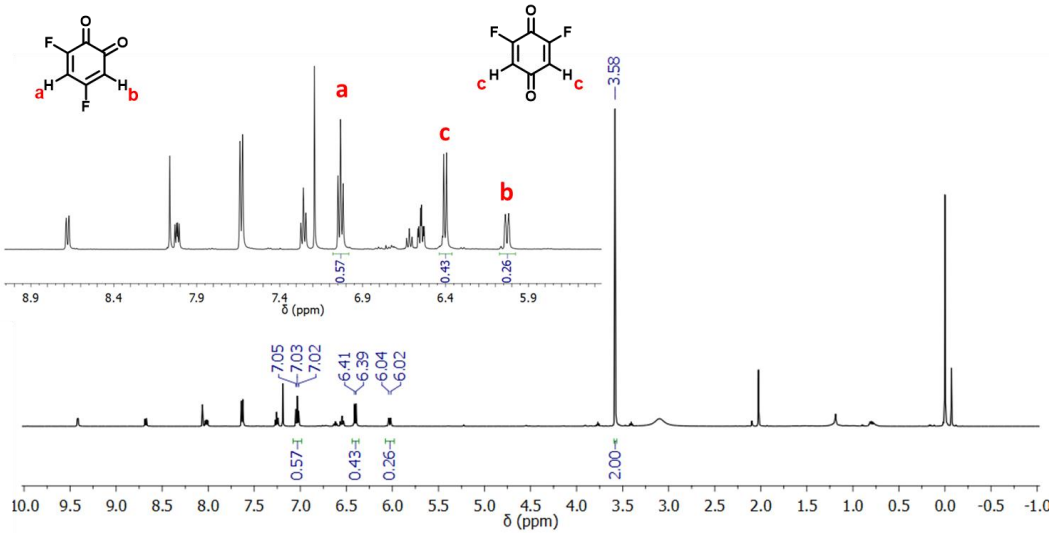

Fig. 5.10. ^{1}H NMR spectrum of the reaction mixture of oxidized products of 2,4,6-trifluorophenol in $CDCl_3$. Peak at 3.58 ppm corresponds to 1,2-dibromoethane.

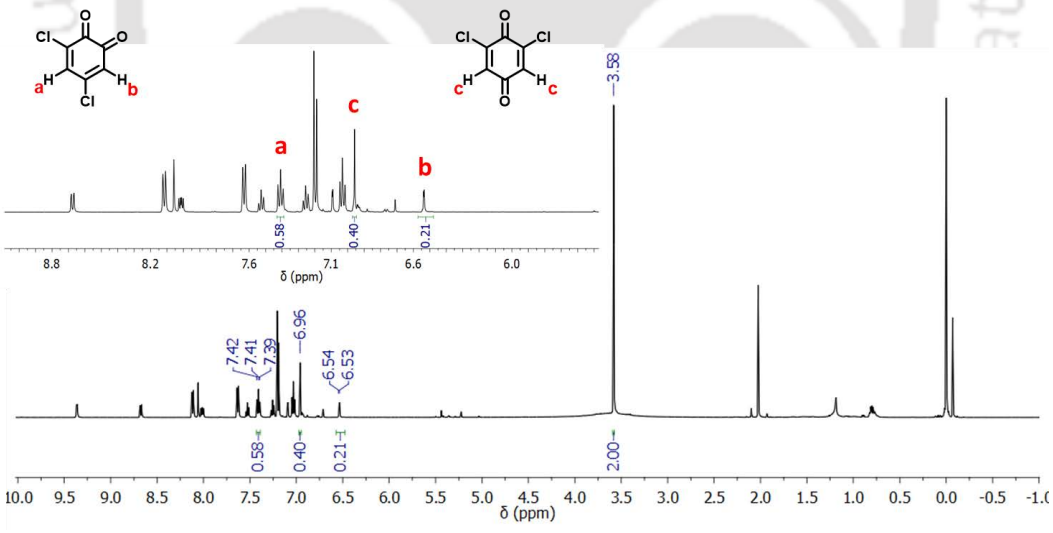

Fig. 5.11. ^{1}H NMR spectrum of the reaction mixture of oxidized products of 2,4,6-trichlorophenol in $CDCl_3$. Peak at 3.58 ppm corresponds to 1,2-dibromoethane.

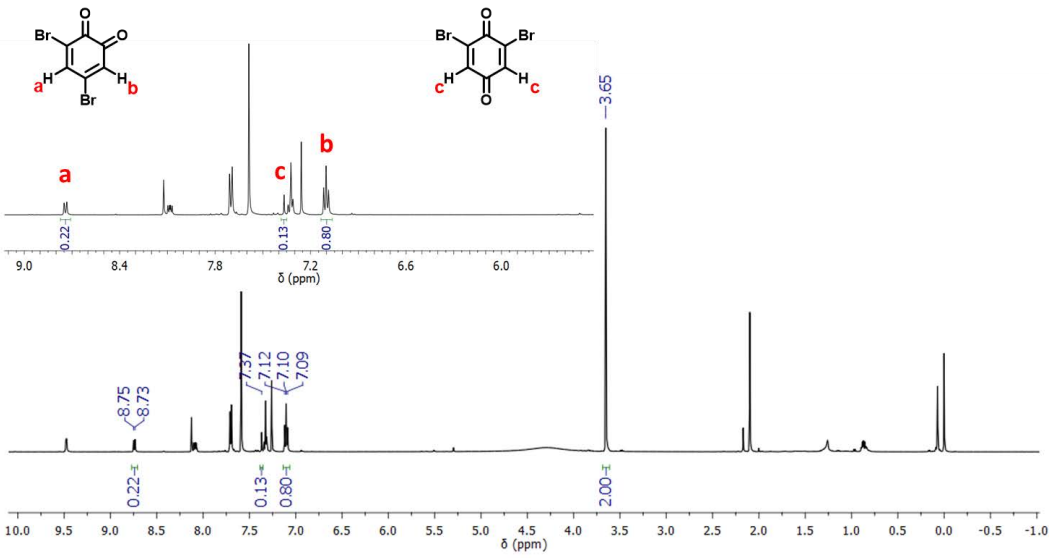

Fig. 5.12. [1]H NMR spectrum of the reaction mixture of oxidized products of 2,4,6-tribromophenol in $CDCl_3$. Peak at 3.58 ppm corresponds to 1,2-dibromoethane.

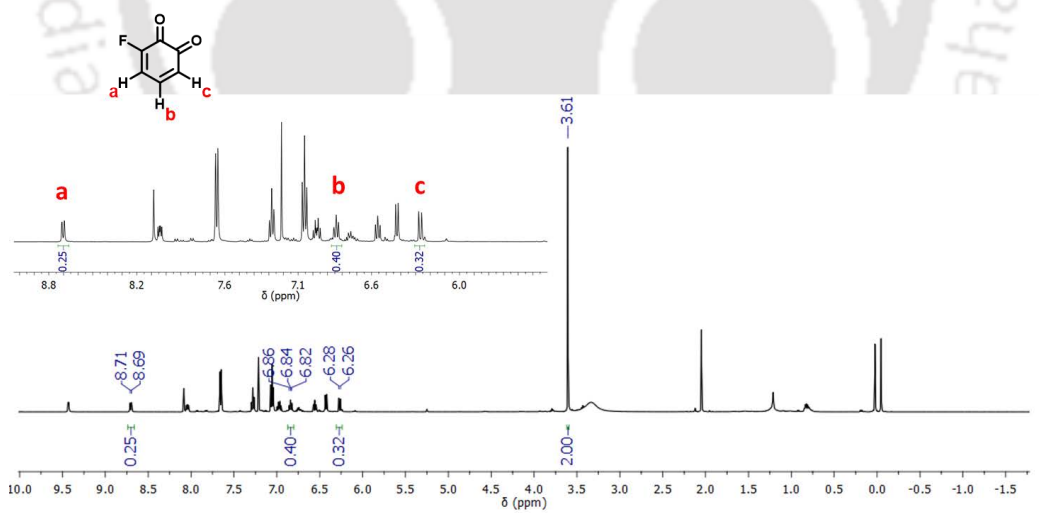

Fig. 5.13. [1]H NMR spectrum of the reaction mixture of oxidized product of 2,6-difluorophenol in $CDCl_3$. Peak at 3.58 ppm corresponds to 1,2-dibromoethane.

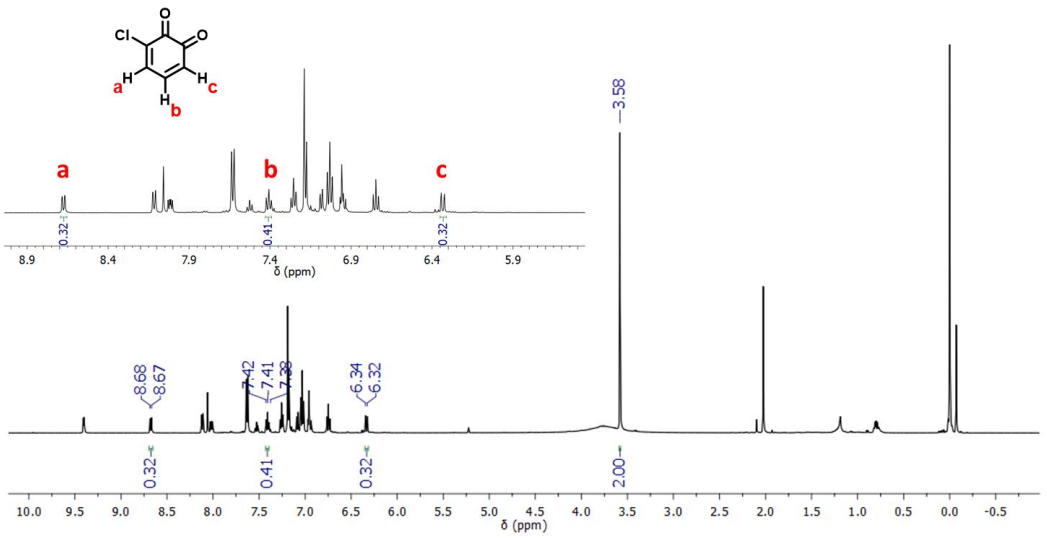

Fig. 5.14. ^{1}H NMR spectrum of the reaction mixture of oxidized product of 2,6-dichlorophenol in $CDCl_3$. Peak at 3.58 ppm corresponds to 1,2-dibromoethane.

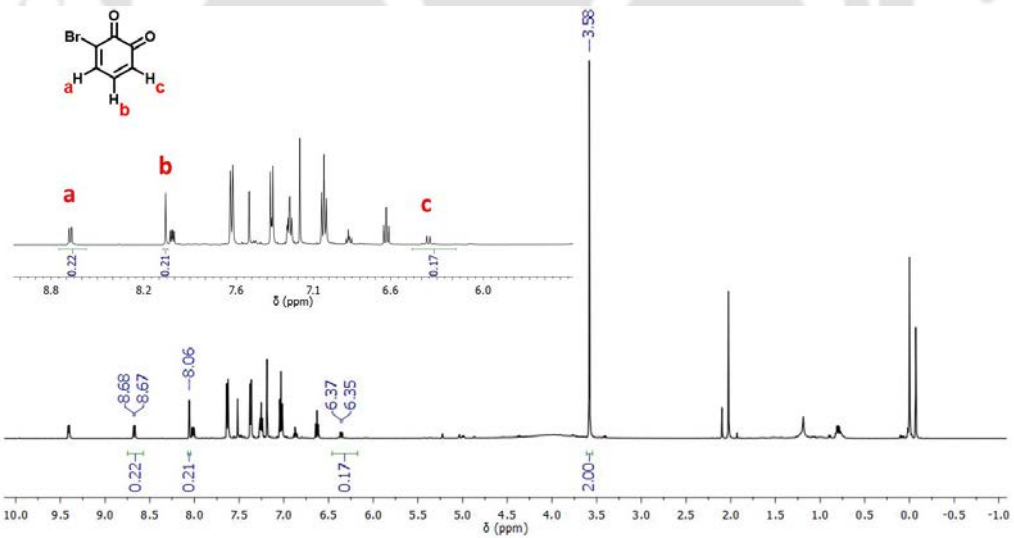

Fig. 5.15. ^{1}H NMR spectrum of the reaction mixture of oxidized product of 2,6-dibromophenol in $CDCl_3$. Peak at 3.58 ppm corresponds to 1,2-dibromoethane.

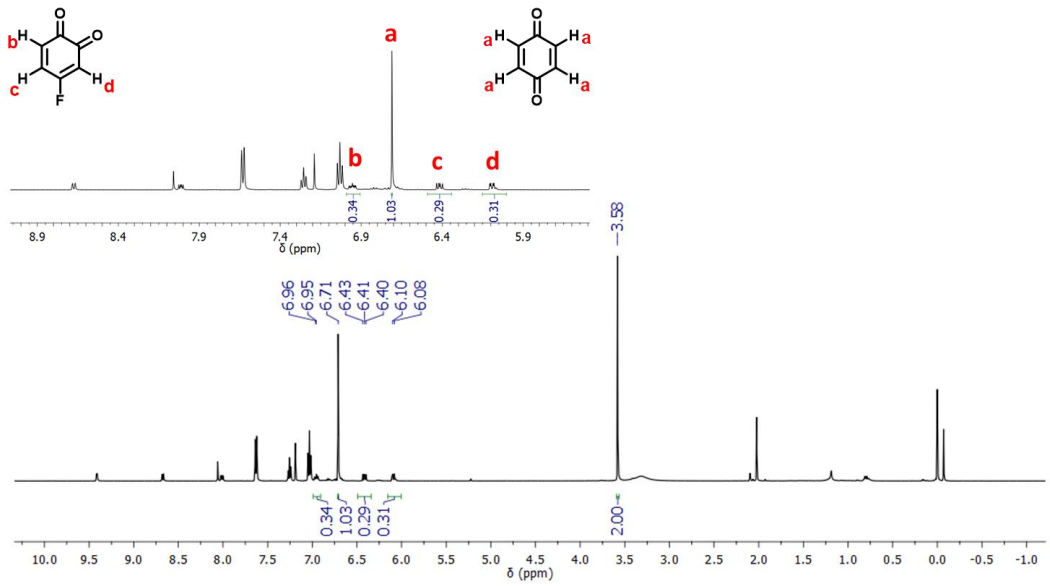

Fig. 5.16. ^{1}H NMR spectrum of the reaction mixture of oxidized products of 4-fluorophenol in $CDCl_3$. Peak at 3.58 ppm corresponds to 1,2-dibromoethane.

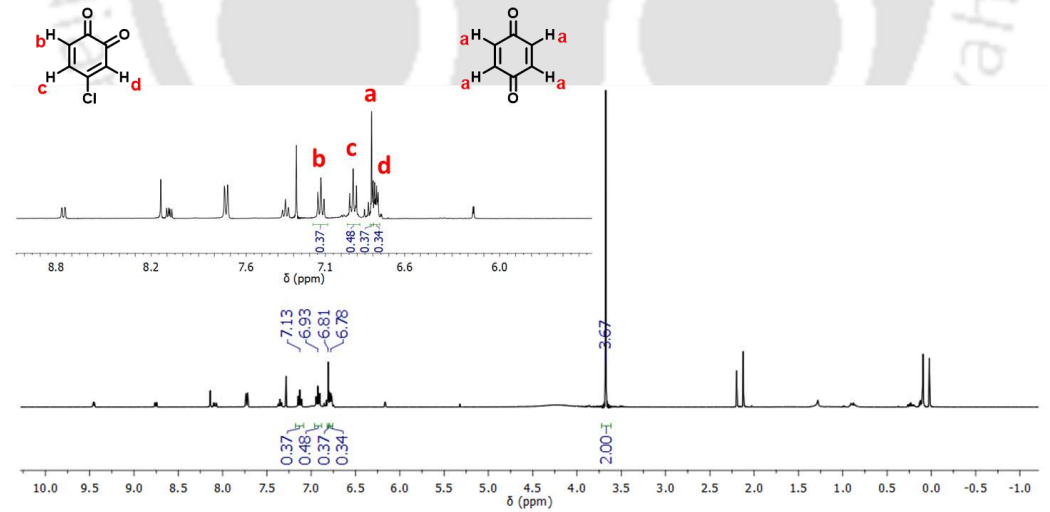

Fig. 5.17. ^{1}H NMR spectrum of the reaction mixture of oxidized products of 4-chlorophenol in $CDCl_3$. Peak at 3.67 ppm corresponds to 1,2-dibromoethane.

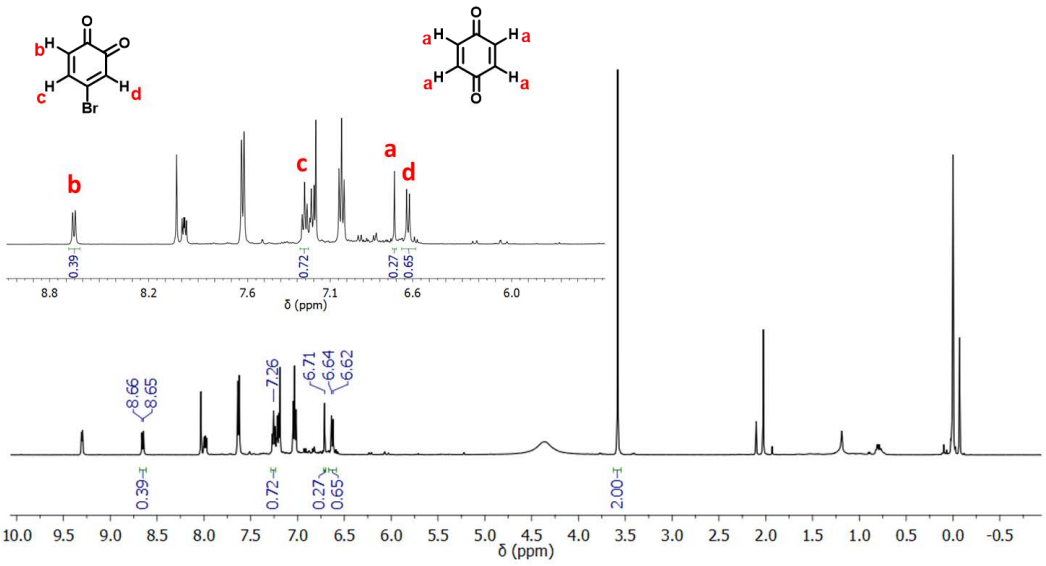

Fig. 5.18. ^{1}H NMR spectrum of the reaction mixture of oxidized products of 4-bromophenol in $CDCl_3$. Peak at 3.58 ppm corresponds to 1,2-dibromoethane.

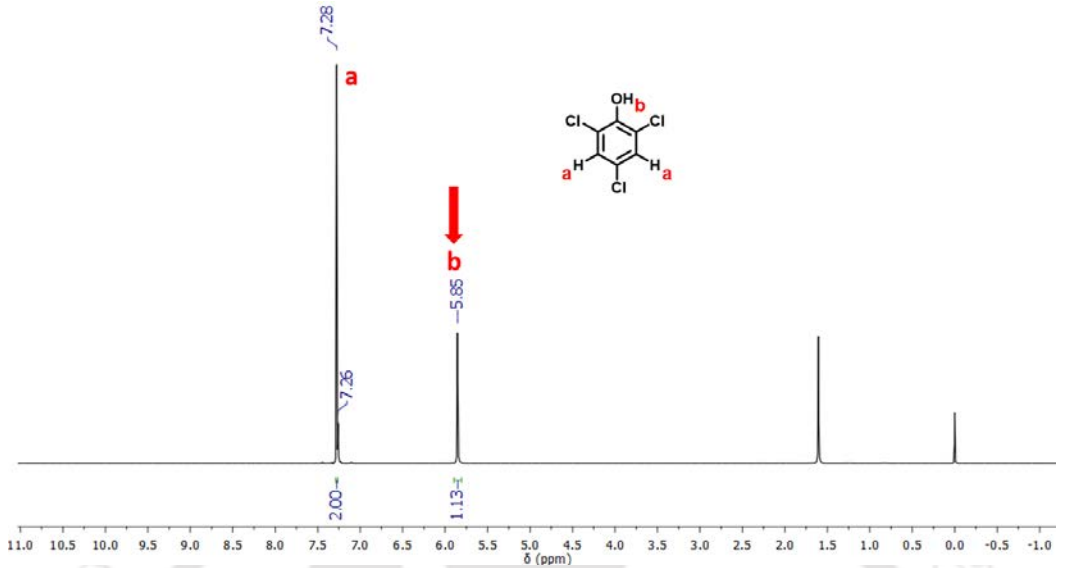

Fig. 5.19. ^{1}H NMR spectrum of 2,4,6-trichlorophenol in $CDCl_3$.

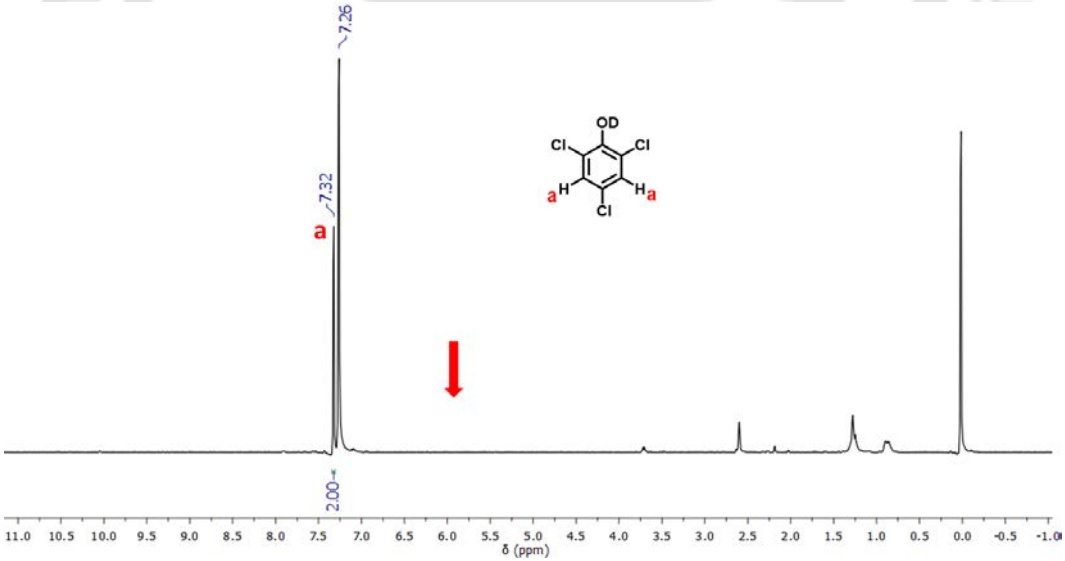

Fig. 5.20. ^{1}H NMR spectrum of 2,4,6-trichlorophenol-D in $CDCl_3$.

The asymmetric skeleton in $[Fe^{IV}(O)(2PyN2Q)]^{2+}$, **5b** due to the presence of two bulkier quinoline moieties on one side of its iron-oxo core was found to guide and direct the substrate approach to the oxo group. It was observed that all the *p*-halophenols easily form substrate-bound adducts due to the absence of halogen atoms at the *o*-positions of the phenolic group. However, among di- and tri-halophenols, the formation of the substrate-bound adducts was observed only in 2,6-difluorophenol (2,6-DFP) and 2,4,6-trifluorophenol (2,4,6-TFP) owing to the presence of smaller fluorine atoms at the *o*-positions of the phenolic group. Adduct formation in other halophenols was not observed, probably because of the steric hindrance from the bulkier halogen atoms such as chlorine and bromine at the *o*-positions. Inspired by the adduct formation by an asymmetric complex with different halophenols, we have employed an iron(IV)-oxo complex, $[Fe^{IV}(O)(N4Py)]^{2+}$, **4b** bearing a symmetric ligand backbone as shown in Fig. 5.1 to examine its effect on the substrate approach to the oxo group during adduct formation.

The starting iron(II) complex, $[Fe^{II}(N4Py)(CH_3CN)](OTf)_2$, (**4a**) was synthesized by reacting $Fe^{II}(OTf)_2{\cdot}2CH_3CN$ with the N4Py ligand under an argon atmosphere inside a glove box using a previously reported procedure.[63] The iron(iv)-oxo complex, $[Fe^{IV}(O)(N4Py)]^{2+}$, (**4b**) was generated by the addition of PhIO as the oxygen donor in CH_3CN solvent at ambient conditions as reported before.[64] The complex **4b** was characterized by different spectroscopic techniques such as UV-vis spectroscopy and mass spectrometry. UV-vis spectroscopy confirms the generation of complex **4b** by its characteristic *d-d* absorption band at λ_{max} = 695 nm as shown in Fig. 5.21 with a half-life of over 60 hrs at room temperature. Further, the electrospray ionization mass spectrum (ESI-MS) of **4b** shows a prominent peak at *m/z* 587.91 which corresponds to the formation of $[Fe^{IV}(O)(N4Py)(OTf)]^{+}$ complex (see Fig. 5.22). Also, the formation of the iron(iv)-oxo complex was confirmed by its isotopic distribution patterns at *m/z* 587.91.

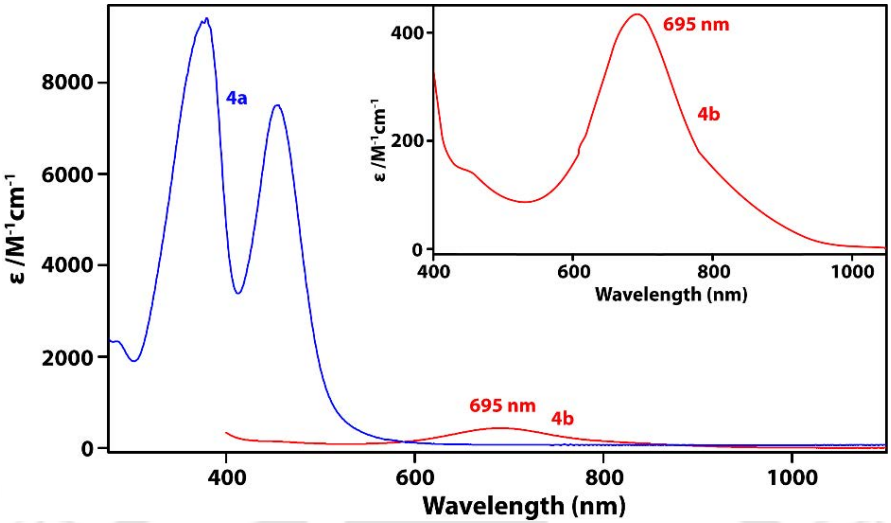

Fig. 5.21. UV-vis spectrum of $[Fe^{II}(N4Py)(CH_3CN)](OTf)_2$, (0.25 mM) **4a** (blue line) and $[Fe^{IV}(O)(N4Py)]^{2+}$ (1 mM) **4b** (red line) in CH_3CN at 25 °C. Insert shows the d-d transition band at 695 nm for **4b** (red line).

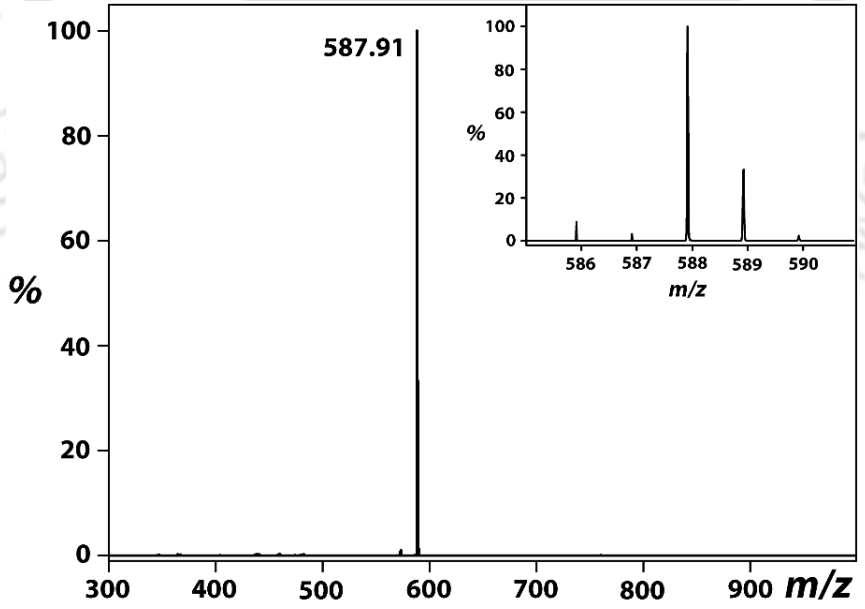

Fig. 5.22. ESI-MS spectrum of complex **4b** in CH_3CN at 25 °C. The peak at *m/z* 587.91 corresponds to $[Fe^{IV}(O)(N4Py)(OTf)]^+$. The inset shows the isotopic distribution pattern of *m/z* 587.91.

The electrophilic nature of complex **4b** was then investigated with a series of tri-halophenols with halogen atoms at the *ortho*- and *para*-positions, namely 2,4,6-trifluorophenol (2,4,6-TFP), 2,4,6-trichlorophenol (2,4,6-TCP) and 2,4,6-tribromophenol (2,4,6-TBP). The reactivity patterns of these substrates with complex **4b** were monitored by the change in the UV-vis absorption as a function of time. Upon addition of 10 equiv. of tri-halophenol to complex **4b** at ambient conditions in CH_3CN solvent resulted in the immediate decay of the iron(IV)-oxo characteristic d-d-transition band at 695 nm and concomitant formation of the purple-coloured intermediates at a wavelength range of 558 – 595 nm depending on the phenolic substrates used (see Fig. 5.23). The formation of such intermediates was also observed with di- and mono-halophenols under identical reaction conditions (see Fig. 5.24).

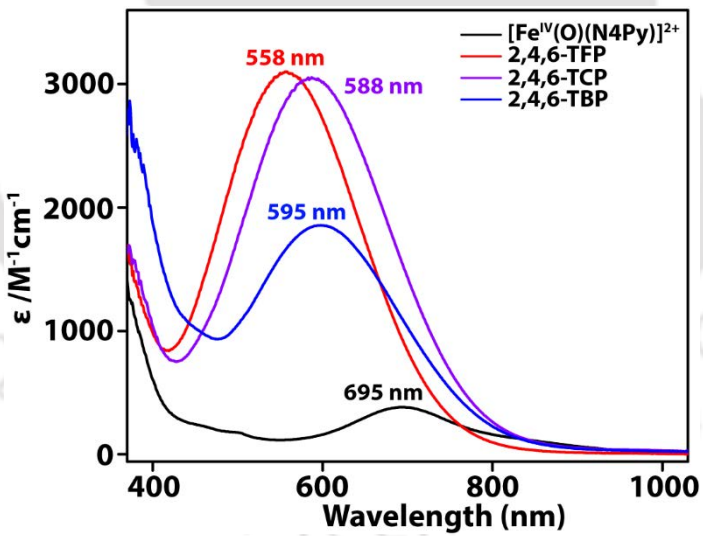

Fig. 5.23. UV/Vis spectral changes by the addition of tri-halophenols to an acetonitrile solution at 25 °C containing 0.5 mM $[Fe^{IV}(O)(N4Py)]^{2+}$, **4b**. The UV-Vis spectrum of the complex **4b** is given by the black line and the obtained UV-Vis spectra upon the addition of 10 equiv. of 2,4,6-TFP (red line), 2,4,6-TCP (violet line) and 2,4,6-TBP (blue line) are shown as an overlay.

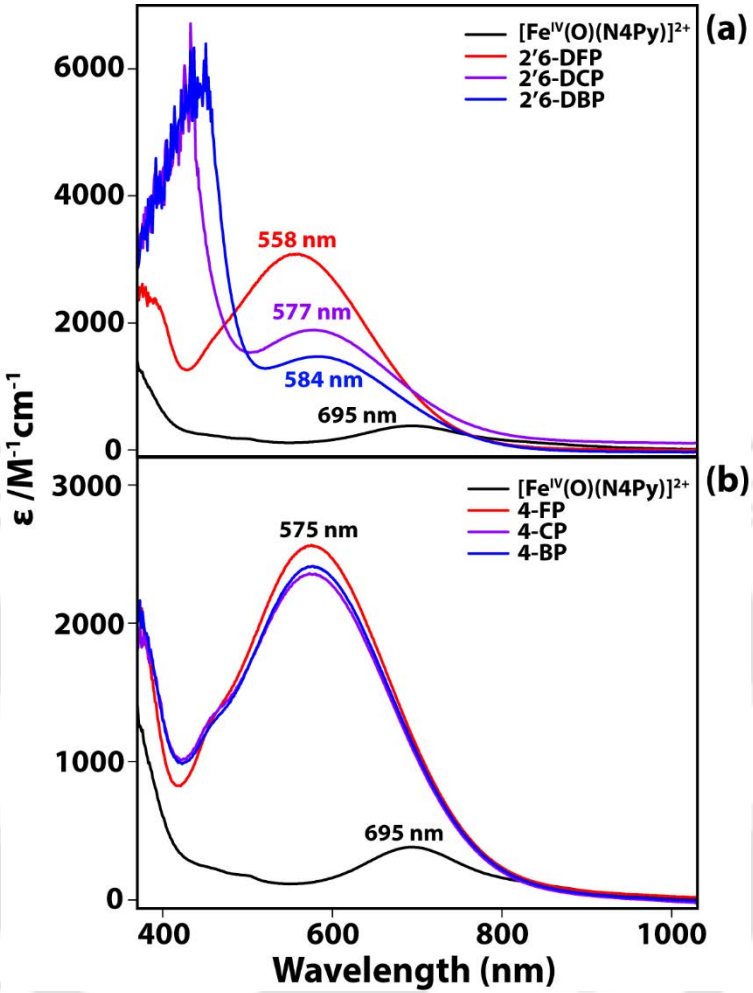

Fig. 5.24. UV/Vis spectra for the formation of substrate-bound adducts by addition of 10 equiv. of phenol substrates to complex 0.5 mM $[Fe^{IV}(O)(N4Py)]^{2+}$ (**4b**) (black line) in CH_3CN at 25 °C (a) 2,6-DFP (red line), 2,6-DCP (violet line) and 2,6-DBP (blue line). (b) 4-FP (red line), 4-CP (violet line) and 4-BP (blue line).

To establish the nature of the species with 588 nm absorption as obtained for the reaction of **4b** with 2,4,6-TCP, we extracted a sample and analyzed it with ESI-MS, (see Fig. 5.25). The mass and isotope ratio characterizes this species as the $[Fe(O_2C_6Cl_3H_2)(N4Py)\text{-}(H^+)]^+$ adduct complex with *m*/*z* 634.03. We propose this species to originate from a hydrogen atom abstraction from 2,4,6-TCP by the iron(IV)-oxo

species followed by proton release to the solvent, while retaining the oxidized substrate-bound complex. This would be the first characterization of a radical intermediate in substrate dehalogenation reactions.

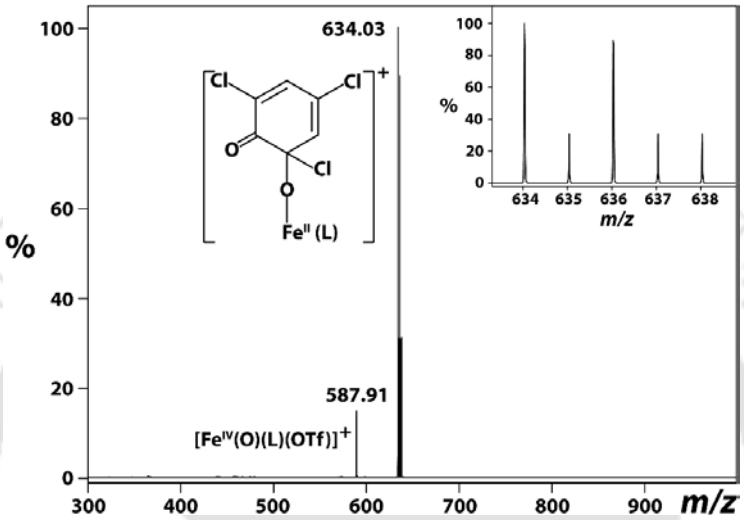

Fig. 5.25. Positive ESI-MS spectrum obtained from the reaction of $[Fe^{IV}(O)(N4Py)]^{2+}$, **4b** with 2,4,6-TCP in CH_3CN at 25 °C. The inset shows the isotopic distribution pattern around *m/z* 634. (L= N4Py)

To understand whether the reaction proceeds with any alternative pathway other than initial hydrogen atom abstraction from the phenolic O–H group, we synthesized deuterated phenol (2,4,6-TFP-d_1) and reacted it with complex **4b** under identical reaction conditions as that for 2,4,6-TFP (see Fig. 5.26 and 5.27). The formation of the substrate-bound adduct was monitored for both substrates as we could not obtain a decay profile of the iron(IV)-oxo band. Formation of the substrate-bound adduct was slower in the case of the 2,4,6-TFP-d_1 as the bond dissociation energy of O–D bond is greater than that of O–H bond. This clearly indicates that the mechanism for the dehalogenation of halophenols by complex **4b** starts with the abstraction of an H-atom from the phenolic O–H group resulting in the formation of phenolate radicals and an iron(III)-OH species.

The formation of the phenolate radicals was observed in all the halophenols irrespective of their size and nucleophilicity characters. These phenolate radicals are oxidized and bind the iron(III)-OH species on the *ortho*- and *para*-position of the -C=O group in the oxidized substrates to form an adduct. The formation of these adducts could be attributed to the fact that $[Fe^{IV}(O)(N4Py)]^{2+}$, **4b** complex has a symmetric ligand backbone, which provides an open space around its iron-oxo core for the easy approach of the substrates.

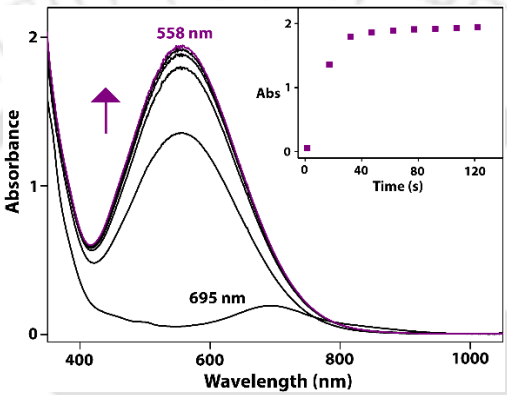

Fig. 5.26. UV-Vis spectrum for the formation of substrate-bound adducts by addition of 50 equiv. of 2,4,6-TFP to complex **4b** (0.5 mM) in CH_3CN at 25 °C. Inset shows the time trace for formation at 558 nm. The data were recorded at 15 seconds intervals.

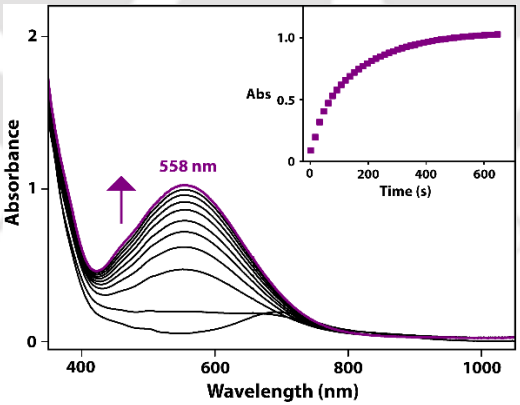

Fig. 5.27. UV-Vis spectrum for the formation of substrate-bound adducts by addition of 50 equiv. of 2,4,6-TFP-d_1 to complex **4b** (0.5 mM) in CH_3CN at 25 °C. Inset shows the time trace for formation at 558 nm. The data were recorded at 15 seconds intervals.

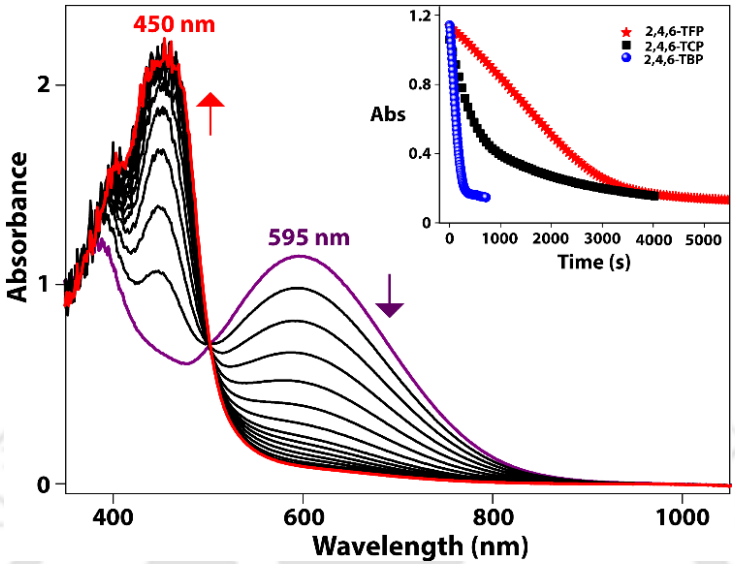

Fig. 5.28. UV-Vis spectrum for the decay of substrate-bound adduct of 2,4,6-TBP at 595 nm and concomitant formation of the iron(II)-precursor at 450 nm in CH_3CN at 25 °C. Inset shows the decay time trace for all the adducts with tri-halophenols. The data were recorded at 60 seconds interval for the adducts with 2,4,6-TFP and 2,4,6-TCP and at 7 seconds interval for adducts with 2,4,6-TBP.

Furthermore, the formation of the adducts was evidenced by the UV-vis absorption as a shift in the wavelength from 558 nm to 595 nm is witnessed by changing the substrates from trifluorophenol to tribromophenol (see Fig. 5.23). This red shift in the wavelength for the adducts can be explained based on the inductive effect (–I effect) from the halogen atoms. In particular, since fluorine is a more electronegative element it withdraws electrons from the phenyl ring and thereby reduced the λ_{max} as compared to the adducts with chlorine and bromine. The self-decay of these intermediates resulted in the formation of the iron(II)-precursors under ambient conditions and their stability was determined by observing their half-life periods (see Fig. 5.28 and Table 5.2). The rate of decay of these adducts is slower as compared to the rate of formation of phenolate radicals and is the rate-determining step in the dehalogenation of all the halophenols. The pseudo-first-order rate constants ($k_{obs,formation}$) for the formation of adducts are 3.88 x 10^{-2} s^{-1}, 9.9

x 10^{-2} s^{-1} and 0.16 s^{-1} for 2,4,6-TFP, 2,4,6-TCP and 2,4,6-TBP, respectively, at room temperature. By contrast, the pseudo-first-order rate constants ($k_{obs,decay}$) for the decay of adducts are 3.35 x 10^{-4} s^{-1}, 1.51 x 10^{-3} s^{-1} and 5.26 x 10^{-3} s^{-1} for 2,4,6-TFP, 2,4,6-TCP and 2,4,6-TBP, respectively, at room temperature.

Table 5.2. Spectroscopic features of halophenol bound iron adducts in CH_3CN at 25 °C.

Sl. No.	Halophenols		λ_{max} (nm)	ε ($M^{-1}cm^{-1}$)	$t_{1/2}$ (in sec)
1	2,4,6-tri-halophenols	2,4,6-TFP	558	3080	1800
2		2,4,6-TCP	588	3040	600
3		2,4,6-TBP	595	1840	133
4	2,6-di-halophenols	2,6-DFP	558	3080	2220
5		2,6-DCP	577	1880	480
6		2,6-DBP	584	1470	185
7	4-halophenols	4-FP	575	2564	5010
8		4-CP	575	2406	2520
9		4-BP	575	2352	4080

The first-order rate constants for the oxidative dehalogenation of a range of halophenols by complex **4b** were determined at variable temperatures to calculate activation parameters. The pseudo-first-order rate constants were obtained by the addition of 10 equiv. of the substrate solution to the iron(IV)-oxo solution at variable temperatures. The enthalpy of activation ($\Delta H^{\ddagger}$) and entropy of activation ($\Delta S^{\ddagger}$) values were obtained from Eyring plots for the oxidation of tri-halophenol substrates with complex **4b** (see Fig. 5.29 and Table 5.3).

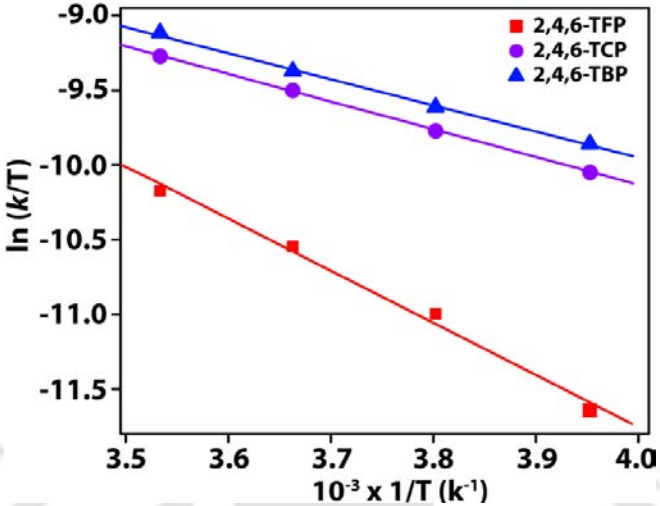

Fig. 5.29. Activation parameters determined for the oxidation of 2,4,6-TFP (■), 2,4,6-TCP (●) and 2,4,6-TBP (▲) by complex **4b** in CH_3CN at a temperature range of 253-283 K. The substrate solution (10 equiv.) was added to complex **4b** solution (0.5 mM) and the absorption change measured.

Table 5.3. Activation parameters for the oxidation of tri-halophenols with complex 4b in CH_3CN.

Substrates	$\Delta H^{\ddagger}$ (kcal mol^{-1})	$\Delta S^{\ddagger}$ (cal mol^{-1} K^{-1})
2,4,6-TFP	6.9	-42.8
2,4,6-TCP	3.7	-52.6
2,4,6-TBP	3.5	-53.1

To gain more insight into the reaction mechanism for the reaction of halophenols with complex **4b**, oxidized products were analyzed by ^{1}H NMR spectroscopy. When the reaction mixture obtained by the reaction of complex **4b** and 2,4,6-TFP was analyzed, we found mixtures of 2,4-fluoro-*ortho*-benzoquinone (*o*-quinone) and 2,6-difluoro-*para*-benzoquinone (*p*-quinone) with the former as the major product. To get further details,

reaction mixtures of all the halophenols were analyzed and the ratio of *ortho*- to *para*-quinone was evaluated (see Table 5.4). Interestingly, *o*-quinone was found to be the major product in all cases. Overall, our experimental work shows that non-heme iron(IV)-oxo complexes can react through dehalogenation including defluorination of aromatic phenols in a stepwise reaction mechanism that is initiated by hydrogen atom abstraction from the phenol to form an adduct.

Table 5.4. Product distributions for the reaction of 0.5 mM of 4b in CH_3CN with mono-, di-, and tri-halophenols at 25 °C.

Substrates	Product distribution, % (*ortho*:*para*) quinone
2,4,6-TFP	44:25
2,4,6-TCP	21:10
2,4,6-TBP	22:10
2,6-DFP	48:0
2,6-DCP	25:0
2,6-DBP	20:0
4-FP	42:35
4-CP	53:30
4-BP	25:10

5.2.3. Computational Backup

To gain further insight into the aromatic dehalogenation reactions by $[Fe^{IV}(O)(N4Py)]^{2+}$, **4b** we performed a density functional theory study for 2,4,6-TFP and 2,4,6-TCP activation and tested various pathways leading to products. The mechanism is established with an initial step from the substrate-iron(IV)-oxo reactant complex (**RC**) for an H-atom abstraction from the phenol group by the iron(IV)-oxo species via transition state **TS1** to form an iron(III)-hydroxo complex with nearby radical (**IM1**). Thereafter, the **IM1** complex reacts through OH rebound to form complex **IM2** via transition state **TS2** takes place on either the *ortho*- or *para*-position of the radical as identified with a subscript o or p. This **IM2** complex is proposed to be the experimentally determined adduct complex with an absorption of 558 nm for 2,4,6-TFP. In agreement with experimental observation,[63] the reactant complexes are in a triplet spin ground state with the quintet well higher in energy, see Fig. 5.30. Interestingly, the H-atom abstraction takes

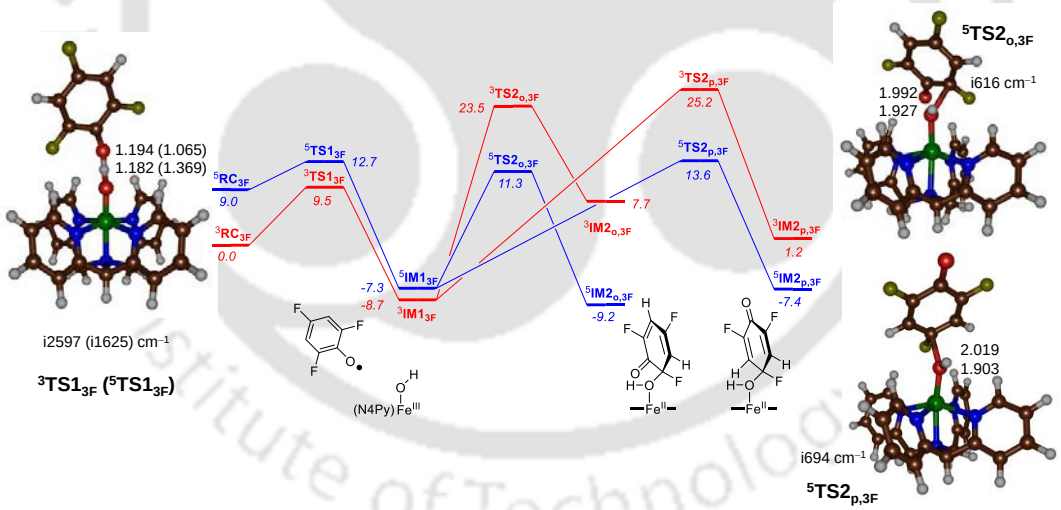

Fig. 5.30. Free energy landscape (ΔG values at 298 K with zero-point energy, and thermal, solvent and entropic corrections included in kcal mol^{-1}) for the reaction of 2,4,6-TFP activation by $[Fe^{IV}(O)(N4Py)]^{2+}$ (**4b**). On the sides are shown the optimized geometries of the H-atom abstraction and OH rebound barriers with bond lengths in Armstrongs and the imaginary frequency in cm^{-1}.

place on the triplet spin state surface with a barrier of $\Delta G^{\ddagger}$ = 9.5 kcal mol^{-1} for 2,4,6-TFP and $\Delta G^{\ddagger}$ = 9.3 kcal mol^{-1} for 2,4,6-TCP. The former free energy of activation contains an enthalpy of activation of ΔE+ZPE = 7.8 kcal mol^{-1}, which matches the experimentally determined enthalpy of activation of ΔH = 6.9 kcal mol^{-1}, excellently. The entropy of activation is calculated from gas-phase cluster models that ignore the solvent cage and hence overestimate the rotational and vibrational partition functions dramatically.[65]

Previous calculations on H-atom abstraction from substrates by $[Fe^{IV}(O)(N4Py)]^{2+}$ showed a spin-state-crossing from triplet to quintet before the transition state, so that a high-spin iron(III)-hydroxo complex is formed.[24,25,66-75] Here, for both substrates ^{3}**TS1** is below ^{5}**TS1**, while the two spin states for the radical intermediates are within 1.5 kcal mol^{-1}. Therefore, phenol hydrogen atom abstraction takes place on the triplet spin state surface rather than on a dominant quintet spin state surface. Moreover, using halophenols as substrate the spin state crossing from triplet to quintet happens much later during the reaction mechanism most likely during the lifetime of the radical intermediate **IM1**, while for aliphatic substrates early spin state crossing close or before **TS1** were found. After the radical intermediate, the spin state crossing happens and an OH rebound barrier to the *ortho*- or *para*-position of the phenol takes place. These OH rebound barriers are relatively high in free energy and with respect to the radical intermediates **IM1** we find values of $\Delta G^{\ddagger}$ = 20.0 kcal mol^{-1} for *ortho*-rebound to 2,4,6-TFP and $\Delta G^{\ddagger}$ = 22.3 kcal mol^{-1} for *para*-rebound. Using transition state theory the experimental $k_{obs,decay}$ barrier for the adduct complex of 2,4,6-TFP corresponds to a $\Delta G^{\ddagger}$ = 22.2 kcal mol^{-1} and is in good quantitative agreement with the ^{5}**TS2**$_{o,3F}$ barrier in Fig. 5.30 and predicts the correct selectivity.

After the rebound barriers, the systems relax to adduct complexes **IM2**; however, these are weakly bound complexes that separate into an $[Fe^{II}(N4Py)]^{2+}$ and adduct

$C_6H_2X_3O(OH)$ rapidly. The latter, in the presence of a base, such as OH^-, in solution dissociates further into quinone and halide (X^- = F^-/Cl^-). Optimized geometries of the hydrogen atom abstraction transition states are shown in Fig. 5.30. They have very large imaginary frequencies that are i2597 cm^{-1} for ^{3}**TS1**$_{3F}$ and i2879 cm^{-1} for ^{3}**TS1**$_{3Cl}$. These are well higher than typical H-atom abstraction barriers from aliphatic groups or phenols by non-heme and heme iron(IV)-oxo complexes.[76,77] Both triplet barriers are relatively central with two short O–H distances. By contrast, in the quintet spin state, the structures are reactant-like with short phenol O–H distances but a long distance toward the oxo group.

5.2.4. Reaction Mechanism

The product distribution obtained and controlled experiments hereby guided us to propose a plausible mechanism for the oxidative dehalogenation reactions of tri-halophenols with the iron(IV)-oxo complex **4b**. The reaction mechanism involves two successive one-electron reductions of the iron(IV)-oxo species.[44-48] The reaction initiates with the abstraction of the phenolic hydrogen atom thereby forming Fe(III)-OH and a phenolate radial species. Thereafter, the phenolate radical is oxidized and the Fe(III)-OH binds to this oxidized substrate either at *ortho*- or *para*-position of -C=O group to form adducts with a loss of proton as shown in Scheme 5.3. Finally, the self-decay of these adducts results in the formation of either *o*-quinone or *p*-quinone products with the concomitant formation of Fe(II)-complex with a loss of HX molecule (X= F, Cl or Br).

Scheme 5.3. A plausible mechanism for the oxidative dehalogenation of tri-halophenols by the intermediate 4b.

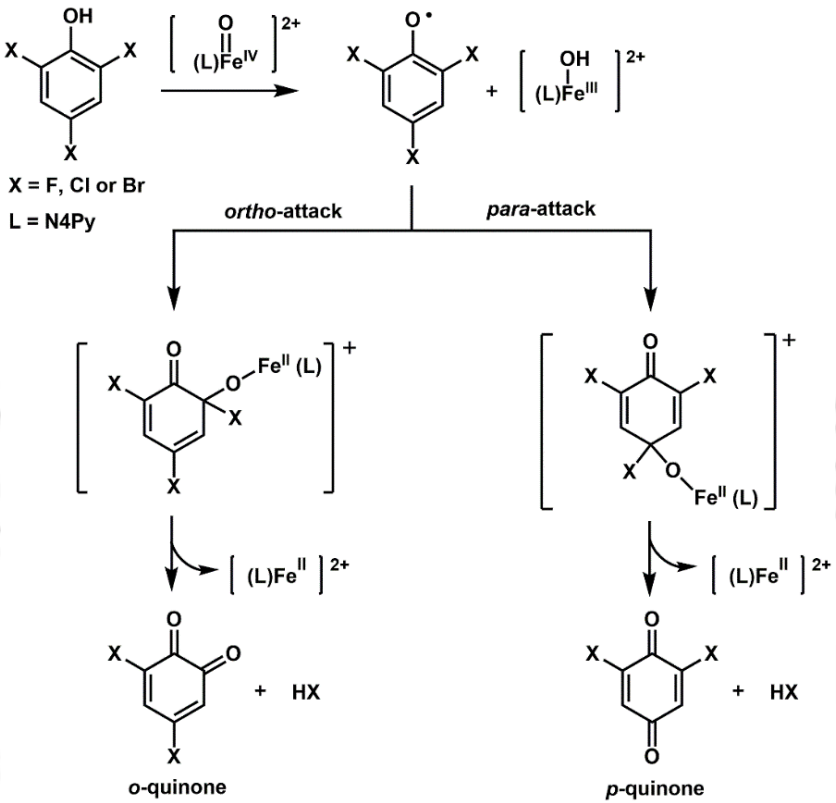

5.3. Conclusion

In summary, we have synthesized two iron(IV)-oxo complexes, one is asymmetric and another is symmetric which act as excellent oxidants for the oxidative degradation of halo-phenolic compounds that are potential environmental pollutants. Earlier we have seen this complex to be a highly active catalyst for heteroatom oxidation. Likewise, in oxidative dehalogenation, a detailed comparative analysis of several mono- di and tri-halophenols have been studied. We have observed a substrate-bound species being generated as an intermediate during the reaction. Although the reaction rates of the iron(IV)-oxo compound are guided by its inherent electrophilicity, interestingly, the

formation of the substrate-bound adduct is dependent upon the steric factor imposed by the bulkiness of the halogen atom in its *ortho*-position. In asymmetric oxo complex $[Fe^{IV}(O)(2PyN2Q)]^{2+}$, the ligand backbone, therefore, also plays a crucial role in directing the approach of the halophenols towards the active site. Further, the tentative formation of a hepta-coordinated species along the reaction coordinate brings forth the selective formation of the *ortho*-quinone product in major amounts. However, adduct formation in all the halophenols was not observed, probably because of the steric hindrance from the ligand skeleton with the bulkier halogen atoms such as chlorine and bromine at the *o*-positions. Thus, we have employed an iron(IV)-oxo complex $[Fe^{IV}(O)(N4Py)]^{2+}$ supported by a symmetric N4Py ligand, which detoxifies a wide range of halophenols including trifluorophenol efficiently into their non-hazardous forms. The symmetric backbone around the iron(IV)-oxo core provides enough space and guides the substrate approach which leads to the substrate-bound adduct formation with various halophenols irrespective of their size and nucleophilic behavior. A combined experimental and theoretical studies reveal a unique reaction mechanism for the oxidative dehalogenation of $[Fe^{IV}(O)(N4Py)]^{2+}$ with these halophenols which proceeds via a Fe(II)-phenolate adduct formation instead of earlier proposed hepta-coordinated Fe(III)-OH species in the dehalogenation of halophenols by $[Fe^{IV}(O)(2PyN2Q)]^{2+}$ complex.

5.4. References

1. M. Costas, M. P. Mehn, M. P. Jensen, L. Que, Jr., *Chem. Rev.* **2004**, *104*, 939-986.
2. M. M. Abu-Omar, A. Loaiza, N. Hontzeas, *Chem. Rev.* **2005**, *105*, 2227-2252.
3. J. M. Bollinger, Jr., J. C. Price, L. M. Hoffart, E. W. Barr, C. Krebs, *Eur. J. Inorg. Chem.* **2005**, 4245-4254.
4. C. V. Sastri, M. S. Seo, M. J. Park, K. M. Kim, W. Nam, *Chem. Commun.* **2005**, 1405-1407.
5. W. Nam, *Acc. Chem. Res.* **2007**, *40*, 522-531.
6. E. I. Solomon, T. C. Brunold, M. I. Davis, J. N. Kemsley, S. K. Lee, N. Lehnert, F. Neese, A. J. Skulan, Y. S. Yang, J. Zhou, *Chem. Rev.* **2000**, *100*, 235-350.
7. N. Y. Oh, Y. Suh, M. J. Park, M. S. Seo, J. Kim, W. Nam, *Angew. Chem.* **2005**, *117*, 4307-4311; *Angew. Chem. Int. Ed.* **2005**, *44*, 4235-4239.
8. S. O. Kim, C. V. Sastri, M. S. Seo, J. Kim, W. Nam, *J. Am. Chem. Soc.* **2005**, *127*, 4178-4179.
9. P. C. A. Bruijnincx, G. van Koten, R. J. M. Klein Gebbink, *Chem. Soc. Rev.* **2008**, *37*, 2716-2744.
10. A. R. McDonald, L. Que Jr., *Coord. Chem. Rev.* **2013**, *257*, 414-428.
11. W. Nam, Y.-M. Lee, S. Fukuzumi, *Acc. Chem. Res.* **2014**, *47*, 1146-1154.
12. M. Sono, M. P. Roach, E. D. Coulter, J. H. Dawson, *Chem. Rev.* **1996**, *96*, 2841-2888.
13. J. T. Groves, *Proc. Natl. Acad. Sci. U. S. A.* **2003**, *100*, 3569-3574.
14. B. Meunier, S. P. de Visser, S. Shaik, *Chem. Rev.* **2004**, *104*, 3947-3980.
15. I. G. Denisov, T. M. Makris, S. G. Sligar, I. Schlichting, *Chem. Rev.* **2005**, *105*, 2253-2278.

16. Iron-containing enzymes: Versatile catalysts of hydroxylation reactions in nature, ed. S. P. de Visser, D. Kumar, *RSC Publishing, Cambridge* **2011**.
17. S. P. de Visser, Y. T. Lin, H. S. Ali, U. K. Bagha, G. Mukherjee, C. V. Sastri, *Coord. Chem. Rev.* **2021**, *439*, 213914.
18. D. A. Proshlyakov, T. F. Henshaw, G. R. Monterosso, M. J. Ryle, R. P. Hausinger, *J. Am. Chem. Soc.* **2004**, *126*, 1022-1023.
19. C. Krebs, J. C. Price, J. Baldwin, L. Saleh, M. T. Green, J. M. Bollinger Jr., *Inorg. Chem.* **2005**, *44*, 742-757.
20. S. T. Kleespies, W. N. Oloo, A. Mukherjee, L. Que, Jr., *Inorg. Chem.* **2015**, *54*, 5053-5064.
21. C. V. Sastri, J. Lee, K. Oh, Y. J. Lee, J. Lee, T. A. Jackson, K. Ray, H. Hirao, W. Shin, J. A. Halfen, J. Kim, L. Que, Jr., S. Shaik, W. Nam, *Proc. Natl. Acad. Sci. U. S. A.* **2007**, *104*, 19181-19186.
22. D. Wang, K. Ray, M. J. Collins, E. R. Farquhar, J. R. Frisch, L. Gómez, T. A. Jackson, M. Kerscher, A. Waleska, P. Comba, M. Costas, L. Que Jr., *Chem. Sci.* **2013**, *4*, 282-291.
23. G. Mukherjee, J. K. Satpathy, U. K. Bagha, M. Q. E. Mubarak, C. V. Sastri, S. P. de Visser, *ACS Catal*. **2021**, *11*, 9761-9797.
24. G. Mukherjee, A. Alili, P. Barman, D. Kumar, C. V. Sastri, S. P. de Visser, *Chem. Eur. J.* **2019**, *25*, 5086-5098.
25. G. Mukherjee, F. G. Cantú Reinhard, U. K. Bagha, C. V. Sastri, S. P. de Visser, *Dalton Trans.* **2020**, *49*, 5921-5931.
26. S. C. Peck, W. A. van der Donk, *J. Biol. Inorg. Chem*. **2017**, *22*, 381-394.
27. A. O. Olaniran, E. O. Igbinosa, *Chemosphere* **2011**, *83*, 1297-1306.
28. P. K. Arora, H. Bae, Microb. *Cell Factories* **2014**, *13*, 31-47.
29. S. L. Simonich, R. A. Hites, *Science* **1995**, *269*, 1851-1854.

30. J. Gao, L. Liu, X. Liu, H. Zhou, S. Huang, Z. Wang, *Chemosphere* **2008**, *71*, 1181-1187.
31. W. J. Sim, S. H. Lee, I. S. Lee, S. D. Choi, J. E. Oh, *Chemosphere* **2009**, *77*, 552-558.
32. E. O, Igbinosa, E. E. Odjadjare, V. N. Chigor, I. H. Igbinosa, A, O. Emoghene, F. O. Ekhaise, N. O. Igiehon, O. G. Idemudia, *Sci. World J*. **2013**, *2013*, 1-11.
33. J. Pumarega, M. Gasull, D. H. Lee, T. López, M. Porta, *PLoS One* **2016**, *11*, 1-16.
34. Agency for Toxic Substances and Disease Registry (ATSDR), Toxicological Profile for Chlorophenols, U.S. Department of Health and Human Services, *Public Health Service, Atlanta, GA* **1999**.
35. M. Anbia and S. Amirmahmoodi, *Scientia Iranica C* **2011**, *18*, 446-452.
36. M. Pera-Titus, V. Garcia-Molina, M. A. Banos, J. Gimenez, S. Esplugas. *Appl. Catal. B* **2004**, *47*, 219-256.
37. A. Karci, *Chemosphere* **2014**, *99*, 1-18.
38. S. Y. Oh, Y. D. Seo, *Environ. Sci. Pollut. Res. Int*. **2016**, *23*, 951-961.
39. R. L. Osborne, L. O. Taylor, K. P. Han, B. Ely, J. H. Dawson, *Biochem. Biophys. Res. Commun*. **2004**, *324*, 1194-1198.
40. J. Belyea, L. B. Gilvey, M. F. Davis, M. Godek, T. L. Sit, S. A. Lommel, S. Franzen, *Biochemistry* **2005**, *44*, 15637-15644.
41. C. Colomban, A. H. Tobing, G. Mukherjee, C. V. Sastri, A. B. Sorokin, S. P. de Visser, *Chem. Eur. J*. **2019**, *25*, 14320-14331.
42. M. W. LaCount, E. L. Zhang, Y.-P. Chen, K. Han, M. M. Whitton, D. E. Lincoln, S. A. Woodin, L. Lebioda, *J. Biol. Chem.* **2000**, *275*, 18712-18716.
43. S. Franzen, M. P. Roach, Y.-P. Chen, R. B. Dyer, W. H. Woodruff, J. H. Dawson, *J. Am. Chem. Soc*. **1998**, *120*, 4658-4661.

44. R. L. Osborne, G. M. Raner, L. P. Hager, J. H. Dawson, *J. Am. Chem. Soc*. **2006**, *128*, 1036-1037.
45. R. P. Ferrari, E. Laurenti, F. Trotta, *J. Biol. Inorg. Chem.* **1999**, *4*, 232-237.
46. K. E. Hammel, P. J. Tardone, *Biochemistry* **1988**, *27*, 6563-6568.
47. N. B. J. Vollaard, J. P. Shearman, C. E. Cooper, *Sports Med.* **2005**, *35*, 1045-1062.
48. J. Zhao, V. de Serrano, J. Zhao, P. Le, S. Franzen, *Biochemistry* **2013**, *52*, 2427-2439.
49. S. Munshi, R. D. Jana, T. K. Paine, *Dalton Trans.* **2021**, *50*, 5590-5597.
50. G. Mukherjee, C. W. Z. Lee, S. S. Nag, A. Alili, F. G. Cantú Reinhard, D. Kumar, C. V. Sastri, S. P. de Visser, *Dalton Trans*. **2018**, *47*, 14945-14957.
51. W. K. C. Lo, C. J. McAdam, A. G. Blackman, J. D. Crowley, D. A. McMorran, *Inorg. Chim. Acta* **2015**, *426*, 183-194.
52. A. A. Massie, M. C. Denler, L. T. Cardoso, A. N. Walker, M. K. Hossain, V. W. Day, E. Nordlander, T. A. Jackson, *Angew. Chem., Int. Ed*. **2017**, *56*, 4178-4182.
53. S. Rana, J. P. Biswas, A. Sen, M. Clémancey, G. Blondin, J.-M. Latour, G. Rajaraman, D. Maiti, *Chem. Sci.* **2018**, *9*, 7843-7858.
54. Y. Wang, A. Liu, *Chem. Soc. Rev*. **2020**, *49*, 4906-4925.
55. P. Barman, A. K. Vardhaman, B. Martin, S. J. Wörner, C. V. Sastri, P. Comba, *Angew. Chem., Int. Ed.* **2015**, *54*, 2095-2099.
56. Y. Sheng, C. S. Abelson, J. Prakash, A. Draksharapu, V. G. Young, Jr., L. Que, Jr., *Angew.Chem. Int.Ed.* **2021**, *60*, 20991-20998.
57. A. K. Vardhaman, P. Barman, S. Kumar, C. V. Sastri, D. Kumar, S. P. de Visser, *Chem. Commun.* **2013**, *49*, 10926-10928.
58. A. K. Vardhaman, C. V. Sastri, D. Kumar, S. P. de Visser, *Chem. Commun.* **2011**, *47*, 11044-11046.
59. F. Namuswe, T. Hayashi, Y. Jiang, G. D. Kasper, A. A. N. Sarjeant, P. M. Loccoz, D. P. Goldberg, *J. Am. Chem. Soc.* **2010**, *132*, 157-167.

60. U. K. Bagha. J. K. Satpathy, G. Mukherjee, C. V. Sastri, S. P. de Visser, *Org. Biomol. Chem.* **2021**, *19*, 1879-1899.
61. G. Mukherjee, C. V. Sastri, *Isr. J. Chem*. **2020**, *60*, 1032-1048.
62. S. Sahu, M. G. Quesne, C. G. Davies, M. D rr, I. I. Burmazovi , M. A. Siegler, G. N. L. Jameson, S. P. de Visser, D. P. Goldberg, *J. Am. Chem. Soc*. **2014**, *136*, 13542-13545.
63. M. Lubben, A. Wilkinson, B. Feringa, L. Que Jr, *Angew. Chem. Int. Ed.* **1995**, *34*, 1512-1514.
64. J. Kaizer, E. J. Klinker, N. Y. Oh, J.-U. Rohde, W. J. Song, A. Stubna, J. Kim, E. Münck, W. Nam, L. Que Jr., *J. Am. Chem. Soc*. **2004**, *126*, 472-473.
65. F. G. Cantú Reinhard, A. S. Faponle, S. P. de Visser, *J. Phys. Chem. A* **2016**, *120*, 9805-9814.
66. D. Kumar, H. Hirao, L. Que Jr., S. Shaik, *J. Am. Chem. Soc*. **2005**, *127*, 8026-8027.
67. H. Hirao, D. Kumar, L. Que Jr., S. Shaik, *J. Am. Chem. Soc*. **2006**, *128*, 8590-8606.
68. L. Bernasconi, E.-J. Baerends, *Eur. J. Inorg. Chem*. **2008**, 1672-1681.
69. A. Dey, *J. Am. Chem. Soc*. **2010**, *132*, 13892-13901.
70. H. Hirao, F. Li, L. Que Jr, K. Morokuma, *Inorg. Chem*. **2011**, *50*, 6637-6648.
71. S. D. Wong, C. B. Bell III, L. V. Liu, Y. Kwak, J. England, E. E. Alp, J. Zhao, L. Que Jr., E. I. Solomon, *Angew. Chem. Int. Ed*. **2011**, *50*, 3215-3218.
72. A. Ansari, A. Kaushik, G. Rajaraman, *J. Am. Chem. Soc*. **2013**, *135*, 4235-4249.
73. Y. Liu, X. Guan, E. L.-M. Wong, P. Liu, J.-S. Huang, C.-M. Che, *J. Am. Chem. Soc*. **2013**, *135*, 7194-7204.
74. S. Stepa L. Andjel M. Zlatar, K. And M. Gruden-Pavlovi , M. Swart, *Inorg. Chem*. **2013**, *52*, 13415-13423.

75. G. Mukherjee, F. G. Cantú Reinhard, U. K. Bagha, C. V. Sastri, S. P. de Visser, *Dalton Trans*. **2020**, *49*, 5921-5931.

76. X.-X. Li, V. Postils, W. Sun, A. S. Faponle, M. Solà, Y. Wang, W. Nam, S. P. de Visser, *Chem. Eur. J*. **2017**, *23*, 6406-6418.

77. H. S. Ali, R. H. Henchman, S. P. de Visser, *Chem. Eur. J*. **2020**, *26*, 13093-13102.

CHAPTER-VI

- **Thesis Overview & Future Prospects**

This thesis has aimed to investigate the generation, characterization and reactivity of high-valent non-heme metal intermediates of iron and manganese. In particular, the structure-function relationship of non-heme manganese(III)-peroxo, iron(IV)-oxo, and iron(IV)-imido systems with various organic substrates have been discussed. In Chapter-III, a new mechanism has been established for the aldehyde deformylation reactions by manganese(III)-peroxo complexes. This mechanism proceeds *via* an electrophilic hydrogen atom abstraction pathway instead of the commonly proposed nucleophilic pathway. A new frontier has been explored in aldehyde deformylation reaction by using CCA as a model substrate. An electrophilic aldehyde deformylation by the peroxo complexes takes place by the abstraction of α-hydrogen of CCA. However, the isotopic substitution of the α-hydrogen with deuterium tunes the regio-selective switch of hydrogen atom abstraction from aliphatic to aldehyde hydrogen. In Chapter-IV, the reactivity of iron(IV)-imido complexes has been compared with iron(IV)-oxo complexes of two different ligand systems. It has been observed that the iron(IV)-imido complexes were found to be sluggish as compared to their oxo analogue toward oxidation reactions.

A simple modification in the ligand backbone has a dramatic influence on the substrate approach to the active site of metalloenzymes as well as their reactivity. In Chapter-V, the oxidative dehalogenation reaction has been studied for iron(IV)-oxo complexes bearing both symmetric and asymmetric ligands with a series of mono-, di-, and tri-halophenols. The replacement of pyridine rings in N4Py by bulkier quinoline groups hinders the phenolic substrates with bulkier halogens like chlorine and bromine. The dehalogenation of these halophenols by the iron(IV)-oxo complexes results in the

formation of quinones as products. A new mechanism has been proposed for the oxidative dehalogenation of halophenols which proceeds *via* the formation of a new reaction intermediate that is a substrate-bound adduct. Thus, the overall reactivity of the intermediates and their mechanisms can be dependent on several factors. It would be great to explore such effects that isolate each species from the other.

List of Publications

1. **U. K. Bagha**, J. K. Satpathy, G. Mukherjee, P. Barman, D. Kumar, S. P. de Visser, C. V. Sastri, Oxidative Dehalogenation of Halophenols by High-Valent Nonheme Iron(IV)-oxo Intermediates. *Faraday Discuss.* **2022**, *234*, 58-69.

2. G. Mukherjee, J. K. Satpathy, **U. K. Bagha**, M. Q. E. Mubarak, C. V. Sastri, S. P. de Visser, Inspiration from Nature: Influence of Engineered Ligand Scaffolds and Auxiliary Factors on the Reactivity of Biomimetic Oxidants. ACS Catal. **2021**, *11*, 15, 9761-9797.

3. S. P. de Visser, Y-Ting Lin, H. S. Ali, **U. K. Bagha**, G. Mukherjee, C. V. Sastri, Negative Catalysis or non-Bell-Evans-Polanyi Reactivity by Metalloenzymes: Examples from Mononuclear heme and Nonheme Iron Oxygenases. *Coord. Chem. Rev*. **2021**, *439*, 213914.

4. **U. K. Bagha**, J. K. Satpathy, G. Mukherjee, C. V. Sastri, S. P. de Visser, A Comprehensive Insight into Aldehyde Deformylation: Mechanistic Implications from Biology and Chemistry. *Org. Biomol. Chem.* **2021**, *19*, *9*, 1879-1899. **(Selected as Front Cover Picture)**

5. G. Mukherjee, F. G. Cantú Reinhard, **U. K. Bagha**, C. V. Sastri, S. P. de Visser, Sluggish Reactivity by a Nonheme Iron(IV)-Tosylimido Complex as Compared to its Oxo Analogue. *Dalton Trans*. **2020**, *49*, 18, 5921-5931.

6. P. Barman, F. G. Cantú Reinhard, **U. K. Bagha**, D. Kumar, C. V. Sastri, S. P. de Visser, Hydrogen by Deuterium Substitution in an Aldehyde Tunes the

Regioselectivity by a Nonheme Manganese(III)-Peroxo Complex. *Angew. Chem. Int. Ed*. **2019**, *58*, 10639-10643.

7. **U. K. Bagha**, R. Yadav, T. Mokkawes, J. K. Satpathy, D. Kumar, C. V. Sastri, S. P. de Visser, Defluorination of Fluorophenols by a Nonheme Iron(IV)-oxo Species: Observation of a new Intermediate along the Reaction. **(Communicated)**

8. G. Mukherjee, G. Velmurugan, M. Kerscher, **U. K. Bagha**, J. K. Satpathy, C. V. Sastri, P. Comba, Mechanistic Insights into Amphoteric Reactivity of an Iron(III)-Alkylperoxido Intermediate. **(Communicated)**

List of Presentations

1. Umesh Kumar Bagha, ***Poster Presenter*** at International Conference: "Frontiers in Chemical Science" (FICS) IIT Guwahati, India, on December 02-04, 2022.
2. Umesh Kumar Bagha, ***Poster Presenter*** at National Conference: "North-East Research Conclave 2022" (NERC) IIT Guwahati, India, on May 20-22, 2022.
3. Umesh Kumar Bagha, ***Poster Presenter*** at National Conference: "Chemical Research Society of India 28th National Symposium in Chemistry 2022" (CRSI NSC) IIT Guwahati, India, on March 25-27, 2022.
4. Umesh Kumar Bagha, ***Poster Presenter*** at International Conference: "Modern Trends in Inorganic Chemistry" (MTIC-XVIII) IIT Guwahati, India, on December 11-14, 2019.
5. Umesh Kumar Bagha, ***Poster Presenter*** at International Conference and Workshop: "OPENTOX ASIA 2019" CSIR-Indian Institute of ChemicalTechnology, Hyderabad, India, on March 1-3, 2019.
6. Umesh Kumar Bagha, ***Poster Presenter*** at International Conference on Advanced in Chemical Biology and Biologics" (ICACB-2019) CSIR-Indian Institute of Chemical Technology, Hyderabad, India, on February 28- March 2, 2019.
7. Umesh Kumar Bagha, ***Poster Presenter*** at National Conference: Research Conclave 2018 IIT Guwahati, India, on March 8-11, 2018. **(awarded with the Best Poster Prize)**

~: Short Biography :~

Umesh Kumar Bagha *is a post-graduate researcher at the Department of Chemistry, IIT Guwahati. He was born to Shri. Surath Bagha and Smt. Laxmi Bagha in the city of Nayagarh, Odisha, India. He did his schooling from Banigochha Govt. High School, Nayagarh, and higher secondary education from Uniitech Residential College, Nayagarh. He obtained his graduation in 2014 from Nayagarh Auto. College with Chemistry (Hons.). He completed his Master's Degree (M.Sc.) in Chemistry from the University of Hyderabad, Telangana in 2016. Later he joined the research group of Prof. Chivukula Vasudeva Sastri at IIT Guwahati and carried out his Ph.D. research work on the investigation of bioispired oxidation mechanism by high-valent metal intermediates. In the future, he is quite interested to explore other areas in Chemistry.*

TH-3026_166122104